Coupling fluid flow, heat and mass transfer with thermo-mechanical process : application to cracked solid oxide fuel cell

Qian Shao

UNIVERSITÉ DE STRASBOURG

Ecole et Observatoire des Sciences de la Terre

Coupling Fluid Flow, Heat and Mass Transfer with Thermo-mechanical Process

Application to Cracked Solid Oxide Fuel Cell

Submitted to the Université de Strasbourg in fulfilment of the requirements for the Degree of Doctor of Philosophy

Qian SHAO

Dissertation Defense on 24 March 2015

Membres du Jury

Directeur de thèse:	A. Younes	Dr Cnrs, Lhyges, Strasbourg
Co-directeur de thèse:	A. Makradi	Chercheur, List, Luxembourg
Rapporteur externe:	H. Zahrouni	Pr, Lem3, Université de Lorraine
Rapporteur externe:	M. Quintard	Dr Cnrs, Imft, Toulouse
Examinateur:	P. Ackerer	Dr Cnrs, Lhyges, Strasbourg
Examinateur:	L. Bouhala	Chercheur, List, Luxembourg

Acknowledgments

I would like to express my special gratitude to my supervisors, Dr. Anis Younes and Dr. Ahmed Makradi, for imparting their vast knowledge and expertise in this work. Without their continuous guidance and persistent help, this thesis would not have been possible.

I would like to thank Dr. Michel Quintard and Dr. Hamid Zahrouni for taking time out from their busy schedules to be my external rapporteurs, and for providing their valuable ideas and comprehensive advices to this work.

I must also acknowledge the other members of my defense committee, Dr. Philippe Ackerer, Dr. Lyazid Bouhala, Dr. Salim Belouettar and Dr. Marwan Fahs.

An appreciation goes out to all my colleagues and friends from Luxembourg Institute of Science and Technology and University of Strasbourg, particularly Sandra Hoffmann, Alex Gansen, Ricardo Fernandez Gonzalez, Dr. Fan Xu, Dr. Mohamed El Hachemi, Dr. Heng Hu, Dr. Kui Wang, Yi Pan and Dr. Noura Fajraoui.

At last, I am grateful to my family, my parents Guangxiang and Aizhi, my brother Ran, my sister in law Min and my niece Yubai, for their constant support, love and encouragement.

Esch-sur-Alzette, 24 April 2015

Contents

List of Figures

List of Tables

Abstract

Over the last few decades, Solid Oxide Fuel Cell (SOFC) has been a promising energy conversion device that has drawn a lot of attention due to its high energy conversion efficiency, fuel flexibility and low pollutant emission. However, as the high operating temperature leads to complex material problems in the SOFC, the energy conversion efficiency and life expectancy optimization remain as the challenging issues regarding the design and manufacturing of fuel cells.

In this thesis, a numerical approach based on a combination of Finite Element (FEM) and eXtended Finite Element (XFEM) methods is developed to model the coupled fluid flow, heat and mass transfer as well as the electrochemical reactions with thermo-mechanical process in the SOFC unit. At first, to predict the temperature and species distribution within the porous electrodes of a SOFC unit, a Darcy-Brinkman (DB) model coupling the gas flow, heat and mass transport in porous media is developed. Then, the XFEM is introduced to deal with the presence of crack in the porous electrodes. The combined DB-XFEM model is used to investigate the effect of fluid flow, heat transfer, porous material properties and the material anisotropy on the onset of crack growth and the propagation path in the SOFC unit. At last, an electrochemistry (EC) model is developed and combined with the DB model to couple the electrochemical reactions to energy and mass transfer in the SOFC. With the DB-EC model, the cell energy conversion performances are studied.

The proposed model is demonstrated to be robust, accurate and efficient in solving the multi-physical problems in the SOFC unit. The advanced numerical methods used in the model not only ensure the accuracy of the calculation, but also simplifies the computation and reduces the computational cost. The parametric studies that have been done in this thesis reveal the dependence of the crack propagation and electrochemical performance on the porous materials properties in the SOFC.

1. Introduction

The demand for energy generation has increased dramatically over the last few years, as well as the need to reduce its impact on the environment. Fuel cell systems are one of the most promising technologies that can help achieve these objectives. A fuel cell unit is an electrochemical device that combines a gaseous fuel (e.g. hydrogen) and an oxidizing gas (e.g. oxygen) to produce electricity, with water and heat as its by-product. The main characteristics of fuel cells are its lower pollutant emission and its higher energy conversion efficiency (40% and higher) compared to most conventional thermomechanical-based power generation processes (only 25% to 30% at best). However, due to the high manufacturing costs and low-reliability of fuel cells, major developments are still required to reach the performance where fuel cells can be widely commercialized. The energy conversion efficiency and life expectancy optimization remain as the major challenging issues regarding the design and manufacturing of fuel cells.

1.1. Background

Among the existing fuel cell systems, planar Solid Oxide Fuel Cell (SOFC) is a promising technology that offers a clean alternative to fossil fuels due to its several potential benefits. Being operated at a high temperature of around 873K - 1273K, SOFCs have a high kinetic activity, which results in a relatively high power density and high energy conversion efficiency. Also the high operating temperature allows the fuel reforming within the unit cell, which enables the utilization of various fuels, such as methane, propane, butane, biomass, coal gas ... etc. Further, the heat produced by the SOFC's electrochemical reactions can be used in applications where a combined heat and power (CHP) is needed such as in residential area. Thanks to its high kinetic activity, its fuel flexibility and the possibility of internal reforming, SOFCs can be used extensively in large and small

stationary, and even non-stationary power generations to replace conventional fossil fuel. Besides, SOFCs are identified as a potential candidate to be used as auxiliary power units of vehicles and aircrafts, as well as for propelling force in heavy transportations.

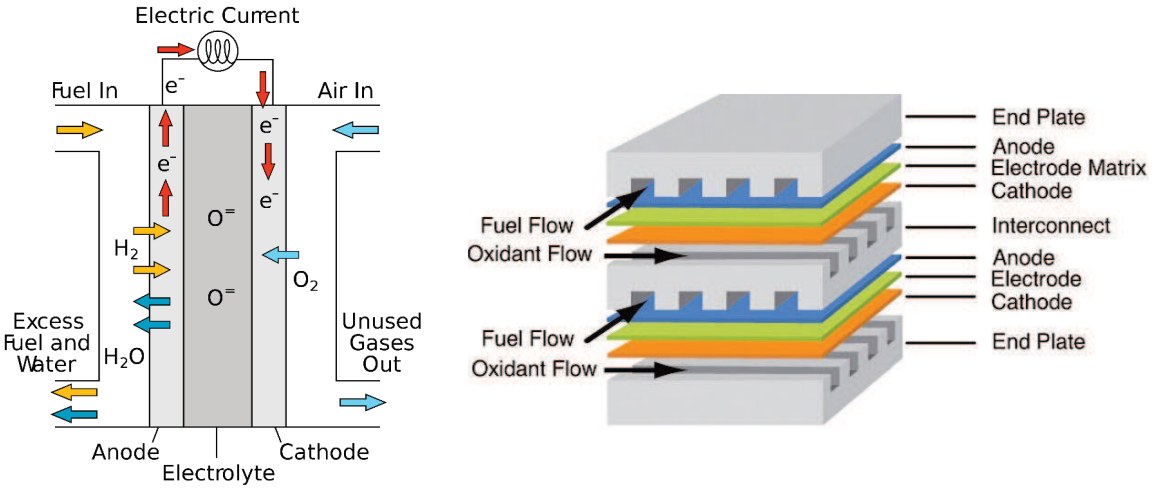

(a) (b)

Figure 1.1.: Schematic view of (a) a planar SOFC unit, (b) a planar SOFC stack

A SOFC unit consists of a solid dense gas-tight electrolyte sandwiched between two electrodes, an anode and a cathode, that present sufficient porosity to allow for the flow of fuel and oxygen to the fuel cell active sites (Fig. 1.1). In-service, oxygen is fed to the cathode/electrolyte interface via the flow channel which is adjacent to the cathode; and hydrogen is fed to the anode/electrolyte interface via the flow channel adjacent to the anode. On the cathode/electrolyte and anode/electrolyte interfaces, there are catalyst layers where the electrochemical reactions take place. At the cathodic catalyst layer, oxygen ions are formed by combining the oxygen molecules with electrons (oxygen reduction reaction):

$$\frac{1}{2}O_2 + 2e^- \rightarrow O^{2-} \tag{1.1}$$

Then oxygen ions migrate through the ion-conducting electrolyte to the anode/electrolyte interface where they react with the hydrogen, producing water while releasing electrons

(hydrogen reduction reaction):

$$H_2 + O^{2-} \rightarrow H_2O + 2e^- \tag{1.2}$$

The electrons produced at the anodic catalyst layer are transported to the cathodic catalyst layer via an external circuit, which also used to harvest the produced energy. Meanwhile, the water produced by the electrochemical reaction is transported out of the cell through the flow channels together with the unreacted hydrogen and oxygen.

To ensure the working conditions of the SOFC, the material of the electrolyte should be dense and gas-tight, so that the fuel at the anode and the oxidant at the cathode can be separated spatially to avoid any fuel crossover. Also the electrolyte should be non-conductive for electrons, but allows sufficient ionic conductivity at an operating temperature between 873K - 1273K. To fulfill these characteristics, a dense ceramic called yttria-stabilized-zirconia (YSZ) is usually used as electrolyte for SOFCs. The anode material can be made of porous nickel/yttria-stabilized-zirconia (Ni/YSZ) cermet that has similar thermal and mechanical properties as the ones of the YSZ electrolyte. This anode material contains yttria-stabilized-zirconia (YSZ) that is conductive for ions, and nickel (Ni) which provides an effective conductivity for electrons and sufficient catalytic activity for electrochemical reactions. In YSZ-based SOFCs, Strontium-doped-lanthanummanganite (LSM) is commonly used as a material for the cathode. This material is electronically conductive and also provides relatively stable physical and chemical properties at high operating temperature.

To guarantee the mechanical stability of each SOFC unit and that of the whole SOFC stack, supported configurations (design) are usually used in planar SOFC, which can be either anode-supported, cathode-supported or electrolyte-supported. In an electrolyte-supported SOFC, the anode and cathode are thin, while the electrolyte is the thickest component and works as the supporting structure. This design works preferably at high operating temperatures (around 1273K), where the large Ohmic losses can be reduced (Aguiar et al., 2004). In an electrode-supported SOFC (anode-/cathode- supported SOFC), the electrode is thick enough to serve as the supporting structure and substrate for the cell fabrication. This supported configuration is used preferably for low operating temperature SOFCs due to the low Ohmic losses of the thin electrolyte.

1.2. Problem Statement

As mentioned in the previous section, the particularity of SOFC is its high operating temperature that has numerous advantages. For instance, at high operating temperature, the kinetic activity is high and nickel is a sufficiently good catalyst, eliminating the need to use costly precious metals (Yakabe et al., 2004; Recknagle et al., 2010). However, the high operating temperature can lead to complex material problems. The temperature gradients in SOFC unit and the different thermal expansion coefficients of cell components (anode/electrolyte/cathode) lead to a built-up of residual stresses in the vicinity of the cell interfaces, which contribute to the cell degradation (Yakabe et al., 2004; Bouhala et al., 2010). Also, the cooling and heating processes, involved during the SOFC service, result in residual stresses and possible crack nucleation in the vicinity of the anode/electrolyte and electrolyte/cathode interfaces (Qu et al., 2006). Due to the thermo-mechanical loading during SOFC service, these cracks can further propagate to either deflect at the electrodes/electrolyte interfaces or penetrate into the electrolyte (Joulaee et al., 2009). As consequences, on one hand, the presence of cracks in the SOFC stack generates heat due to the Ohmic resistance at the crack tips, which in turn affects dramatically the electrochemical performances of the SOFC unit. On the other hand, cracks that penetrate into the electrolyte allow for fuel leakage from the anode side to the cathode side, which can deteriorate the SOFC unit. Further, cracks propagation paths depend not only on the multilayered nature of the SOFC structure, but also on the microstructure of the porous electrodes. Indeed, microstructure inhomogeneities introduced by pores spatial distribution contribute to crack propagation paths.

1.3. State of the Art

1.3.1. Experimental Research

Experimental research dealing with the control of the porous microstructure is being carried out to avoid cracks and improve the mechanical and the electrochemical performances of SOFC. Literature reviews (see for instance, Peng et al., 2000; Boaro et al., 2003) showed that most experimental methods used to fabricate optimized porous SOFC

components (anode and cathode) are based on a templating method, i.e. mixing a ceramic powder with pores formers (e.g. PMMA microspheres). Then the pores formers can be removed by heat treatment. The main difficulties for making porous materials for SOFC technology are the poor interconnection between pores and the collapse of the porous structure (walls) during the calcination of porous SOFC components (1273K - 1673K). High porosity in SOFC is a required condition to transport the gas (fuel and oxygen) effectively and also to avoid important Ohmic losses in the SOFC unit. These limitations are now being overcome through the use of novel techniques to control the porosity in SOFC components. For instance, Ruiz-Morales et al. (2006) and Lashtabeg et al. (2009) proposed novel processing routes to produce SOFC materials with long range periodic pores ordering, and showed that homogeneous porosity of the anode and the cathode improves the electrochemical performance of the SOFC.

Further research is being also carried out to develop new materials that improve SOFCs energy conversation efficiency and can use directly the natural gas (methane) instead of hydrogen as a fuel. Barnett and co-workers (Tsai and Barnett, 1997; Perry Murray and Barnett, 2001) showed that the addition of YSZ to LMS improves significantly the cathode performance. In fact, the addition of YSZ, which is an ion-conducting material to LMS leads to a broad zone of active sites deep in the cathode electrode. Further, Chen et al. (2007) used $Sm_{0.2}Ce_{0.8}O_{1.9}$-impregnated LMS to make composites cathodes with high electrochemical performance. In case of pure hydrogen (fuel), Ni/YSZ anodes can provide excellent catalytic properties and stability. While in case of using natural gases as a fuel, Jiang et al. (2006) found that the addition of YSZ to $(La_{0.75}Sr_{0.25})(Cr_{0.5}Mn_{0.5})O_3$ makes good alternative anodes for a direct utilization of methane instead of Ni/YSZ anodes.

1.3.2. Modeling of SOFCs

Along with the experimental investigations, different modeling efforts are being developed to validate an optimal design of SOFCs. Internal processes taking place within SOFCs in-service are complex and strongly dependent on the processing parameters such as temperature, gases flow rate, cell pressure and flow configuration (cross-flow, co-flow and counter-flow). The modeling of SOFCs is usually performed by combining multi-physics

phenomena taking place during SOFC service, which include fluid flow, energy and mass transfer, and electrochemical reactions. On what follow we will recall different existing modeling strategies and assumptions used to predict the energy conversion efficiency and failure modes in SOFCs unit:

Multiphysics modeling and investigation of process parameters: flow configurations
Achenbach (1994) presented a 3-D time-dependent model to investigate the energy conversion performance of a planar SOFC with internal methane-steam reforming. The model considers temperature-dependent Ohmic resistances and activation polarizations. The mass flow distribution is assumed uniform across all channels. The species concentration, current density and temperature variation within the cell are investigated using different flow configurations (cross-flow, co-flow and counter-flow). It was found that the counter-flow configuration results in the highest cell efficiency; the co-flow leads to the most uniform current density distribution in the cell; and the cross-flow results in the largest temperature gradients in the SOFC structure.

Ferguson et al. (1996) developed a 3-D model for the simulation of both SOFC unit and SOFC stack using the finite volume method. The model predicts the potential, temperature and current distributions at the unit (cell) level. In this numerical model, the heat and mass transfer are considered purely conductive and diffusive in the PEN (positive-electrolyte-negative: cathode/electrolyte/anode) structure. While in the flow channels, the thermal and molar flux are dominated by convection phenomenon in the flow direction. The heat conduction and species diffusion between the flow channels and the solid parts are taken into account using interface boundary conditions. With this model, the authors compared cross-, counter- and co- flow designs for a planar SOFC and concluded that the counter-flow configuration is the most efficient with the hydrogen as fuel.

Aguiar et al. (2004) presented an anode-supported intermediate-temperature planar 1-D SOFC stack model with direct internal reforming at steady and transient states. The model includes mass and energy balances, as well as an electrochemical model. The molar/heat flux is assumed convective in the flow channels, and pure diffusive/conductive in the PEN (positive-electrolyte-negative) structure. It was shown in the simulated results that, at the same operating conditions, counter-flow configuration leads to high

temperature gradients and uneven current density distributions compared to the co-flow case.

Multiphysics modeling based on commercial finite element codes Further, significant multi-physics models mostly based on commercial finite element codes are introduced to simulate SOFCs in service. For instance, Recknagle et al. (2003) proposed a simulation tool which combines a commercial computational fluid dynamics (CFD) simulation code (STAR-CD) and a validated electrochemistry module for 3-D modeling of planar SOFC. Navier-stokes equation is used to model the fluid flow. However, the PEN structure is considered as a monolithic structure containing only one element in the stack direction. Effects of three different cell flow configurations on the distribution of temperature, current density and fuel species were investigated. It was concluded that the co-flow case results in the most uniform temperature distribution and the smallest thermal gradients.

Similarly, with the help of a commercial CFD code "Fluent", Campanari and Iora (2004) developed a finite volume model for simulation of the tubular SOFC based on a detailed electrochemical model and a thermal analysis of the internal heat exchange. The evaluations of Ohmic, activation and diffusion losses as well as a kinetic model of hydrocarbon reactions were included in the electrochemical analysis.

Khaleel et al. (2004) proposed a 3-D simulation tool for the modeling of the SOFC, which combines the commercial finite element code MARC® with an in-house developed electrochemical module. In this model, MARC® is used to perform the fluid flow and thermal analyses. Using the temperature profile provided by MARC®, the electrochemical module is used to calculate the current density distribution, heat generation and species concentrations. The authors highlighted that the tool offers significant advantages in terms of stability and computational efficiency over other existing CFD codes.

Wang et al. (2007) coupled an electrochemical module with a commercial CFD code (ANSYS-CFX code) to investigate the thermo-fluid and electrochemical performances for planar SOFC. Distributions of temperature, species concentration, current density and overpotentials were calculated in a single SOFC unit cell using co-flow and counter-flow configurations. The authors concluded that the co-flow case offers thermostructural advantages compared to the counter-flow case, as the former leads to more uniform current density and smaller temperature gradient within the cell.

More recently, Xia et al. (2009) proposed a 3-D mathematical model coupling an electrochemical module with the commercial CFD code "Fluent". The distributions of temperature, current density and overpotential losses were calculated. They stated that the counter-flow case results in a more uniform current density, lower temperature gradient and higher fuel efficiency than the co-flow case. This statement is contradictory to the conclusions of Achenbach (1994), Recknagle et al. (2003) and Wang et al. (2007), where the co-flow results in the most uniform current density and the smallest thermal gradient.

Simplified models intended for real time simulation Besides, some researchers put efforts on the validation of SOFC performances by using simplified numerical models. They study the accuracy, the stability and the computational speed of the proposed models. For instance, in Costamagna et al. (2004), the electrochemical modeling of Integrated Planar SOFC (IP-SOFC) is studied, where they assumed an isothermal SOFC model and the gases flow only in the direction along the fuel/air channel, without any transversal flows. The comparison between the model predicted results and the experimental data shows a good agreement under a reasonably wide range of operating conditions.

Xue et al. (2005) developed a dynamic model of a single tubular SOFC unit using the control volume (CV) approach. In this model, the unit cell is divided into four CVs, including the thermal insulator, the cathode channel, PEN and the anode channel. Within each control volume, uniform physical properties are assumed. They show that this simplified model is capable of simulating the heat, mass transfer and electrochemical reactions at steady and transient states. The predicted results are compared to the experimental ones such as the polarization curve and power density to verify the model and to explore the underlying dynamic behavior.

Cheddie and Munroe (2007) used SIMULINK commercial code to solve the mass and heat transfer in a 1-D SOFC model in real time system simulation. In this work, the flow channel and interconnect are treated as one integrated domain; while the anode, cathode and electrolyte are similarly integrated into one region. The current density distribution is assumed uniform in the cell, and the cell current or voltage is not calculated iteratively, which greatly enhance the computational speed. The authors argued that this model is able to more accurately predict the transport phenomena than other existing real time models.

Arpino et al. (2008) constructed a mathematical model to solve the fluid flow, heat and mass transfer regimes in SOFC using a unified finite element-based approach. The fuel cell is divided into three computational domains, including the anodic compartment, the electrolyte domain and the cathodic compartment, which are linked by imposing appropriate interface boundary conditions. The model is able to calculate the local variation in current density, which improves the solution of SOFC. A good agreement was found when comparing the numerical results with the experimental data that are available in literature.

Kang et al. (2009) proposed a reduced 1-D dynamic model for a planar direct internal reforming SOFC by introducing two simplifications, which are similar to that introduced by Cheddie and Munroe (2007). The first assumption is that the PEN, interconnects and flow channels are integrated together along the perpendicular direction. Therefore the SOFC is considered to have only one temperature layer. And the second one is the current density distribution is considered to be uniform within the SOFC, and the cell voltage is determined by the average gas molar fractions and cell temperature. The authors concluded in this paper that the accuracy of the reduced model is not significantly compromised by the two simplifications, while its computational time is significantly decreased.

Modeling of SOFC failure The modeling of mechanical degradation and fracture prediction in SOFC has also drawn some attention in the past few years. Laurencin et al. (2007) conducted a study on the calculation of stress field inside anode-supported planar SOFCs. A failure statistical approach was used to estimate the fracture in SOFC. In service SOFC demonstrate a high residual compressive stress in the electrolyte and a slight tensile stress in the anode close to the anode/electrolyte interface. They highlighted that the cathode is damaged when the anodic expansion reaches values between 0.05-0.09%, whereas the electrolyte fracture occurs for the anodic strain ranging between 0.l2-0.15%.

Laurencin et al. (2008) then extended this work to the electrolyte-supported planar SOFC. Unlike the anode-supported cell, the elaboration of electrolyte-supported cell leads to the anode layer cracking. Also when the anodic strain is high, the cermet re-oxidation induces a risk of anode/electrolyte delamination.

A further study focusing on the effect of Ni-YSZ cermet re-oxidation on anode-supported

SOFC damage was also conducted by Laurencin et al. (2009). The failure mode is modeled considering both the bulk expansion of the cermet induced by the transformation of the Ni phase and the change of mechanical stresses in the multilayered cell.

1.4. Objectives

Although the existing investigations in the literature have shown a real progress on the modeling of SOFC during service, a general comprehensive numerical model is still at its early stage of development. In fact, most of these computational tools are based on commercial finite element codes or homemade simplified codes, where the multiphysics within the SOFC unit is not fully solved, mostly ignoring the porous zones (Recknagle et al., 2003; Aguiar et al., 2004). Further the existing numerical tools do not take into account the correlation between the SOFC microstructure components, the energy conversion performance and the degradation (failure) that can affect significantly the SOFC unit outputs. In fact, pores concentration and distribution affects the resistance to fracture of the porous SOFC materials (Joulaee et al., 2007). Further, pores orientation within a porous materials leads to higher pores connectivity and higher thermal and electrical conductivities in the pores orientation direction (Mikdam et al., 2013a;b), which improves gases transfer to the active sites and reduces thermal gradients within the SOFC unit.

The objective of this thesis is to develop a numerical tool based on a combination of Finite Element (FEM) and eXtended Finite Element (XFEM) Methods that deal with the multiphysics problem governing equations in SOFC unit's free flow/porous zones, and also to predict onset and propagation path of an existing crack within the SOFC porous electrodes. Advanced FEM will be considered to solve the problem governing equations in the SOFC unit free flow/porous zones. XFEM will be introduced to deal with discontinuities through a crack and singularities at the crack-tip. Also effect of microstructure porosity (pores volume fraction) and anisotropy on the crack's onset and propagation path will be investigated during SOFC in-service. Finally the capability of the developed FEM based model on predicting the SOFC energy conversion performance will be demonstrated and validated.

1.5. Overview of the Thesis

To achieve these objectives, the thesis is organized in seven chapters: the first chapter introduces the thesis objectives and a short literature review on the recent advances in SOFC experiments and modeling. The second chapter deals with the development of a numerical tool based on the Finite Element Method (FEM) for coupling the fluid flow, heat and mass transfer in porous media. Validation is conducted by comparing the FEM solution with the Fourier Galerkin (FG) solution, considering fluid flow, heat and mass transfer in a square porous cavity. The third chapter is devoted to the modeling and simulation of fluid flow and heat transfer in a cracked porous media where the eXtended Finite Element Method (XFEM) is used to deal with the material discontinuity induced by the crack. In the fourth chapter, the influence of heat transfer and fluid flow on crack growth in SOFC-like multilayered porous/dense isotropic materials is investigated. In the fifth chapter, the effect of the microstructure anisotropy on crack propagation within a SOFC unit is studied. In the sixth chapter, the developed numerical tool is used to predict the energy conversion performance of a SOFC. Finally, concluding remarks as well as some future perspectives are introduced in chapter seven. Here below a summary of the second to the sixth chapters:

Second chapter: In this chapter, fluid flow, heat and mass transfer in porous materials are investigated. To this aim, the coupled Navier-Stokes flow/heat transfer model developed by Younes et al. (2014) is extended to include both heat and mass buoyancy effects on Darcy-Brinkman flow. In this DB model, the fluid flow which is governed by Darcy-Brinkman equation is solved by the nonconforming Crouzeix-Raviart (CR) finite-element method with an upstream scheme for the nonlinear convective term (Djadel and Nicaise, 2008). A combination of Discontinuous Galerkin (DG) and Multi-Point Flux Approximation (MPFA) methods is used to solve the convection-diffusion heat and mass equations (Younes and Ackerer, 2008). The DB model is used to investigate a double-diffusive natural convection in a square porous cavity with different Rayleigh, Darcy, Lewis and Buoyancy numbers. For validation, a steady state semi-analytical solution based on the spectral Fourier-Galerkin (FG) method is also developed for this problem. In the FG model, the governing equations are firstly reformulated in terms of stream function, temperature and mass concentration. Then, these unknowns are expanded in an infinite

Fourier series truncated at a given order. Finally, the substitution of the expansions in the governing equations leads to a highly nonlinear system of algebraic equations that is solved using an efficient nonlinear algorithm based on the modified Powell hybrid method. To reduce the computational effort of the nonlinear algorithm, the Jacobian matrix is evaluated analytically instead of its finite-difference approximation. The performance of the DB numerical model is studied by comparing the obtained results to the FG reference solutions. The comparison shows that the combined advanced numerical methods (CR, DG, MPFA) used to build the DB numerical model provide accurate results for high nonlinear coupling of fluid flow, heat and mass transfer problems in porous media.

Third chapter: In this chapter, the influence of fluid flow and heat transfer on the thermo-mechanical response of a cracked isotropic porous media is investigated. To this aim, a numerical model is developed (Darcy-XFEM model) where FEM and XFEM are combined to solve the Darcy flow, heat transfer and thermo-mechanical problem in the cracked porous media. In this model, the fluid flow, governed by the Darcy's law, is discretized with the nonconforming finite element method. Time splitting scheme is used with the energy conservation equation to solve the heat transfer in two steps. A combination of DG, MPFA and XFEM methods is used to solve the advection-diffusion heat transfer equation in the porous media to better handle the influence of cracks on temperature distribution. Further, the resulted temperature is used as body force to solve the thermo-mechanical problem with XFEM. In the post processing stage, the thermal Stress Intensity Factor (SIF) is computed using the interaction integral technique at each time step and used to validate the obtained results (Bouhala et al., 2012).

Fourth chapter: In this chapter, the influence of heat transfer, fluid flow and material properties on crack propagation in the SOFC-like multilayered porous materials is investigated, where the porous SOFC electrodes microstructures are taken isotropic. To this aim, the DB model (chapter-1) is combined with XFEM to solve the fluid flow, heat transfer and thermo-mechanical problem in the multilayered structure. In this DB-XFEM model, the fluid flow is governed by Navier-Stokes in the SOFC flow channels and Darcy-Brinkman in the porous media (anode and cathode). The presence of cracks is assumed to affect the heat diffusion within the porous material. It also induces a

discontinuity of the displacement at the crack surfaces and a singularity of the stress at the crack tip. Thus, the XFEM is used to solve the thermo-mechanical problem and to track the crack propagation. The multi-physics model is implemented and then validated for the transient regime; this called for a post processing treatment in which, the SIFs are computed for each time step. The SIFs are then used in the crack propagation criterion and the calculation of crack orientation angle (Moës et al., 1999). Finally, a parametric study is carried out to investigate the effect of the fluid flow, heat transfer and material properties on the crack propagation path.

Fifth chapter: In this chapter, the effect of the porous material microstructural anisotropy on crack propagation in multilayered SOFC unit is investigated using the DB-XFEM model (chapter-4). To this aim, porous material with different anisotropic thermal and mechanical properties is constructed using an existing in-house code. At each degree of anisotropy of the anode and cathode SOFC electrodes, simulations are conducted to investigate the effect of fluid flow and heat transfer on crack propagation path within the SOFC unit. Therefore the DB-XFEM model developed in the fourth chapter for the isotropic case is upgraded to take into account the anisotropy through the effective properties of the anode and cathode electrodes. To compute the crack propagation in the anisotropic material, the enrichment functions and interaction integral equation which are different from those in the isotropic material are used. Further, in contrast with the isotropic case where the analytical solution of the crack orientation angle exists, the crack propagation direction in case of anisotropic material is calculated numerically (Asadpoure and Mohammadi, 2007). Numerical results show a strong influence of the material anisotropy on crack propagation path in the multilayered SOFC structure.

Sixth chapter: In this chapter, energy conversion performances of a SOFC unit is investigated by taking into account the heat generated by electrochemical reactions. Thereby the DB model (chapter-1) that deals with fluid flow, heat and mass transport is extended to include the electrochemical (EC) reactions taking place at anode/electrolyte and cathode/electrolyte interfaces of the SOFC unit. In what follow this model will be called DB-EC model. In this model, the fluid flow is governed by Darcy-Brinkman equation in the porous electrodes and Navier-Stokes in the channels. Heat transfer in the

channels, the porous electrodes and the solid dense electrolyte is governed by conduction and convection in both the fluid and solid phases. Mass transfer occurs in the channels and in the porous electrodes by advection and dispersion phenomena in the fluid phase. Heat generation and species consumption/production due to the electrochemical reactions are taken into account in heat and mass transport equations. The electrochemical model considers the Ohmic, activation and concentration losses. The model governing equations are solved without any special treatment for transition between flow-channel/porous electrodes interfaces. This reduces numerical schemes constraints on the cell interfaces, which are the origin of the solution errors. The results are validated using laboratory experiments performed at different constant temperatures (973K - 1123K). After validation, the DB-EC model is used to investigate the temperature variation along the cell due to the heat generation by the electrochemical reactions.

2. Coupled Fluid Flow, Heat and Mass Transfer in Porous Media: Model Development and Validation

2.1. Introduction

The SOFC is an energy conversion device that combines fuel (e.g. hydrogen) and oxidant (oxygen) to produce electricity, with water and heat as its by-product. The SOFC consists of a gas-tight electrode and two porous electrodes (an anode and a cathode), to which two flow channels are adjacent. During service of a SOFC, the gases (fuel and oxidant) flow into the channels at constant velocity and temperature, then diffuse into the porous anode and cathode to reach the electrolyte interfaces where the electrochemical reactions take place. The distributions of species concentration and temperature in the SOFC components (anode/electrolyte/cathode) have a significant influence on both the mechanical integrity and energy conversion efficiency of a SOFC unit. Therefore an accurate and efficient numerical model is required, to better understand the effects and contributions of the multi-physics phenomenon on the mechanical response and the electrochemical performance of the SOFC unit during service.

In the planar SOFC, the fluid flow regime in porous electrodes was demonstrated to be laminar on both the fuel side and the air side (Autissier et al., 2004). Darcy's law is used to model the gases flow by many researchers, due to its simplicity (Berning et al., 2002; Larrain et al., 2004; Lin and Beale, 2006). However, It neglects the viscous effect and the inertial forces of the flow, which play an important role when the velocity is not small. To get a more accurate fluid flow solution in the porous media, Shi and Wang (2007)

suggested the use of Brinkman equation. This equation considers the viscous effect of the flow by adding the viscous term to the Darcy's equation. Other researchers proposed the use of a more general equation by adding the Darcy's term to the Navier-Stokes equation to correct the velocity in porous media (Arpino et al., 2008). In the present model, the Darcy-Brinkman equation including viscous, inertial forces and Darcy terms, is used to guarantee an accurate flow velocity. To solve this equation, the non-conforming Crouzeix-Raviart (CR) finite element method is used with the nonlinear convection term being treated by an upstream approach. For the heat and mass transfer problem, energy and species conservation equations are commonly used in the numerical models. Here we take into account the heat transport by convection phenomena in the fluid phase, and by conduction in both the fluid and solid phases. While the mass transport takes place only in the fluid phase by advection and diffusion phenomenon. The same numerical approach is used to solve the advection-diffusion heat and mass equations, where a combination of Discontinuous Galerkin (DG) and Multi-Point Flux Approximation (MPFA) methods is used. Besides, to reduce the computational time of the coupled problem, a non-iterative time stepping scheme is used to adapt the time step length.

To verify the accuracy and reliability of the developed numerical model, a double-diffusive natural convection problem in a square porous cavity is studied and the results are compared to a reference semi-analytical solution developed using the Fourier Galerkin (FG) method. The FG method is one of the spectral methods used for solving partial differential equations (Costa, 2004; Canuto et al., 2006; Kopriva, 2009), which have been extensively used during the last decades due to their greater accuracy when compared to finite difference and finite element (FE) methods. Indeed, the only error generated by these methods is due to the truncation to a finite set of trial functions/coefficients (Durran, 1999; Fahs and Younes, 2014). Their rate of convergence depends only on the smoothness of the solution, yielding the ability to achieve high precision with a relatively small number of degrees of freedom (Costa, 2004). For complex solutions with relatively steeper profiles, high truncation orders, leading to large systems of nonlinear equations, are required to ensure the stability and the high accuracy of the FG solution. In this work, the obtained nonlinear systems are solved using the modified Powell hybrid algorithm (Powell, 1968). Besides, the Jacobian matrix is evaluated analytically instead of its finite difference approximation, which saves dramatically the computational time and provides

the possibility of using large number of Fourier coefficients.

The present chapter is organized as follows: In Section 2.2, the governing equations of fluid flow, heat and mass transfer are introduced. Section 2.3 is devoted to the description of the finite element numerical model (DB model), where each numerical method and the discretization of the equation is detailed. In Section 2.4, in sake of validation, a double-diffusive natural convection problem in a porous cavity is simulated by using the proposed DB model. The performance of the model is studied by comparing the obtained results with a semi-analytical solution performed by the FG method.

2.2. Problem Formulation

2.2.1. Fluid Flow

A planar SOFC unit consists of the air and fuel channels, the porous cathode and anode, as well as the solid electrolyte. During service of a SOFC, the gas species flow into the channels, then penetrate into the porous anode and cathode to reach the electrolyte interfaces where the electrochemical reactions take place. The major difficulty of the simulation for gas flow in the SOFC unit lies in the coupling between the pure liquid flow in the channel and the flow in the porous media.

A classical approach to model such a problem is to solve the Navier-Stokes equation in the channel and the Darcy's equation in the porous medium. However, the main limitation of this approach is that in Darcy's equation, the no-slip boundary condition can not be imposed. Thus the use of appropriate boundary conditions at the interface between the two domains is required (Ehrhardt, 2000; Le Bars and Worster, 2006). Work published by Beavers and Joseph (1967) was one of the first attempts to study the fluid flow boundary conditions at the fluid/porous interface. They performed several experiments in a fluid channel with a porous media and detected a slip in the velocity at the interface, which allows for a discontinuity in the tangential velocity. Later on Saffman (1971) gave an analytical justification of the Beavers-Joseph interfacial condition. He found out that the Beavers-Joseph slip coefficient depends on the interfacial location and the tangential velocity at the interface is proportional to the shear stress. In the following years, the proposed Beavers-Joseph interface condition was further improved

and justified by many other studies, such as Taylor (1971); Richardson (1971); Jones (1973); Payne and Straughan (1998); Jäger et al. (1996); Jäger and Mikelić (2001), etc. Although it is difficult to determine the slip coefficient, the Beavers-Joseph condition is found to be widely used in practical computations for coupled fluid/porous flow problems, for instance, Discacciati et al. (2002); Layton et al. (2002); Miglio et al. (2003); Riviére (2005); Chang et al. (2006); Urquiza et al. (2008), etc. Besides, other types of interfacial boundary conditions have been proposed in the past few decades as well. Ene and Sanchez-Palencia (1975) investigated on the pressure jump across the interface. Ochoa-Tapia and Whitaker (1995a;b) assumed the continuity of velocity with a jump in the shear stress at the interface region. This condition was used in Kuznetsov (1996; 1997; 1998a;b; 1999) to compute the coupled fluid/porous flow problems. Further, Cieszko and Kubik (1999) proposed an interfacial condition with the discontinuity of both the tangential velocity and the tangential shear stress.

Instead of using Darcy's equation in the porous region, Neale and Nader (1974) suggested the use of Brinkman extension to the Darcy model. Since the Brinkman and Navier-Stokes equations are of the same order, the continuity of the velocity and stress at the interface can be invoked by using the effective viscosity. Due to its simplicity, this approach is widely used in most commercial CFD software, such as the STAR-CD, FLUENT and so on (Ehrhardt, 2010). Then this single-domain approach was used to analytically study the fluid flow and heat transfer at three different types of interfaces in Vafai and Thiyagaraja (1987). Vafai and Kim (1990) adopted this approach to compute the exact solution for the fluid flow at the interface between a porous medium and a fluid layer. Sahraoui and Kaviany (1992) found that the Darcy-Brinkman model predicts the correct slip velocity but does not satisfactorily model the flow field in the porous region near the interface. However, this shortcoming can be overcome using a variable effective viscosity in the porous medium.

Another popular approach to deal with the interfacial problem is to define a transition zone between the channel and porous region. In Nield (1983), the transition region between the fluid layer and the porous medium was modeled by the Brinkman equation. The fluid flow in the channel and the porous region were computed by Navier-Stokes and Darcy equations, respectively. This approach was then validated in Goharzadeh et al. (2005) by experiments. Further, Goyeau et al. (2003) introduced a continuously varying transition

zone between the fluid layer and the porous medium with a stress jump at the interface. Le Bars and Worster (2006) defined a viscous transition zone inside the porous medium, where the Stokes equation still applies and the continuity of pressure and velocities is imposed. Investigations on some analytically tractable flows through the fluid/porous domain reveal that the Darcy-Brinkman and Beavers-Joseph can result in exactly equal velocity in the fluid layer and deep in the porous layer. Some disparities can be found in the viscous transition zone, where the exponential decay in Darcy-Brinkman formulation is replaced by a sharp jump in Beavers-Joseph.

In this work, a single-domain, Darcy-Brinkman model is used to compute the fluid flow in the SOFC structure, where the conditions of continuous velocity and continuity of the normal component of the stress tensor would naturally arise (Ehrhardt, 2010).

2.2.2. Heat Transfer

To describe the heat transfer process in the porous media, two approaches are commonly used in the literatures. One approach called local thermal non-equilibrium (LTNE) assumes a temperature difference between the solid and fluid phases. It has been studies in Vortmeyer and Schaefer (1974); Vortmeyer (1975); Schlünder (1975); Carbonell and Whitaker (1984); Zanotti and Carbonell (1984a;c;b); Levec and Carbonell (1985b;a); Glatzmaier and Ramirez (1988); Quintard and Whitaker (1993), etc. Accordingly, the other approach named local thermal equilibrium (LTE) assumes the same temperature for the moving fluid phase and the solid phase in the porous medium. This hypothesis has also been investigated by many researchers, such as Truong and Zinsmeister (1978); Whitaker (1991); Kaviany (1995); Gobbe and Quintard (1994); Quintard and Whitaker (1995; 1996a;b); Nield and Bejan (2006) and so on.

In the LTNE model, two co-existing temperature fields associated respectively with the solid and fluid phases are used to characterize the internal thermal state of the porous media (Amhalhel and Furmański, 1997). Due to the presence of two different temperatures, the heat exchange between the two phases can take place during the heat transfer in the porous media. According to Wakao et al. (1979), the LTNE models can be classified to three categories. In the first category, the heat conduction in both fluid and solid phases is neglected in the heat transfer model, which is simple to analyze. In the second category,

the models are based on the concept of two macroscopic continua, one for the fluid phase and the other for the solid phase, where the heat conduction in each phase is taken into account separately. The resulting macroscopic model is a two-equation heat transfer model such as in Vortmeyer and Schaefer (1974); Schlünder (1975); Vortmeyer (1975); Glatzmaier and Ramirez (1988), etc. In the third category, on the basis of local volume averaging, the authors treat the porous medium as periodic arrays of spheres or cylinders. By considering the relation between the pore-scale structure and the macroscopic description of the porous medium, a two-equation system can be obtained as described in Carbonell and Whitaker (1984); Zanotti and Carbonell (1984a;c;b); Levec and Carbonell (1985b;a); Quintard and Whitaker (1993); Quintard et al. (1997).

We define the response time for the local heat transfer between the fluid and the solid phases as t_r, the characteristic time for variation of the mean temperature of the system as t_c. If $t_r \ll t_c$, the temperature difference between the two phases dies away with the increase of time (Amhalhel and Furmański, 1997). Under this condition, the LTE model can be used, where only one single temperature is utilized to describe the heat transfer process in the multiphase system. Wong and Dybbs (1976) conducted an experimental study of the LTE in liquid saturated porous media for different boundary conditions. They found that the LTE is satisfied for flow rate where the Reynolds number is smaller than 10. Amiri and Vafai (1994) pointed out that the Darcy number (defined as the ratio of the permeability to the characteristic length squared), had a significant influence on the validity of the LTE. With the increase of the Darcy number, the LTE becomes less pronounced. Besides, regarding the validity of the LTE, Whitaker (1986) reported that some additional constraints must be fulfilled for the LTE to be valid for the heat transfer in a two-phase system. Then Quintard and Whitaker (1995) improved the prior studies and developed two constraints that must be satisfied in order that the principle of LTE can be used with confidence.

Concerning the heat transfer at the fluid/porous interface, different assumptions have been made to consider the thermal state at the interface region. Vafai and Thiyagaraja (1987) simply assumed that the temperature and heat flux are continuous across the interface. Such interfacial boundary conditions are very widely used, such as in Poulikakos and Kazmierczak (1987); Vafai and Kim (1990); Kim and Choi (1996); Ochoa-Tapia and Whitaker (1997) and so on. However, Sahraoui and Kaviany (1992) introduced a slip

condition for the temperature with the continuity of the heat flux at the interface. Later on, Ochoa-Tapia and Whitaker (1998) took into account the possible excess in the heat flux and proposed a jump condition for the heat flux at the interface. Alazmi and Vafai (2001) conducted a comprehensive comparative study on different types of heat transfer interfacial conditions between a porous medium and a fluid layer. They reported that the temperature fields and Nusselt numbers, generated from different interfacial conditions, are quite close to each other for most practical applications.

In this work, a hypothesis of local thermal equilibrium is used to describe the heat transfer process in the SOFC electrodes. For the fluid/porous interface, a continuity of temperature and heat flux at the interface is assumed to match the energy equations in the fluid and the porous medium.

2.2.3. Governing Equations

We assume an isotropic and homogeneous porous media saturated with viscous, incompressible and Newtonian fluid. The Boussinesq approximation is assumed valid for the fluid density such that

$$\rho\left(T,\ C\right) = \rho_0\left[1 - \beta_T\left(T - T_0\right) - \beta_C\left(C - C_0\right)\right] \tag{2.1}$$

where T and C are temperature and species concentration; ρ_0, T_0 and C_0 are the reference fluid density, temperature and species concentration, respectively. β_T and β_C are the thermal and solutal expansion coefficients, respectively.

The Darcy-Brinkman formulation is used to represent the fluid flow in the porous media. The advection-diffusion heat and mass equations are used to simulate the heat and mass transfer in the model. The mass, momentum, energy and species conservation equations are given by

$$\nabla.\mathbf{v} = 0 \tag{2.2}$$

$$\frac{\rho_0}{\varepsilon}\frac{\partial \mathbf{v}}{\partial t} + \frac{\mu}{K}\mathbf{v} + \frac{\rho_0}{\varepsilon^2}\left(\mathbf{v}.\nabla\right)\mathbf{v} - \mu_e\nabla.\left(\nabla\mathbf{v}\right) + \nabla p = -\rho \mathrm{g}\nabla y \tag{2.3}$$

$$(\rho c)_{PM} \frac{\partial T}{\partial t} + \rho_f c_f \mathbf{v}.\nabla T - \nabla.(\mathbf{k}_{PM} \nabla T) = 0 \tag{2.4}$$

$$\varepsilon \frac{\partial C}{\partial t} + \mathbf{v}.\nabla C - \nabla.(D_e \nabla C) = 0 \tag{2.5}$$

p and $\mathbf{v}$ are the fluid pressure and the velocity vector, respectively; ε, K, μ and μ_e are the medium porosity, the medium permeability, the fluid dynamic viscosity and the effective viscosity (i.e. the viscosity in the Brinkman model); c is the specific heat capacity; D_e is the effective species diffusivity through the fluid-saturated porous matrix; and g is gravitational acceleration. The volumetric heat capacity $(\rho c)_{PM}$ and the effective thermal conductivity tensor $\mathbf{k}_{PM}$ of the porous medium are calculated from the medium porosity and the corresponding properties of the fluid and solid phases as follow (Quintard and Whitaker, 1995; Quintard et al., 1997)

$$(\rho c)_{PM} = \varepsilon \rho_f c_f + (1-\varepsilon)\rho_s c_s \tag{2.6}$$

$$\mathbf{k}_{PM} = (\varepsilon k_f + (1-\varepsilon)k_s)\mathbf{I} + \frac{k_f - k_s}{V}\int_{A_{fs}} \mathbf{n}_{fs}\mathbf{b}_f dA - \rho_f c_f \langle \tilde{\mathbf{v}}_f \mathbf{b}_f \rangle \tag{2.7}$$

$\rho_f c_f$, $\rho_s c_s$ and k_f, k_s are the volumetric heat capacity and thermal conductivity of the fluid phase and the solid phase, respectively. The tensor $\int_{A_{fs}} \mathbf{n}_{fs}\mathbf{b}_f dA$ represents the tortuosity of the porous medium (Kaviany, 1995), which is related to the topology of the porous matrix. However, this term is very difficult to be measured and calculated. Thereby, in this study the tortuosity term is neglected. $-\rho_f c_f \langle \tilde{\mathbf{v}}_f \mathbf{b}_f \rangle$ is the dispersive term, which is normally assumed to be equal to the diffusion tensor $\mathbf{k}^d$, with the expression of its components given by (Bear, 1972; Dagan et al., 1989; Kaviany, 1995)

$$k_{ij}^d = \rho_f c_f \left[\alpha_T |\mathbf{q}| \delta_{ij} + (\alpha_L - \alpha_T)\frac{q_i q_j}{|\mathbf{q}|} \right] \tag{2.8}$$

where α_L and α_T are the longitudinal and transverse thermal dispersivities, δ_{ij} is the Kronecker delta function.

2.3. The Finite-Element Numerical Model

In this work, accurate numerical methods are used to solve the coupled system of partial differential Eq. (2.2)-Eq. (2.5) on a general triangular mesh. The Darcy-Brinkman Eq. (2.3) is solved using the nonconforming Crouzeix-Raviart (CR) method. This mixed finite element method employs different basis functions for the pressure and the velocity approximations. Normally, the drawback of general mixed finite elements (for instance the Taylor-Hood finite elements) is that, with the degrees of freedom of both pressure and velocity being the unknowns, they lead to a large final system to solve. However, the CR finite element method avoids this drawback by taking advantages of the lowest order P0-P1 method with linear velocity and constant pressure in each element. This approximation also satisfies the Babuska-Brezzi condition (Fortin and Brezzi, 1991; Girault and Raviart, 1979; Gresho et al., 1998), which is essential to ensure a final non-singular linear system to solve without resorting to any stabilization technique. Moreover, the CR finite element method can be used for both steady-state and transient flows, and it is able to avoid artificial sources and sinks, due to the local mass conservation property (Gresho et al., 1998). In order to ensure a stable solution of the flow equation, an appropriate upstream scheme is used to deal with the nonlinear convection term.

For the heat and mass transfer Eq. (2.4) and Eq. (2.5), a combination of Discontinuous Galerkin (DG) and Multi-Point Flux Approximation (MPFA) methods are used in this work. Indeed, standard numerical methods, such as Finite Element Method (FEM) or Finite Volume Method (FVM), usually result in numerical diffusion and/or non-physical oscillations in advection dominated heat or mass transfer problems. The use of the DG method for the discretization of the advective term can avoid this numerical diffusion/non-physical oscillation and lead to a high-resolution scheme for advection, which is clearly superior to the already existing finite element methods (Arnold et al., 2002). Besides, the DG method satisfies the local conservation property as in finite volume, and allows high-order approximations to enter through a variational formulation rather than by some hybridized difference or functional reconstruction (Kirby, 2000). Moreover, the DG method deals with the advective fluxes by solving a Riemann problem at the interface of two elements, where the solution is found to be total variation diminishing (Gowda et al., 1993).

Note that, in elliptic and parabolic systems, the DG method cannot provide numerical results that are significantly superior to the existing finite element methods as in hyperbolic systems (Arnold et al., 2002). Therefore, the diffusive term in the heat/mass transfer equation is discretized by the MPFA method, which uses more than two elements to compute the fluxes across edges (Aavatsmark et al., 1996). Similar to the mixed finite element method, the MPFA method is locally conservative, and is able to handle general irregular grids on anisotropic heterogeneous domains. Moreover, the MPFA method uses the same type of unknowns as the DG method. Thereby the discretizations of the advective term and the diffusive term in the heat/mass equation can be assembled into one matrix system, which avoids the operator splitting errors (Younes and Ackerer, 2008).

In order to couple the fluid flow, heat and mass transfer Eq. (2.2)-Eq. (2.5), the Picard method is usually used for the linearization of the coupled system at each time step. The flow, heat and mass equations are solved sequentially, which enables the utilization of different temporal discretization to guarantee a high accuracy for each equation. In this model, an implicit time discretization is used for the flow system equations (Eq. (2.2) and Eq. (2.3)) and for the diffusion terms in Eq. (2.4) and Eq. (2.5). However, the convective terms in Eq. (2.4) and Eq. (2.5) are treated explicitly to reduce numerical diffusion.

Time stepping schemes are used to reduce the computational cost by optimizing the time step size. Time stepping schemes with embedded error control have been developed in many non-linear problems like density-driven flow in porous media (Diersch and Kolditz, 1998), incompressible Navier-Stokes problems (Turek, 1996), unsaturated flow (Williams and Miller, 1999; Kavetski et al., 2001), elastoplastic consolidation in geomechanics (Sloan and Abbo, 1999), reactive transport problems (Saaltink et al., 2004). In the present work, the non-iterative time stepping scheme of Younes and Ackerer (2010), based on local truncation error control, is used to solve the fluid flow, the heat transfer and the mass transfer equations sequentially.

2.3.1. The Darcy-Brinkman Flow Discretization

Due to stability conditions, the flow system Eq. (2.2)-Eq. (2.3) cannot be discretized with the same order for pressure and velocity approximations. Otherwise, some sort of

stabilization has to be added to the mixed formulation (Li and Chen, 2008). To avoid these difficulties, non-conforming CR elements for the velocity approximation in combination with constant pressure per element are used. The CR method has been used in to solve several problems such as the Darcy-Stokes problem (Burman and Hansbo, 2005), the Stokes problem (Crouzeix and Raviart, 1973) and the elasticity problem (Hansbo and Larson, 2003). It results in a simple, stable and optimal order approximation of the Stokes equations (Arnold, 1993).

In the following, the main steps for the discretization of the Darcy-Brinkman Eq. (2.2) and Eq. (2.3) with the CR triangular elements are detailed. The nonlinear convective term is treated using an upstream approach with weight function as in Schieweck and Tobiska (1989); Djadel and Nicaise (2008).

With the non-conforming finite element method, the velocity ($\mathbf{v}$) degrees of freedom are the two component (v_i^x, v_i^y) at the mid-edge i facing the node i (see Fig. 2.1).

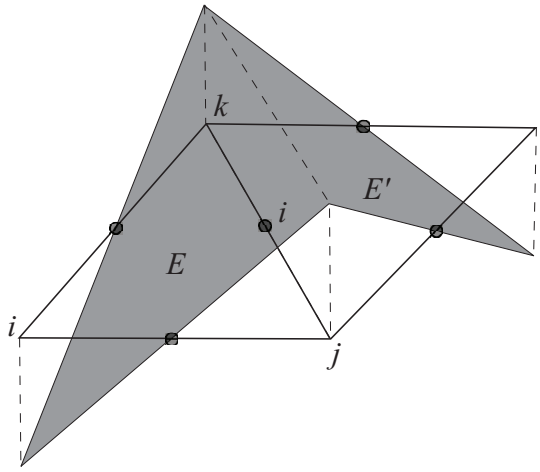

Figure 2.1.: The linear interpolation function of the velocity field

The interpolation function φ_i is non-zero only inside the element E and its adjacent element E' that shares the edge i. Inside the element E, a linear variation of the velocity $\mathbf{v}_E\,(v_E^x, v_E^y)$ is assumed:

$$v_E^x = v_i^x \varphi_i^E + v_j^x \varphi_j^E + v_k^x \varphi_k^E \;,\; v_E^y = v_i^y \varphi_i^E + v_j^y \varphi_j^E + v_k^y \varphi_k^E \tag{2.9}$$

For an interior edge i, the linear interpolation function φ_i is given by:

$$\varphi_i^E = \frac{1}{|E|}\left[x\left(y_k - y_j\right) + y\left(x_j - x_k\right) + \frac{1}{2}\left(y_j x_k + y_j x_i - y_k x_i - y_k x_j - y_i x_j + y_i x_k\right)\right] \tag{2.10}$$

where $|E|$ is the area of the element E; x_i and y_i are the coordinates of the vertex i of the triangular element E. The interpolation function φ_i^E equals 1 on the mid-edge i and zero on the mid-edges j and k of E (see Fig. 2.1). The gradient components of the interpolation function Eq. (2.10) are

$$\nabla\varphi_i^E = \frac{1}{|E|}\begin{pmatrix} y_k - y_j \\ x_j - x_k \end{pmatrix} = \frac{1}{|E|}\begin{pmatrix} \Delta y^i \\ \Delta x^i \end{pmatrix} \tag{2.11}$$

with $\Delta y^i = y_k - y_j$ and $\Delta x^i = x_j - x_k$.

2.3.1.1. Discretization of the Momentum Conservation Equation

Using the test function φ_i over the domain Ω, we can write the variational formulation of the flow Eq. (2.3) as

$$\int_\Omega \left(\frac{\rho_0}{\varepsilon}\frac{\partial \mathbf{v}}{\partial t} + \frac{\mu}{K}\mathbf{v} + \frac{\rho_0}{\varepsilon^2}\left(\mathbf{v}.\nabla\right)\mathbf{v} - \mu_e\nabla.\left(\nabla\mathbf{v}\right) + \nabla p\right)\varphi_i = \int_\Omega -\rho \mathrm{g}\nabla y\varphi_i \tag{2.12}$$

Mass and Darcy terms Using an implicit time discretization, the mass and Darcy terms for an interior edge i sharing two adjacent elements E and E' can be written as follows:

$$\int_\Omega \left(\frac{\rho_0}{\varepsilon}\frac{\partial \mathbf{v}}{\partial t} + \frac{\mu}{K}\mathbf{v}\right)\varphi_i = \frac{\rho_0}{3\varepsilon\Delta t}\left(|E| + |E'|\right)\begin{pmatrix} \left(v_i^x\right)^{n+1} - \left(v_i^x\right)^n \\ \\ \left(v_i^y\right)^{n+1} - \left(v_i^y\right)^n \end{pmatrix} + \frac{\mu}{3K}\left(|E| + |E'|\right)\begin{pmatrix} \left(v_i^x\right)^{n+1} \\ \\ \left(v_i^y\right)^{n+1} \end{pmatrix} \tag{2.13}$$

The convective term The nonlinear convective term can lead to unstable scheme for problems with high Rayleigh numbers. Therefore an upwind technique introduced in Schieweck and Tobiska (1989) is used for the discretization of the convective term. In this technique, a lumping region R_i assigned to the edge i is defined as shown in the hatched area in Fig. 2.2. The lumping area R_i is formed by two simplex regions S_i^E and $S_i^{E'}$ for an inner edge i and by the sole simplex region S_i^E for a boundary edge. The simplex region S_i^E is a triangular area formed by the centroid point G with two nodes j and k of the element E (see Fig. 2.2).

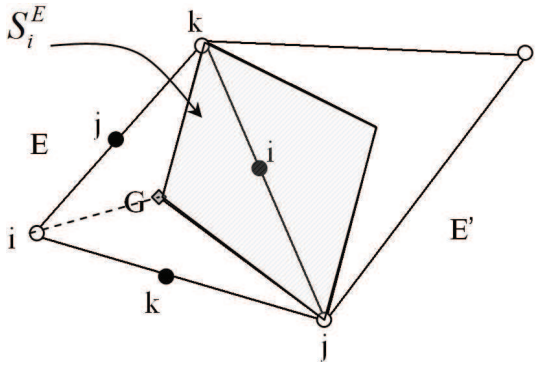

Figure 2.2.: The lumped region R_i (hatched area) formed by the two simplex regions S_i^E and $S_i^{E'}$.

We use the lumping operator which transforms a given function into a piecewise constant function. Denoting $\bar{\omega} = \mathbf{v}$, the variational formulation of the convective term writes:

$$\int_\Omega \frac{\rho_0}{\varepsilon^2} (\mathbf{v}.\nabla)\, \mathbf{v}\varphi_i = \int_\Omega \frac{\rho_0}{\varepsilon^2} (\bar{\omega}.\nabla)\, \mathbf{v}\varphi_i \approx \frac{\rho_0}{\varepsilon^2} \int_{Ri} (\bar{\omega}.\nabla)\, \mathbf{v} \tag{2.14}$$

Using Green's formula leads to

$$\frac{\rho_0}{\varepsilon^2} \int_{Ri} (\bar{\omega}.\nabla)\, \mathbf{v} = \frac{\rho_0}{\varepsilon^2} \begin{pmatrix} \int_{Ri} \nabla.\,(\bar{\omega} v_x) - \int_{Ri} v_x \nabla.\bar{\omega} \\ \\ \int_{Ri} \nabla.\,(\bar{\omega} v_y) - \int_{Ri} v_y \nabla.\bar{\omega} \end{pmatrix} \tag{2.15}$$

Use the upwind scheme for the first term and the lumping operator for the second integral

of Eq. (2.15), we can write

$$\int_{Ri} \nabla.\left(\bar{\omega} v_x\right) - \int_{Ri} v_x \nabla.\bar{\omega} \approx \sum_l v_x^{il} \int_{\Gamma_{il}} \bar{\omega}.\eta_{il} - v_i^x \sum_l \int_{\Gamma_{il}} \bar{\omega}.\eta_{il} \tag{2.16}$$

where v_x^{il} is the upwind value given by

$$v_x^{il} = v_x^{upw} = \mathfrak{y}_{il} v_i^x + \left(1 - \mathfrak{y}_{il}\right) v_l^x \tag{2.17}$$

If we denote $Q_{il} = \int_{\Gamma_{il}} \bar{\omega}.\eta_{il}$, we obtain

$$\int_{Ri} \nabla.\left(\bar{\omega} v_x\right) - \int_{Ri} v_x \nabla.\bar{\omega} = \sum_l Q_{il} \left(1 - \mathfrak{y}_{il}\right) \left(v_l^x - v_i^x\right) \tag{2.18}$$

Two functions can be used for $\mathfrak{y}_{il} = f\left(\mathfrak{t}\right)$ (see Schieweck and Tobiska, 1989):

$$f_1\left(\mathfrak{t}\right) = \begin{cases} 1 & \text{if } \mathfrak{t} \geq 0 \\ \\ 0 & \text{else} \end{cases} \quad \text{or } f_2\left(\mathfrak{t}\right) = \begin{cases} \dfrac{1/2 + \mathfrak{t}}{1 + \mathfrak{t}} & \text{if } \mathfrak{t} \geq 0 \\ \\ \dfrac{1}{2 - 2\mathfrak{t}} & \text{else} \end{cases} \tag{2.19}$$

with $\mathfrak{t} = \dfrac{Q_{il}}{\mathfrak{e}}$.

Finally, the convective term writes

$$\begin{aligned} \frac{\rho_0}{\varepsilon^2} \int_{Ri} \left(\bar{\omega}.\nabla\right) \mathbf{v} = \frac{\rho_0}{\varepsilon^2} \Bigg\{ & \begin{pmatrix} \sum_l Q_{il} \left(1 - \mathfrak{y}_{il}\right) \left(v_l^x - v_i^x\right) \\ \sum_l Q_{il} \left(1 - \mathfrak{y}_{il}\right) \left(v_l^y - v_i^y\right) \end{pmatrix}_E \\ & + \begin{pmatrix} \sum_l Q_{il} \left(1 - \mathfrak{y}_{il}\right) \left(v_l^x - v_i^x\right) \\ \sum_l Q_{il} \left(1 - \mathfrak{y}_{il}\right) \left(v_l^y - v_i^y\right) \end{pmatrix}_{E'} \Bigg\} \end{aligned} \tag{2.20}$$

with $Q_{ij} = \int_{\Gamma_{ij}} \bar{\omega}.\eta_{ij} = \dfrac{1}{9}\left[\left(2v_i^x + 2v_j^x - v_k^x\right)\left(\Delta z^j - \Delta z^i\right) + \left(2v_i^y + 2v_j^y - v_k^y\right)\left(\Delta x^j - \Delta x^i\right)\right]$.

The viscous and pressure terms The pressure is assumed to be piecewise constant with degrees of freedom located in the center of triangular elements. Therefore, the viscous

and pressure terms in Eq. (2.12) write

$$\int_\Omega \left(-\mu_e \nabla.\left(\nabla \mathbf{v}\right) + \nabla p\right)\varphi_i = \int_\Omega \nabla.\left(-\mu_e \nabla \mathbf{v} + p\mathbf{Id}\right)\varphi_i = \int_\Omega -\nabla.\boldsymbol{\varsigma}\varphi_i \tag{2.21}$$

with $\boldsymbol{\varsigma} = \mu_e \nabla \mathbf{v} - p\mathbf{Id}$ and $\mathbf{Id}$ the 2×2 identity matrix.

For an interior edge i sharing two elements E and E', using Green's formula, the previous integral can be reduced to

$$\int_\Omega -\nabla.\boldsymbol{\varsigma}\varphi_i = \int_E \boldsymbol{\varsigma}\nabla\varphi_i + \int_{E'} \boldsymbol{\varsigma}\nabla\varphi_i \tag{2.22}$$

Therefore, using Eq. (2.11), we obtain the final form of the viscous and pressure terms

$$\begin{aligned}
&\int_\Omega \left(-\mu_e \nabla.\left(\nabla \mathbf{v}\right) + \nabla p\right)\varphi_i \\
&= \left\{ \frac{\mu_e}{|E|} \begin{pmatrix} \sum_{j=1}^{3} \left(\Delta x^i \Delta x^j + \Delta y^i \Delta y^j\right) v_j^x \\ \\ \sum_{j=1}^{3} \left(\Delta x^i \Delta x^j + \Delta y^i \Delta y^j\right) v_j^y \end{pmatrix} - \begin{pmatrix} \Delta y^i \\ \\ \Delta x^i \end{pmatrix} p_E \right\}_E \\
&+ \left\{ \frac{\mu_e}{|E'|} \begin{pmatrix} \sum_{j=1}^{3} \left(\Delta x^i \Delta x^j + \Delta y^i \Delta y^j\right) v_j^x \\ \\ \sum_{j=1}^{3} \left(\Delta x^i \Delta x^j + \Delta y^i \Delta y^j\right) v_j^y \end{pmatrix} - \begin{pmatrix} \Delta y^i \\ \\ \Delta x^i \end{pmatrix} p_{E'} \right\}_{E'}
\end{aligned} \tag{2.23}$$

The buoyancy term Use Green's formula, the variational form of the buoyancy term gives

$$\begin{aligned}
-\int_\Omega \rho \mathrm{g} \nabla y \varphi_i = &-\rho_E \mathrm{g} \left(\sum_j \int_{Ej} y\varphi_i.\eta_{Ej} - \int_E y \nabla \varphi_i \right) \\
&- \rho_{E'} \mathrm{g} \left(\sum_j \int_{Ej'} y\varphi_i.\eta_{Ej'} - \int_{E'} y \nabla \varphi_i \right)
\end{aligned} \tag{2.24}$$

The integrations in the above equation are calculated numerically based on the values on the mid-edges and the triangular centroids respectively. Thus we obtain

$$\sum_j \int_{Ej} y\varphi_i.\eta_{Ej} - \int_E y\nabla\varphi_i = \bar{y}_{Ei} \begin{pmatrix} \Delta y^i \\ \Delta x^i \end{pmatrix} - \bar{y}_E \begin{pmatrix} \Delta y^i \\ \Delta x^i \end{pmatrix} \tag{2.25}$$

where $\bar{y}_{Ei}$ and $\bar{y}_E$ are the altitude of the mid-edge and the center of the element E, respectively. Therefore, combining Eq. (2.24) and Eq. (2.25), the buoyancy term writes

$$\begin{aligned} -\int_\Omega \rho \mathrm{g} \nabla y \varphi_i = & \left\{ \rho_E \mathrm{g} \left(\bar{y}_E - \bar{y}_{Ei} \right) \begin{pmatrix} \Delta y^i \\ \Delta x^i \end{pmatrix} \right\}_E \\ & + \left\{ \rho_{E'} \mathrm{g} \left(\bar{y}_E - \bar{y}_{Ei'} \right) \begin{pmatrix} \Delta y^i \\ \Delta x^i \end{pmatrix} \right\}_{E'} \end{aligned} \tag{2.26}$$

2.3.1.2. Discretization of the Mass Conservation Equation

The mass conservation equation is discretized for each element E as

$$\int_E \frac{\partial v_x}{\partial x} + \frac{\partial v_y}{\partial y} = 0 \tag{2.27}$$

Using the velocity approximation Eq. (2.9), we obtain

$$\int_E \sum_j \left(v_j^x \frac{\partial \varphi_j}{\partial x} + v_j^y \frac{\partial \varphi_j}{\partial y} \right) = 0 \tag{2.28}$$

which writes

$$\sum_j \left(\Delta y^j v_j^x + \Delta x^j v_j^y \right) = 0 \tag{2.29}$$

The final flow system is obtained by substituting Eq. (2.13), Eq. (2.20), Eq. (2.23), Eq. (2.26) and Eq. (2.29) into Eq. (2.12).

2.3.2. The Heat and Mass Transfer Discretization

For the heat and mass transfer Eq. (2.4) and Eq. (2.5), the explicit DG method, where fluxes are upwinded using a Riemann solver is used to solve the advection equation and combined with the symmetric MPFA method for the diffusion equation. Konz et al. (2009) used the DG method for the simulation of density-driven flow experiments in porous media, where a very good matching between the DG and the experimental results for all concentration isolines was obtained. The MPFA method was also studied by many researchers (Edwards and Rogers, 1998; Klausen and Russell, 2004; Younes and Fontaine, 2008a;b). It provides flow fluxes at the element interfaces explicitly by weighted sums of discrete element values.

In the following, we summarize the main developments for the discretization of the heat transfer Eq. (2.4). Similar developments can be applied for the discretization of the mass transfer Eq. (2.5).

The heat equation can be written in the following mixed form:

$$\begin{cases} \mathfrak{d}\dfrac{\partial T}{\partial t} + \mathbf{v}.\nabla T + \dfrac{1}{\rho_f c_f}\nabla.\mathbf{q}^{cd} = 0 \\ \\ \mathbf{q}^{cd} = -k_{PM}\nabla T \end{cases} \tag{2.30}$$

where $\mathfrak{d}$ is the heat capacities ratio; $\mathbf{q}^{cd}$ is the conduction-diffusion flux, assumed to vary linearly inside the element E, therefore,

$$\mathfrak{d} = \frac{(\rho c)_{PM}}{\rho_f c_f} \tag{2.31}$$

$$\nabla.\mathbf{q}^{cd} = \frac{1}{|E|}\sum_i Q^{cd}_{\partial Ei} \tag{2.32}$$

where $Q^{cd}_{\partial Ei}$ is the conduction-diffusion heat flux across the edge i of the element E.

We use the $P1$ DG method where the approximated solution $T_h(\boldsymbol{x}, t)$ is expressed with

linear basis functions ψ_i^E on each element E by:

$$T_h\left(\boldsymbol{x},t\right)\mid_E=\sum_{i=1}^{3}T_i^E\left(t\right)\psi_i^E\left(\boldsymbol{x}\right) \tag{2.33}$$

$T_i^E\left(t\right)$ $(i=1,\ 2,\ 3)$ are the three degrees of freedom in element E, which are the average value of the temperature defined at the triangle centroid $(\bar{x}_E,\bar{y}_E)$ and its deviations in each space direction (Cockburn et al., 1989) with the corresponding interpolation functions:

$$\psi_1^E\left(x,y\right)=1,\ \psi_2^E\left(x,y\right)=x-\bar{x}_E,\ \psi_3^E\left(x,y\right)=y-\bar{y}_E \tag{2.34}$$

Thus the variational formulation of the heat transport Eq. (2.30) over the element E using ψ_i^E as test functions leads to (Younes and Ackerer, 2010)

$$\int_E\mathfrak{d}\frac{\partial T}{\partial t}\psi_i^E+\int_E\left(\mathbf{v}.\nabla T\right)\psi_i^E+\frac{1}{\rho_f c_f.\left|E\right|}\int_E\left(\sum_j Q_{\partial Ej}^{cd}\right)\psi_i^E=0 \tag{2.35}$$

Using Green's formula, Eq. (2.35) becomes:

$$\int_E\mathfrak{d}\frac{\partial T}{\partial t}\psi_i^E+\int_{\partial E}T\psi_i^E\mathbf{v}\cdot\boldsymbol{\eta}_{\partial E}-\int_E T\mathbf{v}\cdot\nabla\psi_i^E+\frac{1}{\rho_f c_f}\sum_j\frac{Q_{\partial Ej}^{cd}}{\left|E\right|}\int_E\psi_i^E=0 \tag{2.36}$$

Substituting the approximated temperature Eq. (2.33) into the equation and applying an upwind scheme to the advective term of the equation results in

$$\left[G\right]\begin{pmatrix}\dfrac{dT_1^E}{dt}\\[2ex]\dfrac{dT_2^E}{dt}\\[2ex]\dfrac{dT_3^E}{dt}\end{pmatrix}=\left[H-M^0\right]\begin{pmatrix}T_1^E\\[2ex]T_2^E\\[2ex]T_3^E\end{pmatrix}-\sum_{l=1}^{3}\left[M^l\right]\begin{pmatrix}T_1^{El}\\[2ex]T_2^{El}\\[2ex]T_3^{El}\end{pmatrix}+\begin{pmatrix}\sum_{\partial Ej}Q_j^{cd}\\[2ex]0\\[2ex]0\end{pmatrix} \tag{2.37}$$

with,

$$G_{ij}=\textstyle\int_E\psi_j^E\psi_i^E,\qquad\qquad H_{ij}=\int_E\psi_j^E\mathbf{v}.\nabla\psi_i^E$$

$$M_{ij}^{0} = \sum_{l=1}^{N_E} \lambda_{\partial El}^{E} \frac{Q_{\partial El}^{E}}{|\partial El|} \int_{\partial El} \psi_i^E \psi_j^E, \quad M_{ij}^{l} = \left(1 - \lambda_{\partial El}^{E}\right) \frac{Q_{\partial El}^{E}}{|\partial El|} \int_{\partial El} \psi_i^E \psi_j^{El} \quad (l = 1, ..., 3)$$

where El is the adjacent element to element E with ∂El as the common edge. $Q_{\partial El}^{E}$ is the fluid flux across edge ∂El with the expression $Q_{\partial El}^{E} = \int_{\partial El} \mathbf{v}.\boldsymbol{\eta}_{\partial El}$. The upwind parameter $\lambda_{\partial El}^{E}$ is defined by

$$\lambda_{\partial El}^{E} = \begin{cases} 1 & \text{if } \mathbf{v}.\boldsymbol{\eta}_{\partial El} \geqslant 0 \\ 0 & \text{if } \mathbf{v}.\boldsymbol{\eta}_{\partial El} < 0 \end{cases} \tag{2.38}$$

To reduce numerical diffusion, an explicit scheme is used for the temporal discretization of advection in Eq. (2.37).

The heat fluxes Q_j^{cd} across edges are approximated at the new time level using the MPFA method. The basic idea of this method is to divide each triangle into three sub-cells as in Fig. 2.3.

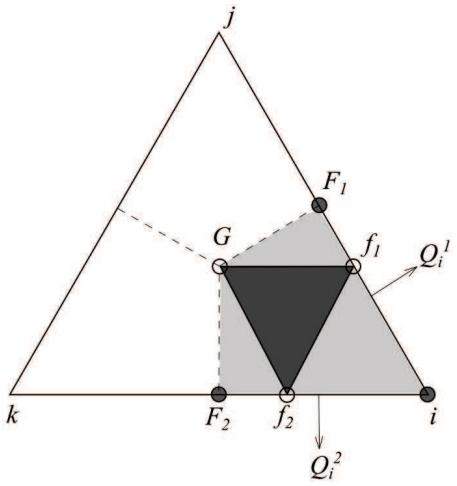

Figure 2.3.: Triangle splitting into three sub-cells and linear temperature approximation on the sub-cell

Inside the sub-cell ($i,\ F_1,\ G,\ F_2$) formed by the vertex of triangle i, the triangle centroid G and the midpoints of edges F_1 and F_2, we assume a linear variation of the temperature among T^E, Tf_1 and Tf_2, which are the values of temperature at G and the two continuity points f_1 and f_2, respectively. The symmetry of the MPFA is achieved when the continuity points are localized at $|if_1| \,/\, |iF_1| = |if_2| \,/\, |iF_2| = 2/3$. In this case ($i,\ f_1,\ G,\ f_2$) is a par-

allelogram. Therefore, half-edge heat fluxes $\left(Q_i^1 = \int_i^{F_1} -k_{PM}\nabla T \text{ and } Q_i^2 = \int_i^{F_2} -k_{PM}\nabla T\right)$ can be simplified to (outflow is taken positive):

$$\begin{pmatrix} Q_i^1 \\ \\ Q_i^2 \end{pmatrix} = \frac{3k_{PM}}{|E|} \begin{pmatrix} -\overrightarrow{iF_1}.\overrightarrow{iF_1} & \overrightarrow{iF_1}.\overrightarrow{iF_2} \\ \\ \overrightarrow{iF_1}.\overrightarrow{iF_2} & -\overrightarrow{iF_2}.\overrightarrow{iF_2} \end{pmatrix} \begin{pmatrix} Tf_1 - T^E \\ \\ Tf_2 - T^E \end{pmatrix} \tag{2.39}$$

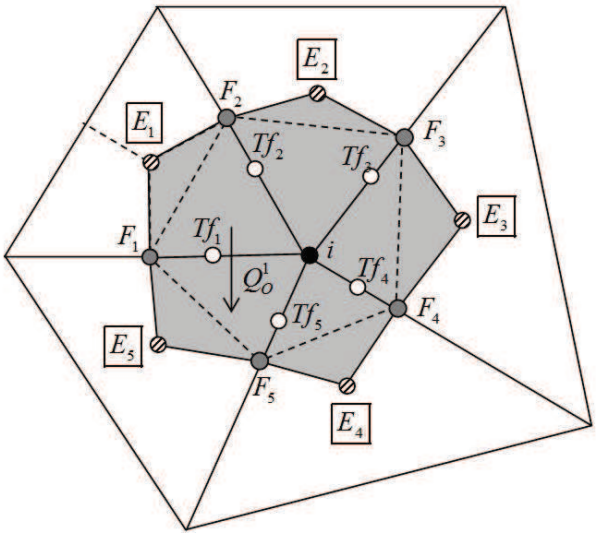

Figure 2.4.: The interaction region sharing the vertex i

An interaction region is defined by gathering all the sub-cells that share the vertex i (see Fig. 2.4). Eq. (2.39) is written for each sub-cell in the interaction region. Then by writing continuity of heat fluxes across half-edges and continuity of temperature at continuity points, we obtain a local system $[A]\,(Tf) = [B]\,(T)$. This local system is solved to obtain the temperature at the continuity points (Tf_i) as function of the temperature at all elements sharing the vertex i. The obtained relation is then substituted to Eq. (2.39) to obtain half-edge heat fluxes explicitly as a weighted sum of the temperature at cells forming the interaction volume. Finally, the summation of these heat fluxes is written using an implicit time discretization and substituted into Eq. (2.37).

2.3.3. Coupling Darcy-Brinkman Flow, Heat and Mass Transfer

With the Boussinesq approximation, the density differences are confined to the buoyancy term. Due to the high order of nonlinearities, the simulations can be excessively time-consuming. To reduce the computational cost while maintaining accuracy of the model, a non-iterative time stepping scheme based on local truncation error control (Younes and Ackerer, 2010) is used. The main stages of the scheme are recalled in the following.

The local time truncation errors of the temperature and mass are evaluated using two approximations of adjacent order of accuracy

$$e_C^{n+1} \approx \frac{1}{2}\left[C^{n+1} - \left(C^n + \frac{\Delta t^{n+1}}{\Delta t^n}\left(C^n - C^{n-1}\right)\right)\right] \tag{2.40}$$

$$e_T^{n+1} \approx \frac{1}{2}\left[T^{n+1} - \left(T^n + \frac{\Delta t^{n+1}}{\Delta t^n}\left(T^n - T^{n-1}\right)\right)\right] \tag{2.41}$$

The time step is accepted if the absolute error criterion is verified

$$max\left(\left|e_C^{n+1}\right|, \left|e_T^{n+1}\right|\right) < \gamma_e \tag{2.42}$$

If this criterion is satisfied, the following time step is controlled by the temporal truncation error tolerance γ_e using

$$\Delta t^{n+1} = \Delta t^n \times min\left(s_a\sqrt{\frac{\gamma_e}{max\left(\left|e_C^{n+1}\right|, \left|e_T^{n+1}\right|\right)}},\ r_{max}\right) \tag{2.43}$$

If the error criterion is not satisfied, the current time step is repeated using the latest error estimate

$$\Delta t_{j+1}^{n+1} = \Delta t_j^{n+1} \times max\left(s_a\sqrt{\frac{\gamma_e}{max\left(\left|e_C^{n+1}\right|, \left|e_T^{n+1}\right|\right)}},\ r_{min}\right) \tag{2.44}$$

where j indexes the recursive step size reduction, r_{max} and r_{min} are used to limit multiplication and reduction factors. They are set equal to 1.05 and 0.1 in this work, respectively.

s_a is a safe factor (Sloan and Abbo, 1999), taken as 0.4. All the simulations in this chapter are performed with a temporal truncation error tolerance $\gamma_e = 0.03$.

Note that the time step size should also satisfy the Courant-Friedrichs-Lewy condition (CFL<1). Unphysical oscillations appearing near sharp fronts are avoided using an efficient geometric slope limiter (Younes and Ackerer, 2010).

2.4. Validation of the Coupled Flow-Heat-Mass Problem

To validate the developed DB model, a double-diffusive natural convection problem in the porous cavity is studied. A lot of studies have been documented by the book of Nield and Bejan (2006). Trevisan and Bejan (1985) have performed a numerical study of the double-diffusive natural convection in porous media on the basis of Darcy model by considering a square cavity submitted to horizontal temperature and concentration gradients. Lin et al. (1990) and Lin (1993) have studied numerically the effects of buoyancy ratio on the transient thermosolutal natural convection in a square enclosure. Rosenberg and Spera (1992) investigated the influence of Rayleigh, Lewis and buoyancy numbers on fluid flow in a saturated porous cavity, under various boundary conditions. Malashetty (1993) and Bennacer et al. (2001) considered the anisotropy of the porous medium in the simulation. Alavyoon (1993) and Alavyoon et al. (1994) performed analysis based on Darcy's law in a rectangular fluid-saturated vertical porous enclosure subject to opposing heat and mass fluxes. Goyeau et al. (1996) carried out a numerical study on natural convection in a porous cavity, driven by cooperating thermal and solutal buoyancy forces, making use of the Darcy-Brinkman formulation. The non-Darcy effects on flow, heat and mass transfer within a rectangular porous enclosure have been studied by Nithiarasu et al. (1996). Angirasa et al. (1997) reported a numerical study of natural convection in a fluid-saturated porous media with opposing buoyancy effects of the same order and unequal thermal and species diffusion coefficients. Kramer et al. (2007) presented a boundary domain integral method for the solution of thermosolutal natural convection in porous media. Recently, Khadiri et al. (2011) analyzed the double-diffusive natural convection in homogeneous and isotropic porous media heated and salted from below in two- and three-dimensions, with the flow through the medium governed by Darcy's law. Mchirgui et al. (2012) carried out a numerical study of entropy generation in double-diffusive convection

in a square porous cavity. In this study, a non-dimensional form of the flow, heat and mass equations for the double-diffusive natural convection problem is introduced, based on which the semi-analytical solutions for this problem are developed by using the FG method. Then the numerical results are compared with the semi-analytical solutions with different Rayleigh, Darcy, Lewis and buoyancy numbers to investigate the accuracy and sensitivity of the proposed numerical model.

2.4.1. The Test Problem and Non-Dimensional Form of Governing Equations

The double-diffusive problem considers natural convection of a fluid composed by gas mixture in a differentially heated square cavity (Fig. 2.5), saturated by a porous medium. The left and right vertical walls are maintained at constant temperatures and concentrations (T_h, C_h) and (T_c, C_c), respectively. The horizontal surfaces are assumed to be adiabatic and insulted. Slip velocity boundary conditions are proposed on all walls and surfaces in this work.

The non-dimensional form of mass, momentum, energy and species conservation equations can be written as follows

$$\frac{\partial V_X}{\partial X} + \frac{\partial V_Y}{\partial Y} = 0 \tag{2.45}$$

$$\frac{1}{\varepsilon}\frac{\partial V_X}{\partial \tau} + \frac{1}{\varepsilon^2}\left(V_X\frac{\partial V_X}{\partial X} + V_Y\frac{\partial V_X}{\partial Y}\right) = -\frac{1}{D_A}V_X - \frac{\partial P}{\partial X} + \Lambda\left(\frac{\partial^2 V_X}{\partial^2 X} + \frac{\partial^2 V_X}{\partial^2 Y}\right) \tag{2.46}$$

$$\begin{aligned}\frac{1}{\varepsilon}\frac{\partial V_Y}{\partial \tau} + \frac{1}{\varepsilon^2}\left(V_X\frac{\partial V_Y}{\partial X} + V_Y\frac{\partial V_Y}{\partial Y}\right) = -\frac{1}{D_A}V_Y - \frac{\partial P}{\partial Y} + \Lambda\left(\frac{\partial^2 V_Y}{\partial^2 X} + \frac{\partial^2 V_Y}{\partial^2 Y}\right) \\ + Gr_T\left(\theta + N\phi\right)\end{aligned} \tag{2.47}$$

$$\mathfrak{d}\frac{\partial \theta}{\partial \tau} + V_X\frac{\partial \theta}{\partial X} + V_Y\frac{\partial \theta}{\partial Y} = \frac{R_k}{Pr}\left(\frac{\partial^2 \theta}{\partial X^2} + \frac{\partial^2 \theta}{\partial Y^2}\right) \tag{2.48}$$

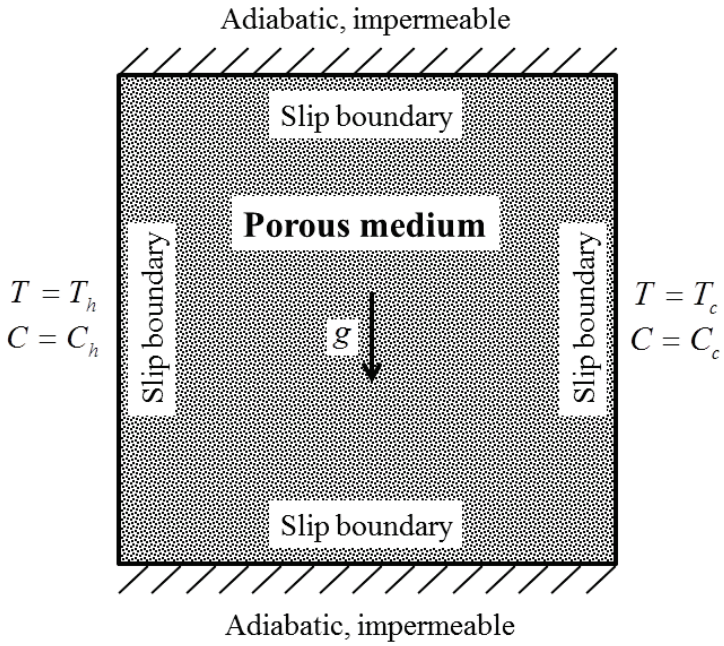

Figure 2.5.: Domain and boundary conditions for the double-diffusive natural convection problem in a porous cavity

$$\varepsilon \frac{\partial \phi}{\partial \tau} + V_X \frac{\partial \phi}{\partial X} + V_Y \frac{\partial \phi}{\partial Y} = \frac{\lambda}{Le.Pr} \left(\frac{\partial^2 \phi}{\partial X^2} + \frac{\partial^2 \phi}{\partial Y^2} \right) \tag{2.49}$$

The governing equations are written using the following scales and parameters:

$$V_X = \frac{v_x L}{\gamma};\ V_Y = \frac{v_y L}{\gamma};\ X = \frac{x}{L};\ Y = \frac{y}{L};\ \tau = \frac{t\gamma}{L^2} \tag{2.50}$$

$$P = \frac{(p - p_0)\, L^2}{\rho_0 \gamma^2};\ \theta = \frac{T - T_c}{T_h - T_c};\ \phi = \frac{C - C_c}{C_h - C_c} \tag{2.51}$$

$$Pr = \frac{\gamma}{\alpha};\ \Lambda = \frac{\mu_e}{\mu};\ R_k = \frac{k_{PM}}{k_f};\ \lambda = \frac{D_e}{D};\ Le = \frac{\alpha_f}{D};\ D_A = \frac{K}{L^2} \tag{2.52}$$

$$Gr_T = \frac{g\beta_T (T_h - T_c) L^3}{\gamma^2};\ Gr_S = \frac{g\beta_C (C_h - C_c) L^3}{\gamma^2};\ N = \frac{Gr_S}{Gr_T} \tag{2.53}$$

where L is the length of the square side; γ, α_f are the kinematic viscosity and thermal diffusivity in the fluid; Λ is the ratio of the viscosity in the Brinkman term to the fluid viscosity; R_k and λ are the ratio of the effective thermal conductivity in the porous matrix to the thermal conductivity in the fluid and species diffusivity in porous medium to species molecular diffusivity through the fluid mixture (D), respectively; Pr, Le, D_A, Gr_T, Gr_S are the Prandtl, Lewis, Darcy, the thermal and solutal Grashof numbers, respectively; and N is the buoyancy ratio. The kinematic viscosity and thermal diffusivity in the fluid γ and α_f are given by

$$\gamma = \frac{\mu}{\rho_0},\ \alpha_f = \frac{k_f}{\rho_f c_f} \tag{2.54}$$

In the analysis, the thermal porous Rayleigh number is used instead of the Grashof number. It is defined as

$$Ra^* = PrD_A Gr_T \tag{2.55}$$

Eq. (2.45)-Eq. (2.49) are subjected to slip boundary conditions, Dirichlet boundary conditions for the temperature and concentration at the vertical walls, and Neumann boundary conditions on the horizontal surfaces. The initial and boundary conditions corresponding to the problem are:

At the left wall: $v_x = 0$, $T = T_h$, $C = C_h$

At the right wall: $v_x = 0$, $T = T_c$, $C = C_c$

On horizontal surfaces: $v_y = 0$, $\dfrac{\partial T}{\partial y} = 0$, $\dfrac{\partial C}{\partial y} = 0$.

2.4.2. The Semi-Analytical FG Solution

A high-accurate steady-state solution of the double-diffusive natural convection problem is investigated using the FG method. In this work, the FG method is chosen because

of its simplicity in implementation in comparison with other spectral methods (Christou and Christov, 2005). The method is carried out as follows. First, the governing equations are reformulated in terms of stream function and temperature. Then, these unknowns are expanded in an infinite Fourier series truncated at a given order. Finally, the substitution of the expansions in the governing equations leads to a highly nonlinear system of algebraic equations that is solved using an efficient nonlinear algorithm based on the modified Powell hybrid method (Powell, 1964; 1968; Press, 2007). The major drawback of the FG method is its impractical use in the presence of nonlinearity, which induces fairly complex summations that resemble a convolution (Costa, 2004). This difficulty is avoided here since terms involving four overlapped summations are reduced to only double sums as in (Fahs and Younes, 2014). The main stages of FG method are recalled as follows.

The divergence-free condition, given by Eq. (2.45), implies the existence of a stream function Ψ that is defined as follows:

$$V_X = \frac{\partial \Psi}{\partial Y},\ V_Y = -\frac{\partial \Psi}{\partial X} \tag{2.56}$$

Differentiating Eq. (2.46) with respect to Y and Eq. (2.47) with respect to X, subtracting them to eliminate the pressure and then substituting Eq. (2.56), gives in the case of steady-state flow:

$$\frac{1}{\varepsilon^2}\left(\frac{\partial \Psi}{\partial Y}\frac{\partial^3 \Psi}{\partial Y^2 \partial X} - \frac{\partial \Psi}{\partial X}\frac{\partial^3 \Psi}{\partial Y^3} + \frac{\partial \Psi}{\partial Y}\frac{\partial^3 \Psi}{\partial X^3} - \frac{\partial \Psi}{\partial X}\frac{\partial^3 \Psi}{\partial X^2 \partial Y}\right) + \frac{1}{D_A}\left(\frac{\partial^2 \Psi}{\partial Y^2} + \frac{\partial^2 \Psi}{\partial X^2}\right) - \Lambda\left(\frac{\partial^4 \Psi}{\partial X^4} + 2\frac{\partial^4 \Psi}{\partial X^2 \partial Y^2} + \frac{\partial^4 \Psi}{\partial Y^4}\right) + \frac{Ra^*}{Pr.D_A}\left(\frac{\partial \theta}{\partial X} + N\frac{\partial \phi}{\partial X}\right) = 0 \tag{2.57}$$

Using Eq. (2.56), the steady state thermal and species conservation equations simplify to

$$\frac{R_k}{Pr}\left(\frac{\partial^2 \theta}{\partial X^2} + \frac{\partial^2 \theta}{\partial Y^2}\right) - \frac{\partial \Psi}{\partial Y}\frac{\partial \theta}{\partial X} + \frac{\partial \Psi}{\partial X}\frac{\partial \theta}{\partial Y} = 0 \tag{2.58}$$

$$\frac{\lambda}{Le.Pr}\left(\frac{\partial^2 \phi}{\partial X^2} + \frac{\partial^2 \phi}{\partial Y^2}\right) - \frac{\partial \Psi}{\partial Y}\frac{\partial \phi}{\partial X} + \frac{\partial \Psi}{\partial X}\frac{\partial \phi}{\partial Y} = 0 \tag{2.59}$$

Eq. (2.57), Eq. (2.58) and Eq. (2.59) are subject to homogeneous Neumann boundary

conditions for the stream function on the walls and surfaces. The temperature and species concentration boundary conditions are homogenized using the following changes of variables:

$$\Theta = \theta + X - 1 \tag{2.60}$$

$$\Phi = \phi + X - 1 \tag{2.61}$$

Substituting Eq. (2.60) and Eq. (2.61) into Eq. (2.57), Eq. (2.58) and Eq. (2.59) leads to the following system:

$$\begin{aligned}
&\frac{1}{\varepsilon^2}\left(\frac{\partial\Psi}{\partial Y}\frac{\partial^3\Psi}{\partial Y^2\partial X} - \frac{\partial\Psi}{\partial X}\frac{\partial^3\Psi}{\partial Y^3} + \frac{\partial\Psi}{\partial Y}\frac{\partial^3\Psi}{\partial X^3} - \frac{\partial\Psi}{\partial X}\frac{\partial^3\Psi}{\partial X^2\partial Y}\right) \\
&+\frac{1}{D_A}\left(\frac{\partial^2\Psi}{\partial Y^2} + \frac{\partial^2\Psi}{\partial X^2}\right) - \Lambda\left(\frac{\partial^4\Psi}{\partial X^4} + 2\frac{\partial^4\Psi}{\partial X^2\partial Y^2} + \frac{\partial^4\Psi}{\partial Y^4}\right) \\
&\qquad +\frac{Ra^*}{Pr.D_A}\left(\frac{\partial\Theta}{\partial X} + N\frac{\partial\Phi}{\partial X}\right) - \frac{Ra^*}{Pr.D_A}(1+N) \;=\; 0
\end{aligned} \tag{2.62}$$

$$\frac{R_k}{Pr}\left(\frac{\partial^2\Theta}{\partial X^2} + \frac{\partial^2\Theta}{\partial Y^2}\right) - \frac{\partial\Psi}{\partial Y}\frac{\partial\Theta}{\partial X} + \frac{\partial\Psi}{\partial Y} + \frac{\partial\Psi}{\partial X}\frac{\partial\Theta}{\partial Y} = 0 \tag{2.63}$$

$$\frac{\lambda}{Le.Pr}\left(\frac{\partial^2\Phi}{\partial X^2} + \frac{\partial^2\Phi}{\partial Y^2}\right) - \frac{\partial\Psi}{\partial Y}\frac{\partial\Phi}{\partial X} + \frac{\partial\Psi}{\partial Y} + \frac{\partial\Psi}{\partial X}\frac{\partial\Phi}{\partial Y} = 0 \tag{2.64}$$

This system of equations is subject to the following homogeneous boundary conditions:

$$\text{At } X = 0 \text{ and } X = 1,\ \Theta = \Phi = 0,\ \frac{\partial\Psi}{\partial Y} = \frac{\partial^2\Psi}{\partial X^2} = 0 \tag{2.65}$$

$$\text{At } Y = 0 \text{ and } Y = 1,\ \frac{\partial\Theta}{\partial Y} = \frac{\partial\Phi}{\partial Y} = 0,\ \frac{\partial\Psi}{\partial X} = \frac{\partial^2\Psi}{\partial Y^2} = 0 \tag{2.66}$$

The FG method consists of expanding the stream function Ψ, the temperature Θ and the

species concentration Φ in infinite double Fourier series, truncated at given orders:

$$\Psi = \sum_{m=1}^{Nm} \sum_{n=1}^{Nn} A_{m,n} \sin(m\pi Y) \sin(n\pi X) \tag{2.67}$$

$$\Theta = \sum_{r=0}^{Nr} \sum_{s=1}^{Ns} B_{r,s} \cos(r\pi Y) \sin(s\pi X) \tag{2.68}$$

$$\Phi = \sum_{r=0}^{Nr} \sum_{s=1}^{Ns} F_{r,s} \cos(r\pi Y) \sin(s\pi X) \tag{2.69}$$

where Nm and Nn (Nr and Ns) are the truncation orders for the stream function (temperature and concentration) in the X and Y directions, respectively. Note that the boundary conditions, Eq. (2.65) and Eq. (2.66), are identically verified by Eq. (2.67), Eq. (2.68) and Eq. (2.69).

Eq. (2.67), Eq. (2.68) and Eq. (2.69) are then substituted into Eq. (2.62), Eq. (2.63) and Eq. (2.64), and the resulting equations are multiplied respectively by $\Psi_{g,h} = 4\sin(g\pi Y)\sin(h\pi X)$ for $(g = 1...Nm,\ h = 1...Nn)$, $\Theta_{g,h} = 4\cos(g\pi Y)\sin(h\pi X)$ for $(g = 0...Nr,\ h = 1...Ns)$ and $\Phi_{g,h} = 4\cos(g\pi Y)\sin(h\pi X)$ for $(g = 0...Nr,\ h = 1...Ns)$ and integrate over the square domain. This leads to the following set of nonlinear algebraic equations with $A_{g,h}$, $B_{g,h}$ and $F_{g,h}$ as unknowns:

$$\begin{aligned} RF_{g,h} = \Lambda\pi^4 A_{g,h}\left(g^2+h^2\right)^2 - \frac{Ra^*}{\pi.Pr.D_A}\sum_{r=0}^{Nr}\sum_{s=1}^{Ns} s.\left(B_{r,s}+N.F_{r,s}\right)\Gamma_{g,r}\Gamma_{h,s} \\ +\frac{Ra^*}{\pi^2.Pr.D_A}(1+N)\,\Gamma_{g,0}\Gamma_{h,0} + \frac{1}{D_A}\pi^2 A_{g,h}\left(g^2+h^2\right) + \frac{\pi^4}{4\varepsilon^2}\sum_{m=1}^{Nm}\sum_{n=1}^{Nn}\sum_{e=1}^{Nm}\sum_{f=1}^{Nn} \\ A_{e,f}A_{m,n}\left[m.f\left(e^2+f^2\right)\xi_{e,g,m}\epsilon_{f,h,n} - n.e\left(f^2+e^2\right)\eta_{e,g,m}\kappa_{f,h,n}\right] = 0 \\ \text{for } (g = 1...Nm,\ h = 1...Nn) \end{aligned} \tag{2.70}$$

$$RT_{g,h} = -\frac{R_k}{Pr}\varepsilon_g \pi^2 \left(g^2 + h^2\right) F_{g,h} + \pi g \Pi_{g,h} - \frac{\pi^2}{4} \sum_{m=1}^{Nm} \sum_{n=1}^{Nn} \sum_{r=0}^{Nr} \sum_{s=1}^{Ns} A_{m,n} B_{r,s} \left(m.s.\upsilon_{g,m,r} \zeta_{h,n,s} + n.r.\chi_{g,m,r} \omega_{h,n,s}\right) = 0 \quad \text{for } (g = 0...Nr,\ h = 1...Ns) \tag{2.71}$$

$$RH_{g,h} = -\frac{\lambda}{Le.Pr}\varepsilon_g \pi^2 \left(g^2 + h^2\right) F_{g,h} + \pi g \Pi_{g,h} - \frac{\pi^2}{4} \sum_{m=1}^{Nm} \sum_{n=1}^{Nn} \sum_{r=0}^{Nr} \sum_{s=1}^{Ns} A_{m,n} F_{r,s} \left(m.s.\upsilon_{g,m,r} \zeta_{h,n,s} + n.r.\chi_{g,m,r} \omega_{h,n,s}\right) = 0 \quad \text{for } (g = 0...Nr,\ h = 1...Ns) \tag{2.72}$$

The coefficients ξ, ϵ, η, κ, υ, ζ, χ, ω and ε_g in Eq. (2.70), Eq. (2.71) and Eq. (2.72) are given by

$$\xi_{e,g,m} = \delta_{e,g-m} + \delta_{e,g+m} - \delta_{e,m-g} \quad \epsilon_{f,h,n} = \delta_{f,h-n} - \delta_{f,h+n} + \delta_{f,n-h} \tag{2.73}$$

$$\eta_{e,g,m} = \delta_{e,g-m} - \delta_{e,g+m} + \delta_{e,m-g} \quad \kappa_{f,h,n} = \delta_{f,h-n} + \delta_{f,h+n} - \delta_{f,n-h} \tag{2.74}$$

$$\upsilon_{g,m,r} = \delta_{g,m-r} + \delta_{g,r-m} + \delta_{g,m+r} \quad \zeta_{h,n,s} = \delta_{h,n+s} + \delta_{h,n-s} - \delta_{h,s-n} \tag{2.75}$$

$$\chi_{g,m,r} = \delta_{g,r-m} + \delta_{g,m-r} - \delta_{g,m+r} \quad \omega_{h,n,s} = \delta_{h,n+s} - \delta_{h,n-s} + \delta_{h,s-n} \tag{2.76}$$

$$\varepsilon_g = \begin{cases} 1 & \text{if } g \neq 0 \\ 2 & \text{if } g = 0 \end{cases} \tag{2.77}$$

The matrices Γ and Π in Eq. (2.70), Eq. (2.71) and Eq. (2.72) are given by

$$\Gamma_{i,j} = \frac{1 - (-1)^{i+j}}{i + j} + \frac{1 - (-1)^{i-j}}{i - j} \tag{2.78}$$

$$\Pi_{i,j} = \begin{cases} A_{i,j} & 1 \leq i \leq Nm \text{ and } 1 \leq j \leq Nn \\ 0 & \text{elsewhere} \end{cases} \tag{2.79}$$

where $\delta_{i,j}$ is the Kronecker delta function.

The terms involving four overlapped summations in Eq. (2.70), Eq. (2.71) and Eq. (2.72) require $O(Nm^2 \times Nn^2)$, $O(Nm \times Nn \times Nr \times Ns)$ and $O(Nm \times Nn \times Nr \times Ns)$ operations, respectively. Therefore, their evaluation can be highly CPU-consuming, making the FG method impractical for a relatively large number of Fourier coefficients. However, a closer look reveals that after substituting Eq. (2.73)-Eq. (2.76), the terms involving four overlapped summations in Eq. (2.70)-Eq. (2.72) reduce to only two overlapped summations requiring $O(Nm \times Nn)$, $O(Nr \times Ns)$ and $O(Nr \times Ns)$ operations, respectively.

The rank of the nonlinear system formed by Eq. (2.70)-Eq. (2.72) is $Nm \times Nn + (Nr + 1) \times Ns \times 2$. To solve the nonlinear system, we used an efficient nonlinear solver included in the IMSL library. The solver is based on the modified Powell hybrid algorithm which is alternative to the Newton's method. This algorithm improves the rate of convergence and ensures better convergence for starting point far from the solution, by estimating the correction using a convex combination of the Newton and scaled gradient directions. The algorithm uses the approach of a generalized trust region. Initially, a standard Newton step is performed. If the new position of solution falls within the trust region, it is used as a trial step in the next iteration. If not, a linear combination of the Newton method and gradient directions is used to predict a new position inside the trust region. The predicted step is then tested by evaluating the residual at the new position. If the norm of the residual is reduced sufficiently, then the step is accepted and the diameter of the trust region is increased; otherwise, the size of the trust region is decreased and another trial step is computed.

To reduce the computational effort of the algorithm, the Jacobian matrix in the algorithm is approximated from iteration to iteration by the rank one method. With this technique, the entire Jacobian is calculated at the first iteration only, or when two successive attempts have failed to reduce the residual. The solver allows for an analytical supply or a numerical (finite difference) calculation of the Jacobian matrix. In this work, an analytical

calculation of the Jacobian matrix is used instead of the finite-difference approximation to improve the convergence of the Powell algorithm and to reduce the computational effort, especially for problems involving a large number of Fourier coefficients. For this purpose, the residuals RF, RT and RH are differentiated with respect to the coefficients $A_{i,j}$, $B_{i,j}$ and $F_{i,j}$ as follows:

$$\begin{aligned}\frac{\partial RF_{g,h}}{\partial A_{i,j}} &= \Lambda\pi^4\left(h^2+g^2\right)^2\delta_{g,i}\delta_{h,j}+\frac{1}{D_A}\pi^2\left(h^2+g^2\right)\delta_{g,i}\delta_{h,j}\\ &+\frac{\pi^4}{4\varepsilon^2}\sum_{m=1}^{Nm}\sum_{n=1}^{Nn}A_{m,n}\Big[i.n\left(m^2+n^2\right)\xi_{m,g,i}\epsilon_{n,h,j}+m.j\left(i^2+j^2\right)\xi_{i,g,m}\epsilon_{j,h,n}\\ &-j.m\left(m^2+n^2\right)\eta_{m,g,i}\kappa_{n,h,j}-n.i\left(i^2+j^2\right)\eta_{i,g,m}\kappa_{j,h,n}\Big]\end{aligned} \tag{2.80}$$

$$\frac{\partial RF_{g,h}}{\partial B_{i,j}} = -\frac{Ra^*}{\pi.Pr.D_A}j.\Gamma_{g,i}\Gamma_{h,j} \tag{2.81}$$

$$\frac{\partial RF_{g,h}}{\partial F_{i,j}} = -\frac{Ra^*}{\pi.Pr.D_A}j.N.\Gamma_{g,i}\Gamma_{h,j} \tag{2.82}$$

$$\frac{\partial RT_{g,h}}{\partial A_{i,j}} = \pi g\delta_{i,g}\delta_{j,h}-\frac{\pi^2}{4}\sum_{r=0}^{Nr}\sum_{s=1}^{Ns}B_{r,s}\left(i.s.\upsilon_{g,i,r}\zeta_{h,j,s}+j.r.\chi_{g,m,i}\omega_{h,n,j}\right) \tag{2.83}$$

$$\begin{aligned}\frac{\partial RT_{g,h}}{\partial B_{i,j}} &= -\frac{R_k}{Pr}\varepsilon_g\pi^2\left(h^2+g^2\right)\delta_{i,g}\delta_{j,h}-\frac{\pi^2}{4}\sum_{m=1}^{Nm}\sum_{n=1}^{Nn}A_{m,n}(m.j.\upsilon_{g,m,i}\zeta_{h,n,j}\\ &+n.i.\chi_{g,m,i}\omega_{h,n,j})\end{aligned} \tag{2.84}$$

$$\frac{\partial RH_{g,h}}{\partial A_{i,j}} = \pi g\delta_{i,g}\delta_{j,h}-\frac{\pi^2}{4}\sum_{r=0}^{Nr}\sum_{s=1}^{Ns}B_{r,s}\left(i.s.\upsilon_{g,i,r}\zeta_{h,j,s}+j.r.\chi_{g,i,r}\omega_{h,j,s}\right) \tag{2.85}$$

$$\frac{\partial RH_{g,h}}{\partial F_{i,j}} = -\frac{\lambda}{Le.Pr}\varepsilon_g \pi^2 \left(h^2 + g^2\right) \delta_{i,g}\delta_{j,h} - \frac{\pi^2}{4}\sum_{m=1}^{Nm}\sum_{n=1}^{Nn} A_{m,n}(m.j.\upsilon_{g,m,i}\zeta_{h,n,j} + n.i.\chi_{g,m,i}\omega_{h,n,j}) \tag{2.86}$$

Note that all double sums in Eq. (2.80)-Eq. (2.86) can be reduced to one term when substituting the expressions of the coefficients ξ, ϵ, η, κ, υ, ζ, χ, ω given in Eq. (2.73)-Eq. (2.76). As a consequence, the Jacobian matrix can be calculated without any summation.

2.4.3. Results and Discussion

In this section, the solution is investigated using the FG and the finite-element model (FEM) for double diffusive natural convection in homogeneous and isotropic porous media. The range of parameters that is examined in this study concerns the $N = 0$, 5 and 10, in which $N = 0$ is the pure thermal natural convection and $N = 5$, 10 are cooperating buoyancy forces. Relatively high values of Lewis number are used: $Le = 10$ and 100. The thermal Rayleigh number is taken as $Ra^* = 100$ and 200 and Darcy number $D_A = 10^{-1}$, 10^{-3} and 10^{-5}. The other parameters are kept constant: the Prandtl number of fluid $Pr = 0.71$, the porosity $\varepsilon = 0.5$, the heat conductivity ratio, heat capacity ratio, species diffusivity ratio and viscosity ratio $R_k = \mathfrak{d} = \lambda = \Lambda = 1.0$.

The porous cavity test problem is simulated using a uniform triangular mesh obtained by subdividing square elements into four equal triangles (by connecting the center of the square to its four nodes). Several levels of grid refinement are used to study the sensitivity of the numerical solution to the grid size. For a given grid level n, the number of squares is $(25 \times 2^{n-1})^2$. Four grid levels are used with n ranging from 1 to 4, which corresponds to a total number of triangles from 2500 (level 1) to 160000 (level 4). Transient simulations are performed until a long non-dimensional time to ensure steady solutions.

The only error introduced by the FG method is due to the truncation of the Fourier series. Hence these truncations should be sufficiently large to guarantee the stability and accuracy of the obtained solution. In this work, 12 levels of truncation orders (see Tab. 2.1) are used for the computation of the FG solution. These levels correspond to a total number of coefficients ranging from 36 (level 1) to 27000 (level 12). In Tab. 2.1, the truncation orders in the Y direction are greater than those in the X direction and the ratio between

them is less than 4. These constraints are fixed empirically after several observations to ensure a significant improvement of the FG solution when going from a truncation level to the next higher one. For all the investigated truncation levels, the same number of Fourier coefficients is used for the stream, temperature and concentration functions. This is obtained by imposing $Nm = Nr + 1$ and $Nn = Ns$.

Table 2.1.: Truncation levels used for the computation of the FG solution (Nc is the total number of Fourier coefficients)

Level	Nc	Nm	Nn	Nr	Ns
1	36	3	4	2	4
2	75	5	5	4	5
3	150	5	10	4	10
4	540	9	20	8	20
5	750	10	25	9	25
6	1530	17	30	16	30
7	2970	15	66	14	66
8	4500	20	75	19	75
9	8100	30	90	29	90
10	12075	35	115	34	115
11	18000	60	100	59	100
12	27000	75	120	74	120

For each test case, the FEM and FG solutions are calculated using different grid and truncation levels, respectively. The accuracy of the solution is assessed on the basis of streamlines, temperature distribution, concentration contours as well as the average Nusselt and Sherwood numbers. The Nusselt and Sherwood numbers represent the rate of heat and mass transfer across the enclosure, respectively. The average Nusselt and Sherwood numbers are defined in dimensionless terms as follows

$$Nu = \int_0^1 \frac{\partial \Theta}{\partial X}\Big|_{X=0} dY \;\; ; \; Sh = \int_0^1 \frac{\partial \Phi}{\partial X}\Big|_{X=0} dY \tag{2.87}$$

The first simulation results show that the average Nusselt and Sherwood numbers are much more sensitive than the isotherm and concentration contours when varying the level of grid refinement in the FEM solution or when varying the level of truncation orders in the FG solution. Therefore, the value of the average Nusselt and Sherwood numbers

are used to check the convergence of both FEM and FG solutions. In the following, we consider that the convergence of the FEM and FG solution is achieved when the average Nusselt and Sherwood numbers Nu, Sh, calculated with a grid or truncation level, vary by less than 2.0% compared with those calculated with the next grid or truncation level.

2.4.3.1. The Sensitivity of the FEM Solutions to the Grid Size

In this section, the Rayleigh number is taken $Ra^* = 100$ and Darcy number $D_A = 10^{-1}$. For these Rayleigh and Darcy numbers, the finite-element numerical solutions are calculated with grid levels 1 to 4 at Lewis numbers Le =10, 100 and buoyancy ratio N =0, 5 and 10. The obtained values of average Nusselt and Sherwood numbers are given in Tab. 2.2. This table shows that both Nusselt and Sherwood numbers are weakly dependent on the grid levels. It is only between level 1 and level 2 that some of the results vary a bit more than 2.0%. For the other levels, the relative differences are always below 2.0%. For instance, in the case of $Le = 100$ and $N = 10$, the relative difference between Nu calculated using grid level 3 and that obtained using grid level 4 is approximately 0.22% and the corresponding variation for Sh is 0.38%. For all the cases shown in Tab. 2.2, the convergence of the FEM solutions are reached at grid level 2 since both values of Nu and Sh vary by less than 2.0% compared with the results of grid level 3.

Table 2.2.: Average Nusselt and Sherwood numbers with $Ra = 100$ and $Da = 10^{-1}$ at four grid levels

		$N = 0$		$N = 5$		$N = 10$	
	Grid level	Nu	Sh	Nu	Sh	Nu	Sh
$Le = 10$	1	1.465	5.333	1.663	7.489	1.662	8.755
	2	1.494	5.451	1.686	7.639	1.679	8.957
	3	1.510	5.509	1.696	7.714	1.687	9.058
	4	1.517	5.538	1.701	7.750	1.691	9.108
$Le = 100$	1	1.465	16.800	1.527	19.332	1.197	19.832
	2	1.494	17.190	1.558	19.709	1.171	20.158
	3	1.510	17.408	1.576	19.959	1.165	20.348
	4	1.517	17.508	1.585	20.071	1.163	20.426

The temperature and concentration contours obtained with all grid levels for ($Ra^* = 100$; $D_A = 10^{-1}$; Le = 10, 100; N = 0, 5 and 10) are shown in Fig. 2.6 and Fig. 2.7. These

figures show that except grid level 1, the contours obtained with levels 2, 3 and 4 are all quite similar, which suggest that convergence of the FEM solution is reached at grid level 2. This behavior is the same as that observed from the Nusselt and Sherwood numbers in Tab. 2.2. Besides, results in Fig. 2.6 and Fig. 2.7 show that with the increasing of Lewis number and buoyancy ratio, the sensitivity of the temperature and concentration contours to the grid size becomes a bit more significant.

2.4.3.2. Comparison between the FEM and FG Solutions

With the converged FEM solutions obtained from section 2.4.3.1, we compare them with the converged FG solutions (truncation level 6 for $Le = 10$ and truncation level 8 for $Le = 100$) to study the accuracy of the proposed finite-element model. The results are compared in terms of streamlines, temperature and concentration contours as shown in Fig. 2.8 and Fig. 2.9. The figures show that the streamlines, temperature and concentration contours of the converged finite-element solutions are in excellent agreement with those of the converged FG solutions for all the cases with $Ra^* = 100$ and $D_A = 10^{-1}$. In Fig. 2.8 (i) and Fig. 2.9 (i), when the buoyancy ratio $N = 0$ (the pure thermal case), the fluid circulates in a clockwise direction, forming a central vortex with a relatively slow motion in the central region, and the mass transfer is induced by the thermally driven flow. With the increasing of the buoyancy ratio N, due to the cooperating of thermal and solutal buoyancy forces, the central vortex starts to become distorted. For $N = 5$, the central vortex takes an elliptic shape (see Fig. 2.8 (ii) and Fig. 2.9 (ii)). And for $N = 10$, the vortex tends to break up into two vortices in the center of the cavity (Fig. 2.8 (iii)).

The values of Nu and Sh obtained with the FEM and the FG solutions are given in Tab. 2.3. Good agreement is found when comparing the Nusselt and Sherwood numbers between the FEM and FG solutions, where the relative difference is in the range of 0.08% - 0.9% for each case listed in Tab. 2.3. The results in Tab. 2.3 show that the increasing of Lewis number increases significantly the value of Sherwood number, while contrarily, it decreases a little bit the Nusselt number except in the pure thermal case ($N = 0$).

Further, in order to validate the proposed numerical model in different parameter conditions, more calculations with Rayleigh number $Ra^* = 200$ and Darcy number $D_A = 10^{-3}$, 10^{-5} are conducted using both the FEM and the FG methods. The obtained average

Table 2.3.: FEM and FG solutions for average Nusselt and Sherwood numbers with $Ra = 100$ and $Da = 10^{-1}$

			$N = 0$		$N = 5$		$N = 10$	
		level	Nu	Sh	Nu	Sh	Nu	Sh
$Le = 10$	FEM	4	1.517	5.538	1.701	7.750	1.691	9.108
	FG	6	1.525	5.565	1.705	7.785	1.695	9.151
$Le = 100$	FEM	4	1.517	17.508	1.585	20.071	1.163	20.426
	FG	8	1.525	17.622	1.597	20.241	1.162	20.488

Nusselt and Sherwood numbers are listed in Tab. 2.4. Note that with the same Rayleigh, Darcy and Lewis numbers, the truncation levels used for the FG solutions at different buoyancy ratios are the same. And all the FEM solutions in the table are with grid level 4. The values of Nu and Sh in Tab. 2.3 and Tab. 2.4 show that when Rayleigh number increases or Darcy number decreases, both of Nu and Sh increase. While in most cases, with the increasing of Lewis number, the corresponding Nu decreases, and Sh increases. In this table, most of the relative differences between the FEM and FG solutions are between 0.1% and 2.0%. For instance, at $Ra^* = 200$, $D_A = 10^{-1}$, $Le = 100$ and $N = 10$, the relative difference between Nu obtained from FEM and FG solutions is 0.38%, and the variation for Sh is 0.40%. With the decrease of Darcy number and the increase of Rayleigh, Lewis numbers and the buoyancy ratio, the relative difference becomes larger. The maximum relative difference in Tab. 2.4 is 5.59%, which is between the value of Sh calculated with FEM and that obtained with FG solutions at $Ra^* = 100$, $D_A = 10^{-5}$, $Le = 10$ and $N = 10$.

Some of the results are plotted and compared between the FEM and FG solutions in terms of streamlines, temperature and concentration contours. The cases with $Ra^* = 100$ are shown in Fig. 2.10 and Fig. 2.11, while those with $Ra^* = 200$ are shown in Fig. 2.12 and Fig. 2.13. For all the cases, the temperature contours from the FEM and FG solutions are almost superimposed. The concentration contours are also very close between the FEM and FG solutions in most of the cases. However, slight disparities can be observed in the concentration contours for example in Fig. 2.10 (i), when $Ra^* = 100$, $D_A = 10^{-3}$, $Le = 10$ and $N = 10$ and in Fig. 2.13 (i) with $Ra^* = 200$, $D_A = 10^{-3}$, $Le = 10$ and $N = 10$.

Table 2.4.: FEM and FG solutions for average Nusselt and Sherwood numbers

				Truncation	FEM		FG	
Ra^*	D_A	Le	N	level	Nu	Sh	Nu	Sh
100	10^{-3}	10	0	8	2.956	12.288	2.960	12.339
			5		3.370	22.988	3.349	23.269
			10		3.863	27.649	3.831	27.997
		100	0	11	2.956	39.091	2.960	38.930
			5		2.377	53.147	2.431	52.216
			10		1.750	62.125	1.746	59.813
	10^{-5}	10	0	12	3.252	13.935	3.110	13.398
			5		5.057	35.965	4.947	34.215
			10		6.464	47.631	6.405	45.109
200	10^{-1}	10	0	7	2.057	7.269	2.075	7.322
			5		2.066	9.473	2.070	9.535
			10		2.004	11.106	2.010	11.187
		100	0	9	2.057	22.982	2.074	23.168
			5		2.147	25.540	2.170	25.775
			10		1.336	24.782	1.331	24.882
	10^{-3}	10	0	9	4.420	17.411	4.433	17.579
			5		4.456	28.851	4.395	29.537
			10		4.973	34.009	4.906	34.969
		100	0	12	4.420	55.104	4.433	55.039
			5		3.711	67.061	3.799	65.632
			10		2.484	76.134	2.475	73.100

2.5. Conclusions

An efficient model (called DB model) based on advanced numerical methods is developed for the coupled flow-heat-mass problem in the porous media. The fluid flow, governed by Darcy-Brinkman equation, is solved using the locally mass conservative CR finite element method with an upstream approach for the nonlinear convective term. A combination of DG and MPFA methods is used to solve the advection-diffusion heat/mass transfer equation. A non-iterative time stepping scheme is used to control the time step length during calculation.

The developed DB model is used to simulate the double-diffusive natural convection in the porous cavity. Four different grid levels are used in the calculations to study the sensitivity of the solution to the grid size. Then a semi analytical solution using the FG method is

developed for the problem. Calculations have been done with different Rayleigh, Darcy, Lewis and Buoyancy numbers using both the numerical model and the FG method, to validate the proposed model in different parameter conditions. Some conclusions can be drawn as follows:

1. With parameters $Ra^* = 100$ and $D_A = 10^{-1}$, the resulted Nusselt and Sherwood numbers as well as the temperature and concentration contours at different grid levels show that the solutions are weakly dependent on the grid size.
2. Good agreement is observed between the numerical and semi analytical solutions when using different parameters, where most of the relative errors for Nusselt and Sherwood numbers are below 2.0%; and the maximum relative error in the all the calculations is 5.59%.
3. With different parameters, temperature contours are always in excellent agreement between FEM and FG solutions. But slight difference is found in concentration contours when $D_A = 10^{-3}$.

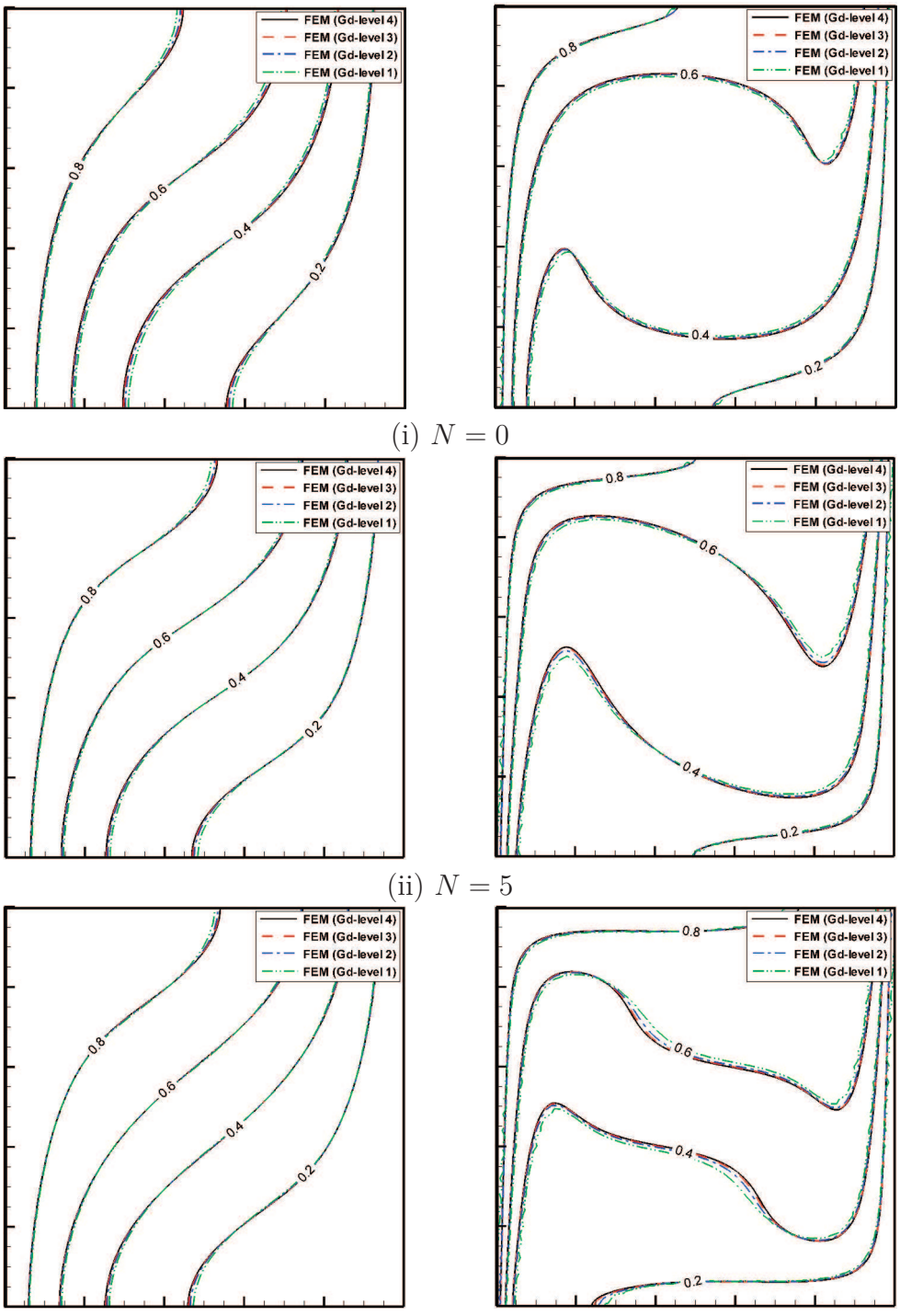

(i) $N = 0$

(ii) $N = 5$

(iii) $N = 10$

(a) Temperature contours (b) Concentration contours

Figure 2.6.: Temperature and concentration contours obtained by the finite-element model with different grid levels for $Ra^* = 100$, $Da = 10^{-1}$ and $Le = 10$

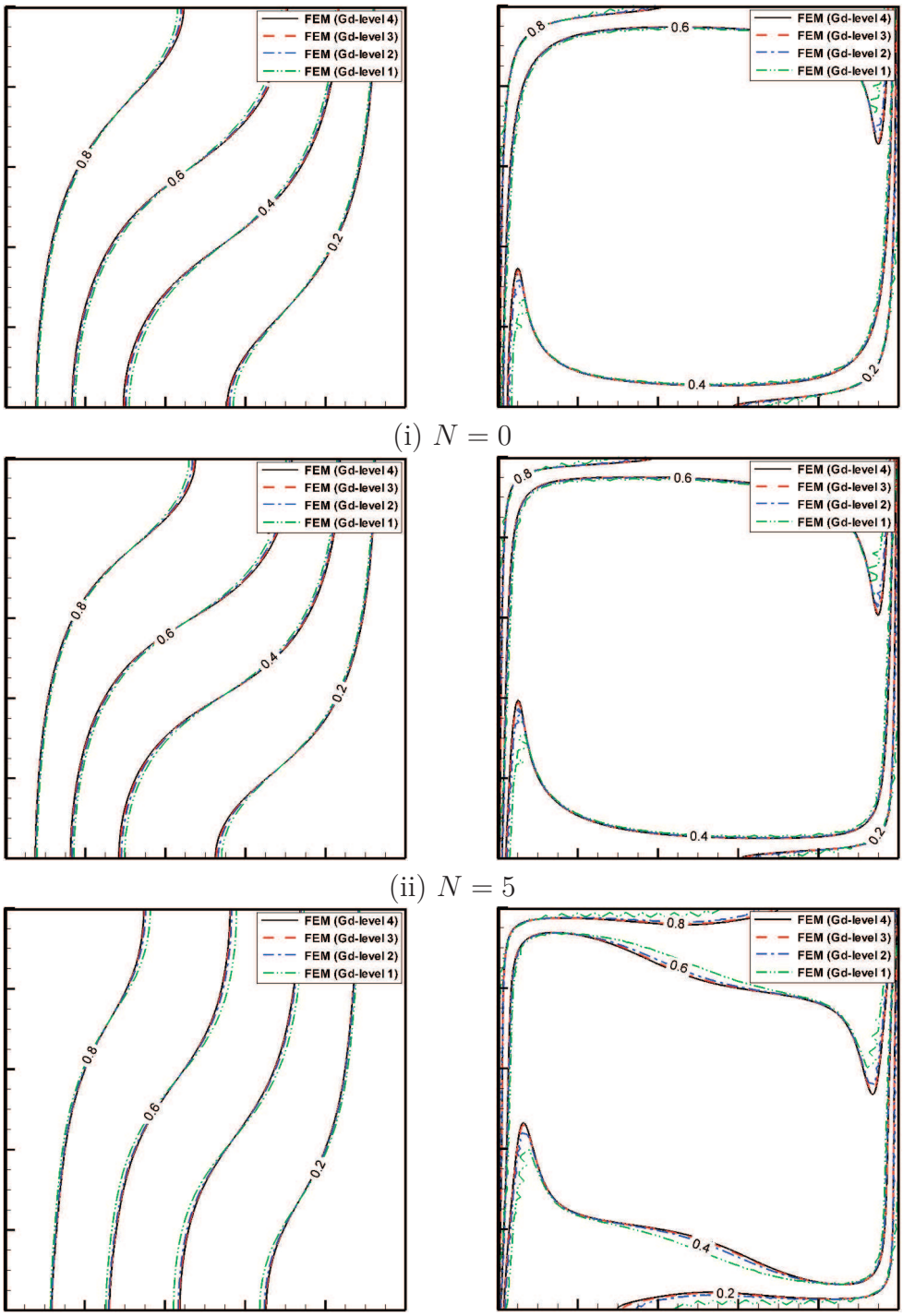

(i) $N = 0$

(ii) $N = 5$

(iii) $N = 10$

(a) Temperature contours (b) Concentration contours

Figure 2.7.: Temperature and concentration contours obtained by the finite-element model with different grid levels for $Ra^* = 100$, $Da = 10^{-1}$ and $Le = 100$

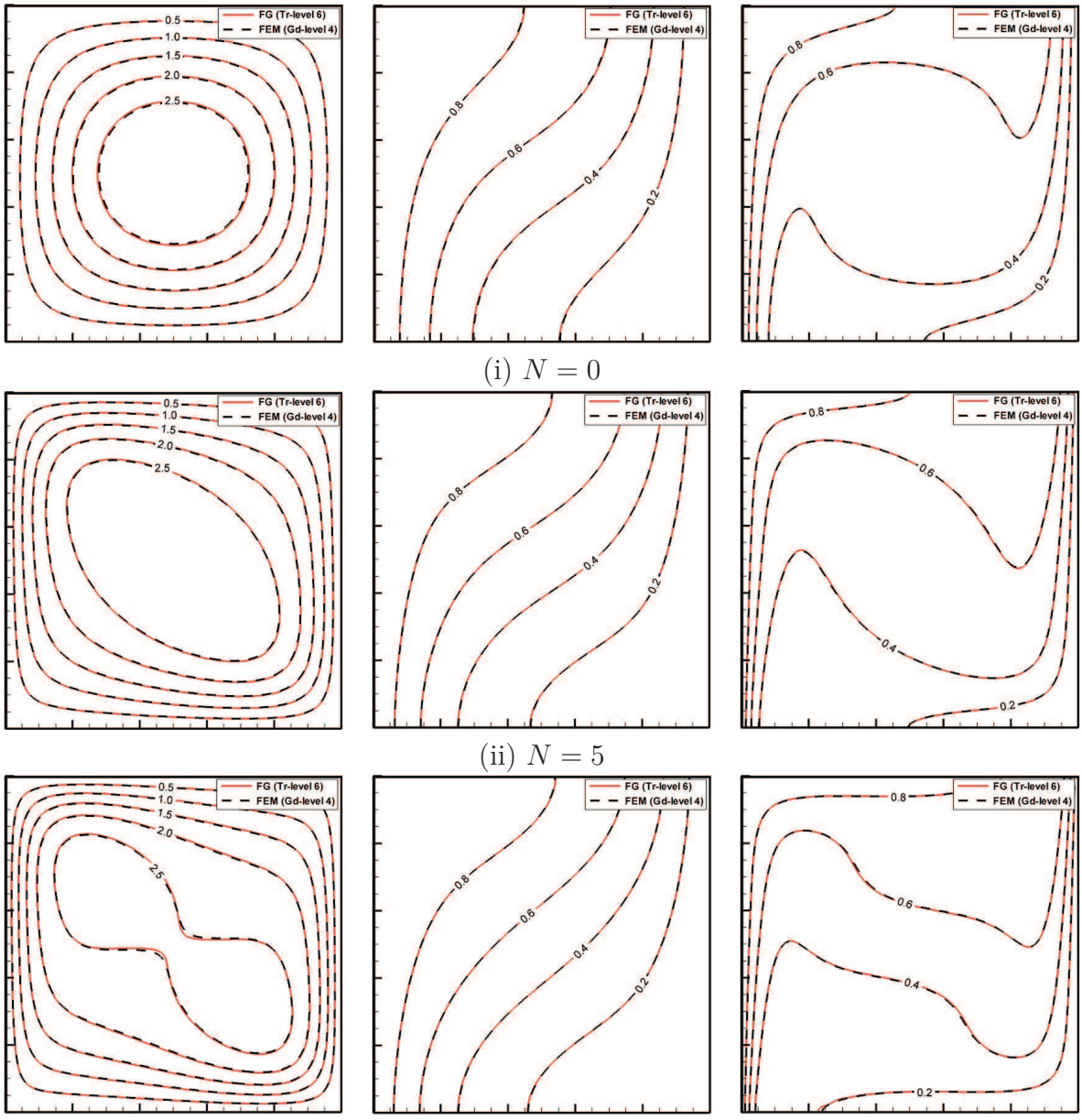

Figure 2.8.: FG and FEM solutions for: (a) streamlines, (b) temperature contours, (c) concentration contours with $Ra^* = 100$, $Da = 10^{-1}$ and $Le = 10$

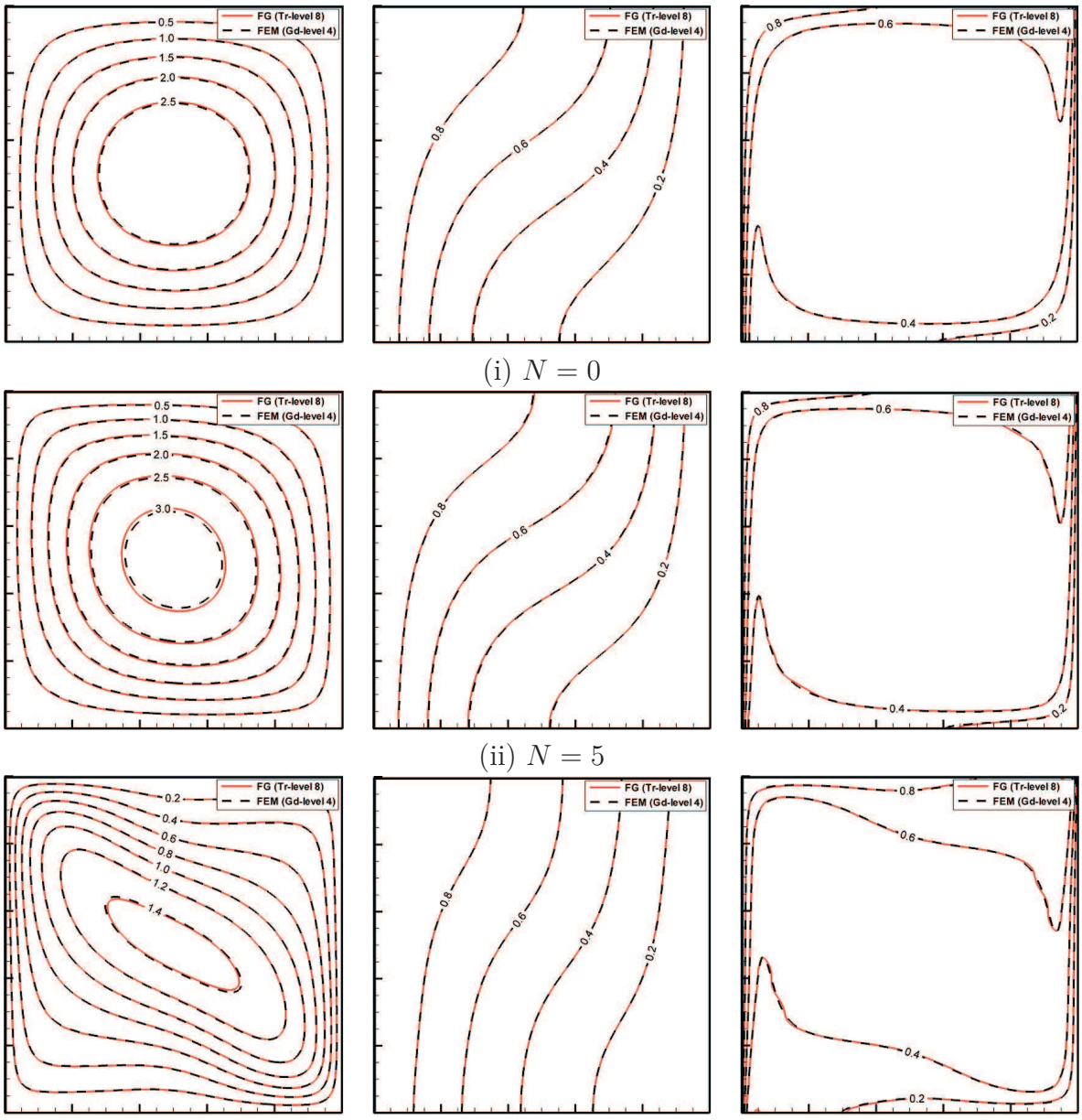

(i) $N = 0$

(ii) $N = 5$

(iii) $N = 10$

(a) Streamlines (b) Temperature contours (c) Concentration contours

Figure 2.9.: FG and FEM solutions for: (a) streamlines, (b) temperature contours, (c) concentration contours with $Ra^* = 100$, $Da = 10^{-1}$ and $Le = 100$

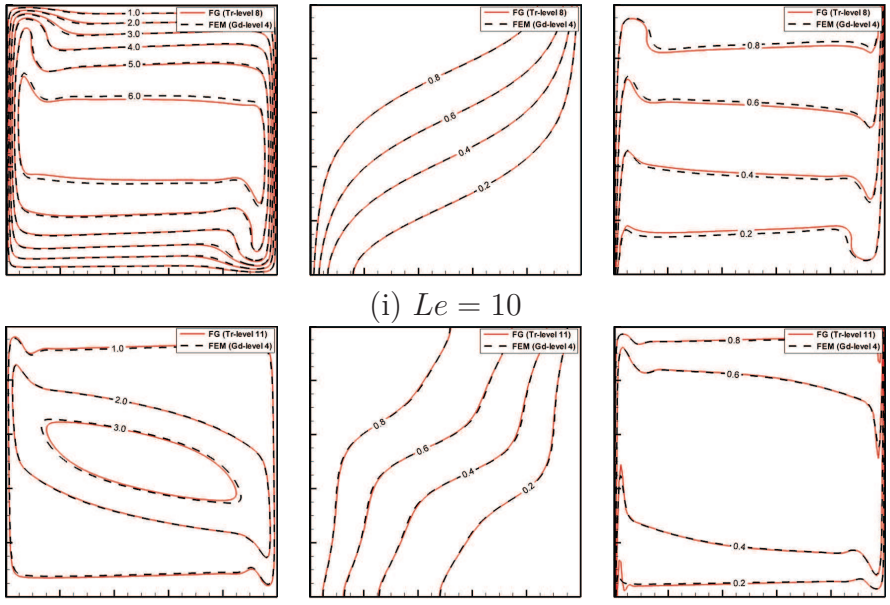

(i) $Le = 10$

(ii) $Le = 100$

(a) Streamlines (b) Temperature (c) Concentration

Figure 2.10.: FG and FEM solutions with $Ra^* = 100$, $D_A = 10^{-3}$ and $N = 10$

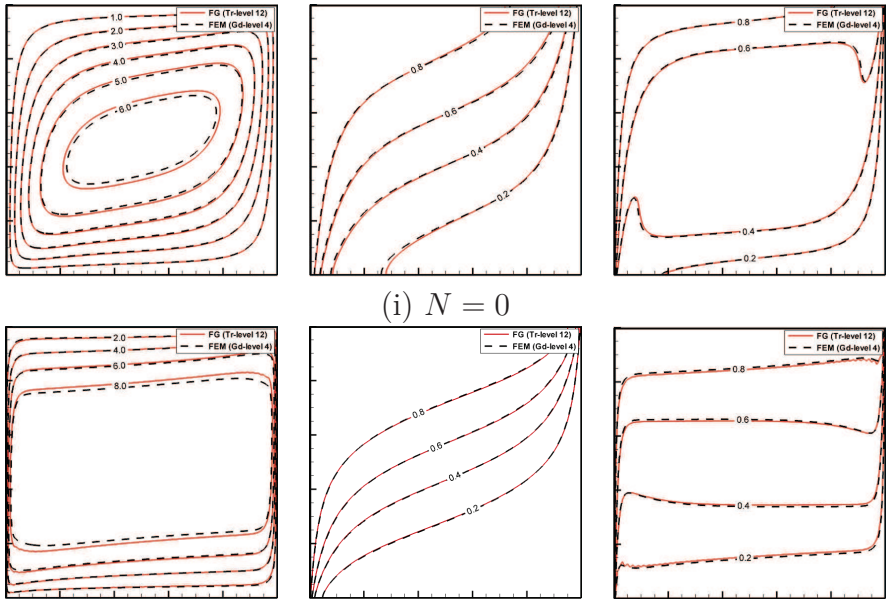

(i) $N = 0$

(ii) $N = 10$

(a) Streamlines (b) Temperature (c) Concentration

Figure 2.11.: FG and FEM solutions with $Ra^* = 100$, $D_A = 10^{-5}$ and $Le = 10$

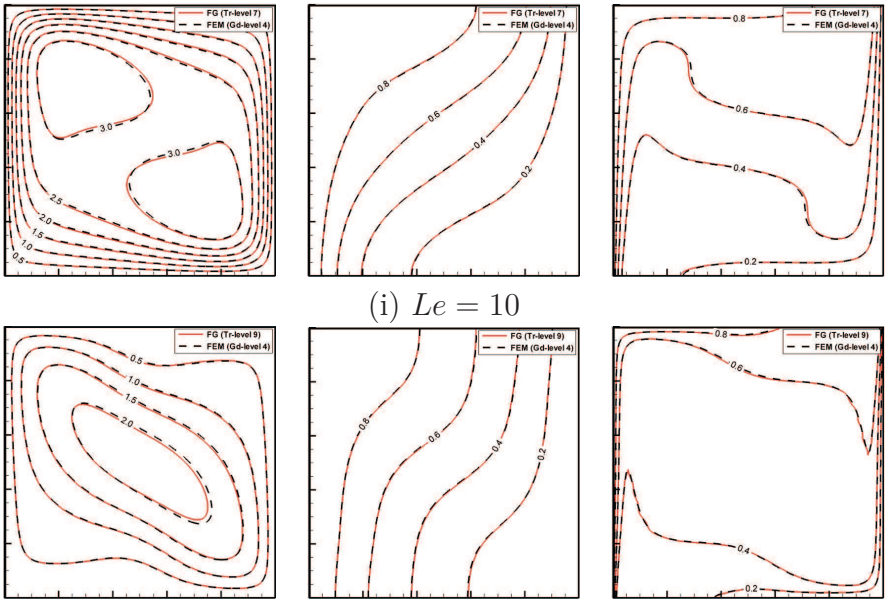

(i) $Le = 10$

(ii) $Le = 100$

(a) Streamlines (b) Temperature (c) Concentration

Figure 2.12.: FG and FEM solutions with $Ra^* = 200$, $D_A = 10^{-1}$ and $N = 10$

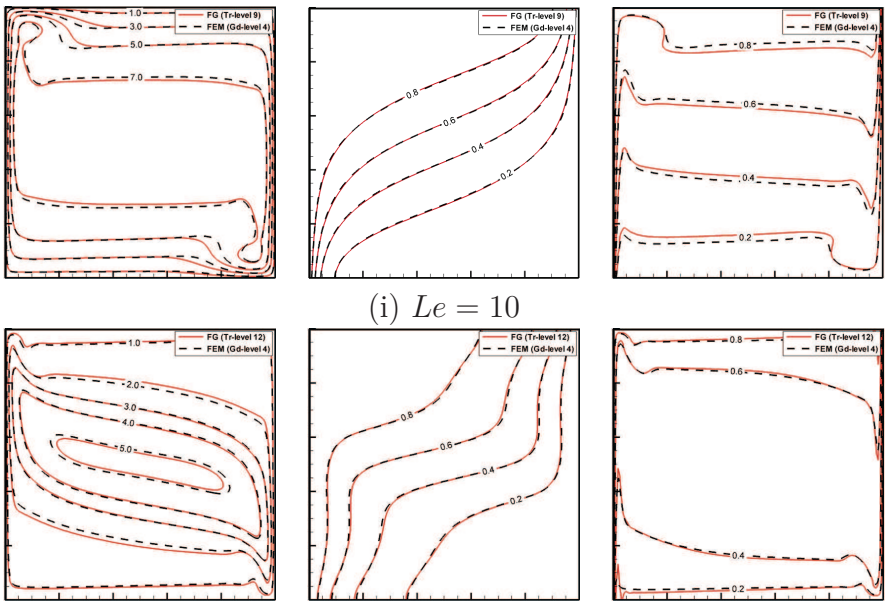

(i) $Le = 10$

(ii) $Le = 100$

(a) Streamlines (b) Temperature (c) Concentration

Figure 2.13.: FG and FEM solutions with $Ra^* = 200$, $D_A = 10^{-3}$ and $N = 10$

3. Thermo-Mechanical Investigation of Cracked Isotropic Porous Material: Effect of Fluid Flow and Heat Transfer

3.1. Introduction

In SOFC porous electrodes (anode and cathode), the nucleation and propagation of cracks usually result from the local temperature gradients, which are induced by different interconnected physical phenomena: flow of gases (hydrogen and oxygen) and electrochemical reactions. Meanwhile, the presences of cracks in the porous electrodes affect the local temperature distributions and the thermal stress concentrations in the vicinity of cracks. To study the fluid flow and heat transfer in a cracked isotropic porous electrode, as well as their effects on the thermal-mechanical response of the porous media, the modeling of the cracks under thermo-mechanical loadings is required. The standard Finite Element Method (FEM) has been successfully used to model static cracks where the mesh has to be conforming to the crack surface. Once the crack starts to evolve, re-meshing and mesh refinement at the crack tip are required. To overcome this drawback, the eXtended Finite Element Method (XFEM) was developed to model more efficiently the cracked media, where discontinuities and singularities within materials can be handled by only using appropriate enrichment functions (Belytschko and Black, 1999; Moës et al., 1999). During the last two decades, XFEM was used successfully to solve problems with evolving material discontinuities under mechanical and thermo-mechanical loading (Moës et al., 1999; 2003; Sukumar and Prévost, 2003). Crack propagation along interface between

dissimilar materials was treated using XFEM in Sukumar et al. (2004); Huang et al. (2005); Hettich and Ramm (2006); Hettich et al. (2008).

In the present chapter, we consider the effect of fluid flow and heat transport on the stress state at the vicinity of the crack-tip in cracked porous media. To this aim, a numerical model is developed (Darcy-XFEM model) where XFEM is used to solve the thermo-mechanical problem and FEM is used to solve the Darcy fluid flow. The heat transfer in the cracked porous media is solved by a combination of FEM and XFEM. Due to the small openings of cracks in the porous media, we assume that the cracks have no influence on the fluid flow (no preferential fluid flow within the fractures). Thereby the nonconforming FEM is used to solve the fluid flow equation, which is represented by the Darcy's law in the porous media. Heat transport in the porous media is described by heat conduction in the solid phase as well as heat convection and diffusion in the fluid phase. Different numerical methods are used to solve the heat transfer equations in the fluid and solid phases. A combination of the DG, MPFA and XFEM is used to discretize the convection-diffusion heat equation. While the thermo-mechanical response of the cracked porous media are solved by means of XFEM. Using this scheme one obtains throughout the structure the following outputs: pressure, flow velocity, temperature, displacement, deformation and stress. Finally, the impact of the fluid flow and the heat transfer on the stress state at the crack tip is evaluated by calculating the Stress Intensity Factor (SIF) evolution.

The chapter is organized as follows: In Section 3.2, the problem is formulated and the Darcy-XFEM model is introduced. This concerns the fluid flow equation, the energy conservation equation and the thermo-mechanical problem. In Section 3.3, heat transfer in cracked porous media is described and modeled. In Section 3.4, all the introduced schemes are discretized and the resolution algorithms are detailed. Then the post processing stage is recalled and the SIF calculation is presented. In Section 3.5, the method is benchmarked and validated by simulating several numerical examples and comparing the results to existing literature solutions. Conclusions are drawn in Section 3.6.

3.2. Governing Equations

The methodology pursued for the solution of the fluid flow, heat transfer and thermo-mechanical response in the cracked isotropic porous media is summarized as follows:

- Darcy's law is used to simulate the fluid flow in cracked porous media. The equation is solved using the nonconforming finite element method.
- A combined FEM/XFEM scheme is used to solve the heat transfer equation in the cracked porous media where the hypothesis of local thermal equilibrium holds.
- Using the obtained temperature as body force, the thermo-mechanical problem in the cracked porous media is solved with XFEM. Then, the stress intensity factors (SIF) are calculated by using the J-integral technique at each time step.

3.2.1. Darcy Flow

Equations describing the flow in a porous medium are given by the mass balance equation and Darcy's law:

$$\begin{cases} s\dfrac{\partial p}{\partial t} + \nabla.\mathbf{q} = Q_f \\ \mathbf{q} = -K\nabla p \end{cases} \tag{3.1}$$

Where s is the specific storativity of the porous material, K is the so called hydraulic conductivity, Q_f is the source or sink term per unit area, p is the pressure head and $\mathbf{q}$ the Darcy's velocity.

Combining mass balance equation with Darcy's equation leads to diffusivity equation:

$$s\frac{\partial p}{\partial t} + \nabla.\left(-K\nabla p\right) = Q_f \tag{3.2}$$

3.2.2. Heat transfer

Heat transfer in porous media is governed by heat conduction in the solid phase and heat transport in the fluid phase. At the Representative Elementary Volume (REV), under the assumption of thermal equilibrium between the fluid and solid phases and neglecting all the density variations, the temperature T of the porous medium is governed by the following total energy conservation equation:

$$(\rho c)_{PM} \frac{\partial T}{\partial t} + \nabla.(\rho_f c_f \mathbf{q} T) - \nabla.(\mathbf{k}_{PM} \nabla T) = Q_T \tag{3.3}$$

where Q_T represents heat source/sink function in the porous medium. In the presence of cracks, the tensor $\mathbf{k}_{PM}$, which includes thermal dispersion in the fluid phase and thermal conduction in both fluid and solid phases, is defined as following:

$$\mathbf{k}_{PM} = \begin{cases} \mathbf{k}^f & \text{inside the crack} \\ \mathbf{k}^f + \mathbf{k}^s & \text{other parts} \end{cases} \tag{3.4}$$

where $\mathbf{k}^f$ includes the thermal dispersion and heat conduction in the fluid phase, and $\mathbf{k}^s$ is the heat conduction in the solid phase, with the expression of their components given by:

$$k_{ij}^f = \underbrace{\rho_f c_f \left[\alpha_T |\mathbf{q}| \delta_{ij} + (\alpha_L - \alpha_T) \frac{q_i q_j}{|\mathbf{q}|} \right]}_{dispersive} + \underbrace{\varepsilon k_f \delta_{ij}}_{conductive} \tag{3.5}$$

$$k_{ij}^s = (1 - \varepsilon) k_s \delta_{ij} \tag{3.6}$$

where α_L and α_T are the longitudinal and transverse thermal dispersivities, δ_{ij} is the Kronecker delta function. k_f and k_s are the thermal conductivity of the fluid phase and the solid phase, respectively.

3.2.3. Thermo-mechanical Model

The equilibrium equation and the boundary conditions of a 2D domain Ω bounded by Γ are given by:

$$\begin{aligned} &\nabla_s \boldsymbol{\sigma} + \mathbf{b} = 0 \quad && \text{in } \Omega \\ &\mathbf{u} = \bar{\mathbf{u}} && \text{on } \Gamma_u \\ &\boldsymbol{\sigma} \cdot \mathbf{n} = \bar{\mathbf{t}} && \text{on } \Gamma_t \end{aligned} \tag{3.7}$$

where, $\boldsymbol{\sigma}$ is the Cauchy stress tensor, ∇_s is the symmetrical part of the divergence operator, $\mathbf{b}$ is the body force per unit volume, $\mathbf{u}$ is the displacement vector, $\mathbf{n}$ is the unit outward normal, $\bar{\mathbf{u}}$ and $\bar{\mathbf{t}}$ are prescribed displacements and traction respectively at boundaries Γ_u, Γ_t.

The constitutive relation for thermal elastic problems is given by the generalized Hooke's law:

$$\boldsymbol{\sigma} = \mathbf{C} : \mathbf{D} - (\beta^* \Delta T)\, \mathbf{I} \tag{3.8}$$

where $\mathbf{C}$ is the material stiffness tensor, $\mathbf{D} = \nabla_s \mathbf{u}$ is the strain tensor, $\Delta T = T - T_0$ is the change of temperature between the initial and the current step in the domain, $\beta^* = \beta_T E_m / (1 - 2\nu)$ is the material constant related in the plain strain conditions to Young's modulus E_m, Poisson's ratio ν and thermal expansion coefficient β_T, $\mathbf{I}$ is the identity tensor.

The weak form of equilibrium equation can be written as:

$$\int_\Omega \delta\mathbf{D} : \boldsymbol{\sigma} d\Omega = \int_\Omega \delta\mathbf{u} \cdot \mathbf{b} d\Omega + \int_{\Gamma_t} \delta\mathbf{u} \cdot \bar{\mathbf{t}} d\Gamma_t \tag{3.9}$$

Substituting equation Eq. (3.8) to equation Eq. (3.9), the weak form writes:

$$\int_\Omega \mathbf{D}(\delta\mathbf{u}) : (\mathbf{C} : \mathbf{D}(\mathbf{u}) - (\beta^* \Delta T)\, \mathbf{I})\, d\Omega = \int_\Omega \delta\mathbf{u} \cdot \mathbf{b} d\Omega + \int_{\Gamma_t} \delta\mathbf{u} \cdot \bar{\mathbf{t}} d\Gamma_t \tag{3.10}$$

3.3. Heat Transfer in Cracked Porous Media

The heat transfer in the porous medium is due to the heat convection by the movement of the fluid and heat conduction in both fluids and solids. At a molecular level, the conduction occurs with the collisions of molecules in fluids. While for solids, the heat conduction takes place between systems in physical contact through the vibrations of particles and free electrons (Lampe, 2013). With the existance of the crack in the porous medium, the physical contact of the solid skeleton on the crack surface is lost, which affects the heat transfer process in the porous matrix.

To study the heat transfer in cracked porous media, the standard FEM has been widely used. For instance, Noorishad et al. (1984) developed a numerical approach to study the coupled thermal-hydraulic-mechanical behavior of the saturated fractured porous rocks. Schrefler et al. (2006) and Secchi et al. (2007) presented a FEM model with an adaptive refinement technique to calculate the nucleation and propagation of cohesive cracks in porous media under thermal and hydraulic loads. However, in these standard FEM models, the cracks are restricted to the inter-element boundaries. The mesh refinement and adaptation are required when dealing with the evolving cracks, which makes the computation quite expensive. Instead, this difficulty can be avoid with XFEM, where the discontinuities in the porous medium are handled by locally enriching the conventional finite element approximations with an appropriate enrichment function (Khoei et al., 2012). During the last two decades, XFEM was used successfully to solve problems with evolving material discontinuities under mechanical and thermo-mechanical loadings (Moës et al., 1999; 2003; Sukumar and Prévost, 2003). The technique was then adopted to model the coupled problems in fractured porous media (De Borst et al., 2006; Rethore et al., 2007; Ren et al., 2009; Lecampion, 2009; Khoei and Haghighat, 2011; Mohammadnejad and Khoei, 2012; Khoei et al., 2012; Mohammadnejad and Khoei, 2013). In addition, XFEM was also found to be used in modeling heat transfer in cracked solids (Duflot, 2008; Zamani and Eslami, 2010). Indeed, in this case, the crack is considered adiabatic which corresponds to a zero heat flux at the crack interface. Consequently its thickness does not affect the heat transfer through the crack. However, this does not hold if both fluid and solid heat transfers are taken into account in the porous medium as considered in this work. Hence, to take advantage of XFEM in this context, we develop and evaluate in this section a time splitting procedure for solving heat transfer in a cracked porous

medium.

In the following, a one-dimensional problem is considered to investigate (i) the validity of the time splitting procedure, (ii) the effect of convection on the temperature distribution, (iii) the effect of the thickness of the crack, and (iv) to search for the adequate mesh discretization of the crack. To this aim, we consider a one-dimensional horizontal column of dimension $L = 1$ m which is formed by saturated porous medium. The porous medium contains a crack at $x = 0.5$ m. The column is subjected to a temperature $T = 1$ on the left boundary and $T = 0$ on the right boundary.

To simplify the problem, the dispersion/diffusion in the fluid is neglected and only convection and conduction are considered. The porosity of the porous medium is taken $\varepsilon = 0.2$. The thermal conductions in the fluid and the solid phases are taken into account by using $k_f = 0.1$ W/(m °C) and $k_s = 2.0$ W/(m °C). The volumetric heat capacities of the fluid and solid are$\rho_f c_f = 1.6 \times 10^3$ J/(m^3 °C) and $\rho_s c_s = 2.1 \times 10^5$ J/(m^3 °C), respectively. The final simulation time is $t_{max} = 100000$ s.

To test the validity of the time splitting procedure, two numerical Finite Volume models are developed: the first one solves the full heat equation (Eq. (3.3)) in the whole column where the thermal conductivity in the crack is reduced to $\mathbf{k}^f$ whereas in the rest of the column it equals $\mathbf{k}^f + \mathbf{k}^s$; in the second scheme, a time splitting technique is used to allow different numerical treatment for the processes included in the heat Eq. (3.3) as follows:

At each time step Δt, the heat transport equation is firstly solved to calculate $T^{n+1,*}$, the temperature caused by heat transfer in the fluid phase:

$$(\rho c)_{PM} \frac{T^{n+1,*} - T^n}{\Delta t} + \nabla.\left(\rho_f c_f \mathbf{q} T\right) - \nabla.\left(\mathbf{k}^f \nabla T\right) = Q_T^f \tag{3.11}$$

Then, the final temperature T^{n+1} is obtained by taking into account heat transfer in the solid phase using $T^{n+1,*}$ as initial temperature:

$$(\rho c)_{PM} \frac{T^{n+1} - T^{n+1,*}}{\Delta t} - \nabla.\left(\mathbf{k}^s \nabla T\right) = Q_T^s \tag{3.12}$$

Imitating the XFEM resolution, Eq. (3.12) is solved for the porous medium (not the crack region) with a zero heat flux at the porous/crack interface. Note that to reduce time splitting errors, small time steps are used with the splitting scheme. After calculation,

we plot the temperature profiles along the column resulted from the full procedure and the time splitting in Fig. 3.1 (i). Then, to show the effect of convection, two values of the velocity are used corresponding to $q = 0.0625$ mm/s (low convection) and $q = 3.125$ mm/s (high convection). The resulted temperature profiles are plotted in Fig. 3.1 (ii). Further, to investigate the effect of the crack thickness on the temperature distribution, two thickness of the crack are studied corresponding to $h_f = 2.0$ mm and $h_f = 0.5$ mm. Fig. 3.1 (iii) shows the temperature distributions of these two cases. At last, in order to search for the adequate mesh discretization of the crack for the computation, the crack is respectively discretized with three elements and only one element in the calculation. Accordingly, the results of temperature are shown in Fig. 3.1 (iv).

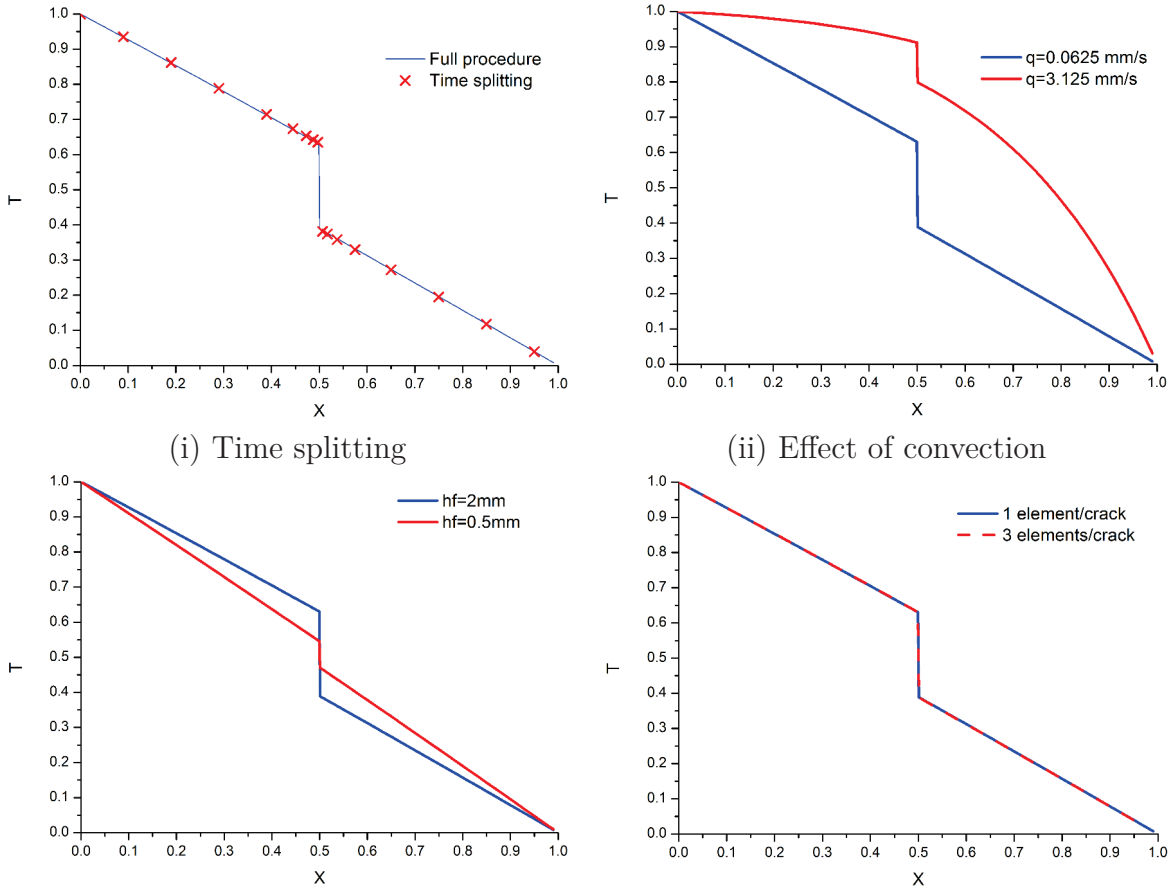

(i) Time splitting

(ii) Effect of convection

(iii) Effect of crack thickness

(iv) Effect of discretization

Figure 3.1.: Temperature distributions along the column with the presence of a crack

The comparison of the temperature values from Fig. 3.1 (i) show that the time splitting is a purely numerical procedure which does not introduce significant numerical errors. In Fig. 3.1 (ii), we can find that the ratio of thermal convection and conduction can influence dramatically the temperature distribution in the cracked porous medium. Moreover, the thickness of the crack also has an important effect on the temperature field (see Fig. 3.1 (iii)). From the comparison of temperature in Fig. 3.1 (iv), we can conclude that one single element is adequate for the discretization of crack.

In the following studies, heat transfer in the cracked porous medium is solved with a FEM/XFEM scheme using the time splitting procedure where FEM is used for the solution of Eq. (3.11) and XFEM is used for the solution of Eq. (3.12). We consider that all the cracks have a constant thickness which does not vary when the cracks evolve. Moreover, the mesh is adapted to the thickness of the crack and the latter is discretized with a single element.

3.4. Numerical Methods

The Darcy's Eq. (3.2) is solved with the nonconforming FEM. This method can provide continuous fluid fluxes at element boundaries. It also satisfies the mass balance locally at the element level, which is essential to avoid artificial sources and sinks. For the advection-diffusion heat transfer Eq. (3.11), a combination of DG and MPFA methods is used as mentioned in Chapter 2. The DG method is used for the advection part of the heat transport equation to reduce numerical diffusion (Arnold et al., 2002), whereas, the diffusion part is solved using the MPFA method (Aavatsmark et al., 1996; Younes and Fontaine, 2008a). Regarding the heat conduction Eq. (3.12), the XFEM is introduced to better handle the presence of cracks. The resulted temperature field from the heat transfer equation is used as a body force to solve the thermo-mechanical problem by means of XFEM, where appropriate enrichment functions are introduced to enforce the discontinuity of the displacement field at the crack surface and the stress singularity at the crack tip. Finally, to evaluate the fluid flow and the heat transport effects on the stress state at the crack-tip, the interaction integral (Bouhala et al., 2010; 2012), is used to calculate the Stress Intensity Factor (SIF) evolution. In the following, details on the discretization of the heat transport equation in the sold phase will be given. However, the

discretization of the heat transport in the fluid phase will be recalled briefly, the reader might refer to Chapter 2 for more details.

3.4.1. Discretization of the Flow Equation

The nonconforming FEM is used to solve the fluid flow equation because of its simplicity and mass conservation properties. The main steps of the flow discretization on linear triangular elements are recalled in this section.

The pressure is assumed to vary linearly inside each triangular element E:

$$p_E = p_i \varphi_i^E + p_j \varphi_j^E + p_k \varphi_k^E \tag{3.13}$$

where the degrees of freedom of the pressure are located at the mid-edges.

Note that p_i, the unknown pressure at the mid-edge i, is located facing the node i and φ_i^E is the interpolation function, which is nonzero only inside the two adjacent elements E and E' sharing the edge i. The interpolation function φ_i^E is the same as Eq. (2.10) in Chapter 2.

The variational formulation of the flow equation Eq. (3.2) using the test function φ_i writes:

$$\int_\Omega s \frac{\partial p}{\partial t} \varphi_i + \int_\Omega \nabla . \left(-K \nabla p\right) \varphi_i = \int_\Omega Q_f \varphi_i \tag{3.14}$$

The first term for an interior edge i leads to

$$\int_\Omega s \frac{\partial p}{\partial t} \varphi_i = \frac{1}{3} \frac{\partial p_i}{\partial t} \left(s_E \left|E\right| + s_{E'} \left|E'\right|\right) \tag{3.15}$$

In the same way, the source/sink term leads to:

$$\int_\Omega Q_f \varphi_i = \frac{Q_f^E \left|E\right|}{3} + \frac{Q_f^{E'} \left|E'\right|}{3} \tag{3.16}$$

Using Green's formula, the second term in equation Eq. (3.14) writes,

$$\int_{\Omega} \nabla.\left(-K\nabla p\right)\varphi_i = \int_{\Omega} \left(K\nabla p\right)\nabla\varphi_i - \int_{\Gamma} \varphi_i \left(K\nabla p\right)\eta_{\Gamma} d\Gamma \tag{3.17}$$

In the case of an interior edge i, it simplifies to

$$\begin{aligned}\int_{\Omega} \nabla.\left(-K\nabla p\right)\varphi_i = &\frac{1}{|E|}\sum_{j=1}^{3} p_{E,j}\left(\nabla\varphi_{E,j}^{T} K_E \nabla\varphi_{E,i}\right) \\ &+ \frac{1}{|E'|}\sum_{j=1}^{3} p_{E',j}\left(\nabla\varphi_{E',j}^{T} K_{E'} \nabla\varphi_{E',i}\right)\end{aligned} \tag{3.18}$$

Using an implicit time discretization, the final form gives:

$$\begin{aligned}&\left(\frac{s_E\,|E| + s_{E'}\,|E'|}{3}\right)\frac{p_i^{n+1} - p_i^{n}}{\triangle t} - \frac{1}{|E|}\sum_{j=1}^{3} p_{E,j}^{n+1}\left(\nabla\varphi_{E,j}^{T} K_E \nabla\varphi_{E,i}\right) \\ &-\frac{1}{|E'|}\sum_{j=1}^{3} p_{E,j}^{n+1}\left(\nabla\varphi_{E',j}^{T} K_{E'} \nabla\varphi_{E',i}\right) = \frac{Q_f^{E}\,|E|}{3} + \frac{Q_f^{E'}\,|E'|}{3}\end{aligned} \tag{3.19}$$

This leads to a final system to solve with a symmetric positive definite matrix.

Once this system is solved, the Darcy's velocity $\mathbf{q}^E$ at the element E and the fluid flux Q_i^E on each edge of element E can be calculated using the local values of the pressure $p_{E,j}^{n+1}$.

3.4.2. Discretization of the Heat Transfer Equation (3.12)

The XFEM is used for the discretization of the heat 3.12 to take into account the effects of the cracks on the temperature distribution. Indeed, the concept of XFEM uses the partition of unity principle to enrich the set of nodes located in the vicinity of the crack by adding some additional degrees of freedom. The temperature is approximated by a continuous term in the whole domain, a discontinuous term near the crack surface and a singular term in the crack tip region, which is given by:

$$T^h\left(\boldsymbol{x}\right) = \sum_{i\in N_{\Omega}} \Upsilon_i\left(\boldsymbol{x}\right) T_i + \sum_{i\in N_{\Gamma}} \Upsilon_i\left(\boldsymbol{x}\right) H^T\left(\boldsymbol{x}\right) a_i + \sum_{i\in N_{\Lambda}} \Upsilon_i\left(\boldsymbol{x}\right) br^T\left(\boldsymbol{x}\right) b_i \tag{3.20}$$

where Υ_i is the shape function of the node i. It is equal to 1 at node i, and zero on all the other nodes. In a triangular element, it is defined as:

$$\Upsilon_i = \frac{1}{2\,|E|}\left[x_j y_k - x_k y_j + (y_j - y_k)\,x + (x_k - x_j)\,y\right] \tag{3.21}$$

N_Ω is the set of nodes in the whole domain, N_Γ the set of nodes of the elements crossed by the crack surface, and N_Λ the set of nodes of the crack tip zone, as shown in Fig. 3.2.

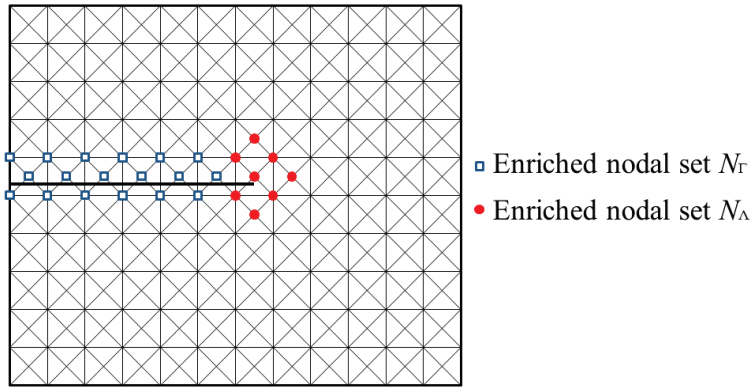

Figure 3.2.: Crack on a uniform mesh and the enriched nodal sets on crack surface and the crack tip

T_i is the nodal temperature of the continuous part of the finite element solution. a_i is the nodal enriched degree of freedom of the discontinuous function on the crack surface. b_i is the nodal enriched degree of freedom of the asymptotic function on the crack tip. $H^T(\boldsymbol{x})$ and $br^T(\boldsymbol{x})$ are the enrichment functions of the discontinuous field and the singular field, respectively.

In the case of adiabatic crack (no flux normal to the crack surface), the signed distance function is used as enrichment function to model the jump in the temperature field at the crack surface:

$$\begin{cases} H^T(\boldsymbol{x}) = sign\left[\mathbf{n}\cdot(\boldsymbol{x}-\boldsymbol{x}_i)\right] \\ sign(x) = \begin{cases} 1 & \text{if } x > 0 \\ -1 & \text{if } x < 0 \end{cases} \end{cases} \tag{3.22}$$

The singular enrichment in the crack tip region is given by:

$$br^T(r,\vartheta) = \sqrt{r}\sin\left(\frac{\vartheta}{2}\right) \tag{3.23}$$

where r and ϑ are the polar coordinates of the considered point in a local system based on the crack tip, as shown in Fig. 3.3.

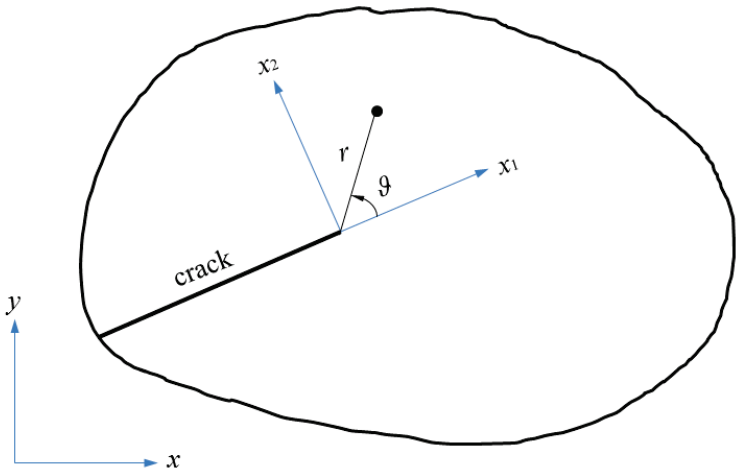

Figure 3.3.: Local coordinates system based on the crack tip

By multiplying the heat transfer Eq. (3.12) with shape function (Eq. (3.21)) and using Green's formula, the variational form of the heat equation in the solid phase can be written as:

$$\int_\Omega (\rho c)_{PM}\frac{\partial T}{\partial t}\Upsilon_i + \int_\Omega (k^s\nabla T)\cdot\nabla\Upsilon_i - \int_{\partial\Omega}\Upsilon_i\,(k^s\nabla T\cdot\mathbf{n}_{\partial\Omega}) = \int_\Omega Q_T^s\cdot\Upsilon_i \tag{3.24}$$

Substituting the approximated temperature (Eq. (3.20)) in the variational form of the

heat transport (Eq. (3.24)), the following system can be obtained:

$$(\rho c)_{PM}\begin{bmatrix} R_{ij}^{TT} & R_{ij}^{Ta} & R_{ij}^{Tb} \\ R_{ij}^{aT} & R_{ij}^{aa} & R_{ij}^{ab} \\ R_{ij}^{bT} & R_{ij}^{ba} & R_{ij}^{bb} \end{bmatrix}\begin{bmatrix} \dfrac{\partial T_j}{\partial t} \\ \dfrac{\partial a_j}{\partial t} \\ \dfrac{\partial b_j}{\partial t} \end{bmatrix} + k^s\begin{bmatrix} G_{ij}^{TT} & G_{ij}^{Ta} & G_{ij}^{Tb} \\ G_{ij}^{aT} & G_{ij}^{aa} & G_{ij}^{ab} \\ G_{ij}^{bT} & G_{ij}^{ba} & G_{ij}^{bb} \end{bmatrix}\begin{bmatrix} T_j \\ a_j \\ b_j \end{bmatrix}$$
$$= Q_T^s \cdot |E| + k^s \left(\nabla T \cdot \mathbf{n}_{\partial\Omega}\right) \frac{|\partial El|}{2} \tag{3.25}$$

where $k^s \left(\nabla T \cdot \mathbf{n}_{\partial\Omega}\right) |\partial El| /2$ is the boundary condition with a prescribed heat flux. The elements of the global matrices $[R]$ and $[G]$ are detailed as follows

$$\begin{cases} R_{ij}^{TT} = \int_E \Upsilon_j \Upsilon_i \\ R_{ij}^{Ta} = \int_E H^T(\boldsymbol{x})\, \Upsilon_j \Upsilon_i \\ R_{ij}^{Tb} = \int_E br^T(\boldsymbol{x})\, \Upsilon_j \Upsilon_i \end{cases} \tag{3.26}$$

$$\begin{cases} R_{ij}^{aT} = \int_E \Upsilon_j H^T(\boldsymbol{x})\, \Upsilon_i \\ R_{ij}^{aa} = \int_E H^T(\boldsymbol{x})\, \Upsilon_j H^T(\boldsymbol{x})\, \Upsilon_i \\ R_{ij}^{ab} = \int_E br^T(\boldsymbol{x})\, \Upsilon_j H^T(\boldsymbol{x})\, \Upsilon_i \end{cases} \tag{3.27}$$

$$\begin{cases} R_{ij}^{bT} = \int_E \Upsilon_j br^T(\boldsymbol{x})\,\Upsilon_i \\ R_{ij}^{ba} = \int_E H^T(\boldsymbol{x})\,\Upsilon_j br^T(\boldsymbol{x})\,\Upsilon_i \\ R_{ij}^{bb} = \int_E br^T(\boldsymbol{x})\,\Upsilon_j br^T(\boldsymbol{x})\,\Upsilon_i \end{cases} \tag{3.28}$$

$$\begin{cases} G_{ij}^{TT} = \int_E \left(\dfrac{\partial \Upsilon_j}{\partial x}\dfrac{\partial \Upsilon_i}{\partial x} + \dfrac{\partial \Upsilon_j}{\partial y}\dfrac{\partial \Upsilon_i}{\partial y} \right) \\ G_{ij}^{Ta} = \int_E \left(\dfrac{\partial \left(H^T(\boldsymbol{x})\,\Upsilon_j \right)}{\partial x}\dfrac{\partial \Upsilon_i}{\partial x} + \dfrac{\partial \left(H^T(\boldsymbol{x})\,\Upsilon_j \right)}{\partial y}\dfrac{\partial \Upsilon_i}{\partial y} \right) \\ G_{ij}^{Tb} = \int_E \left(\dfrac{\partial \left(br^T(\boldsymbol{x})\,\Upsilon_j \right)}{\partial x}\dfrac{\partial \Upsilon_i}{\partial x} + \dfrac{\partial \left(br^T(\boldsymbol{x})\,\Upsilon_j \right)}{\partial y}\dfrac{\partial \Upsilon_i}{\partial y} \right) \end{cases} \tag{3.29}$$

$$\begin{cases} G_{ij}^{aT} = \int_E \left(\dfrac{\partial \Upsilon_j}{\partial x}\dfrac{\partial \left(H^T(\boldsymbol{x})\,\Upsilon_i \right)}{\partial x} + \dfrac{\partial \Upsilon_j}{\partial y}\dfrac{\left(H^T(\boldsymbol{x})\,\Upsilon_i \right)}{\partial y} \right) \\ G_{ij}^{aa} = \int_E \left(\dfrac{\partial \left(H^T(\boldsymbol{x})\,\Upsilon_j \right)}{\partial x}\dfrac{\left(H^T(\boldsymbol{x})\,\Upsilon_i \right)}{\partial x} + \dfrac{\partial \left(H^T(\boldsymbol{x})\,\Upsilon_j \right)}{\partial y}\dfrac{\left(H^T(\boldsymbol{x})\,\Upsilon_i \right)}{\partial y} \right) \\ G_{ij}^{ab} = \int_E \left(\dfrac{\partial \left(br^T(\boldsymbol{x})\,\Upsilon_j \right)}{\partial x}\dfrac{\left(H^T(\boldsymbol{x})\,\Upsilon_i \right)}{\partial x} + \dfrac{\partial \left(br^T(\boldsymbol{x})\,\Upsilon_j \right)}{\partial y}\dfrac{\left(H^T(\boldsymbol{x})\,\Upsilon_i \right)}{\partial y} \right) \end{cases} \tag{3.30}$$

$$\begin{cases} G_{ij}^{bT} = \int_E \left(\dfrac{\partial \Upsilon_j}{\partial x} \dfrac{\partial \left(br^T(\boldsymbol{x}) \Upsilon_i \right)}{\partial x} + \dfrac{\partial \Upsilon_j}{\partial y} \dfrac{\left(br^T(\boldsymbol{x}) \Upsilon_i \right)}{\partial y} \right) \\ G_{ij}^{ba} = \int_E \left(\dfrac{\partial \left(H^T(\boldsymbol{x}) \Upsilon_j \right)}{\partial x} \dfrac{\left(br^T(\boldsymbol{x}) \Upsilon_i \right)}{\partial x} + \dfrac{\partial \left(H^T(\boldsymbol{x}) \Upsilon_j \right)}{\partial y} \dfrac{\left(br^T(\boldsymbol{x}) \Upsilon_i \right)}{\partial y} \right) \\ G_{ij}^{bb} = \int_E \left(\dfrac{\partial \left(br^T(\boldsymbol{x}) \Upsilon_j \right)}{\partial x} \dfrac{\left(br^T(\boldsymbol{x}) \Upsilon_i \right)}{\partial x} + \dfrac{\partial \left(br^T(\boldsymbol{x}) \Upsilon_j \right)}{\partial y} \dfrac{\left(br^T(\boldsymbol{x}) \Upsilon_i \right)}{\partial y} \right) \end{cases} \tag{3.31}$$

3.4.3. Discretization of the Thermo-mechanical Equilibrium Equation

Using the XFEM, the displacement approximation is assumed to have a continuous term in the whole domain, with two enrichment functions augmented for the nodes on crack surfaces and crack tips. Suppose that N is the set of nodes in the whole domain; N_Γ the nodes whose supports are cut by the crack surface; andN_Λ the nodes which are in the vicinity of the crack tip. The displacement can be approximated by:

$$\mathbf{u}^h(\boldsymbol{x}) = \sum_{i \in N} \Upsilon_i \mathbf{u}_i + \sum_{i \in N_\Gamma} \Upsilon_i H(\boldsymbol{x}) \mathbf{c}_i + \sum_{i \in N_\Lambda} \Upsilon_i \sum_k br_k(\boldsymbol{x}) \mathbf{d}_i^k \tag{3.32}$$

where $\mathbf{c}_i$ and $\mathbf{d}_i^k$ are added degrees of freedom vectors. The jump function $H(\boldsymbol{x})$ is the same as in Eq. (3.22) which is used in temperature field approximation. The singular functions $br_k(\boldsymbol{x})$ given in the local system centered at the crack tip (Fig. 3.3) are defined as:

$$br_{1-4}(r, \vartheta) = \left\{ \sqrt{r} \sin \frac{\vartheta}{2}, \sqrt{r} \cos \frac{\vartheta}{2}, \sqrt{r} \sin \frac{\vartheta}{2} \sin \vartheta, \sqrt{r} \cos \frac{\vartheta}{2} \sin \vartheta \right\} \tag{3.33}$$

By substituting the approximated displacement in the variational form of Eq. (3.9), the following system to solve can be obtained:

$$\mathbf{KU} = \mathbf{F} \tag{3.34}$$

where $\mathbf{K}$, $\mathbf{U}$ and $\mathbf{F}$ are global stiffness matrix, global unknowns vector and global loading vector respectively, with:

$$\mathbf{K}_{ij} = \int_{\Omega} \mathbf{B}_i^T \mathbf{C} \mathbf{B}_j d\Omega \tag{3.35}$$

$$\mathbf{f}_i = \int_{\Omega} \mathbf{B}_i^T \left(\beta^* \triangle T\right) \mathbf{I} d\Omega + \int_{\Omega} \Upsilon_i^T \mathbf{b} d\Omega + \int_{\Gamma_t} \Upsilon_i^T \bar{\mathbf{t}} d\Gamma_t \tag{3.36}$$

$\mathbf{B}_i$ is the matrix of shape function derivatives on node i. When the node is not enriched it reads:

$$\mathbf{B}_i = \begin{bmatrix} \Upsilon_{i,x} & 0 \\ 0 & \Upsilon_{i,y} \\ \Upsilon_{i,y} & \Upsilon_{i,x} \end{bmatrix} \tag{3.37}$$

where $\Upsilon_{i,x}$ and $\Upsilon_{i,y}$ are the derivatives of the shape function Υ_i on x and y directions, respectively,

$$\Upsilon_{i,x} = \frac{\partial \Upsilon_i}{\partial x},\ \Upsilon_{i,y} = \frac{\partial \Upsilon_i}{\partial y} \tag{3.38}$$

When the node is enriched by the Heaviside function (near the crack surface), $\mathbf{B}_i$ reads:

$$\mathbf{B}_i = \begin{bmatrix} \Upsilon_{i,x} & 0 & \Upsilon_{i,x} H\left(\boldsymbol{x}\right) & 0 \\ 0 & \Upsilon_{i,y} & 0 & \Upsilon_{i,y} H\left(\boldsymbol{x}\right) \\ \Upsilon_{i,y} & \Upsilon_{i,x} & \Upsilon_{i,y} H\left(\boldsymbol{x}\right) & \Upsilon_{i,x} H\left(\boldsymbol{x}\right) \end{bmatrix} \tag{3.39}$$

When the node i is enriched by the crack-tip enrichment functions, $\mathbf{B}_i$ becomes:

$$\mathbf{B}_i = \begin{bmatrix} \Upsilon_{i,x} & 0 & \mathcal{X}^i_{1,x} & 0 & \mathcal{X}^i_{2,x} & 0 & \mathcal{X}^i_{3,x} & 0 & \mathcal{X}^i_{4,x} & 0 \\ 0 & \Upsilon_{i,y} & 0 & \mathcal{X}^i_{1,y} & 0 & \mathcal{X}^i_{2,y} & 0 & \mathcal{X}^i_{3,y} & 0 & \mathcal{X}^i_{4,y} \\ \Upsilon_{i,y} & \Upsilon_{i,x} & \mathcal{X}^i_{1,y} & \mathcal{X}^i_{1,x} & \mathcal{X}^i_{2,y} & \mathcal{X}^i_{2,x} & \mathcal{X}^i_{3,y} & \mathcal{X}^i_{3,x} & \mathcal{X}^i_{4,y} & \mathcal{X}^i_{4,x} \end{bmatrix} \tag{3.40}$$

where $\mathcal{X}^i_{k,x} = \Upsilon_{i,x} br_k(\boldsymbol{x}) + \Upsilon_i br_{k,x}(\boldsymbol{x})$ and $\mathcal{X}^i_{k,y} = \Upsilon_{i,y} br_k(\boldsymbol{x}) + \Upsilon_i br_{k,y}(\boldsymbol{x})$, with $k = 1...4$.

3.4.4. Thermal Stress Intensity Factors

The Stress Intensity Factors (SIFs) are computed using the interaction integral which is derived from the path independent J-integral technique. The technique assumes the existence of an auxiliary mode $\left(\sigma^{(2)}_{ij}, D^{(2)}_{ij}, u^{(2)}_i\right)$ associated to the real mode $\left(\sigma^{(1)}_{ij}, D^{(1)}_{ij}, u^{(1)}_i\right)$. By using the superposition principle, Green's theory and separating terms, the interaction integral between state (1) and state (2) is (Bouhala et al., 2010; 2012; Duflot, 2008):

$$I^{(1,2)} = \int_A \left[\sigma^{(1)}_{ij} \frac{\partial u^{(2)}_i}{\partial x_1} + \sigma^{(2)}_{ij} \frac{\partial u^{(1)}_i}{\partial x_1} - \mathcal{W}^{(1,2)} \delta_{1j}\right] \frac{\partial q_A}{\partial x_j} dA + \int_A \left[\beta^* trace\left(D^{(2)}\right) \frac{\partial T}{\partial x_1}\right] q_A dA \tag{3.41}$$

where A is an integral domain surrounding the crack tip, as shown in Fig. 3.4. q_A is the weighting function, i.e. a smooth function defined over the integral domain A which takes a value of unity at the crack tip and zero on the contour Γ (Fig. 3.4).

The interaction strain energy $\mathcal{W}^{(1,2)}$ is calculated in thermo-mechanical problems as

$$\mathcal{W}^{(1,2)} = \frac{1}{2}\left(\sigma^{(1)}_{ij} D^{(2)}_{ij} + \sigma^{(2)}_{ij} D^{(1)}_{ij} - \beta^* D^{(2)}_{ij} \Delta T\right) \tag{3.42}$$

Note that the interaction integral is a function of the SIFs of the two aforementioned

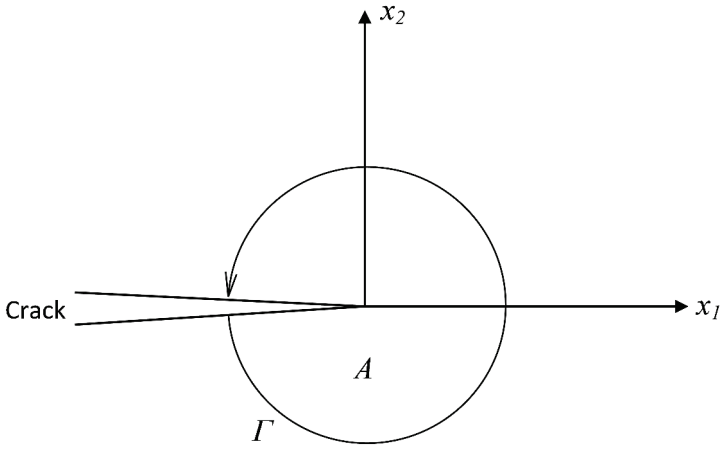

Figure 3.4.: Integration path Γ and domain A around the crack tip

states (1) and (2):

$$I^{(1,2)} = \frac{2}{E_m^*}\left(K_I^{(1)}K_I^{(2)} + K_{II}^{(1)}K_{II}^{(2)}\right) \tag{3.43}$$

where K_I and K_{II} are the SIFs for mode I and mode II respectively, with $E_m^* = E_m/\left(1-\nu^2\right)$ when plane strain is assumed and $E_m^* = E_m$ for plane stress.

Combining Eq. (3.41) and Eq. (3.43), the SIFs can be calculated by choosing the adequate auxiliary mode. For instance, to compute K_I, we choose pure mode one as auxiliary mode with unitary SIF. This choice leads to $K_I^{(2)} = 1$, $K_{II}^{(2)} = 0$, thus Eq. (3.43) is reduced to $I^{(1,2)} = 2K_I^{(1)}/E_m^*$, with which $K_I^{(1)}$ can be obtained. For this pure opening mode one, the exact stress and displacement fields are given in terms of local polar coordinates around the crack tip (see Fig. 3.3) as:

$$\sigma_{xx} = \frac{K_I}{\sqrt{2\pi r}}\cos\frac{\vartheta}{2}\left(1 - \sin\frac{\vartheta}{2}\sin\frac{3\vartheta}{2}\right) \tag{3.44}$$

$$\sigma_{yy} = \frac{K_I}{\sqrt{2\pi r}}\cos\frac{\vartheta}{2}\left(1 + \sin\frac{\vartheta}{2}\sin\frac{3\vartheta}{2}\right) \tag{3.45}$$

$$\sigma_{xy} = \frac{K_I}{\sqrt{2\pi r}} \sin\frac{\vartheta}{2}\cos\frac{\vartheta}{2}\cos\frac{3\vartheta}{2} \tag{3.46}$$

$$u_x = \frac{K_I}{2\mu}\sqrt{\frac{r}{2\pi}}\cos\frac{\vartheta}{2}\left(\kappa - 1 + 2\sin^2\frac{\vartheta}{2}\right) \tag{3.47}$$

$$u_y = \frac{K_I}{2\mu}\sqrt{\frac{r}{2\pi}}\sin\frac{\vartheta}{2}\left(\kappa + 1 - 2\cos^2\frac{\vartheta}{2}\right) \tag{3.48}$$

Similarly, K_{II} can be obtained by choosing a pure mode two as auxiliary mode with unitary SIF ($K_I^{(2)} = 0$, $K_{II}^{(2)} = 1$). And the exact solutions of stress and displacement for shearing mode are given by:

$$\sigma_{xx} = -\frac{K_{II}}{\sqrt{2\pi r}} \sin\frac{\vartheta}{2}\left(2 + \cos\frac{\vartheta}{2}\cos\frac{3\vartheta}{2}\right) \tag{3.49}$$

$$\sigma_{yy} = \frac{K_{II}}{\sqrt{2\pi r}} \sin\frac{\vartheta}{2}\cos\frac{\vartheta}{2}\cos\frac{3\vartheta}{2} \tag{3.50}$$

$$\sigma_{xy} = \frac{K_{II}}{\sqrt{2\pi r}} \cos\frac{\vartheta}{2}\left(1 - \sin\frac{\vartheta}{2}\sin\frac{3\vartheta}{2}\right) \tag{3.51}$$

$$u_x = \frac{K_{II}}{2\mu}\sqrt{\frac{r}{2\pi}}\sin\frac{\vartheta}{2}\left(\kappa + 1 + 2\cos^2\frac{\vartheta}{2}\right) \tag{3.52}$$

$$u_y = -\frac{K_{II}}{2\mu}\sqrt{\frac{r}{2\pi}}\cos\frac{\vartheta}{2}\left(\kappa - 1 - 2\sin^2\frac{\vartheta}{2}\right) \tag{3.53}$$

Here the shear modulus μ_m and Kolosov constant κ are defined in terms of Young's

modulus and Poisson's ratio by:

$$\mu_m = \frac{E_m}{2\,(1+\nu)},\ \kappa = 3 - 4\nu \tag{3.54}$$

3.5. Numerical Results

In this section, the theory and the numerical techniques mentioned in the previous sections are implemented and validated. We consider three numerical examples; the objective of the first one is to verify the solution of the transient flow coupled to the heat transfer in the porous media. Another interest of this example is to check the accuracy and the robustness of the time splitting procedure used to solve separately heat transfer in the solid and fluid phases. The second example is dedicated to the validation of thermo-mechanical problem considering a cracked medium without fluid flow, by comparing the resulted SIFs at the steady state to existing ones from the literature. Further, the time evolution of the stress state at the crack-tip is investigated by reporting the evolution of SIFs at the transient state. The third example concerns a mixture of the two previous ones, where the fluid flow and the heat transfer problems are coupled to the thermo-mechanical model to investigate the stress concentration generated by cracks within a porous media. A parametric study is conducted to demonstrate the effect of the crack on the temperature distribution and the stress concentration. The first and the last examples are carried out using an unstructured mesh of 8174 triangular elements corresponding to 4187 nodes, whereas an unstructured mesh of 9380 triangular elements corresponding to 4793 nodes is used in the second example.

3.5.1. Heat Transfer and Fluid Flow in Porous Media

In this example, a transient heat transfer equation is coupled to the fluid flow and solved in a rectangular shaped porous medium of dimensions 2.0×1.0 m^2 (see Fig. 3.5). The material parameters and boundary conditions are respectively reported in Tab. 3.1 and Tab. 3.2. The fluid flow in the porous medium is solved using Darcy's law, while the energy

conservation equation is solved using both the operator splitting (OS) procedure and the total energy conservation (TEC) equation. The accuracy of the OS procedure is verified by comparing the OS solution to that resulted from the TEC. To do the comparison, four points (A1, A2, A3 and A4) located randomly within the porous medium are designated as shown in Fig. 3.5. Then the temperature evolutions obtained from the OS solution and the TEC solution at points A1, A2, A3 and A4 are plotted in Fig. 3.6, where good agreements are found between the two schemes on all the four points. These results demonstrate that the time splitting of heat transfer equation doesn't lead to any significant error that reduces the accuracy the computation.

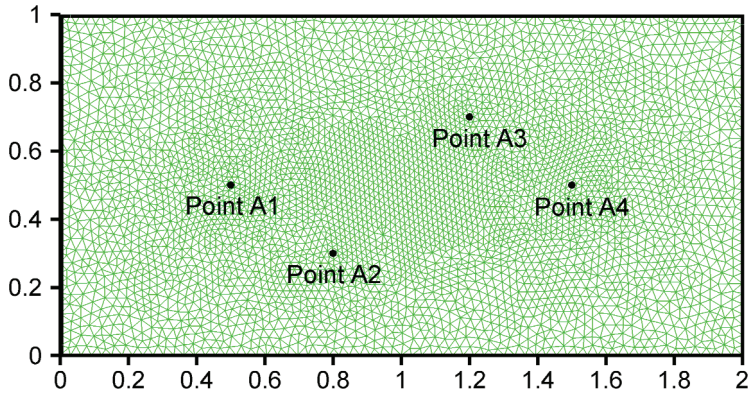

Figure 3.5.: Geometry and mesh of the rectangular shaped porous medium

Table 3.1.: Fluid and porous medium properties

Effective porosity	$\varepsilon = 0.1$
Specific mass storativity	$s = 6.0 \times 10^{-6}$ m^{-1}
Hydraulic conductivity	$K = 5.0 \times 10^{-5}$ m/s
Volumetric heat capacity	$\rho_f C_f = 4.2 \times 10^5$ J/(m^3°C)
	$\rho_s C_s = 2.3 \times 10^5$ J/(m^3°C)
Dispersivity	$\alpha_L = 0.02$ m, $\alpha_T = 0.002$ m
Thermal conductivity	$k_f = 0.65$ J/(sm°C)
	$k_s = 600.0$ J/(sm°C)

Table 3.2.: Boundary conditions on the porous medium

Boundaries	Flow condition	Heat condition
Top	No fluid flux	No heat flux
Bottom	No fluid flux	No heat flux
Left	$p = 100$ m water head	$T = 100$ °C
Right	$p = 0$	$T = -100$ °C

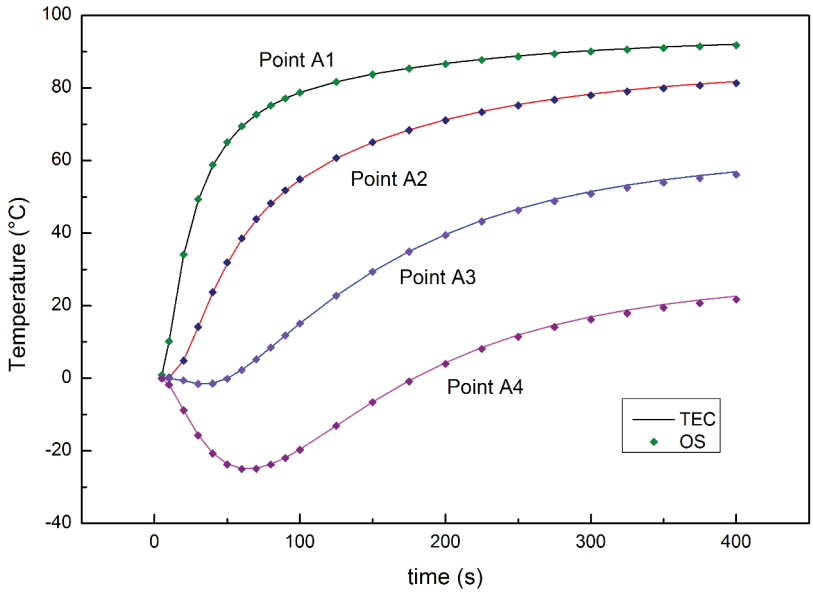

Figure 3.6.: Temperature evolution at points A1, A2, A3 and A4 using TEC and OS respectively

3.5.2. Heat Transfer in Cracked Porous Medium: Thermo-Mechanical Problem

In the SOFC electrode, the presence of crack has a significant effect on the heat conduction in the solid medium. The temperature gradient at the vicinity of the crack contributes to the stress concentration at the crack tip, which leads to possible crack propagation within the medium. In this example, we consider a cracked medium without fluid flow, where the heat transfer at the transient state and the mechanical response of the medium under thermal loading are studied.

A rectangular plate with dimensions ($W = 1$ m, $L = 0.5$ m) and boundary conditions

(see Fig. 3.7) as those used in the literature (Duflot, 2008; Murakami et al., 1987; Prasad et al., 1994a), is considered in this work. An inclined crack is assumed to locate in the center of the plate. As boundary conditions, the bottom of the plate is maintained to a temperature $T = -T_0$, and the top of the plate has a prescribed temperature $T = T_0$ ($T_0 = 100$°C in this example). The left and right boundaries as well as the crack are supposed to be adiabatic. The material properties of the plate are reported in Tab. 3.3. The simulation is conducted using a crack length $2a$ that vary from 0.4 m to 1.2 m with a step of 0.2 m, while the crack angle ζ varies from 0° to 90° with a step of 15°.

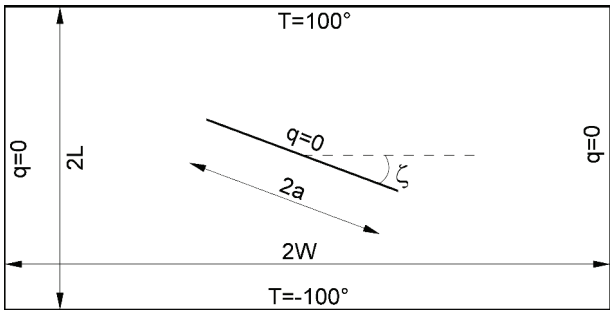

Figure 3.7.: Rectangular plate with an inclined adiabatic crack

Table 3.3.: Material properties of the rectangular plate

Young's modulus	$E_m = 7.4 \times 10^4$ MPa
Poisson's ratio	$\nu = 0.3$
Thermal expansion coefficient	$\beta_T = 1.67 \times 10^{-5}$/°C
Volumetric heat capacity	$\rho C = 2.3 \times 10^5$ J/(m^3°C)
Thermal conductivity	$k = 4.0 \times 10^2$ J/(sm°C)

Fig. 3.8 shows the obtained temperature contour and the computed stresses after 5 s, 30 s and 400 s in case of $a/W = 0.3$ and $\zeta = 45°$. The temperature discontinuities at the crack surface and the stress concentrations at the crack tips can be obviously observed.

To investigate the transient stress state at the crack tip, the SIFs are computed from the displacement and stress solutions at the post-processing stage at each time step. The obtained SIFs at the transient state are normalized by:

$$F_{I,II} = \frac{K_{I,II}}{\beta_T T_0 \, (W/L) \, E_m \sqrt{2W}} \tag{3.55}$$

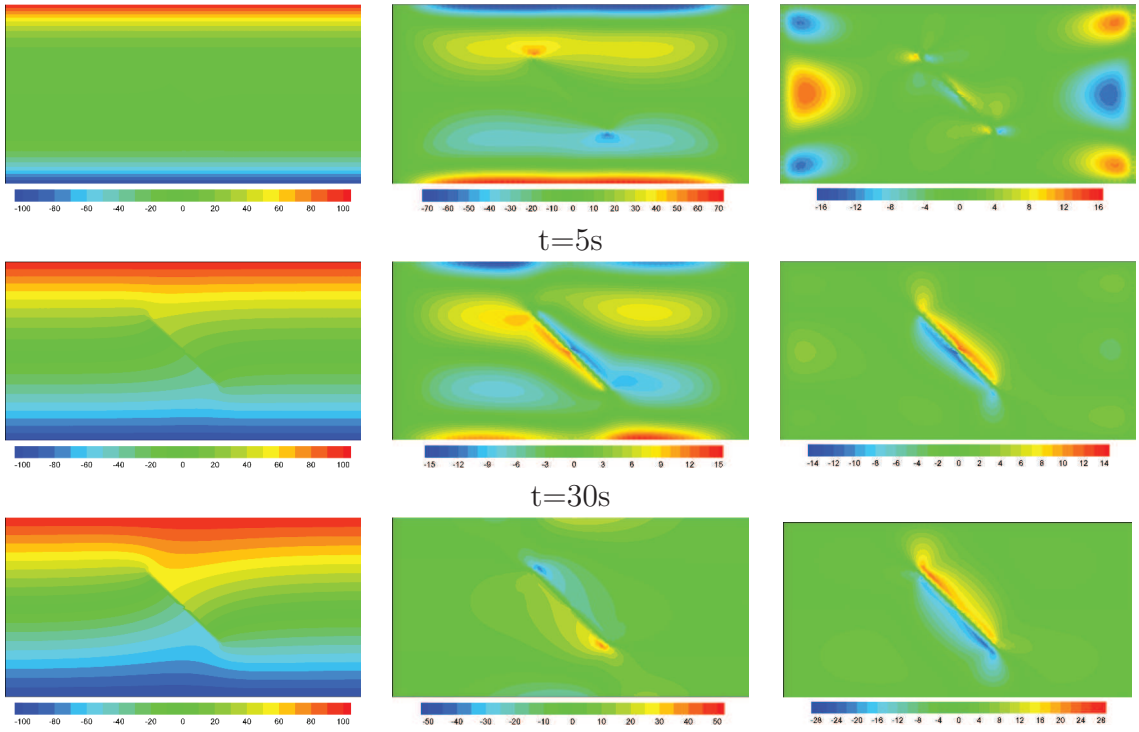

Figure 3.8.: Temperature and Stress fields at different simulation time ($a/W = 0.3$, $\zeta = 45°$)

where T_0 is the prescribed temperature on the boundary of the plate, $F_{I,II}$ the normalized SIFs for mode I and mode II. The curves of Fig. 3.9 illustrate the evolution of the normalized SIFs as a function of time for different crack lengths while the curves of Fig. 3.10 show their evolution for different crack angles. The figures show that the in some cases, the SIFs may have maximum values before reaching the steady state. For example, in the case of $a/W = 0.3$ and $\zeta = 90°$, the value of F_I is big at the beginning of the simulation (time $<$ 30s) and becomes zero at the steady state (time $>$ 100s), see Fig. 3.10 (a). Another important remark can be raised concerning the negative F_{II} at the beginning of simulations, see Fig. 3.9 (b) and Fig. 3.10 (b). Note that, both F_I and F_{II} undergo a significant change before converging to their steady state values. Therefore, crack nucleation and growth criteria needs to take into account this evolution of SIFs.

To further verify the accuracy of the proposed XFEM-based thermo-mechanical model,

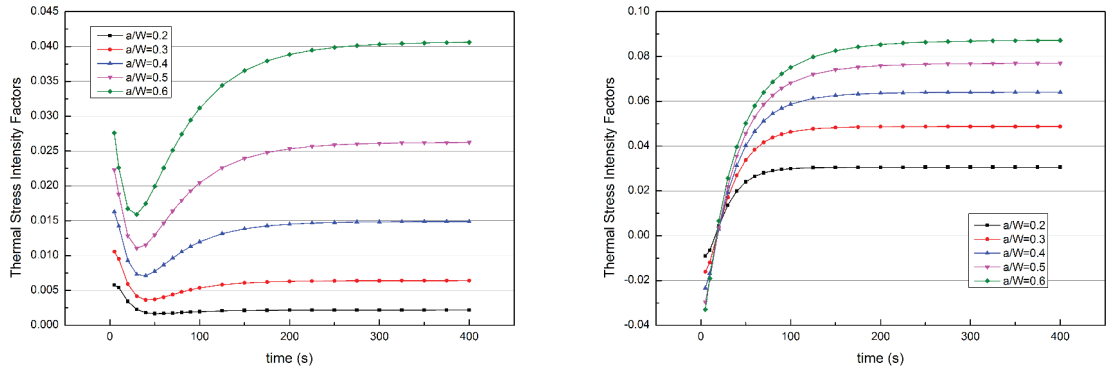

(a) F_I (b) F_{II}

Figure 3.9.: Normalized SIF evolution from the transient to the steady state for $\zeta = 30°$ and various a/W

the obtained normalized SIFs at the steady state are compared with those published in Duflot (2008), Murakami et al. (1987) and Prasad et al. (1994a). Tab. 3.4 summarizes the obtained F_I and F_{II} at the steady state for various crack lengths and a crack angle equals to 30°. Whereas Tab. 3.5 summarizes the obtained F_I and F_{II} at the steady state from present study, and those from literature for different crack angles and a crack length of $a/W = 0.3$. The obtained results are in good agreement with the ones from the literature once the steady state is reached.

Table 3.4.: Normalized SIFs for the inclined adiabatic crack, $\zeta = 30°$ and various a/W

	F_I				F_{II}			
a/W	This study	Duflot (2008)	Prasad (1994)	Murakami (1987)	This study	Duflot (2008)	Prasad (1994)	Murakami (1987)
0.2	0.0022	0.0020	0.002	0.002	0.0306	0.0302	0.030	0.030
0.3	0.0064	0.0068	0.006	0.008	0.0488	0.0489	0.048	0.048
0.4	0.0149	0.0149	0.014	0.015	0.0641	0.0650	0.064	0.064
0.5	0.0262	0.0265	0.026	0.027	0.0769	0.0774	0.076	0.076
0.6	0.0406	0.0407	0.040	0.041	0.0872	0.0878	0.087	0.086

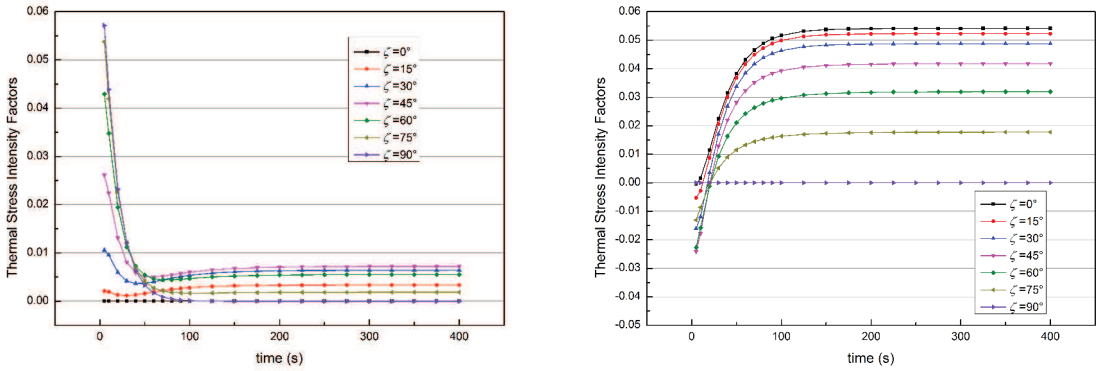

(a) F_I (b) F_{II}

Figure 3.10.: Normalized SIF evolution from the transient to the steady state for $a/W = 0.3$ and various crack angles ζ

Table 3.5.: Normalized SIFs for the inclined adiabatic crack, $a/W = 0.3$ and various ζ

	F_I				F_{II}			
ζ	This study	Duflot (2008)	Prasad (1994)	Murakami (1987)	This study	Duflot (2008)	Prasad (1994)	Murakami (1987)
0°	0.0000	0.0000	0.0000	0.0000	0.0541	0.0546	0.054	0.054
15°	0.0034	0.0038	0.0036	0.0038	0.0523	0.0533	0.054	0.054
30°	0.0064	0.0068	0.0064	0.0071	0.0488	0.0489	0.048	0.048
45°	0.0072	0.0076	0.0071	0.0077	0.0418	0.0420	0.041	0.042
60°	0.0055	0.0054	0.0049	0.0053	0.0319	0.0322	0.032	0.032
75°	0.0018	0.0017	0.0010	0.0023	0.0178	0.0180	0.018	0.018
90°	0.0000	0.0000	0.0003	0.0000	0.0000	0.0000	0.000	0.000

3.5.3. Fluid Flow and Heat Transfer in Cracked Porous Media

In this example, the transient fluid flow and heat transfer equations are coupled to the thermo-mechanical problem to investigate the effect of the presence of crack on temperature and stress distributions in an isotropic porous media. The material properties and boundary conditions are reported in Tab. 3.1, Tab. 3.2 and Tab. 3.3. The domain of simulation is taken rectangular with dimensions 2.0×1.0 m^2. A crack of thickness 0.01 m and length 0.6 m is introduced at the center of the rectangular plate. Simulations are conducted for different crack angles ζ varying clockwise from 0° to 90° with a step of 15°.

In Fig. 3.11, the distributions of pressure, temperature and stress in the horizontal direction for $\zeta = 60°$ are reported at 5 s, 50 s and 400 s. One can clearly notice that the crack affects significantly the distributions of stress and temperature over the domain.

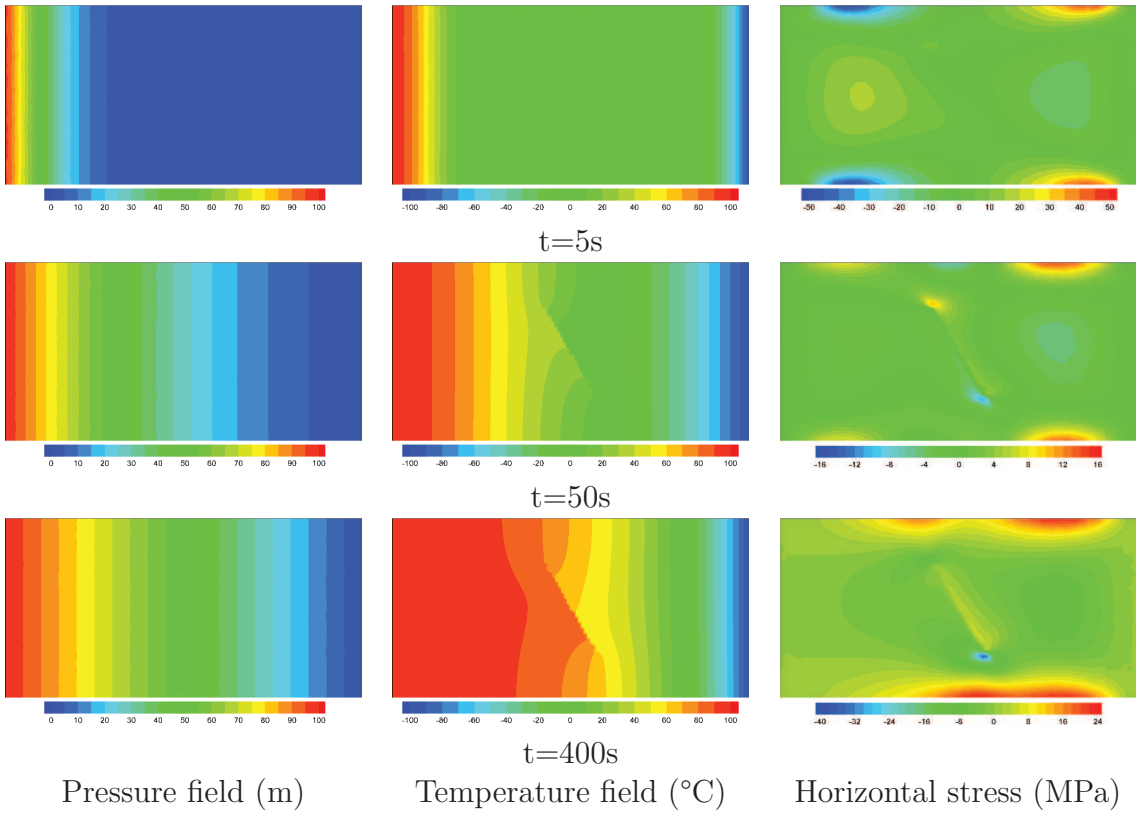

Figure 3.11.: Pressure, temperature and stress field contours at different simulation time for $\zeta = 60°$

To further investigate the influence of crack on heat transfer, four points A1, A2, A3 and A4 are selected as shown in Fig. 3.5. The evolution of temperature at the selected points is plotted in Fig. 3.12 (a), (b), (c), and (d) for various crack angles. Since there is no heat flux from the solid phase on the crack surface, the crack prevents the heat conduction in the solid skeleton. As a result, the temperature increases at points A1 and A2 (left of the crack, see Fig. 3.12 (a) and (b)) and decreases at points A3 and A4 (right of the crack, see Fig. 3.12 (c) and (d)) with the increasing of the crack angle. When the crack becomes horizontal ($\zeta = 0°$), the temperature evolution is almost identical to that obtained from the domain without crack (see Fig. 3.12).

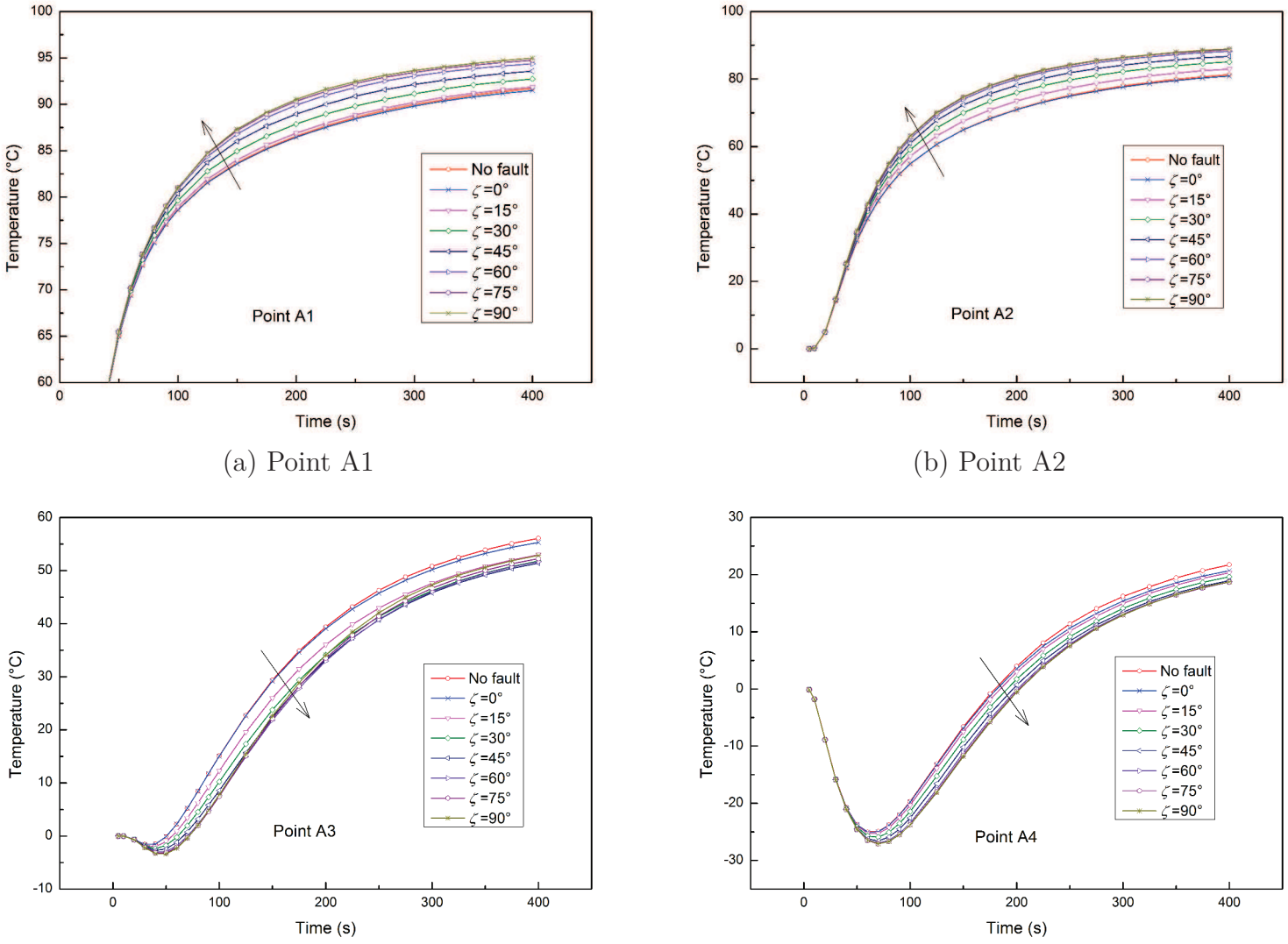

(a) Point A1

(b) Point A2

(c) Point A3

(d) Point A4

Figure 3.12.: The evolution of the temperature for various crack angles at different points

Finally, the thermal SIFs are computed at each time step for both of the crack tips and normalized by equation Eq. (3.55). The first crack tip (crack-tip1) is considered to be on the left while the second is on the right (crack-tip2). The results are illustrated for the two crack-tips in Fig. 3.13 (a), (b), (c) and (d) at various crack angles. The evolution of SIFs is linked to the gradient of the temperature. The amplitude of the SIFs follows the moving wave of the transported temperature. It reaches a peak before attaining a plateau which corresponds to the steady state.

3.6. Conclusions

Fluid flow, heat transfer and thermo-mechanical problems are coupled to study the effect of fluid flow and heat transfer in cracked isotropic porous media at the transient state using the Darcy-XFEM model. The nonconforming FEM is used to solve the Darcy's flow. The heat transfer equation in the cracked porous medium is solved with a FEM/XFEM scheme using a time splitting procedure. With this model, the mesh has to be adapted to the thickness of the crack which can be discretized with a single element. The FEM scheme is based on the DG and MPFA methods for the solution of the advection and dispersion fluid heat transfer. The XFEM is used to better handle the influence of cracks on solid heat transfer. The thermo-mechanical problem is solved using the XFEM and the SIFs are calculated with the interaction integral technique. All these advanced methods are implemented and solved sequentially in the same time step. After some numerical applications, several conclusions have been raised:

1. Time splitting allows to solve heat transfer in two steps and therefore to use different numerical techniques while maintaining the accuracy of the results.
2. Good agreement is found when comparing the calculated SIFs with the existing results of the steady state in the literature.
3. The computation of the SIFs in the transient state reveals that they can be maximum or negative before the steady state. This can be crucial to decide whether the crack would propagate or not and in which direction.
4. The crack angle influences significantly the temperature distribution and stress concentration in all cases but the crack length influences them in some cases only

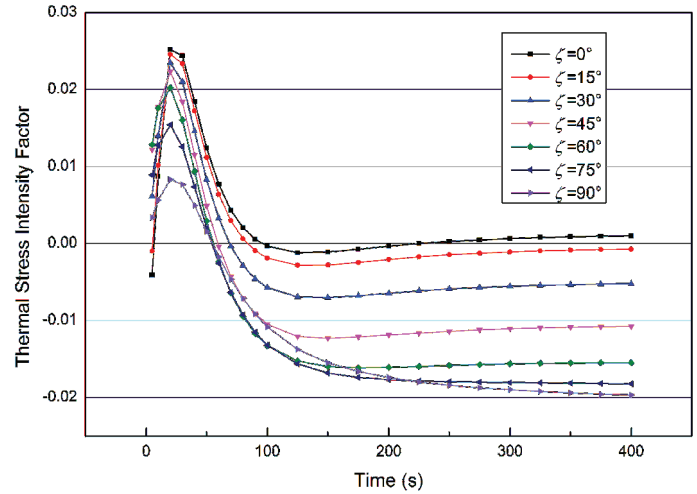

(a) F_I for crack-tip1

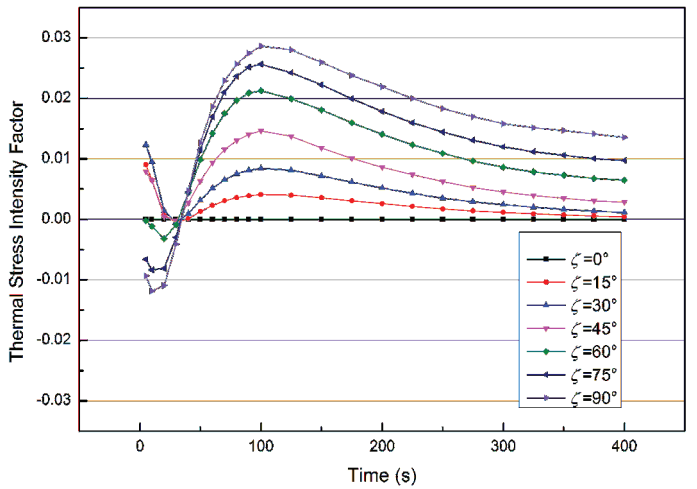

(b) F_{II} for crack-tip1

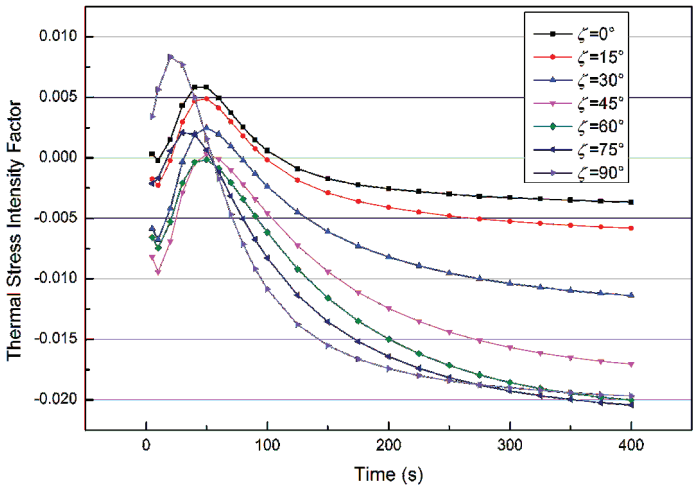

(c) F_I for crack-tip2

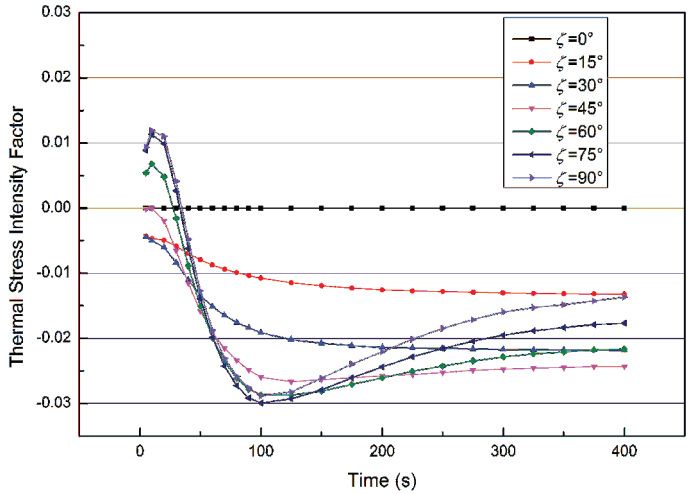

(d) F_{II} for crack-tip2

Figure 3.13.: Normalized SIF variations with time for various crack angle ζ

(when the angle is not null).

5. The SIFs are influenced directly by the temperature gradient which is varying with time. This could explain the peak in their amplitude before reaching a constant value corresponding to the steady state.

After these parametric studies, it is found that the combination of these advanced numerical methods can model accurately the transient fluid flow and heat transfer which allows studying the thermo-mechanical behavior of cracked porous media. The introduction of the XFEM to enrich the temperature field and then the displacement field near discontinuities and singularities could increase significantly the accuracy and be very useful when the crack grows.

4. Crack Propagation in Solid Dense/Porous Multilayered Structure: Application to SOFC

4.1. Introduction

A planar Solid Oxide Fuel Cell (SOFC) unit consists of a solid dense gas-tight electrolyte sandwiched between two porous electrodes (anode and cathode) that present sufficient porosity to allow for the flow of air and fuel into the porous electrodes through flow channels. The major drawback of this technology is the high operating temperature that can lead to complex material problems, including residual stresses due to different thermal expansion coefficients of the unit cell components (Yakabe et al., 2004). The cooling and heating process, involved during SOFC service, result in residual stresses and possible crack nucleation and propagation in the porous electrodes (Qu et al., 2006).

In the last decade, crack propagation has become the center of interest of lot of studies where advanced numerical methods such as mesh-less methods and the eXtended Finite Element Method (XFEM) are widely used, see Moës and Belytschko (2002); Zi and Belytschko (2003); Sukumar and Prévost (2003); Duflot (2008); Natarajan et al. (2014); Bordas et al. (2011); Fries and Belytschko (2010); Bouhala et al. (2012). The main feature of XFEM is the enrichment of the fields and/or their gradients in the vicinity of singularities and discontinuities. This allows the use of a non-conforming mesh and avoids re-meshing when cracks grow. Studies of crack growth under pure mechanical loads are reported for instance in Moës et al. (1999); Bouhala et al. (2010), to site only few. Crack growth under thermal and thermo-mechanical loading is introduced

for instance in Duflot (2008); Bouhala et al. (2012) using the XFEM and the eXtended Free Element Galerkin method (XFEG), respectively. Interaction of crack growth with an interface and crack growth along an interface in bi-material structures are studied in Bae and Krishnaswamy (2001); Bhatnagar et al. (2010); Sukumar et al. (2004); Bouhala et al. (2013). Further, XFEM is used to model interfaces between different materials by using appropriate enrichment functions that guaranty the continuity of fields (such as temperature and displacement) and discontinuity of their gradients (heat flux and stresses) (Belytschko et al., 2001; Moës et al., 2003).

In the previous chapter (Chapter 3), we modeled the response of a cracked porous media under multi-physics loading by using FEM/XFEM. The study was limited to a porous medium with static cracks, where the fluid flow was described by Darcy's equation. The present chapter (Chapter 4) is devoted to crack propagation in porous material layer located between a flow channel and dense materials layer (see Fig. 4.1). This structural staking (flow channel/porous layer/dense layer) is typical to the SOFC technology, where the fluid (air and fuel) enters the multilayered structure, with constant flow rate and temperature, through the flow channel then diffuses into the porous layer. In this chapter, the influence of heat transfer, fluid flow and material properties on crack propagation in the SOFC-like multilayered porous materials is investigated, where the porous SOFC electrodes microstructures are taken isotropic.

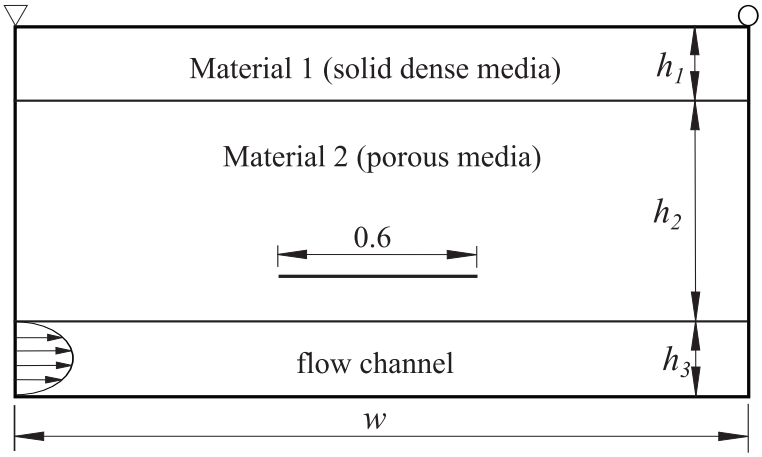

Figure 4.1.: A three-layered half structure with an internal crack

This work is a continuation of the study introduced in Chapter 3, the novelty here lies in the modeling of a multilayered structure with the resolution of the Navier-Stokes and Darcy-Brinkman equations which provide distributions of pressure and velocity in the flow channels and porous media respectively. In addition, the possibility of crack propagation can be triggered by the complex multi-physics loading. Indeed, this study deals with the fluid flow and heat transfer effects on the crack propagation during the transient regime. The crack propagation path is tracked and studied under different scenarii. The XFEM is introduced to solve the thermo-mechanical problem within the porous media (solid phase) in order to avoid re-meshing when the crack propagates and also to enhance the accuracy by adopting the partition of unity principle.

This chapter is organized as follows: Section 4.2 is devoted to the governing equations and solving procedures of the coupled multi-physics problem. In Sections 4.3, the effective thermal and mechanical properties of the porous material are computed using statistical continuum theory (existing code) and experimental data conducted for this purpose. In Section 4.4, the multi-physics model is validated, then used to investigate effects of fluid flow and heat transfer on crack propagation in SOFC like multi-layered material. Finally, some concluding remarks are drawn in Section 4.5.

4.2. Problem Formulation

A DB-XFEM model described in Chapter 2 and Chapter 3, is used here to solve the fluid flow, heat transfer, thermo-mechanical response and crack propagation in the multilayered structure. The pursued methodology is summarized as follows:

- Navier-Stokes and Darcy-Brinkman equations are solved respectively in the flow channel and in the porous media using the nonconforming Crouzeix-Raviart method.
- The heat transfer is split into two equations and then solved with different numerical methods: one is calculated with a combination of DG and MPFA methods, the other is solved with XFEM to take into account the impact of cracks.
- Using the temperature field resulted from the heat transport equation as a body force, the thermo-mechanical problem in the multilayered structure is solved with the XFEM.

- The stress intensity factors (SIFs) are calculated for each step to decide whether the crack propagates or not.
- The maximum principal stress criterion is used to determine crack propagation orientation (crack propagation path).

4.2.1. Governing Equations

The fluid flow in the channel and the porous media are described by Navier-Stokes and Darcy-Brinkman equations, respectively. the fluid flow in the porous layer, governed by Darcy-Brinkman Eq. (2.3), is discretized with the nonconforming Crouzeix-Raviart (CR) finite element method, as mentioned in Chapter 2. While, the Navier-Stokes equation, which is used to simulate the free flow in the channel, can be derived from the Darcy-Brinkman equation by taking the parameters $\varepsilon = 1.0$ and $K \to \infty$ (see Chapter 2, Section 2.2, 2.3). Therefore, the same equation (Darcy-Brinkman) and method can be used to deal with the fluid flow in both the flow channel and the porous media.

Due to the small opening of the crack in the brittle material, the crack is assumed to affect the heat diffusion within the porous layer. A combination of DG, MPFA and XFEM methods is used to solve the advection-diffusion heat transfer equation in the flow channel and in the porous material to better handle the influence of cracks. The XFEM is also used to solve the thermo-mechanical problem and to track the crack propagation. The governing equations and discretizations of fluid flow, heat transfer and thermo-mechanical problem are detailed in Chapter 2 and Chapter 3.

The multi-physics model is implemented for the transient regime. In the post processing stage, the SIFs are calculated for each time step by using the J-integral technique (See Chapter 3, Section 3.3.4). Once the SIFs are computed, the crack orientation angle can be deduced using the maximum principal hoop stress by solving the equation: $\tau_{r\vartheta} = 0$, where $\tau_{r\vartheta}$ is the shear stress derived from the asymptotic displacement expression at the crack-tip

$$\tau_{r\vartheta} = \frac{1}{\sqrt{2\pi r}} \cos\left(\frac{\vartheta}{2}\right)\left(\frac{1}{2}K_I \sin\vartheta + \frac{1}{2}K_{II}\left(3\cos\vartheta - 1\right)\right) = 0 \tag{4.1}$$

Then, the crack growth direction ϑ_p is given by:

$$\vartheta_p = 2 \arctan \left(\frac{K_I \pm \sqrt{K_I^2 + 8K_{II}^2}}{4K_{II}} \right) \tag{4.2}$$

The initial existing crack is considered to grow instantaneously once the equivalent SIF (K_{Ieq}) overcomes the material toughness (K_{Ic}). The equivalent stress intensity factor is given by

$$K_{Ieq} = K_I \cos^2 \left(\frac{\vartheta_p}{2} \right) - 3K_{II} \cos^2 \left(\frac{\vartheta_p}{2} \right) \sin \left(\frac{\vartheta_p}{2} \right) \tag{4.3}$$

4.2.2. Solving Procedures

In this multi-physics problem, the fluid flow, heat transfer, thermo-mechanical response as well as the crack propagation are coupled and solved sequentially at each time step, which allows the use of different temporal discretization and therefore, allows achieving high accuracy for each equation. In this work, the flow system Eq. (2.2) and Eq. (2.3) is solved using an implicit time discretization whereas an explicit time discretization is preferred for the advective part of the heat Eq. (3.11). The unknowns are progressed from the time increment t_n to t_{n+1} as follows:

Step 1: Darcy-Brinkman Eq. (2.3) is solved and fluid flow velocity for the current time step $\mathbf{v}^{n+1}$ is obtained.

Step 2: The heat transfer Eq. (3.11) is solved using the flow velocity $\mathbf{v}^{n+1}$ to get $T^{n+1,*}$.

Step 3: The thermal conductivity in the solid phase is updated: $(\mathbf{k}^s)^{n+1} = F\left(T^n\right)$ (the updating function is fitted from experimental results).

Step 4: The heat transfer Eq. (3.12) is computed with the presence of cracks using $T^{n+1,*}$ as the initial temperature field and $(\mathbf{k}^s)^{n+1}$ as the thermal conductivity, then the final temperature at the current time step T^{n+1} is obtained.

Step 5: The temperature T^{n+1} is injected as a body force in the thermal-mechanical problem Eq. (3.9) then the displacements, stresses, stress intensity factors as well as the direction of crack propagation are calculated.

Step 6: The equivalent SIF K_{Ieq} is compared with the fracture toughness K_{Ic} to decide whether the crack propagates or not. If the crack criterion is not satisfied $K_{Ieq} < K_{Ic}$, go back to step 1 and start a new cycle from t_{n+1} to t_{n+2}. If the crack propagation criterion is satisfied then go to step 7.

Step 7: The crack is extended by one increment along the growing direction computed in step 5.

Step 8: The step 5 and step 7 are repeated until the threshold number of crack extension increments is reached.

4.3. Effective Properties of SOFC Components

Before investigating fluid flow and heat transfer effects on crack growth in the SOFC unit, the effective thermal and mechanical properties of the SOFC components are determined. To this aim experiments are conducted to measure the thermal and mechanical properties of the SOFC components dense material then a homogenization method is used to derive the effective properties of the corresponding porous anode and cathode materials.

Solid dense electrolyte thermal and mechanical properties are measured directly on prepared electrolyte specimens. However, due to the difficulty preparing porous samples with the required dimensions for the measurement equipment, the cathode and the anode electrodes properties are estimated using a homogenization method.

4.3.1. Experiments of Solid Dense Materials

Within a collaboration project between LIST and La Laguna University, the experiments are conducted by R. Fernández-González (PhD student) and Professor Núñez from La Laguna University, Spain. Commercially available chemicals are used to prepare solid dense specimens from SOFC electrodes: electrolyte, cathode and anode. For preparing electrolyte specimens, YSZ powder TZ8YS (8 mol % Y_2O_3, Tosoh, Tokyo, Japan) with an average particle size of ~1.3 μm was used. In order to fabricate the cathode specimens $La_{0.6}Sr_{0.4}Co_{0.2}Fe_{0.8}O_3$, LSCF (Fuel cell materials, Ohio, OH, USA) with an average particle size of ~1 μm was utilized. And for the anode specimens, a handled mix of 30 wt% of NiO (Sigma-Aldrich, St. Louis, MO, USA) with an average particle size of ~44 μm, and 70 wt% of TZ8YS was used for making the pellets.

Cylindrical shaped specimens with specific sizes are prepared for the measurement of the thermal diffusivity, thermal expansion, density and Young's modulus. Due to the sample size requirement for each used measurement's equipment, specifically for the thermal diffusivity and thermal expansion, dies with different size are used. For instance the measurement of diffusivity requires specimens with a diameter between 7.3 and 8.2 mm and a height between 2 and 3 mm. To this end uniaxial die with 10 mm diameter is used and the specimens are pressed twice during 30 seconds at 1 metric ton. Regarding the measurement of the thermal expansion, the used cylindrical specimens should be less than 12 mm diameter with a length between 20 and 25 mm. This was achieved by using an isotactic press, where the specimen is pressed during 10 min at 7.5 metric ton.

The different obtained specimens were calcined at high temperatures to obtain well sintered samples: the electrolyte was heated for 2 hours at 1500 °C, the cathode was heated for 3 hours at 1250 °C and the anode was heated for 2 hours at 1400 °C.

The Young's modulus is deduced from Dynamic mechanical analysis (DMA) measurements conducted on a DMA242C apparatus. Since the Young's moduli of the studied materials are relatively not sensitive to the temperature variation, the DMA measurements are conducted at room temperature and assumed independent of the temperature. The measured Young's moduli of the three SOFC materials are summarized in Tab. 4.1.

Regarding the thermal properties, the measurements were performed in a range of 200 °C between 1000 °C and 200 °C. The thermal conductivity is deduced from the measured

Table 4.1.: SOFC electrode mechanical properties

Electrode	Electrolyte	Cathode	Anode
Young's Modulus (MPa)	3530	1680	2448

thermal diffusivity $\alpha(T)$, specific heat $c(T)$ and bulk density $\rho(T)$ according to the following equation $k_s(T) = \rho(T)\, c(T)\, \alpha(T)$. The thermal diffusivity of the sintered specimens was measured by a LFA 457 laser flash thermal diffusivity apparatus. The thermal expansion coefficient was obtained thanks to a DIL 402 C dilatometer. The specific heat capacity was acquired thanks to the differential scanning calorimetry of a DSC F1 Phoenix calorimeter. All the instruments were supplied by Netzch Group, Germany.

The measured thermal properties versus the temperature are summarized in Tab. 4.2 for the electrolyte, cathode and anode.

4.3.2. Effective Thermal and Mechanical Properties

The effective thermal expansion coefficient of ceramic porous material is independent of the pores volume fraction variation and remains equal to the one of the ceramic matrix (Boey and Tok, 2003; Tummala and Friedberg, 1970a;b). Therefore, cathode and anode effective thermal expansion coefficients are taken equal to those measured from their corresponding matrices (see Tab. 4.2).

However, the effective mechanical properties and the effective thermal conductivity of porous materials depend on the pores volume fraction, and can be estimated using homogenization methods appropriate for composite materials with a strong-contrast between the individual properties of its constituents (Koutsawa et al., 2011; Mikdam et al., 2013a;b; Azoti et al., 2013).

To this aim, the effective thermal conductivities and mechanical properties of the anode and cathode porous materials are calculated using the strong-contrast version of the statistical continuum theory (Torquato, 2002). The porous material is assumed to be isotropic and represented by micrographs (Fig. 4.2) with different pores volume fraction ($\varepsilon = 0.2,\ 0.3,\ 0.4$ and 0.5) which are computer-generated using a statistical continuum theory based algorithm (Mikdam et al., 2013a). Within the statistical continuum theory,

Table 4.2.: Thermal properties versus the temperature of SOFC dense materials

Electrode	T(°C)	Specific heat J/(g.°C)	Diffusivity mm^2/s	Density g/cm^3	Conductivity W/(m°C)
Electrolyte	200	0.55	0.52	5.84	1.67
	400	0.57	0.49	5.80	1.62
	600	0.57	0.47	5.73	1.53
	800	0.59	0.46	5.69	1.55
	1000	0.61	0.43	5.65	1.47
	Measured thermal expansion coefficient [200 °C-1000 °C] $= 11.5 \times 10^{-6}$/°C				
Cathode	200	0.55	0.55	6.12	1.84
	400	0.59	0.58	6.05	2.08
	600	0.60	0.64	5.99	2.29
	800	0.66	0.60	5.68	2.26
	1000	0.70	0.51	5.56	1.99
	Measured thermal expansion coefficient [200 °C-600 °C] $= 18.0 \times 10^{-6}$/°C [600 °C-1000 °C] $= 37.7 \times 10^{-6}$/°C				
Anode	200	0.60	0.96	1.45	0.84
	400	0.65	0.84	1.44	0.78
	600	0.66	0.75	1.43	0.71
	800	0.62	0.69	1.42	0.60
	1000	0.55	0.64	1.41	0.49
	Measured thermal expansion coefficient [200 °C-1000 °C] $= 12.7 \times 10^{-6}$/°C				

the microstructure morphology (Fig. 4.2) of the porous materials is represented by statistical correlation functions that take into account the shape, orientation and distribution of pores. The details on mathematical formulation of the effective properties are discussed in Mikdam et al. (2009; 2013a).

The calculated isotropic effective conductivity for cathode and anode are reported in Tab. 4.3, respectively. Regarding the mechanical properties, the cathode and anode dense matrix Young's modulus (see Tab. 4.1) are combined with a Poisson coefficient of $\nu = 0.32$ (Selcuk and Atkinson, 1997) to compute the effective shear modulus and bulk modulus, which are summarized in Tab. 4.4 as functions of the pores volume fraction.

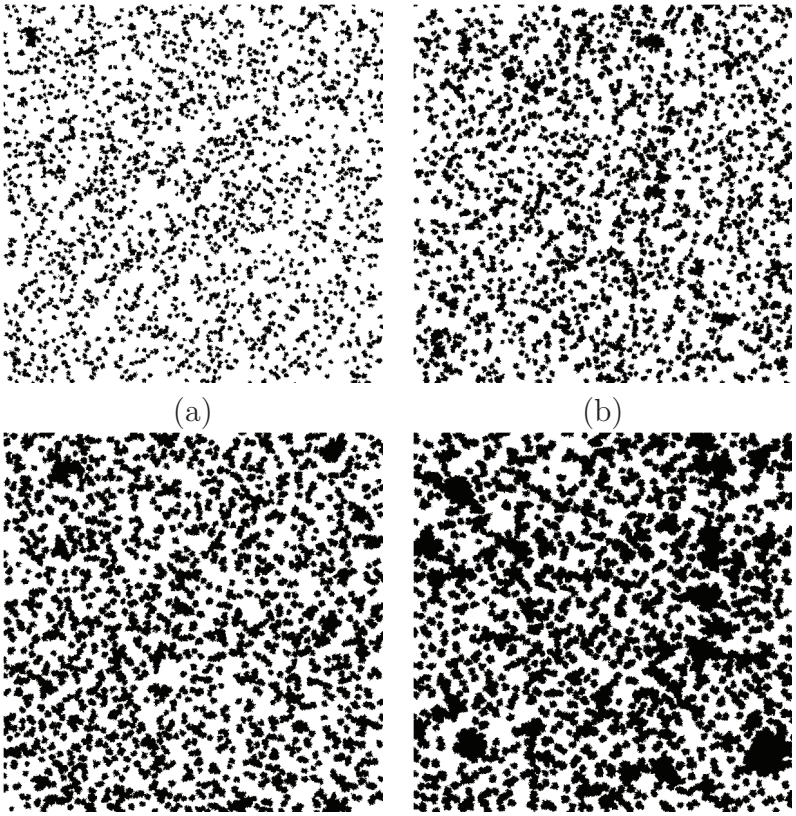

Figure 4.2.: Micrographs of a porous (heterogeneous) material with different pores volume fraction (black phase): (a) $\varepsilon = 0.2$; (b) $\varepsilon = 0.3$; (c) $\varepsilon = 0.4$; (d) $\varepsilon = 0.5$

4.4. Numerical Results

4.4.1. Validation of the Crack Propagation under Thermal Loading

Before using the developed mathematical model to investigate crack propagation in a SOFC multi-layered structure, a validation is required to study the accuracy and stability of the model. Due to the difficulty finding benchmark examples in literature to validate the whole model, a partial validation is conducted. Part of the validations have already been done in Chapter 2 (see Chapter 2, Section 2.4) and Chapter 3 (see Chapter 3, Section 3.4.1 and 3.4.2) regarding the thermo-fluid coupling problem and the thermo-mechanical problem, where the calculated SIFs for a static crack are compared to those found in the literature. In this section crack propagation under thermo-mechanical loading is validated

Table 4.3.: Effective thermal conductivity of SOFC components

Electrode	T(°C)	Dense matrix W/(m°C)	k_e at 20% of pores W/(m°C)	k_e at 30% of pores W/(m°C)	k_e at 40% of pores W/(m°C)	k_e at 50% of pores W/(m°C)
Cathode	200	1.84	1.3229	1.1065	0.9082	0.7263
	400	2.08	1.4953	1.2508	1.0269	0.8211
	600	2.29	1.6463	1.3771	1.1305	0.9039
	800	2.26	1.6247	1.3591	1.1157	0.8921
	1000	1.99	1.4306	1.1967	0.9824	0.7855
Anode	200	0.84	0.6039	0.5051	0.4149	0.3316
	400	0.78	0.5607	0.4690	0.3851	0.3079
	600	0.71	0.5104	0.4269	0.3505	0.2803
	800	0.60	0.4313	0.3608	0.2962	0.2368
	1000	0.49	0.3522	0.2946	0.2419	0.1934

Table 4.4.: Effective mechanical properties of SOFC components

Electrode	Shear modulus (MPa)	Bulk modulus (MPa)	Pores volume fraction
Anode	585.451	1062.171	20%
	458.755	747.256	30%
	352.346	521.945	40%
	264.326	363.951	50%
Cathode	401.780	728.941	20%
	314.832	512.823	30%
	241.806	358.197	40%
	181.400	249.770	50%

considering the benchmarking test of the cruciform shaped plate (Prasad et al., 1994b). The geometry of the plate is depicted in Fig. 4.3. The initial crack notch length is set to $a = 0.2L$ and is tilted by 135° from the horizontal axis. The simulation of the crack propagation is conducted for: (1) pure thermal loading; (2) pure mechanical loading and (3) mixed loading. The three boundary condition sets (BC sets) are given in Tab. 4.5.

The domain is discretized with unstructured triangular elements in three different levels: 4188 elements, 7830 elements and 10438 elements. We calculated the heat transfer at the transient regime until the steady state is attained then the crack propagation is tracked. The SIFs are computed using Eq. (3.41) and Eq. (3.43). Then Eq. (4.2) is used

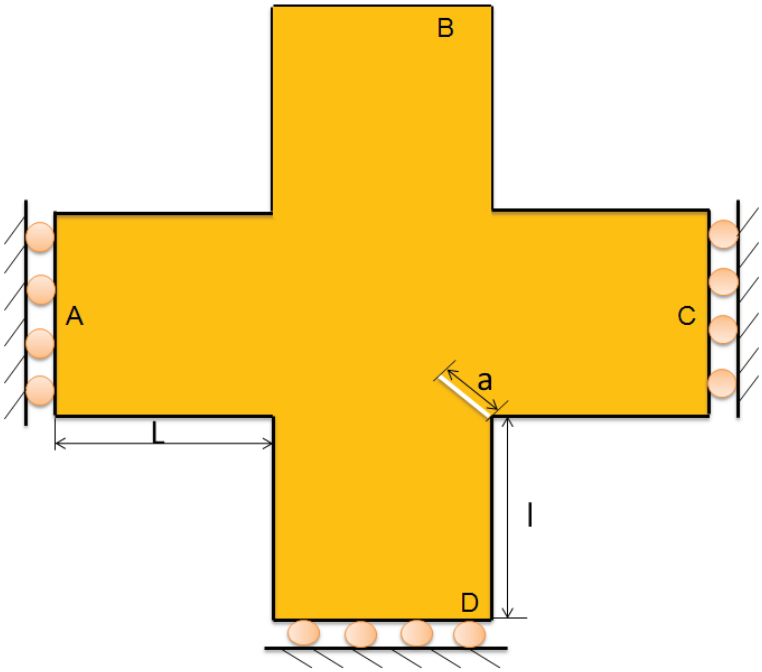

Figure 4.3.: The cruciform shaped plate

Table 4.5.: Boundary condition sets

BC set	Temperature (°C)				Traction (MPa)
	Boundary A	Boundary B	Boundary C	Boundary D	Boundary B
1	0	10	0	-10	0
2	0	0	0	0	10
3	-5	10	-5	-10	10

to determine the crack growth angle at each iteration. Fig. 4.4 shows that the crack changes its propagation direction and moves towards the right side of the plate under pure thermal loading (BC set 1). While under pure mechanical loading (BC set 2), the crack propagates in a completely different direction comparing to the case with BC set 1. The mixed loading leads to a crack propagation path in between of the two former cases, growing to the corner in the diagonal direction of the initial crack. In Fig. 4.4, crack propagation paths at different mesh levels are also plotted, where we can find that the number of elements has little influence on the calculation.

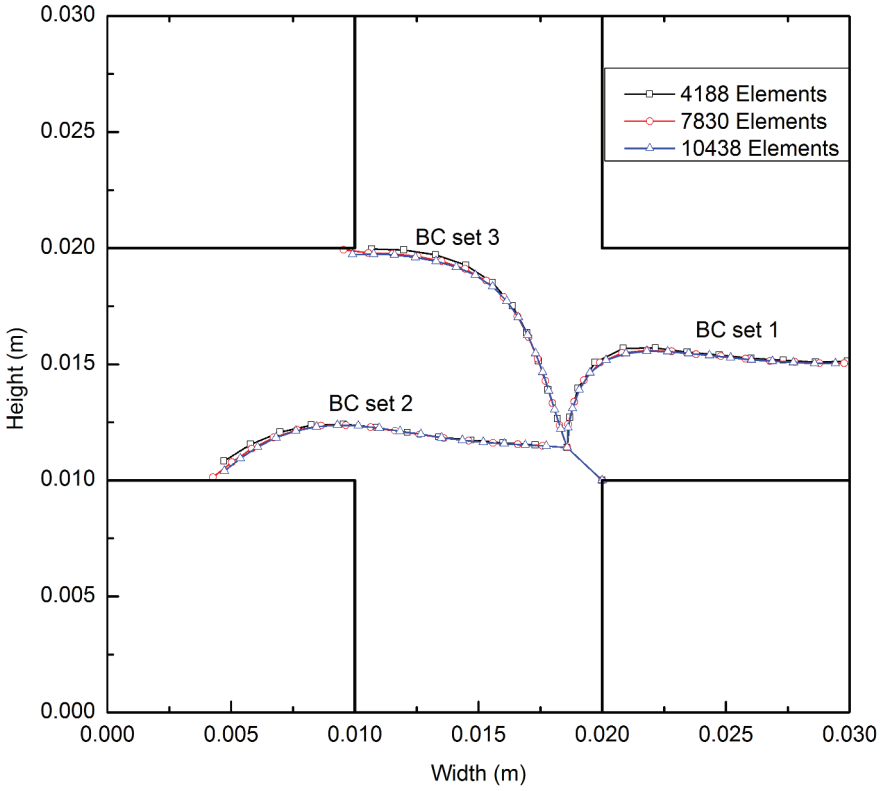

Figure 4.4.: Crack tip positions for three BC sets

Moreover, these crack paths at different BC sets are found in good agreement with those reported in Prasad et al. (1994b), where the authors obtained the fields using the dual boundary element method combined with a general thermo-elastic analysis. The SIFs are also computed in this reference using the J-integral technique and the maximum principal stress is used as the crack propagation criterion.

4.4.2. Application to Planar SOFC Multi-layered Structure

SOFC unit consists of a solid dense electrolyte sandwiched between a porous anode and a porous cathode, with two flow channels adjacent to the porous layers. During the working process of a SOFC unit, the flow enters the multilayered structure through the flow channel, with a constant inflow temperature and flow rate, and then diffuses into the adjacent porous cracked layer (see Fig. 4.5). A horizontal crack of thickness 0.25 mm and

length 6 mm is assumed to locate in the porous cathode. The crack starts to grow when the equivalent SIF overcomes the material toughness. During the propagation, the crack is assumed to keep a constant thickness.

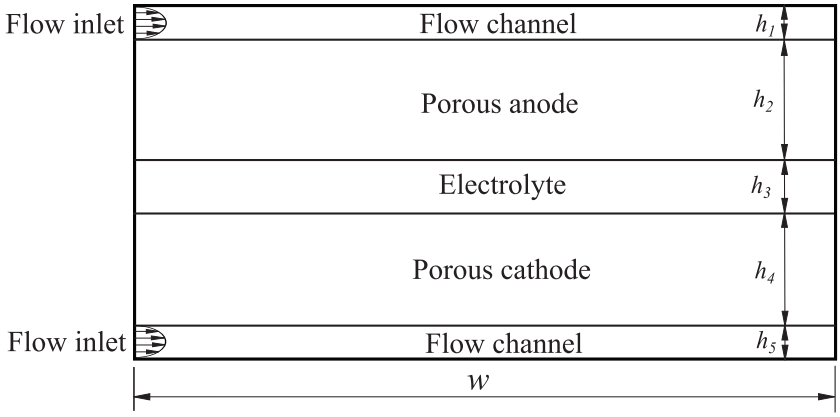

Figure 4.5.: A SOFC unit

The crack propagation path versus the material porosity in the cathode porous layer is investigated for two different fluid inflow configurations. In the first configuration (configuration-1), the air enters into the flow channel adjacent to the cathode from the right side while the fuel enters into the channel adjacent to the anode from the left side, and in the second configuration (configuration-2) both fluids (air and fuel) are assumed to enter the SOFC unit channels from the same side (left side, see Fig. 4.5). The crack is assumed to propagate instantaneously once the equivalent SIF at each crack-tip overcomes the critical one. Note that the toughness of the porous material K_{Ic} is calculated from the toughness of the dense material K_{Ic0} and the porosity ε through the following equation (Joulaee et al., 2007)

$$K_{Ic}(\varepsilon) = K_{Ic0}\left\{\frac{(1-\varepsilon)^2}{1+b_e\varepsilon}\left[1-\pi\left(\frac{3\varepsilon}{4\pi}\right)^{\frac{2}{3}}\right]\right\}^{\frac{1}{2}} \tag{4.4}$$

The onset of the crack propagation is due to residual stresses resulting from the properties' mismatch of the cell components and the spatial variation of the temperature during the heating process (transient state). For both configurations the initial cell temperature is taken equal to 25°C and the temperature at the channels inflow is of 800°C. The

cell components dimensions and the material properties are given in Tab. 4.1, Tab. 4.2, Tab. 4.3, Tab. 4.4, Tab. 4.6, Tab. 4.7.

Table 4.6.: Geometry dimensions and material parameters for SOFC

Width	$w = 20.0$ mm
Height	$h_1 = 1.0$ mm
	$h_2 = 2.0$ mm
	$h_3 = 1.0$ mm
	$h_4 = 5.0$ mm
	$h_5 = 1.0$ mm
Effective porosity of porous media	$\varepsilon = 0.2 \sim 0.5$
Fluid density	$\rho_{air} = 0.3236$ kg/m^3
	$\rho_{fuel} = 0.0224$ kg/m^3
Dynamic viscosity	$\mu_{air} = 3.48 \times 10^{-5}$ Pa.s
	$\mu_{fuel} = 2.65 \times 10^{-5}$ Pa.s
Permeability	$K = 15.13 \times 10^{-12}$ m^2
Volumetric heat capacity	$(\rho C)_{air} = 0.3741 \times 10^3$ J/(m^3°C)
	$(\rho C)_{fuel} = 0.3395 \times 10^3$ J/(m^3°C)
Thermal conductivity	$k_{air} = 0.0692$ J/(sm°C)
	$k_{fuel} = 0.450$ J/(sm°C)
	$k_{electrolyte} = -2.35 \times 10^{-4} \times T + 1.709$ J/(sm°C)
	$k_{cathode} = m_1 T^3 + m_2 T^2 + m_3 T + m_4$ J/(sm°C)
	$k_{anode} = n_1 T^2 + n_2 T + n_3$ J/(sm°C)
Dense material toughness	$K_{Ic0} = 0.022$ MPa.m$^{\frac{1}{2}}$
Toughness parameter	$b_e = 0.46$

Fig. 4.6 shows the crack propagation path corresponding to the configuration-1 for different material porosities of the anode and the cathode. For all considered material porosities, the propagation starts at the crack-tip1 (tip on the left) then followed by the crack-tip2 (tip on the right). Further, the crack propagation onset time increases with the decrease of the porosity. Due to the complex loading induced by the variation of temperature spatial distribution, the crack-tip1 propagates towards the cathode/electrolyte interface while the crack-tip2 propagates towards the free channel/cathode interface. Once close to the cathode/electrolyte interface, the crack deviates because of the mismatch of the mechanical proprieties between the cathode and the electrolyte.

Fig. 4.7 illustrates the displacements, temperature and stress components contours at the end of the simulation for the case where the electrodes porosity is 0.2. The residual

Table 4.7.: Coefficients for thermal conductivities

Porosity		0.2	0.3	0.4	0.5
Cathode	m_1	-2.545×10^{-9}	-2.129×10^{-9}	-1.747×10^{-9}	-1.397×10^{-9}
	m_2	3.052×10^{-6}	2.554×10^{-6}	2.096×10^{-6}	1.675×10^{-6}
	m_3	-4.079×10^{-4}	-3.412×10^{-4}	-2.792×10^{-4}	-2.235×10^{-4}
	m_4	1.323	1.107	0.908	0.726
Anode	n_1	-2.369×10^{-7}	-1.982×10^{-7}	-1.623×10^{-7}	-1.302×10^{-7}
	n_2	-2.481×10^{-5}	-2.066×10^{-5}	-1.760×10^{-5}	-1.354×10^{-5}
	n_3	0.610	0.510	0.419	0.335

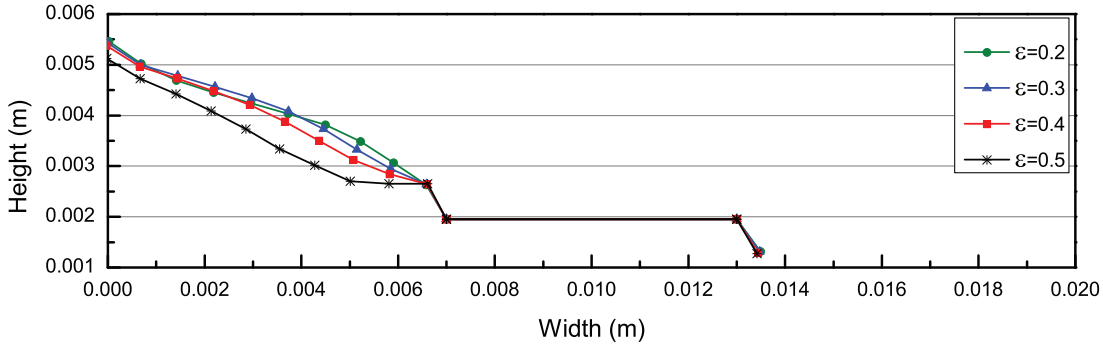

Figure 4.6.: Crack-tip positions corresponding to flow configuration-1, for different porosities

stresses at the vicinity of the electrodes/electrolyte interfaces are higher at the left side of the cell due to the small thickness of anode that allows for higher temperature diffusion. The residual stresses magnitudes vary with the material porosity then in turn affect the crack propagation paths.

For configuration-2, the propagation path of the crack-tip2 (Fig. 4.8) is less affected by the stresses resulting from the mismatch of the thermal expansion coefficient. Therefore, the propagation path variation is more dominated by the mismatch of the mechanical properties between the cathode and the electrolyte (Bouhala et al., 2010).

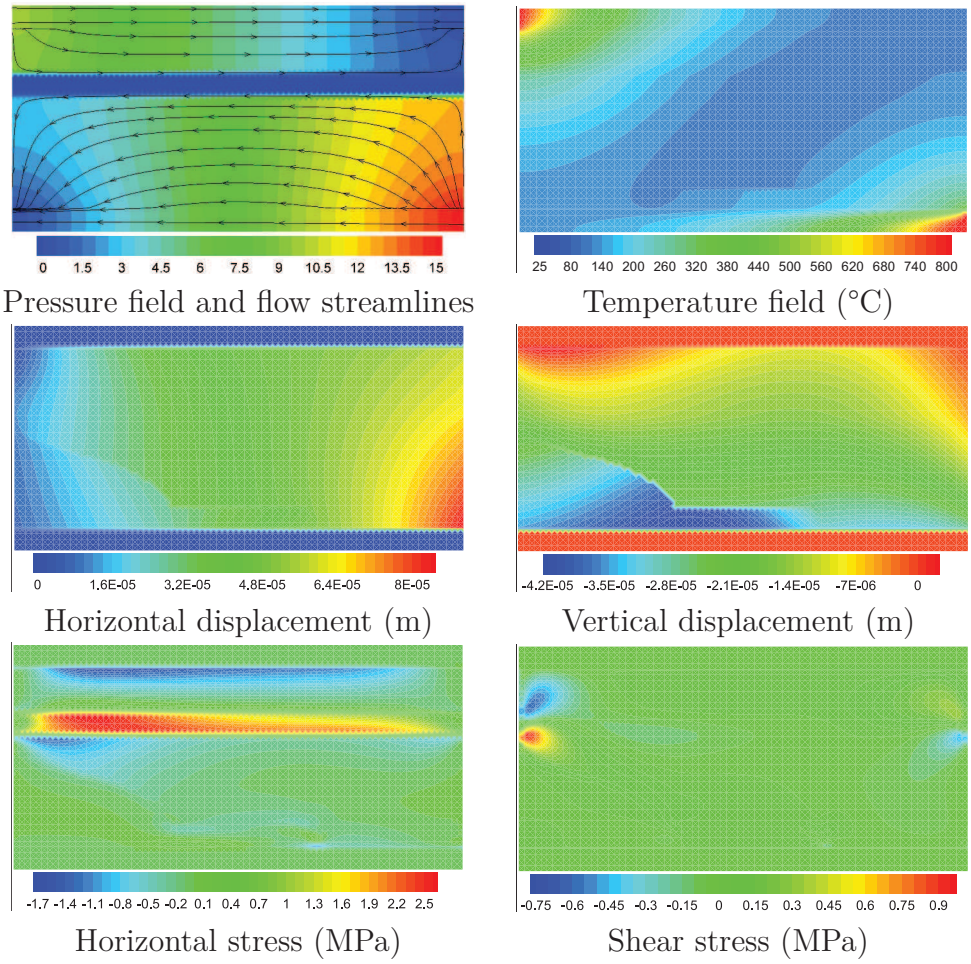

Figure 4.7.: Obtained fields at the end of simulations for configuration-1 and porosity 0.2

4.4.3. Parametric Study

To further investigate the effects of different material parameters on crack propagation, a half SOFC structure made of a flow channel, porous and solid dense materials is considered in the parametric study. The structure contains a horizontal crack of thickness 0.025 mm and length 0.6 mm located in the porous layer. The geometry, dimensions and boundary conditions are reported in Fig. 4.1, while the corresponding material parameters are given in Tab. 4.8. The input flow velocity, within the interval ($x = 0,\ y \in [0,\ 0.2$ mm]), is taken zero in the y direction and follows the equation $v_x = 1000 \times \sqrt{y\,(0.2 - y)}$ mm/s in the x direction. Further the flow enters the channel with a constant temperature $T = 25$°C.

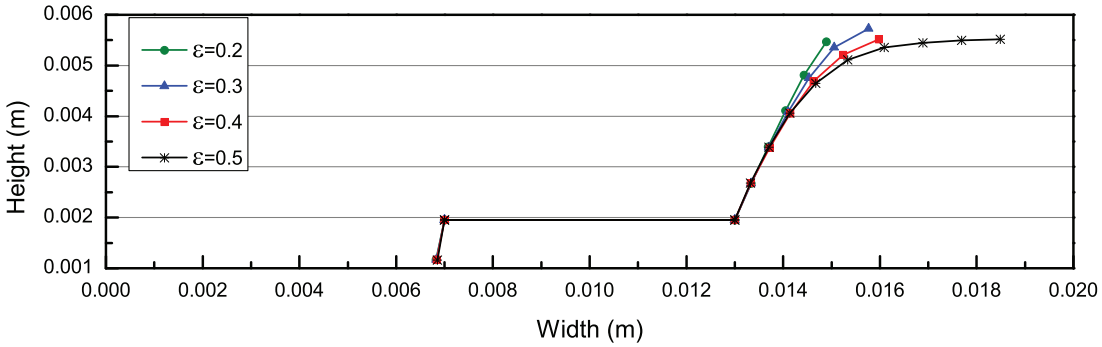

Figure 4.8.: Crack-tip position corresponding to flow configuration-2, for different porosities

Note that, we consider in this parametric study that the material parameters are temperature independent (see Tab. 4.8).

a) - Young's modulus ratio effect: In this test, we restricted the variation of the parameters governing the current problem on the mismatch between Young's modulus of the dense and the porous layers. Fig. 4.9 shows the crack propagation path, the vertical displacement and stress components contours at propagating iteration steps 1, 8 and 15. Note that the crack propagation path is indicated by the enriched elements during crack growth.

The SIFs are calculated at both crack-tips: crack-tip1 on the left side of the crack (see Fig. 4.1) and crack-tip2 on the right side. The thermal load leads to a growth of the crack-tip2 first, and then crack-tip1 starts to grow after the 5th crack propagation step of crack-tip2. The deflection of the crack-tip2 far from the bi-material interface is due to the high mechanical properties of the solid dense material. The interface effect on the crack-tip2 orientation is reported in Fig. 4.10 for different combinations of the dense/porous materials Young's modulus. During the first growth steps, the crack is driven by the developed stress state and does not feel the interface effect until it approaches the interface.

b) - Solid thermal conductivity effect: Another parameter crucial for heat transfer we investigated is the thermal conductivity of the solid, which definitely influences the

Table 4.8.: Geometry dimensions and material parameters

Width	$w = 2.0$ mm
Height	$h_1 = 0.2$ mm
	$h_2 = 0.6$ mm
	$h_3 = 0.2$ mm
Effective porosity of porous media	$\varepsilon = 0.4$
Fluid density	$\rho_f = 1.0 \times 10^3$ kg/m^3
Dynamic viscosity	$\mu = 8.9 \times 10^{-4}$ Pa.s
Permeability	$K_0 = 15.13 \times 10^{-13}$ m^2
Volumetric heat capacity	$(\rho c)_f = 4.2 \times 10^6$ J/(m^3°C)
	$(\rho c)_s = 2.3 \times 10^6$ J/(m^3°C)
Thermal conductivity	$k_f = 0.65$ J/(sm°C)
	$k_s = 1.50$ J/(sm°C)
Young's modulus	$E_{m2} = 7.40 \times 10^4$ MPa
Poisson's ratio	$\nu_1 = \nu_2 = 0.3$
Thermal expansion coefficient	$\beta_T = 1.67 \times 10^{-5}$/°C
Porous material toughness	$K_{Ic} = 0.8$ MPa.mm$^{\frac{1}{2}}$

temperature distribution. Except for the temperature, the impact of thermal conductivity on the rest of the problem, especially on crack propagation is studied here.

The non-linear effect of the solid phase thermal conductivity on the crack propagation path is demonstrated in Fig. 4.11 and Fig. 4.12. The case where $k_s = 1.5$ W/(m°C) and $E_{m1} = E_{m2} \times 50$ MPa (see Fig. 4.10) is taken as a reference then the thermal conductivity is varied to illustrate its effect on the crack propagation path. Fig. 4.11 shows the temperature and the vertical component of the displacement and stress contours for different thermal conductivities ($k_s = 0.5;\ 3.0;\ 5.0$ W/(m°C)). The temperature conduction in the porous material is enhanced by the increase of the thermal conductivity. However due to the presence of crack, the heat flux is blocked at the crack surface, which leads to an increase of the temperature.

Fig. 4.12 shows the shift of the crack propagation path when the solid thermal conductivity changes. Relative to the crack propagation reference curve ($k_s = 1.5$ W/(m°C)), the decrease of the thermal conductivity decreases the temperature diffusion and increases the temperature gradient in the vicinity of the initial crack. More the temperature gradient is high more the amplitude of stresses is high too, which explains the shift of the crack path orientation.

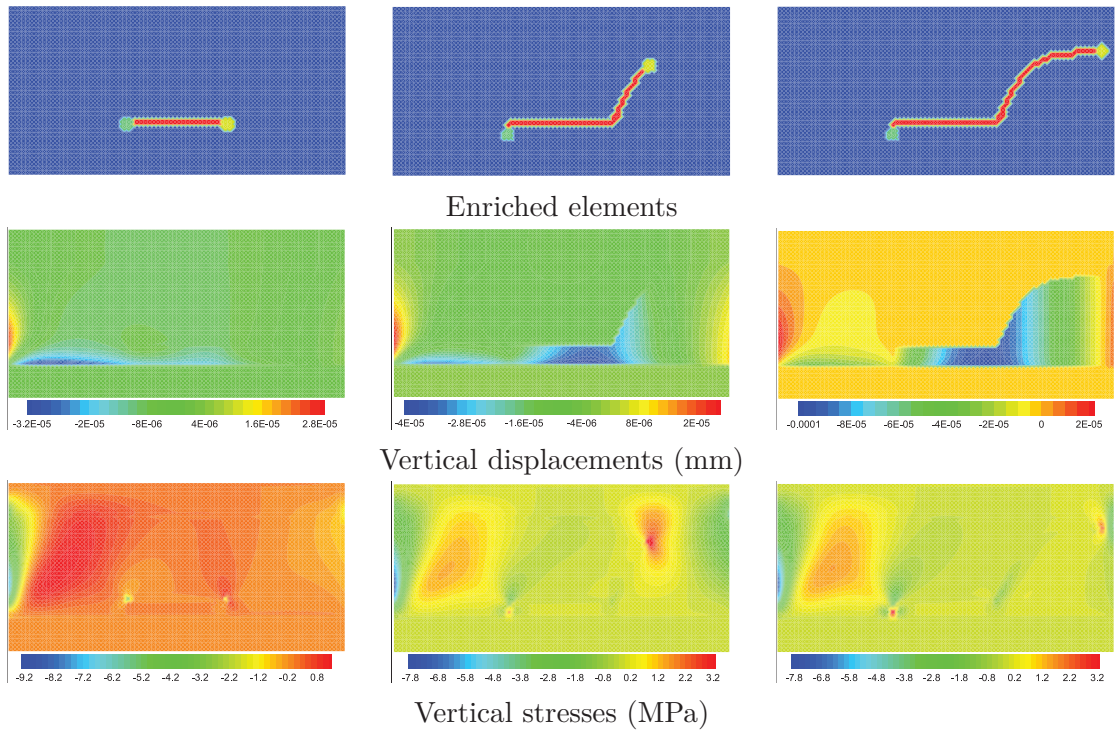

Figure 4.9.: Crack path, displacement and stress fields at different simulation time for $E_{m1} = E_{m2} \times 100$

c) - Permeability effect: The variation of the permeability influences the crack propagation path in the same manner as the thermal conductivity of the solid phase, but with different amplitudes. In fact the increase of the permeability enhances the fluid flow in porous media, which in turn increases the heat transport by advection within the porous material and decreases the temperature gradient. Fig. 4.13 illustrates the temperature and the vertical displacement and stress components contours resulting from three fluid permeabilities ($K = K_0/10,\ K_0 \times 50,\ K_0 \times 500$) with $K_0 = 15.13 \times 10^{-13}$ m^2, solid phase thermal conductivity $k_s = 1.5$ W/(m°C), and Young modulus $E_{m1} = E_{m2} \times 50$ MPa.

For the same simulation time ($t = 0.02$ s), the increase of the permeability increases the fluid flow in porous layer and decreases the temperature gradient in the vicinity of the crack. The decrease of the temperature gradient tends to homogenize the stresses around the crack-tip and decreases the crack orientation amplitude once it starts to propagate. This behavior is illustrated in Fig. 4.14.

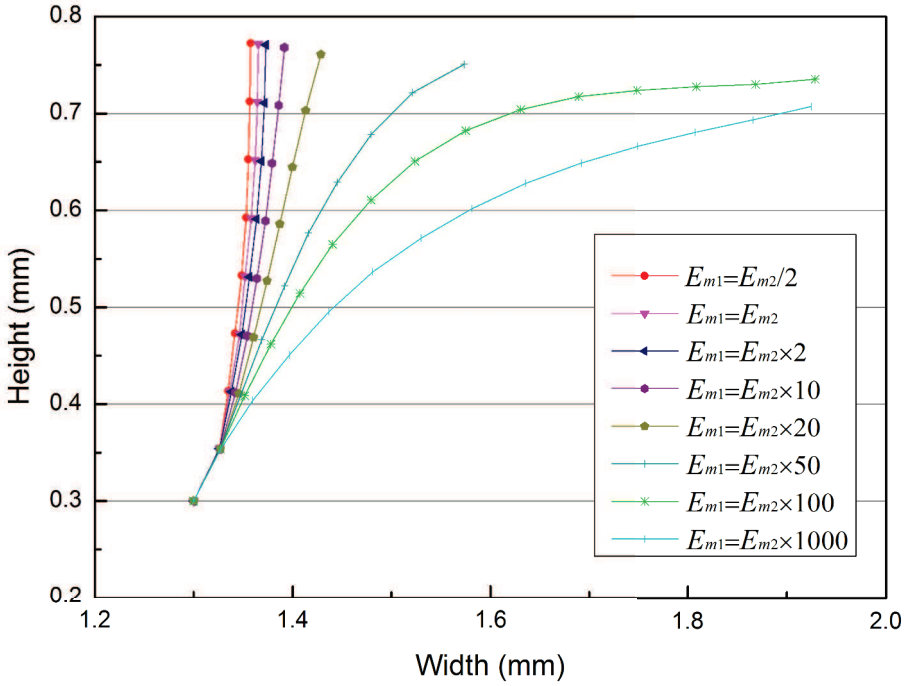

Figure 4.10.: Crack tip position in a three-layered structure for different materials mismatch

4.5. Conclusions

In this chapter, the multi-physics DB-XFEM model, developed is Chapter 2 and Chapter 3, is used to study crack propagation dependence on fluid flow and heat transfer in porous/dense materials. The fluid flow is governed by the Navier-Stokes equations in the channel and the Darcy-Brinkman equations in the porous material. The temperature distribution within the porous material results from thermal conduction in the solid phase and convection-conduction by means of the fluid flow within the pores. The crack is assumed to affect the heat conduction. The fluid flow, heat transfer and thermo-mechanical equations are coupled and solved using advanced numerical methods, where the XFEM is used to avoid burdens related to re-meshing. A post processing treatment is needed at each time-step to monitor the crack propagation. To calculate the crack growth direction, the maximum principal stress criterion is used. The implemented method is proved to be robust and costly efficient due to advantages imported by the XFEM. It is found in the study that:

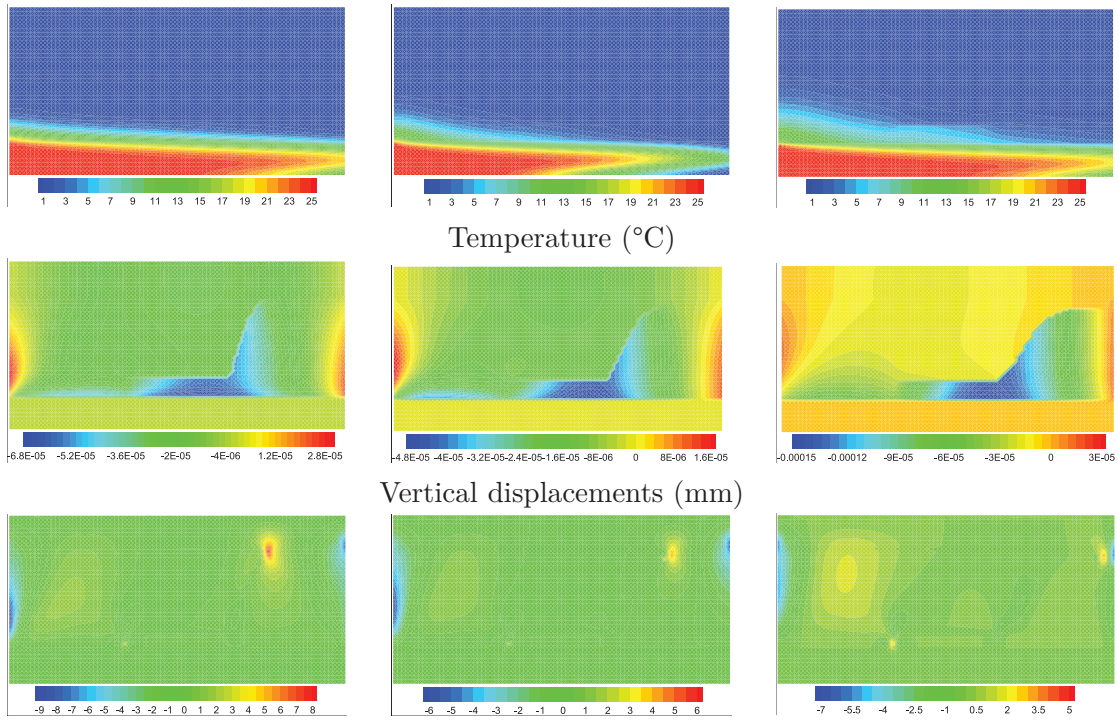

Figure 4.11.: Temperature, displacement and stress fields for different thermal conductivities of the solid

1. The crack propagation is due to the built up of residual stresses resulting from the temperature gradient and the mismatch of the layer's physical properties.
2. More the mismatch between layer's stiffness is high, more the crack deviates from the interface.
3. The temperature gradient in the vicinity of the crack tip influences directly the crack orientation amplitude.
4. The increase of the permeability and solid thermal conductivity both lead to the decreasing of crack orientation amplitude by enhancing the heat transfer within the porous media. The former increases the heat transfer by advection phenomena, while the latter by conduction.
5. The parameters studies show the influence of each material and process parameter on the crack propagation. This parametric study revealed a complex dependence of

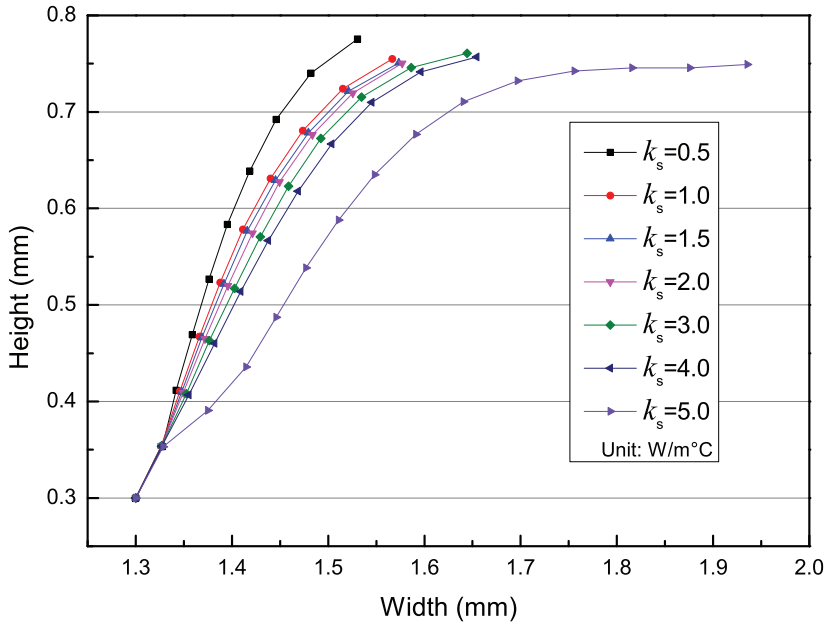

Figure 4.12.: Crack tip position in a three-layered structure for different thermal conductivities of the solid

crack propagation on the material and process parameters within a SOFC unit.

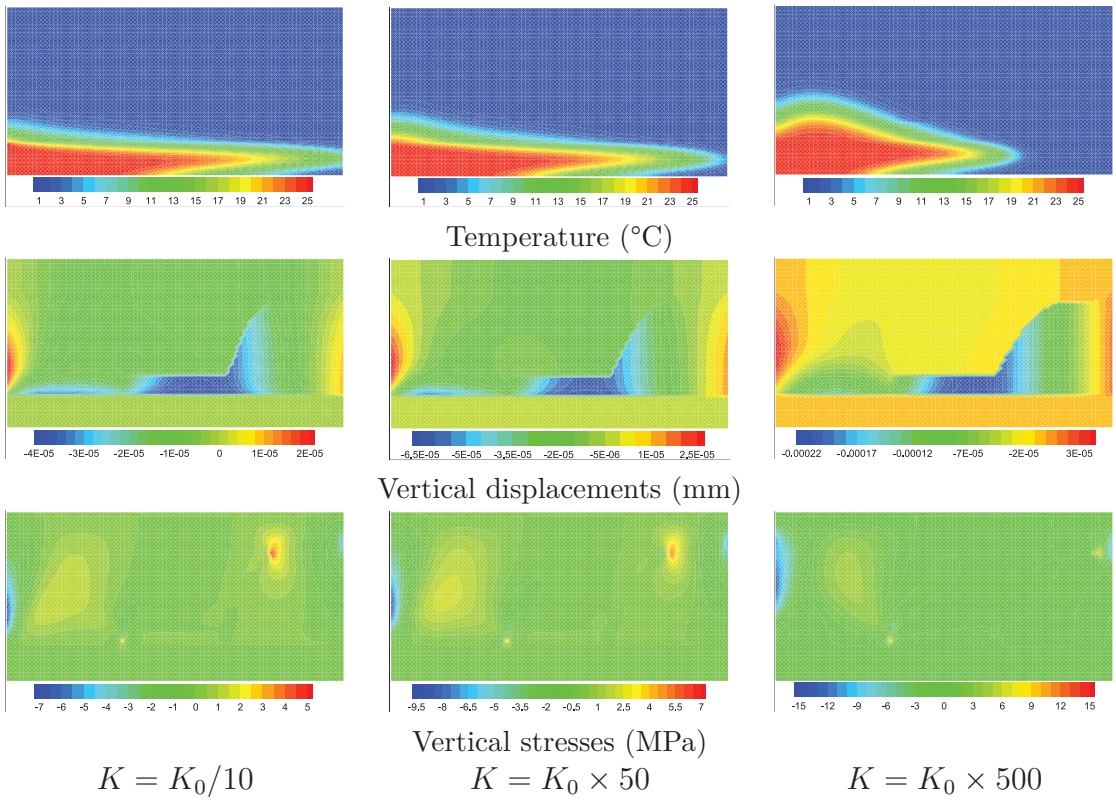

Figure 4.13.: Temperature, displacement and stress fields for different permeability values of the porous layer

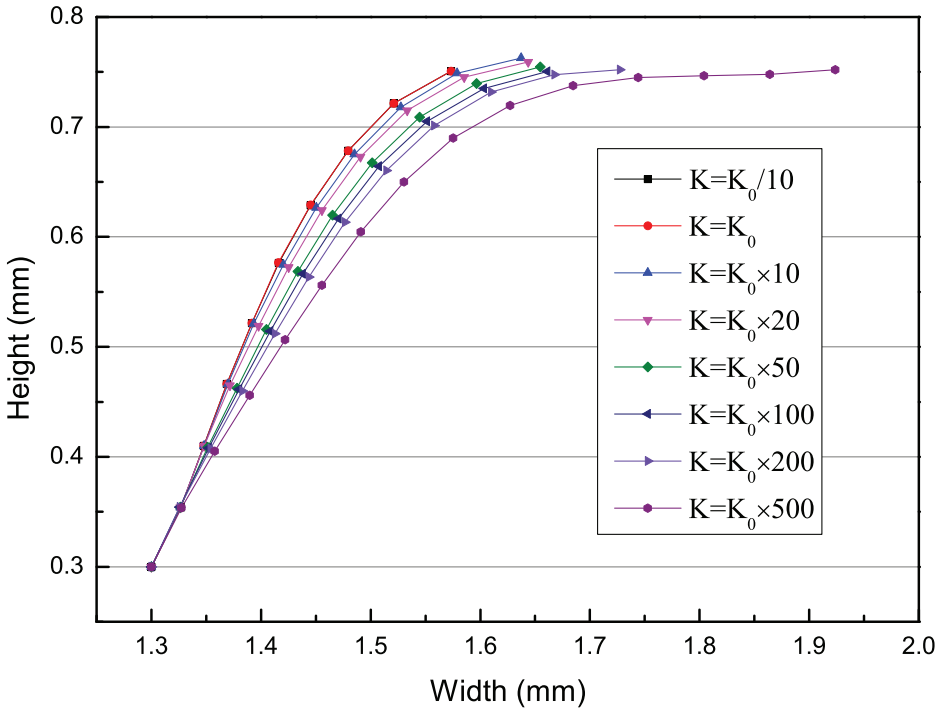

Figure 4.14.: Crack tip position in a three-layered structure for different permeability values of the porous layer

5. Fluid flow, Heat Transfer and Crack Propagation in Anisotropic Porous Media: Application to SOFC

5.1. Introduction

In a SOFC unit, the nucleation of cracks in the vicinity of the anode/electrolyte and cathode/electrolyte interfaces results usually from the cooling and heating processes. These cracks can propagate to deflect at the cell interfaces or penetrate in the electrolyte due to the thermo-mechanical loading during SOFC service. As consequences, the presence of cracks in the SOFC generates heat due to the Ohmic resistance at the crack tips which in turn dramatically affect the electrochemical performances of the SOFC unit. Further, cracks that penetrate in the electrolyte allow for fuel leakage from the anode side to the cathode side, which can deteriorate the SOFC unit. As we already know, due to the porous nature of the SOFC components (anode and cathode), pores concentration and distribution affect significantly the resistance to fracture of the porous SOFC materials. To preserve the mechanical integrity and to decrease the Ohmic losses of SOFC unit, we believe that by optimizing the orientation of pores, the porous media can be more resistant to crack propagation and also capable to diffuse heat in preferential directions to avoid temperature gradients. Therefore, porous material with different anisotropic thermal and mechanical properties is constructed using an existing in-house code. Then, the DB-XFEM code is used to investigate the effect of porous material anisotropy on crack propagation in the multilayered SOFC.

Crack analysis in anisotropic materials has been studied both analytically and numerically in the recent decades. Early researches were mainly focusing on analytical investigations

of fracture behavior and mechanical response of cracked anisotropic materials, such as Sih et al. (1965), Bogy (1972), Bowie and Freese (1972), Barnett and Asaro (1972), Kuo and Bogy (1974), Tupholme (1974), Viola et al. (1989), to set only few. With the development of computational technology, the modeling of crack propagation in anisotropic materials based on numerical methods has drawn more attention. Boundary element and dual boundary element methods were used to perform the analysis of cracks in anisotropic materials in Sollero and Aliabadi (1993); Sollero et al. (1994); Sollero and Aliabadi (1995). Then Aliabadi and Sollero (1998) extended this work to the crack growth analysis in orthotropic materials, where the boundary element formulation was utilized. In García et al. (2004), a general mixed traction boundary element approach was proposed to simulate cracks in anisotropic solids. Moreover, cracks in 2-D anisotropic material under thermal loading were studied by Pasternak (2012). XFEM was also widely used in fracture analysis of anisotropic materials, due to the feature that it enables the utilization of nonconforming meshes by introducing enrichment functions. For instance, Asadpoure et al. (2006a;b); Asadpoure and Mohammadi (2007) developed new XFEM enrichment functions to model crack in orthotropic media. Further time-independent and dynamic analysis of both static crack and crack propagation in orthotropic material using XFEM were found in Motamedi and Mohammadi (2010a;b; 2012).

In Chapter 4, we combined FEM and XFEM to investigate the effect of fluid flow and heat transfer on crack propagation in isotropic porous/dense bi-material. The present chapter concerns crack propagation in multilayered SOFC-like material where an existing crack is assumed to lie within anisotropic porous SOFC electrodes. The novelty here lies in the modeling of the multi-physics problem taking into account the anisotropy of SOFC electrodes (anode and cathode). The DB-XFEM model developed in the fourth chapter for the isotropic case is upgraded to take into account the anisotropy through the effective properties of the anode and cathode electrodes. In this model, three sub-models within the SOFC unit: the fluid flow, heat transfer and thermo-mechanical problems, are derived taking into account the anisotropy and solved iteratively till convergence for each time step. To compute the crack propagation in the anisotropic material, the enrichment functions and interaction integral equation which are different from those in the isotropic material are used.

The present chapter is organized as follows: In Section 5.2, the multi-physics governing

equations in the DB-XFEM model are recalled. In Section 5.3, an optimization algorithm (existing code) to construct anisotropic porous microstructures with different desired effective thermal and mechanical properties is recalled. Then in-service simulations of SOFC are conducted for each porous material anisotropy to investigate effects of anisotropy on crack propagation path within a SOFC unit in Section 5.4. Finally some concluding remarks are drawn in Section 5.5.

5.2. Governing Equations

The fluid flow, governed by Navier-Stokes in the flow channel and Darcy-Brinkman in the porous media, is discretized with the nonconforming CR method. The heat transfer equation is solved with a combination of DG, MPFA and XFEM methods considering the presence of cracks. The thermal conductivity is described by a tensor in the solid phase due to the anisotropy of the porous media. The temperature field resulting from the heat equation is used as body force for solving the thermo-mechanical response, where the XFEM is used with different asymptotic enrichment functions as in the isotropic material. Part of these equations and discretizations were detailed in Chapter 2 and Chapter 3. However, due to the introduction of anisotropy, a description will be dedicated to the heat transfer, the thermo-mechanical problem and the crack propagation in the following section.

5.2.1. Heat Transfer

Heat transfer in the flow channel, the porous media and the solid dense material is governed by heat conduction in the solid phase and heat transport in the fluid phase. In the anisotropic material, the thermal conductivity k_{PM} becomes a tensor of equivalent thermal conductivity of the system $\mathbf{k}_{PM}$. The total energy conservation equation in anisotropic media writes:

$$(\rho c)_{PM} \frac{\partial T}{\partial t} + \rho_f c_f \mathbf{v}.\nabla T - \nabla.(\mathbf{k}_{PM} \nabla T) = Q_T \tag{5.1}$$

By considering thermal dispersion in the fluid phase and heat conduction in both solid and fluid phases, the expression of $\mathbf{k}_{PM}$ components is

$$\begin{aligned} k_{PM,ij} &= k_{ij}^{disp_f} + k_{ij}^{cond_f} + k_{ij}^{cond_s} \\ &= \underbrace{\rho_f c_f \left[\alpha_T \left|\mathbf{v}\right| \delta_{ij} + \left(\alpha_L - \alpha_T\right) \frac{v_i v_j}{\left|\mathbf{v}\right|}\right]}_{dispersive} + \underbrace{\left[\left(1-\varepsilon\right) k_s + \varepsilon k_f\right] \delta_{ij}}_{conductive} \end{aligned} \tag{5.2}$$

with

$$k_{ij}^{disp_f} = \rho_f c_f \left[\alpha_T \left|\mathbf{v}\right| \delta_{ij} + \left(\alpha_L - \alpha_T\right) \frac{v_i v_j}{\left|\mathbf{v}\right|}\right] \tag{5.3}$$

$$k_{ij}^{cond_f} = \varepsilon k_f \delta_{ij} \tag{5.4}$$

$$k_{ij}^{cond_s} = \left(1-\varepsilon\right) k_s \delta_{ij} \tag{5.5}$$

where α_L and α_T are the longitudinal and transverse thermal dispersivities, δ_{ij} is the Kronecker delta function, k_f and k_s are the thermal conductivities of the fluid and solid phases. Crack within the porous SOFC electrodes is assumed to affect the thermal conduction part of the heat transfer. A time splitting is used to allow different treatments of heat transfer equations. At each time step Δt,the heat transport equation is firstly solved to calculate $T^{n+1,*}$, the temperature caused by heat transfer in the fluid phase:

$$\left(\rho c\right)_{PM} \frac{T^{n+1,*} - T^n}{\Delta t} + \rho_f c_f \mathbf{v}.\nabla T - \nabla.\left(\mathbf{k}^f \nabla T\right) = Q_T^f \tag{5.6}$$

where $\mathbf{k}^f = \mathbf{k}^{cond_f} + \mathbf{k}^{disp_f}$ is the conduction-dispersion tensor in the fluid phase.

Then, the final temperature T^{n+1} is obtained by taking into account heat transfer in the solid phase using $T^{n+1,*}$ as initial temperature:

$$\left(\rho c\right)_{PM} \frac{T^{n+1} - T^{n+1,*}}{\Delta t} - \nabla.\left(\mathbf{k}^{cond_s} \nabla T\right) = Q_T^s \tag{5.7}$$

where $\mathbf{k}^{cond_s}$ is the thermal conduction tensor of the solid phase in anisotropic porous medium.

5.2.2. Thermo-Mechanical Problem

5.2.2.1. Governing Equation and Discretization

Equilibrium equation under prescribed boundary conditions of a 2-D domain Ω is given by Eq. (3.7), as mentioned in Chapter 3. In anisotropic material, the constitutive relation for thermal elastic problems is given by the generalized Hooke's law

$$\boldsymbol{\sigma} = \mathbf{C} : \mathbf{D} - (\boldsymbol{\beta}^* \Delta T) \tag{5.8}$$

where $\boldsymbol{\beta}^*$ is a material tensor that relates material stiffness tensor to thermal expansion tensor, with the expression of components given by

$$\beta_{ij}^* = C_{ijkl} \beta_{kl}^T \tag{5.9}$$

Substituting the constitutive relation in the weak form of equilibrium Eq. (3.9) leads to

$$\int_\Omega \mathbf{D}(\delta\mathbf{u}) : (\mathbf{C} : \mathbf{D}(\mathbf{u}) - (\boldsymbol{\beta}^* \Delta T)) \, d\Omega = \int_\Omega \delta\mathbf{u} \cdot \mathbf{b} d\Omega + \int_{\Gamma_t} \delta\mathbf{u} \cdot \bar{\mathbf{t}} d\Gamma_t \tag{5.10}$$

The displacement is approximated using XFEM by

$$\mathbf{u}^h(\boldsymbol{x}) = \sum_{i \in N} \Upsilon_i \mathbf{u}_i + \sum_{i \in N_\Gamma} \Upsilon_i H(\boldsymbol{x}) \mathbf{c}_i + \sum_{i \in N_\Lambda} \Upsilon_i \sum_k br_k(\boldsymbol{x}) \mathbf{d}_i^k \tag{5.11}$$

To get the expressions of these function bases in 2D linear elastic anisotropic materials, consider the stress-strain relation

$$\{\mathbf{D}\} = [\mathbf{S}] \{\boldsymbol{\sigma}\} \tag{5.12}$$

where **S** is the compliance tensor of the material. Using the contracted form, one can write

$$\{\mathbf{D}\} = (D_{11}\ D_{22}\ 2D_{12})^T \tag{5.13}$$

$$\{\boldsymbol{\sigma}\} = (\sigma_{11}\ \sigma_{22}\ \sigma_{12})^T \tag{5.14}$$

$$[\mathbf{S}] = \begin{bmatrix} s_{11} & s_{12} & s_{13} \\ s_{21} & s_{22} & s_{23} \\ s_{31} & s_{32} & s_{33} \end{bmatrix} \tag{5.15}$$

with the assumption that X_1, X_2 are Global Cartesian coordinate system (see Fig. 5.1).

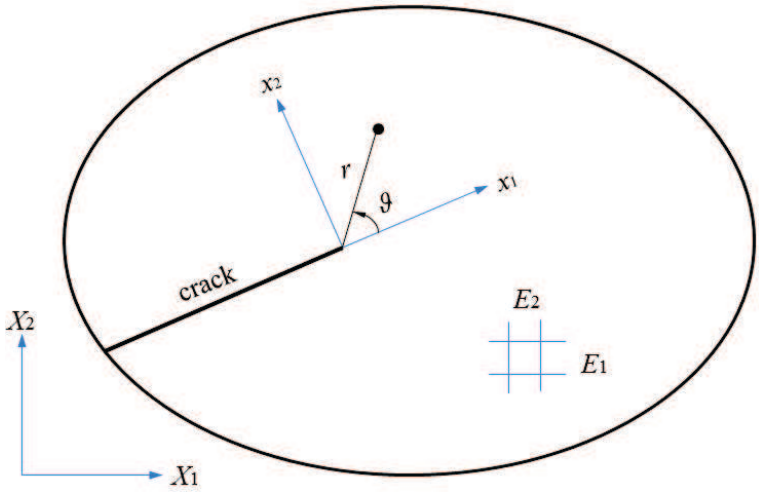

Figure 5.1.: The global Cartesian coordinate ($X_1,\ X_2$) and the local polar coordinate ($r,\ \vartheta$) with the origin at crack tip

To accurately reproduce the singularity of the stress field, the crack tip region has to be enriched according to Eq. (5.11). Using the partition of unity principle, this asymptotic

behavior is introduced in the finite element space. This is performed by adding extra degrees of freedom at the concerned nodes and removing the unknowns such as the SIFs. Applying this principle, the enrichment in the crack tip region can be drawn using the following four bases (Asadpoure et al., 2006a; Asadpoure and Mohammadi, 2007):

$$\{br_k(r,\vartheta)\}_{k=1}^{4} = \left\{ \sqrt{r}\cos\frac{\vartheta_1}{2}\sqrt{f_1(\vartheta)}, \sqrt{r}\cos\frac{\vartheta_2}{2}\sqrt{f_2(\vartheta)}, \right. \\ \left. \sqrt{r}\sin\frac{\vartheta_1}{2}\sqrt{f_1(\vartheta)}, \sqrt{r}\sin\frac{\vartheta_2}{2}\sqrt{f_2(\vartheta)} \right\} \tag{5.16}$$

where ϑ_i and $f_i(\vartheta)$ $(i=1,2)$ are related to local polar coordinates at the crack tip as in Fig. 5.1. The detailed expression of the branch enrichment bases is given by Asadpoure et al. (2006a); Asadpoure and Mohammadi (2007). Firstly, they assumed some definitions:

$$m_1 = \frac{s_{33}}{s_{11}},\ m_2 = \frac{s_{22}}{s_{33}},\ n_1 = \frac{s_{12}+s_{33}}{2s_{11}},\ n_2 = \frac{s_{12}+s_{33}}{2s_{33}} \tag{5.17}$$

$$a_1 = \frac{(m_1 + m_2 - 4n_1n_2)}{2},\ a_2 = m_1m_2 \tag{5.18}$$

If $a_1 > \sqrt{a_2}$, the first category is defined as (Asadpoure et al., 2006a; Asadpoure and Mohammadi, 2007):

$$f_i(\vartheta) = \left(\cos^2\vartheta + \frac{\sin^2\vartheta}{B_i^2}\right)^{\frac{1}{2}},\ i=1,\ 2 \tag{5.19}$$

$$\vartheta_i = \arctan\left(\frac{\tan\vartheta}{B_i}\right) \tag{5.20}$$

where

$$B_i = \left(A + (-1)^i\left(A^2 - \frac{s_{22}}{s_{11}}\right)^{\frac{1}{2}}\right)^{\frac{1}{2}} \tag{5.21}$$

$$A = \frac{1}{2}\left(\frac{s_{33}}{s_{11}} + \frac{s_{22}}{s_{33}} - \frac{\left(s_{12}+s_{33}\right)^2}{s_{11}s_{33}}\right) \tag{5.22}$$

If $|a_1| < \sqrt{a_2}$, the second category writes (Asadpoure et al., 2006a; Asadpoure and Mohammadi, 2007):

$$f_i(\vartheta) = \left(\cos^2\vartheta + B\sin^2\vartheta + (-1)^i B\sin 2\vartheta\right)^{\frac{1}{2}},\ i = 1,\ 2 \tag{5.23}$$

$$\vartheta_i = \arctan\left(\frac{A_2 B\sin\vartheta}{\cos\vartheta + (-1)^i A_1 B\sin\vartheta}\right) \tag{5.24}$$

where

$$B = \left(A_1^2 + A_2^2\right)^{-1} \tag{5.25}$$

$$A_1 = \left(\frac{1}{2}\left(\sqrt{a_2} + a_1\right)\right)^{\frac{1}{2}},\ A_2 = \left(\frac{1}{2} + \left(\sqrt{a_2} - a_1\right)\right)^{\frac{1}{2}} \tag{5.26}$$

By substituting the approximated displacement in the variational form of equilibrium 5.10, the following system to solve can be obtained

$$\int_\Omega \mathbf{B}_i^T\mathbf{C}\mathbf{B}_j d\Omega.\mathbf{U} = \int_\Omega \mathbf{B}_i^T\left(\boldsymbol{\beta}^*\Delta T\right)d\Omega + \int_\Omega \Upsilon_i^T\mathbf{b}d\Omega + \int_{\Gamma_t}\Upsilon_i^T\bar{\mathbf{t}}d\Gamma_t \tag{5.27}$$

where $\mathbf{B}$ is the matrix of shape function derivatives, with its expression detailed in Chapter 3.

5.2.2.2. Stress Intensity Factors Computation

J-integral is one of the efficient existing techniques to compute the SIFs. It is a path independent integral over a contour centered at the crack tip. The contour integral was transformed to surface integral, implemented and used in many studies of isotropic media.

Hereafter, we give a short recall of the methodology of SIFs computation in anisotropic media based on the interaction integral which is derived from the J-integral.

The expression of the J-integral for thermo-mechanical problems over a domain A is obtained over the contour enclosing A by using the divergence theory and it is given by

$$J = \int_A \left[\sigma_{ij}\frac{\partial u_i}{\partial x_1} - \mathcal{W}\delta_{1j}\right]\frac{\partial q_A}{\partial x_j}dA + \int_A \left[\beta^*_{ij}D_{ij}\frac{\partial T}{\partial x_1}\right]q_A dA \tag{5.28}$$

where q_A is the weighting function, and the summation convention over repeated indices holds $i, j = 1, 2$ for two dimensional problems.

To derive the expression of the interaction integral, assume the existence of an auxiliary mode $\left(\sigma^{(2)}_{ij},\ D^{(2)}_{ij},\ u^{(2)}_i\right)$ associated to the real mode $\left(\sigma^{(1)}_{ij},\ D^{(1)}_{ij},\ u^{(1)}_i\right)$. By using the superposition principle, Green's theory and separating terms, the interaction integral between state (1) and state (2) is (Bouhala et al., 2010; 2012; Duflot, 2008; Asadpoure and Mohammadi, 2007):

$$\begin{aligned} I^{(1,2)} = &\int_A \left[\sigma^{(1)}_{ij}\frac{\partial u^{(2)}_i}{\partial x_1} + \sigma^{(2)}_{ij}\frac{\partial u^{(1)}_i}{\partial x_1} - \mathcal{W}^{(1,2)}\delta_{1j}\right]\frac{\partial q_A}{\partial x_j}dA \\ &+ \int_A \left[trace\left(\boldsymbol{\beta}^*\mathbf{D}^{(2)}\right)\frac{\partial T}{\partial x_1}\right]q_A dA \end{aligned} \tag{5.29}$$

The interaction strain energy $\mathcal{W}^{(1,2)}$ is calculated in thermo-mechanical problems as

$$\mathcal{W}^{(1,2)} = \frac{1}{2}\left(\sigma^{(1)}_{ij}D^{(2)}_{ij} + \sigma^{(2)}_{ij}D^{(1)}_{ij} - \beta^*_{ij}D^{(2)}_{ij}\Delta T\right) \tag{5.30}$$

On the other hand, according to Asadpoure and Mohammadi (2007), the expression that relates the interaction integral to the SIFs is given by the following equation

$$I^{(1,2)} = 2a_{11}K^{(1)}_I K^{(2)}_I + a_{12}\left(K^{(1)}_I K^{(2)}_{II} + K^{(2)}_I K^{(1)}_{II}\right) + 2a_{22}K^{(1)}_{II}K^{(2)}_{II} \tag{5.31}$$

with

$$a_{11} = -\frac{s_{22}}{2}\Im\left(\frac{z_1 + z_2}{z_1 z_2}\right) \tag{5.32}$$

$$a_{12} = -\frac{s_{22}}{2}\Im\left(\frac{1}{z_1 z_2}\right) + \frac{s_{11}}{2}\Im\left(z_1 z_2\right) \tag{5.33}$$

$$a_{22} = \frac{s_{11}}{2}\Im\left(z_1 + z_2\right) \tag{5.34}$$

where $\Im(.)$ stands for the imaginary part of the complex number between the brackets. K_I, K_{II} are the opening and the shearing SIFs respectively. The complex numbers z_1 and z_2 are resulted from the following characteristic equation

$$s_{11}z^4 - 2s_{13}z^3 + \left(2s_{12} + s_{33}\right)z^2 - 2s_{23}z + s_{22} = 0 \tag{5.35}$$

which is obtained using equilibrium and compatibility conditions (Lekhnitskii, 1965). This characteristic equation admits two pairs of conjugate complex roots z_k, $\bar{z}_k$ $(k = 1,\ 2)$ but only the roots with positive imaginary part are used in the calculation (Sih et al., 1965).

By choosing the pure opening mode with unitary SIFs as auxiliary mode $\left(K_I^{(2)} = 1,\ K_{II}^{(2)} = 0\right)$ then the pure shearing one with unitary SIFs $\left(K_I^{(2)} = 0,\ K_{II}^{(2)} = 1\right)$, one can obtain the following system to solve

$$\begin{cases} I^{(1,I)} = 2a_{11}K_I^{(1)} + a_{12}K_{II}^{(1)} \\ \\ I^{(1,II)} = a_{12}K_I^{(1)} + 2a_{22}K_{II}^{(1)} \end{cases} \tag{5.36}$$

For pure opening mode and pure shearing mode, the analytical formulation of displacement and stress expressions in the vicinity of the crack tip were derived by Sih et al. (1965). Thus, in the local coordinates centered at the crack tip (Fig. 5.1), the stress and displacement expressions for pure mode one are given by

$$\sigma_{11} = \frac{K_I}{\sqrt{2\pi r}}\Re\left[\frac{z_1 z_2}{z_1 - z_2}\left(\frac{z_2}{\omega_2} - \frac{z_1}{\omega_1}\right)\right] \tag{5.37}$$

$$\sigma_{22} = \frac{K_I}{\sqrt{2\pi r}} \Re \left[\frac{1}{z_1 - z_2} \left(\frac{z_1}{\omega_2} - \frac{z_2}{\omega_1} \right) \right] \tag{5.38}$$

$$\sigma_{12} = \frac{K_I}{\sqrt{2\pi r}} \Re \left[\frac{z_1 z_2}{z_1 - z_2} \left(\frac{1}{\omega_1} - \frac{1}{\omega_2} \right) \right] \tag{5.39}$$

$$u_1 = K_I \sqrt{\frac{2r}{\pi}} \Re \left[\frac{1}{z_1 - z_2} \left(z_1 p_2 \omega_2 - z_2 p_1 \omega_1 \right) \right] \tag{5.40}$$

$$u_2 = K_I \sqrt{\frac{2r}{\pi}} \Re \left[\frac{1}{z_1 - z_2} \left(z_1 q_2 \omega_2 - z_2 q_1 \omega_1 \right) \right] \tag{5.41}$$

Similarly, the exact solutions of stress and displacement for pure mode two are given by

$$\sigma_{11} = \frac{K_{II}}{\sqrt{2\pi r}} \Re \left[\frac{1}{z_1 - z_2} \left(\frac{z_2^2}{\omega_2} - \frac{z_1^2}{\omega_1} \right) \right] \tag{5.42}$$

$$\sigma_{22} = \frac{K_{II}}{\sqrt{2\pi r}} \Re \left[\frac{1}{z_1 - z_2} \left(\frac{1}{\omega_2} - \frac{1}{\omega_1} \right) \right] \tag{5.43}$$

$$\sigma_{12} = \frac{K_{II}}{\sqrt{2\pi r}} \Re \left[\frac{1}{z_1 - z_2} \left(\frac{z_1}{\omega_1} - \frac{z_2}{\omega_2} \right) \right] \tag{5.44}$$

$$u_1 = K_{II} \sqrt{\frac{2r}{\pi}} \Re \left[\frac{1}{z_1 - z_2} \left(p_2 \omega_2 - p_1 \omega_1 \right) \right] \tag{5.45}$$

$$u_2 = K_{II}\sqrt{\frac{2r}{\pi}}\Re\left[\frac{1}{z_1 - z_2}\left(q_2\omega_2 - q_1\omega_1\right)\right] \tag{5.46}$$

where $\Re(.)$ stands for the real part of the complex number between the brackets. ω_k, p_k and q_k $(k = 1,\ 2)$ are defined by

$$\omega_k = \sqrt{\cos\vartheta + z_k \sin\vartheta} \tag{5.47}$$

$$p_k = s_{11}z_k^2 - s_{13}z_k + s_{12} \tag{5.48}$$

$$q_k = s_{12}z_k + \frac{s_{22}}{z_k} - s_{23} \tag{5.49}$$

To get the values of the SIFs expressions the resulting system of equations has to be simultaneously solved.

5.2.2.3. Crack Growth Criterion

The stress intensity factors intervene in the crack growth criterion and in the crack orientation angle calculation. The crack orientation angle is determined using the maximum principal hoop stress; this can be achieved by rewriting the asymptotic stresses solution at the crack tip. The asymptotic analytical formulation of stresses in the local coordinates centered at the crack tip, for the mixed mode is given by Sih et al. (1965).

$$\begin{cases} \sigma_{11} = \dfrac{1}{\sqrt{2\pi r}}\left(K_I\Re\left[\dfrac{z_1 z_2}{z_1 - z_2}\left(\dfrac{z_2}{\omega_2} - \dfrac{z_1}{\omega_1}\right)\right] + K_{II}\Re\left[\dfrac{1}{z_1 - z_2}\left(\dfrac{z_2^2}{\omega_2} - \dfrac{z_1^2}{\omega_1}\right)\right]\right) \\ \sigma_{22} = \dfrac{1}{\sqrt{2\pi r}}\left(K_I\Re\left[\dfrac{1}{z_1 - z_2}\left(\dfrac{z_1}{\omega_2} - \dfrac{z_2}{\omega_1}\right)\right] + K_{II}\Re\left[\dfrac{1}{z_1 - z_2}\left(\dfrac{1}{\omega_2} - \dfrac{1}{\omega_1}\right)\right]\right) \\ \sigma_{12} = \dfrac{1}{\sqrt{2\pi r}}\left(K_I\Re\left[\dfrac{z_1 z_2}{z_1 - z_2}\left(\dfrac{1}{\omega_1} - \dfrac{1}{\omega_2}\right)\right] + K_{II}\Re\left[\dfrac{1}{z_1 - z_2}\left(\dfrac{z_1}{\omega_1} - \dfrac{z_2}{\omega_2}\right)\right]\right) \end{cases} \tag{5.50}$$

Then the crack growth direction is given by

$$\vartheta_p = \left(\vartheta_{[-\pi/2,\pi/2]}, \max\left(\sigma_{\vartheta\vartheta}\right)\right) \tag{5.51}$$

The initial existing crack is considered to grow instantaneously once the equivalent SIF (K_{Ieq}) overcomes the material toughness (K_{Ic}). The equivalent stress intensity factor is given by Eq. (4.3).

5.3. Anisotropic Material Properties

Before investigating the effect of fluid flow and heat transfer on crack propagation in SOFC unit, effective thermal and mechanical properties of SOFC electrodes are determined for different degrees of anisotropy of the porous electrodes (anode and cathode). To this aim, starting from an isotropic porous microstructure, a Monte Carlo based optimization tool is used to construct porous microstructure with desired anisotropic effective thermal properties. Then the mechanical properties of the optimized porous microstructure are computed. The resulted thermal and mechanical properties of the anisotropic porous electrodes are used for further analysis of fluid flow and heat transfer in SOFC unit.

5.3.1. Microstructure Construction

An optimization tool based on statistical continuum theory is used to construct optimized porous isotropic and anisotropic microstructure with desired effective thermal conductivity (see Fig. 5.2).

The inputs of the algorithm are: volume fraction of the porous phase (ε_i), number of initial cells (N) and the desired second order effective thermal conductivity tensor $\left(\mathbf{k}_d^{cond_s}\right)$. Note that, the 3-D numerical integration within the statistical continuum theory using 2-D microstructure results in an axisymmetric homogenized material. The 3-D second order thermal conductivity tensor $\left(\mathbf{k}_d^{cond_s}\right)$ computed from 2-D microstructure has two equal components and an anisotropy along the third material axis. In what follows, we consider the 2-D microstructure lies in $(x,\ z)$ plane $\left(k_x^{cond_s} = k_y^{cond_s}\right)$, and the anisotropy is along

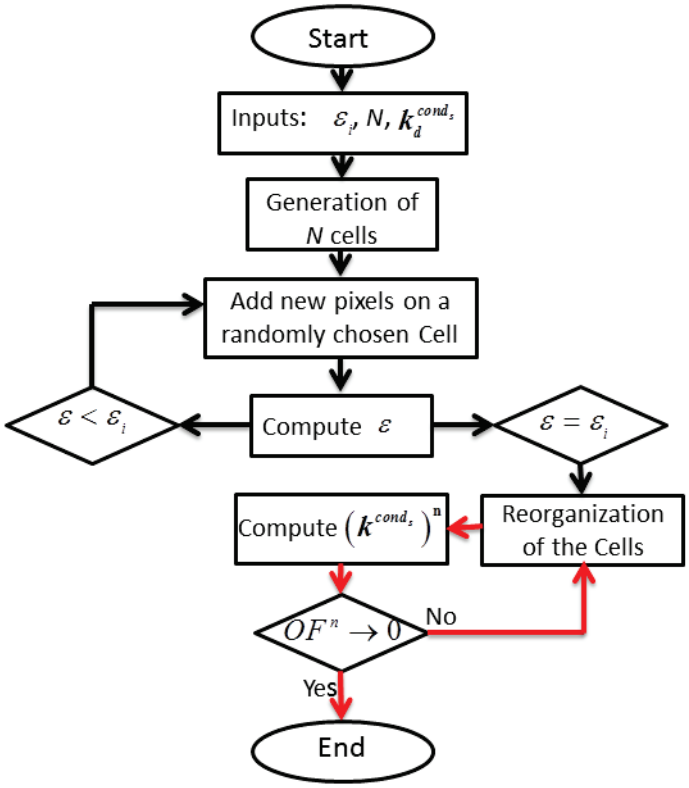

Figure 5.2.: Microstructure construction flow chart diagram

the z-direction (see Fig. 5.3). Therefore the microstructure construction is conducted by constraining the $k_z^{cond_s}$ component to design porous materials with anisotropy along the z-direction.

The algorithm consists of two optimization steps. On the first step of the algorithm, N cells are distributed randomly then grown iteratively, by adding n pixels at each iteration on a randomly chosen cell, among the existing N cells, to reach the desired pores volume fraction ε_i. On the second step, a reorganization procedure is used to reach the desired effective thermal conductivity $\mathbf{k}_d^{cond_s}$, keeping the pores volume fraction ε_i constant. To this aim, an iterative loop is considered where at each iteration n pixels are removed from the external contour of a randomly chosen cell, and added on the external contour of another randomly chosen cell. Then the effective thermal conductivity is calculated using the statistical continuum theory that takes into account the distribution, shape

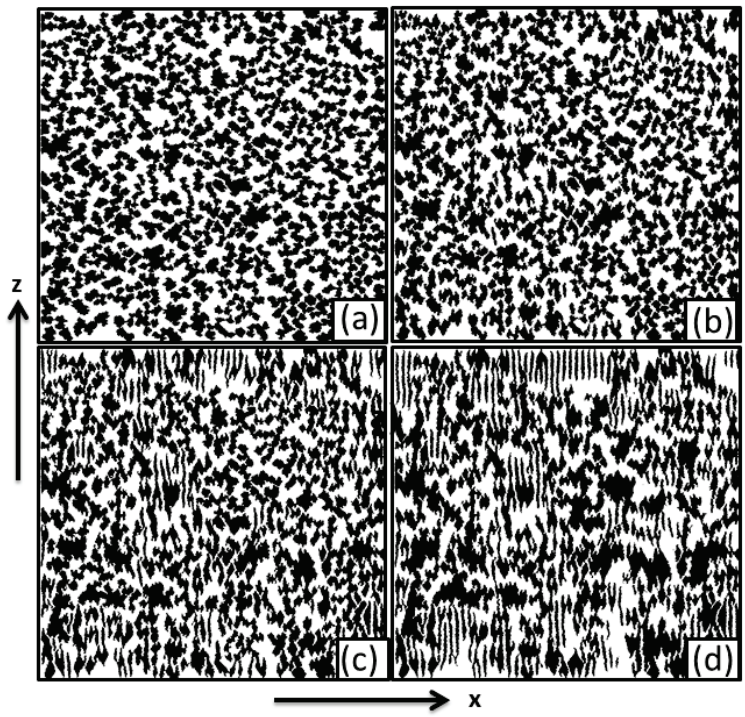

Figure 5.3.: Porous material with 50% porosity (black phase) and different anisotropy (see Tab. 5.1)

and orientation of the material components (Mikdam et al., 2009; 2013b). At each step, the n pixels reorganization is accepted if the objective function ($F^n < F^{n-1}$) is verified otherwise this operation is rejected. The objective function is defined as follows:

$$F^n = \left| \left(k_z^{cond_s} \right)^n - k_{z,d}^{cond_s} \right| \tag{5.52}$$

Note that the algorithm allows two neighboring cells to merge and become one cell once the added pixels bridge the gap between the two cells. Further the removed pixels might lead to a split of a cell into two cells. The value of "n" depends on the resolution of the constructed microstructure (image). Indeed, more the size of the image is large more its resolution (number of pixels) is high. In the present work the size of the constructed microstructure (image) is taken (1000×1000) and the reorganization parameter n is taken equal 5.

5.3.2. Effective Thermal and Mechanical Properties

The optimization algorithm is used to construct anisotropic porous microstructures with volume fractions ε_i =0.2, 0.3, 0.4, 0.5. For instance, Fig. 5.3 shows constructed porous microstructures with a volume fraction $\varepsilon = 0.5$ and different degrees of anisotropy (a), (b), (c) and (d). Tab. 5.1 shows the evolution, for each volume fraction, of the normalized effective thermal conductivity components $\left(k_{x,d}^{cond_s} \text{ and } k_{z,d}^{cond_s}\right)$ for different desired (constrained) thermal conductivities $k_{z,d}^{cond_s}$ along the z-direction. Note that the microstructure corresponding to anisotropy (a) is isotropic. The effective thermal conductivity (without normalization) of the porous SOFC anode and cathode electrodes can be computed by multiplying the normalized components by the measured values of the dense material thermal conductivity given in Tab. 4.2 in Section 4.3 at different temperatures.

Table 5.1.: Predicted normalized thermal conductivity for different anisotropy and pores volume fraction

ε_i	anisotropy	$k_{x,d}^{cond_s}$ (normalized)	$k_{z,d}^{cond_s}$ (normalized)
0.2	(a)	0.72726	0.72726
	(b)	0.71428	0.75
	(c)	0.69014	0.78
	(d)	0.67503	0.79365
0.3	(a)	0.60872	0.60872
	(b)	0.59714	0.63
	(c)	0.57681	0.66
	(d)	0.55969	0.68
0.4	(a)	0.50003	0.50003
	(b)	0.48359	0.53
	(c)	0.4635	0.56
	(d)	0.44754	0.58
0.5	(a)	0.40004	0.40004
	(b)	0.38387	0.43
	(c)	0.36481	0.46
	(d)	0.35014	0.48

The effective mechanical properties of the SOFC anode and cathode electrodes are computed for each pores volume fraction ε_i =0.2, 0.3, 0.4, 0.5 and their corresponding degree

of anisotropy reported in Tab. 5.1 ((a), (b), (c), (d)). For each pores volume fraction (ε_i =0.2, 0.3, 0.4, 0.5) and degree of anisotropy ((a), (b), (c), (d)), the optimized 2-D microstructure is used in conjunction with the statistical continuum theory to compute the porous material effective elastic tensor. To this aim, a measured Young's modulus of the anode and cathode dense material (see Tab. 4.1 in Section 4.3) and a Poisson coefficient of $\nu = 0.32$ (Selcuk and Atkinson, 1997) are used. Since the constructed porous material is transversely isotropic, only five independent components of the effective elasticity tensor are reported in Tab. 5.2. The fourth-order effective elasticity tensor might be written in Voigt notation as

$$\mathbf{C}^e = \begin{bmatrix} C^e_{11} & C^e_{12} & C^e_{13} & 0 & 0 & 0 \\ C^e_{12} & C^e_{11} & C^e_{13} & 0 & 0 & 0 \\ C^e_{13} & C^e_{13} & C^e_{33} & 0 & 0 & 0 \\ 0 & 0 & 0 & C^e_{44} & 0 & 0 \\ 0 & 0 & 0 & 0 & C^e_{44} & 0 \\ 0 & 0 & 0 & 0 & 0 & \left(C^e_{11} - C^e_{12}\right)/2 \end{bmatrix} \tag{5.53}$$

5.4. Numerical Results

5.4.1. Validation of Developed Multi-Physics Model

Partial validation regarding the fracture analysis in 2-D anisotropic thermoelasticity is conducted due to the difficulty finding literature benchmark examples to validate the developed multi-physics model. Note that part of validations have been conducted in the previous chapters regarding the thermo-fluid coupling problem (Chapter 2, Section 2.4), the thermo-mechanical response (Chapter 3, Section 3.4.2), where the computed SIFs are compared with those found in literature, and the benchmark test of the cruciform shaped plate (Chapter 4, Section 4.4.1), where the crack propagates in an isotropic material. In this section, the thermo-mechanical part of the multi-physics model is validated considering an inclined crack in a rectangular anisotropic plate (Pasternak, 2012) (see Fig. 5.4).

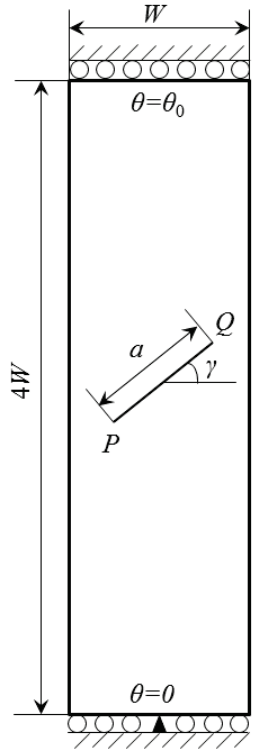

Figure 5.4.: Inclined central crack in anisotropic rectangular plate

The simulation is conducted using a normalized crack length $a/W = 0.5$. The plate height ($L = 4W$) is taken four times its width (W). The plate is made of glass/epoxy material with the following thermo-mechanical properties: $E_{11} = 55$ GPa, $E_{22} = 21$ GPa, $\nu_{12} = 0.25$, $G_{12} = 9.7$ GPa, $\beta_{11}^T = 6.3 \times 10^{-6}$ K^{-1}, $\beta_{22}^T = 2 \times 10^{-5}$ K^{-1} and $k_{11}^{cond_s}/k_{22}^{cond_s} = 3.45/0.35$. As boundary conditions, the bottom of the plate is maintained to a reference temperature $\theta = 0$ and the top of the plate is submitted to a normalized temperature $\theta = -1$. Mode I and II SIFs are calculated for different anisotropy by changing the crack angle γ. The resulted SIFs are normalized by $K_0 = E_{22}\beta_{22}^T\sqrt{\pi a}$ and then reported in Tab. 5.3. These values are compared to those from the literature using the Boundary Element Method (BEM) (Pasternak, 2012; Shiah and Tan, 2000), where a good agreement is found.

5.4.2. Application to Planar SOFC Unit

During service, the fuel and air flow into SOFC unit through the flow channels (see Fig. 5.5) with a constant inflow temperature and flow rate, then diffuse within the porous electrodes to reach the electrodes/electrolyte interfaces where the electrochemistry reactions take place. The mismatch of the mechanical properties of the unit cell electrodes (anode, cathode and electrolyte) as well as the variation of the temperature during service might lead to cracks nucleation and propagation within the cell unit (Qu et al., 2006). Considering an isotropic porous SOFC electrodes and a pre-existing crack in the SOFC cathode, previous study in Chapter 4 showed the strong dependence of the crack propagation path on both the process and material parameters. The present study focuses on effects of the porous material anisotropy (anode and cathode) on crack propagation path for different pores volume fraction.

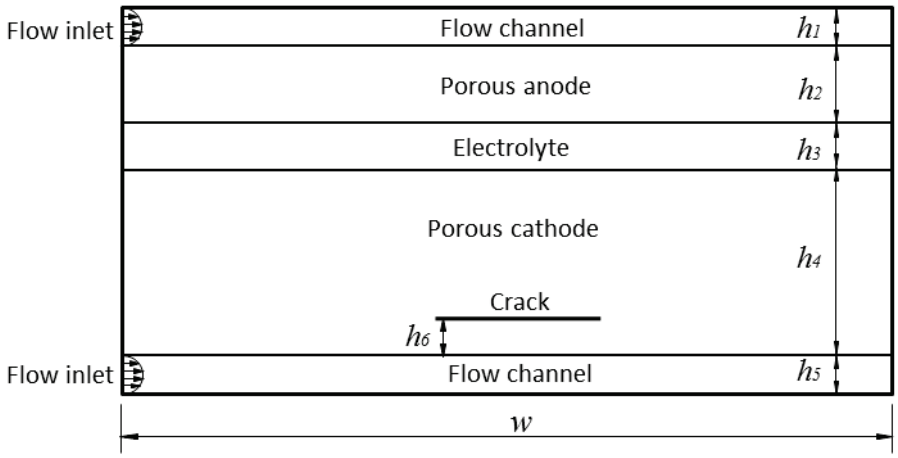

Figure 5.5.: Cracked SOFC unit

Previous investigations show a strong dependence of the SOFC unit mechanical response on the gases inflow configuration such as the inflow position (same side or opposite side) and the flow direction (parallel or perpendicular) (Achenbach, 1994; Recknagle et al., 2003; Wang et al., 2007). In the present study, the fuel and the air are assumed to flow into the SOFC unit from its left side. The SOFC unit dimension and the gases material parameters are given in Tab. 5.4. The pre-existing crack of 0.1 mm thickness and 6 mm

length is assumed to lie horizontally in the cathode electrode, where the left crack tip denoted crack tip-P and the right one denoted crack tip-Q. The crack grows when the equivalent SIF overcomes the material toughness K_{Ic}, which depends on the pores volume fraction and the solid dense material toughness K_{Ic0} (see Tab. 5.4) through Eq. (4.4).

Fig. 5.6 shows the temperature and the vertical displacement contours for an anode and cathode of porosity $\varepsilon = 0.3$ at the end of simulation: once the crack tip-Q crosses the border of the cathode electrode. Even if the time of simulation is not the same for the four cases, these contours show an increase of heat diffusion with the increase of the porous material anisotropy. Further the displacement discontinuity shows the deviation of the crack which is affected by both the electrolyte/cathode stiffness ratio and the anisotropy of the porous material: more the anisotropy is higher more the deviation far from the interface is important.

Fig. 5.7 shows the equivalent SIFs at the crack tip-Q as functions of the pores volume fractions (ε =0.2, 0.3, 0.4, 0.5) at different porous material degrees of anisotropy ((a), (b), (c), (d)). Note that the curves (a), (b), (c) and (d) correspond to the degrees of the porous material anisotropy reported in Tab. 5.1. These investigations lead to the conclusion that the anisotropy delays the onset of the crack propagation. Moreover the decrease of the pores volume fraction leads to stronger porous material that also delays the onset of the crack propagation.

Fig. 5.8 shows the variation of the SIFs at the crack tip-P and crack tip-Q for a material porosity of $\varepsilon = 0.3$ and porous material anisotropies (a), (b), (c), (d). Even the crack tip-P is closer to the fuel inflow at a temperature of 800°C, the crack propagates earlier at the crack tip-Q then the crack tip-P. At small simulation time the SIFs at the crack tip-P reach a maximum far from the porous material toughness. Therefore, it seems that the developed residual stresses due to the variation of the temperature at crack tip-P are not high enough to propagate the crack. Curves in Fig. 5.8 show that, for each material anisotropy, the onset of crack propagation at the crack tip-Q triggers the increase of the SIF at the crack tip-P until it reaches the porous material toughness.

Fig. 5.9, Fig. 5.10, Fig. 5.11 and Fig. 5.12 show crack propagation paths as the function of the porous material anisotropy for pores volume fractions ε =0.2, 0.3, 0.4 and 0.5, respectively. Due to temperature induced residual stresses, after propagation the crack tip-Q propagates towards the cathode/electrolyte interface while the tip-P propagates

towards the cathode free surface between the flow channel and the cathode.

Bouhala et al. (2010) showed in a previous work that in case of isotropic bi-material (material-1, material-2), where a crack lies in the material-1, the crack propagates towards the bi-material interface if the material-1 is stiffer than the material-2. However in case where the material-1 is softer than the material-2, once the crack-tip approaches the interface the crack deviates to propagate far from the interface. This phenomenon is also observed in the present work in the case of isotropic porous material (curves corresponding to anisotropy (a)). Further, the increase of the pores volume fraction of the isotropic porous cathode results in weaker mechanical properties that lead to early crack deviation by the electrolyte/cathode interface.

Once the porous material becomes anisotropic (curves (b), (c), (d)) the crack deviates further far from the interface compared to the isotropic case. This predicted behavior might be due partly to the decrease of the stiffness of the porous material with the increase of the anisotropy in the direction perpendicular to the cathode/electrolyte interface. In fact at constant pores volume fraction, the increase of the anisotropy leads to a decrease of the stiffness tensor component C^e_{11} (see Tab. 5.2) and an increase of the stiffness gap through and perpendicular to the cathode and the electrolyte.

It can be also noted that in case of isotropic porous cathode the deviation of the crack by the interface is due only to the difference of the mechanical properties. However, in case of the anisotropic cathode, from the shape of the propagation curves it can be concluded that the crack deviation is not only due to the difference of the mechanical properties but also to the anisotropy of the porous material. Further the increase of anisotropy leads to zig-zag phenomena of the crack propagation.

5.5. Conclusions

The DB-XFEM model is upgraded and used to study the effect of fluid flow and heat transfer on crack propagation in anisotropic porous/isotropic dense SOFC like material. This investigation focuses on the dependence of the onset and the path of crack propagation on the porous material anisotropy. To this aim porous material for the SOFC anode and cathode with isotropic and anisotropic desired effective thermal and mechanical

properties are constructed using an optimization tool on the basis of statistical continuum theory. Then these porous materials with different degrees of anisotropy are used to study the effect of material anisotropy on crack propagation path in SOFC like structure. The fluid flow, heat transfer and the thermo-mechanical problem are coupled and solved using the DB-XFEM model. The crack propagation was monitored by a post-processing computation of the SIFs. Relative to isotropic porous material, results show that:

1. Once the porous media becomes anisotropic, the onset of crack propagation is delayed.
2. The decrease of the pores volume fraction leads to a stiffer porous material that increases the fracture toughness of the material, which in turn delays the onset of crack propagation.
3. The increase of the material anisotropy leads to a larger deviation of the crack path from the porous media/dense media interface.
4. In anisotropic–porous/isotropic dense bi-material, the crack deviation depends not only on the difference of the mechanical properties, but also on the anisotropy degrees of the porous materials.

Table 5.2.: Predicted effective mechanical properties of SOFC electrodes

	ε_i		C^e_{11} (GPa)	C^e_{33} (GPa)	C^e_{12} (GPa)	C^e_{13} (GPa)	C^e_{44} (GPa)
Anode	0.2	(a)	1.802149	1.802149	0.665875	0.665875	0.576402
		(b)	1.700476	1.995736	0.619483	0.678706	0.585208
		(c)	1.510178	2.242232	0.532095	0.647065	0.577957
		(d)	1.400515	2.332719	0.482745	0.604715	0.563882
	0.3	(a)	1.293266	1.293266	0.429857	0.429857	0.440052
		(b)	1.211902	1.449276	0.398717	0.441581	0.449842
		(c)	1.070907	1.675997	0.344219	0.435139	0.453402
		(d)	0.956325	1.820035	0.394469	0.40833	0.444758
	0.4	(a)	0.915205	0.915205	0.275039	0.275039	0.326295
		(b)	0.812751	1.10765	0.241604	0.286729	0.339413
		(c)	0.691103	1.311844	0.203683	0.278698	0.341385
		(d)	0.600913	1.42682	0.186149	0.263043	0.337044
	0.5	(a)	0.632252	0.632252	0.172872	0.172872	0.234232
		(b)	0.542610	0.82984	0.147888	0.181592	0.246474
		(c)	0.441242	0.984474	0.122340	0.176306	0.249698
		(d)	0.373484	1.089831	0.112035	0.167239	0.248998
Cathode	0.2	(a)	1.236769	1.236769	0.456973	0.456973	0.39557
		(b)	1.165535	1.369623	0.425136	0.465779	0.401613
		(c)	1.036397	1.538787	0.365163	0.444064	0.396637
		(d)	0.961138	1.600886	0.331296	0.415001	0.386978
	0.3	(a)	0.887536	0.887536	0.295000	0.295000	0.301996
		(b)	0.831698	0.994601	0.273629	0.303046	0.308715
		(c)	0.734937	1.150193	0.236229	0.298625	0.311158
		(d)	0.656301	1.249043	0.20895	0.280227	0.305226
	0.4	(a)	0.628082	0.628082	0.188752	0.188752	0.223928
		(b)	0.557770	0.760152	0.165806	0.196775	0.232931
		(c)	0.474287	0.900286	0.139782	0.191263	0.234284
		(d)	0.412392	0.979191	0.127749	0.180519	0.231305
	0.5	(a)	0.433898	0.433898	0.118638	0.118638	0.160747
		(b)	0.372380	0.551067	0.101491	0.124622	0.169149
		(c)	0.302813	0.675619	0.083959	0.120994	0.171361
		(d)	0.256313	0.747923	0.076887	0.114772	0.170881

Table 5.3.: SIFs of inclined crack in anisotropic rectangular plate ($a/W = 0.5$)

Angle of crack		K_I/K_0			K_{II}/K_0		
		Shiah (2000)	Iaroslav (2012)	Present study	Shiah (2000)	Iaroslav (2012)	Present study
0°	tip P	0.379	0.376	0.376	0.002	0.002	0.001
	tip Q	0.379	0.376	0.376	0.002	-0.002	-0.001
15°	tip P	0.361	0.359	0.358	0.082	0.081	0.081
	tip Q	0.360	0.358	0.357	0.078	0.077	0.078
30°	tip P	0.305	0.303	0.303	0.150	0.149	0.148
	tip Q	0.303	0.301	0.301	0.145	0.144	0.144
45°	tip P	0.209	0.214	0.214	0.197	0.186	0.185
	tip Q	0.190	0.213	0.213	0.183	0.180	0.181

Table 5.4.: Geometry dimensions and material parameters for SOFC

Width	$w = 20.0$ mm
Height	$h_1 = 1.0$ mm
	$h_2 = 2.0$ mm
	$h_3 = 1.0$ mm
	$h_4 = 5.0$ mm
	$h_5 = 1.0$ mm
	$h_6 = 0.97$ mm
Effective porosity of porous media	$\varepsilon = 0.2 \sim 0.5$
Fluid density	$\rho_{air} = 0.3236$ kg/m^3
	$\rho_{fuel} = 0.0224$ kg/m^3
Dynamic viscosity	$\mu_{air} = 3.48 \times 10^{-5}$ Pa.s
	$\mu_{fuel} = 2.65 \times 10^{-5}$ Pa.s
Permeability	$K = 15.13 \times 10^{-12}$ m^2
Volumetric heat capacity	$(\rho C)_{air} = 0.3741 \times 10^3$ J/(m^3°C)
	$(\rho C)_{fuel} = 0.3395 \times 10^3$ J/(m^3°C)
Thermal conductivity	$k_{air} = 0.0692$ J/(sm°C)
	$k_{fuel} = 0.450$ J/(sm°C)
Dispersivity	$\alpha_L = 0.0$ m, $\alpha_T = 0.0$ m
Dense material toughness	$K_{Ic0} = 0.0252$ MPa.m$^{\frac{1}{2}}$
Toughness parameter	$b_e = 0.46$

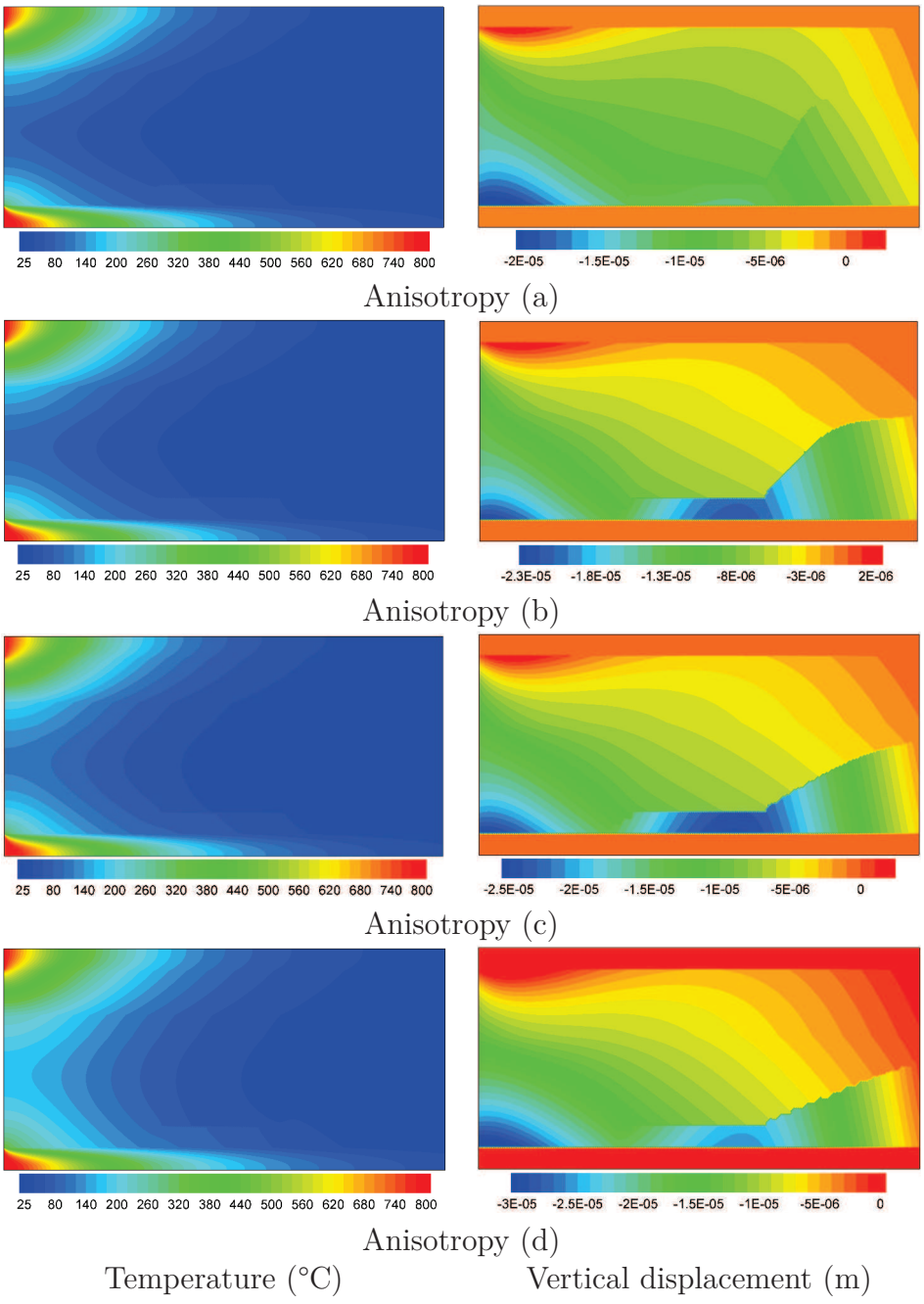

Figure 5.6.: Temperature and displacement fields for a porosity of 30%

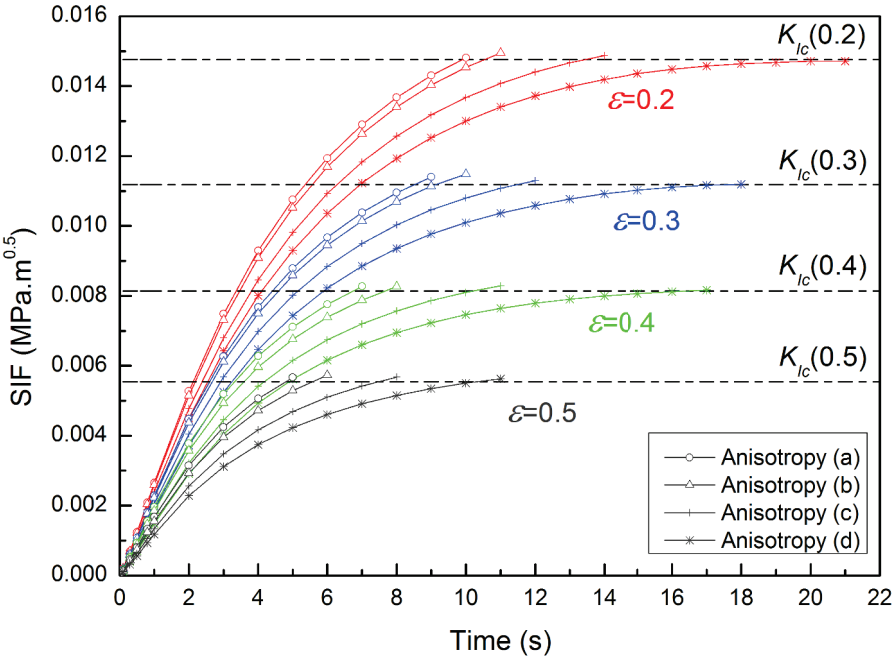

Figure 5.7.: Evolution of SIFs on crack tip-Q before the onset of crack propagation

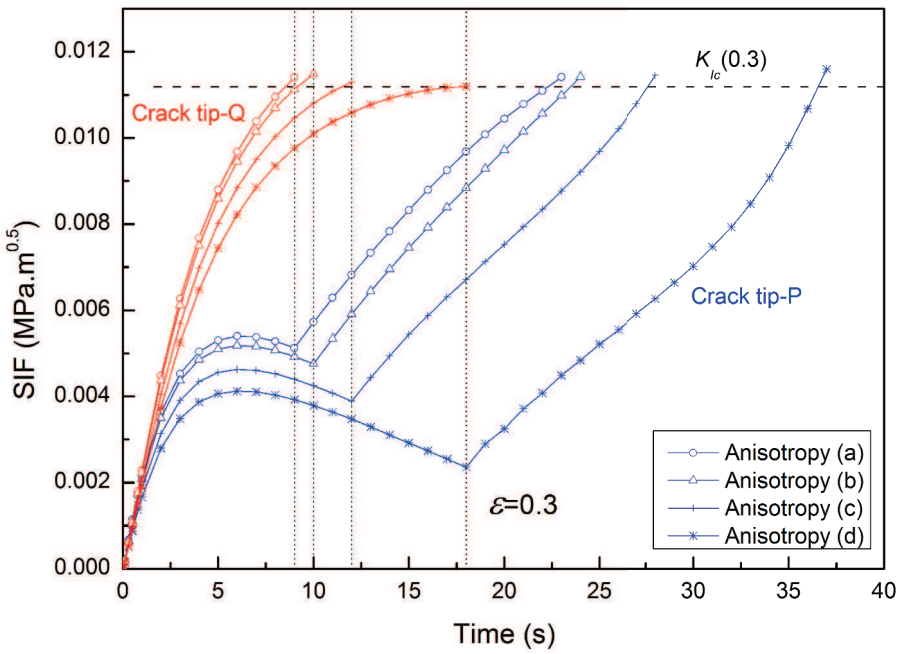

Figure 5.8.: Evolution of SIFs on the two crack tips (P, Q) for a porosity of 30%

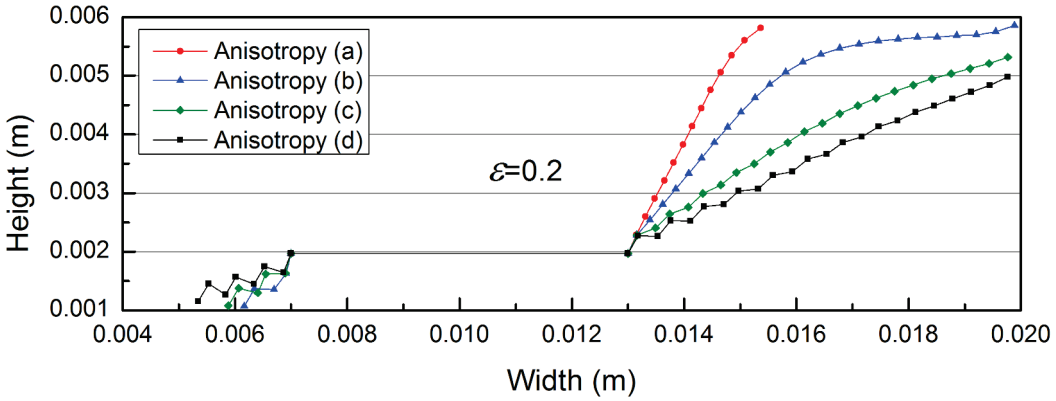

Figure 5.9.: Crack propagation paths for a porosity of 20% and different anisotropy

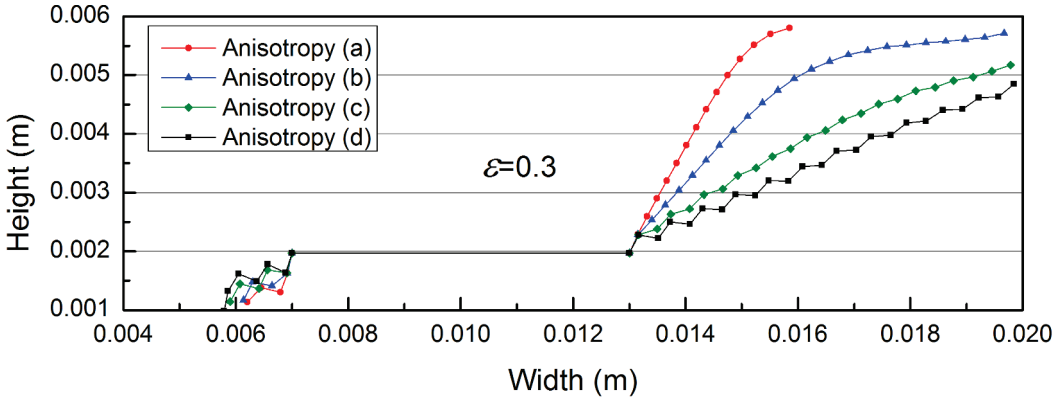

Figure 5.10.: Crack propagation paths for a porosity of 30% and different anisotropy

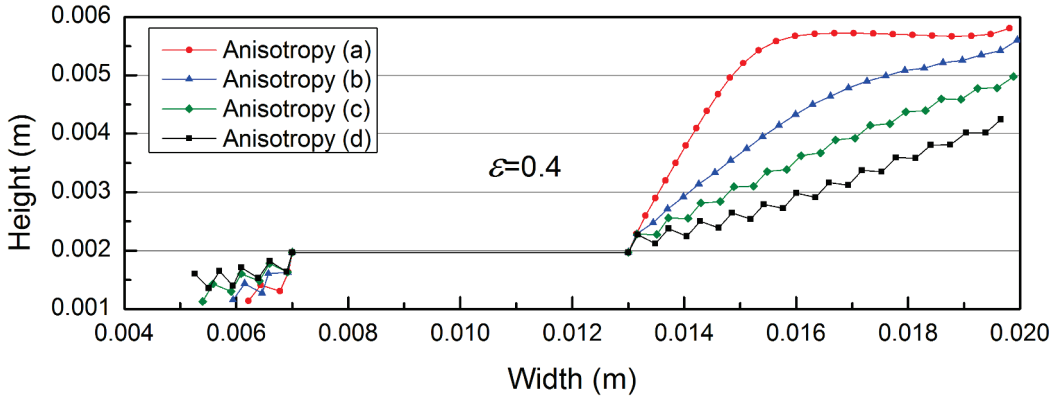

Figure 5.11.: Crack propagation paths for a porosity of 40% and different anisotropy

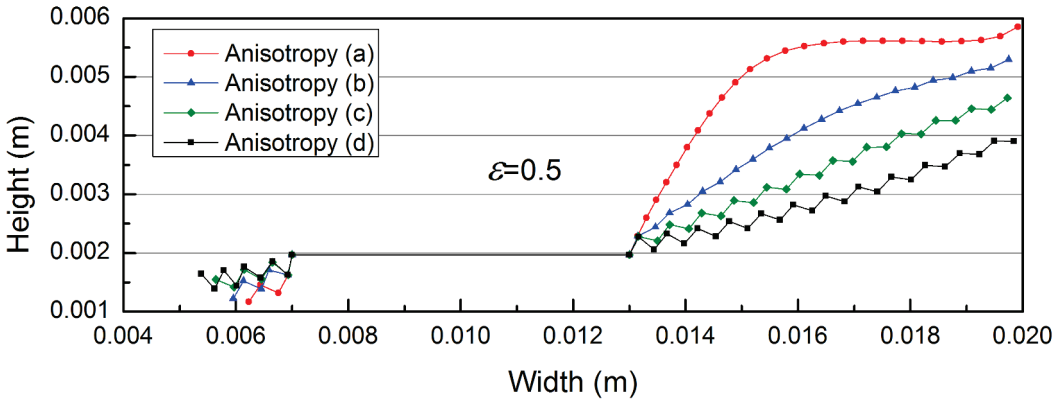

Figure 5.12.: Crack propagation paths for a porosity of 50% and different anisotropy

6. Coupling Chemical Reactions to Energy and Mass Transfer in SOFC: Effect of Temperature on Electrochemical Performance

6.1. Introduction

During service of SOFCs, the heat is generated within the cell due to the electrochemical reactions taking place at the electrodes/electrolyte interfaces, which results in the increase of the cell temperature. As previously stated, the high operating temperature of the SOFC can lead to complex material problems. On one hand, the temperature gradient in the cell and the different thermal expansion coefficients of cell components result in residual mechanical stresses and possible crack nucleation in the vicinity of electrodes/electrolyte interfaces (Yakabe et al., 2004; Qu et al., 2006), which was studied in Chapter 3, Chapter 4 and Chapter 5. On the other hand, the temperature distribution has also a significant effect on the electronic and ionic conductions of the cell components as well as the cell electrochemical performance. The increase of the local temperature at electrodes/electrolyte interfaces yields faster reaction rate; in reverse, the lower local temperature results in a slower reaction rate and a lower fuel utilization (Recknagle et al., 2003). To better understand physical processes within SOFC cell, significant models are proposed to simulate the multi-physics phenomenon taking place during SOFC service. For instance, Aguiar et al. (2004) presented a model for mass and heat transfer and an electrochemical model by neglecting the flow field in the porous electrodes. Thereby the species transfer was considered pure diffusive in the porous media. This assumption was

also used in the model of Campanari and Iora (2004). Other researchers assumed that the gas flow in the porous anode and cathode is governed by Darcy's law (Larrain et al., 2004; Lin and Beale, 2006). Hussain et al. (2006) developed a mathematical model to predict SOFC energy conversion performance considering isothermal cell. Cheddie and Munroe (2007); Kang et al. (2009) proposed 1-D dynamic models for SOFCs by integrating the anode/electrolyte/cathode structure and flow channels as one temperature layer and considering current density as a uniform field within the cell. A more sophisticated and robust model was introduced by Arpino et al. (2008) to deal with gas flow, heat and mass transfer regimes, and electrochemical reactions in SOFCs by dividing the SOFC unit into three computational domains (anodic compartment, electrolyte domain and cathodic compartment). Most of the models cited above are used to predict the flow and distribution of gases in the anode and the cathode, as well as the temperature and the current distributions.

In the present work, an EC model that considers the electrochemical reactions with Ohmic, activation and concentration losses is developed. Then the EC model is combined with the DB model that was introduced in Chapter 2 to solve the multi-physics phenomenon taking place during SOFC service. Investigations are focused on the cell energy conversion performances taking into account the heat generated by electrochemical reactions. The fluid flow, heat transfer and mass transport equations as well as the electrochemical reactions within the SOFC unit are solved in the DB-EC model as following:

- Navier-Stokes and Darcy-Brinkman equations are solved respectively in the flow channel and in the porous electrodes (anode and cathode) using the nonconforming Crouzeix-Raviart (CR) finite element method (Crouzeix and Raviart, 1973), with the nonlinear convective term being treated by an upstream approach with weight as in the previous work of Schieweck and Tobiska (1989).
- Heat generation due to the electrochemical reactions and Ohmic resistance is included in the energy conservation equation. The heat transport equation is solved within the SOFC (flow channels, porous electrodes and solid dense electrolyte) using a combination of Discontinuous Galerkin (DG) and Multi-Point Flux Approximation (MPFA) methods (Younes and Ackerer, 2008).
- The consumption and production of species due to the electrochemical reactions are considered in the species transfer within the SOFC. A combination of DG and

MPFA methods is also used to solve the species transport equation in the flow channels and the porous electrodes.

- The temperature and species concentration resulted from the solution of heat transport and species transport equations are used to solve the electrochemical problem. The current density in the cell is obtained at a given operating voltage.

The present chapter is organized as follows: In Section 6.2, the governing equations in the DB-EC model and the solving procedure of the multi-physics problem are detailed. Numerical validations of the developed model on existing literature results as well as the experiments with a constant temperature are reported in Section 6.3. In Section 6.4, the numerical simulations of in-service SOFC unit are conducted to highlight the effect of temperature generated by electrochemical reactions on the I-V curves. Finally some concluding remarks are drawn in Section 6.5.

6.2. Governing Equations

In the following sections we recall briefly the fluid flow, energy transfer and mass transport equations. The corresponding discretizations of these equations are detailed in Chapter 2. The electrochemistry equations used to compute the cell energy efficiency are introduced and solved.

6.2.1. Heat and Mass Transfer Problems

The flow of gases in SOFC on both the fuel and the air sides is laminar (Autissier et al., 2004; Arpino et al., 2008). In the flow channels, the free flow is governed by Navier-Stokes equation. Regarding fluid flow in the porous SOFC electrodes, literature review shows that Darcy's law is commonly used to simulate the flow in the porous material, which is not accurate when the flow velocity is not small. Also, with Darcy's law, appropriate interfacial boundary condition between the channel and the porous electrodes should be specified (Vafai and Kim, 1990; Vafai, 2000). To overcome these drawbacks, the Darcy-Brinkman equation is used to describe the fluid flow in the porous electrodes. The mass,

momentum, energy and species conservation equations are given by

$$\nabla.\mathbf{v} = 0 \tag{6.1}$$

$$\frac{\rho_f}{\varepsilon}\frac{\partial \mathbf{v}}{\partial t} + \frac{\mu}{K}\mathbf{v} + \frac{\rho_f}{\varepsilon^2}\left(\mathbf{v}.\nabla\right)\mathbf{v} - \frac{\mu}{\varepsilon}\nabla.\left(\nabla\mathbf{v}\right) + \nabla p = 0 \tag{6.2}$$

$$\left(\rho c\right)_{PM}\frac{\partial T}{\partial t} + \rho_f c_f \mathbf{v}.\nabla T - \nabla.\left(k_{PM}\nabla T\right) = Q_T \tag{6.3}$$

$$\varepsilon\frac{\partial C}{\partial t} + \mathbf{v}.\nabla C - \nabla.\left(D_e\nabla C\right) = Q_S \tag{6.4}$$

Note that the same momentum conservation Eq. (6.2) is used for the calculation of fluid flow both in the channel and in the porous electrodes by changing the material properties. Indeed, the Navier-Stokes equation, used to model the free flow in the flow channels, can be derived from the Darcy-Brinkman Eq. (6.2) by taking the porosity $\varepsilon = 1.0$ and the permeability $K \to \infty$. In the porous medium, Darcy-Brinkman equation is used with porosity $0 < \varepsilon < 1$ and permeability $0 < K < \infty$, thereby no interfacial condition between the channel and the porous electrodes has to be specified.

Heat transfer in the channels, the porous electrodes and the solid dense electrolyte is governed by heat conduction in the solid phase and heat conduction and convection in the fluid phase. Mass transfer occurs in the channels and the porous electrodes by advection and dispersion phenomena in the fluid phase. The heat and species source/sink terms Q_T and Q_S in energy and species conservation equations are derived from the electrochemical reactions. The heat generation within the cell is due to the electrochemical reactions at the anode/electrolyte and cathode/electrolyte interfaces, as well as the activation and Ohmic losses (η_{act}, η_{Ohm}). Thus, the heat source can be described as a heat flux at the catalyst layer as follows

$$\dot{Q}_T = \frac{T \cdot j}{4F}\left(2S_{H_2O} - 2S_{H_2} - S_{O_2}\right) + j\left(\eta_{Ohm} + \eta_{act}\right) \tag{6.5}$$

The species source term which is related to the current density can be expressed by the species fluxes at the electrodes/electrolyte interfaces according to Faraday's law (Arpino et al., 2008)

$$\dot{Q}_{S,i} = \frac{j}{n_e F} \tag{6.6}$$

Here j is the current density, F is Faraday constant (96487 C/mol), n_e is the number of electrons transferred in the single elementary rate-limiting reaction step. According to Lu et al. (2006), the entropies S_{H_2O}, S_{H_2} and S_{O_2} have the values 233.71 J/(K.mol), 166.88 J/(K.mol) and 244.35 J/(K.mol), respectively.

Species effective diffusion coefficient (D_e) evaluation is crucial for an accurate estimation of species concentrations. In the absence of experimental data, several models have been proposed in the literature for the evaluation of binary species diffusion coefficients, where the Fuller-Schettler-Giddings equation is mostly used. Suppose we have a gas mixture of A and B, the bulk diffusivity of the binary species writes

$$D_{bulk,AB} = \frac{10^{-3} T^{1.75} \left(\frac{1}{M_A} + \frac{1}{M_B}\right)^{\frac{1}{2}}}{p\left[\left(\sum V_A\right)^{\frac{1}{3}} + \left(\sum V_B\right)^{\frac{1}{3}}\right]^2} \tag{6.7}$$

where M_A and M_B are species molecular weight, $\sum V_A$ and $\sum V_B$ are the sum of the diffusion volume for component A and B, respectively (Campanari and Iora, 2004).

In Eq. (6.7), the effect of the presence of the porous electrode on diffusion coefficient of species A is taken into account through Knudsen diffusion coefficient (Arpino et al., 2008), which is given by

$$D_{knudsen,A} = \frac{4}{3} r_p \sqrt{\frac{8\Re T}{\pi M_A}} \tag{6.8}$$

Therefore, the effective diffusion coefficient of species A in a binary gas mixture in porous media is given by

$$\frac{1}{D_{e,A}} = \frac{\tau_g}{\varepsilon}\left(\frac{1}{D_{bulk,A}} + \frac{1}{D_{knudsen,A}}\right) \tag{6.9}$$

In above Eq. (6.8) and Eq. (6.9), r_p is the average pore size of the porous electrode. τ_g is the tortuosity factor which depends on the pores' tortuous nature and pore constrictions. $\mathfrak{R}$ is universal gas constant with the value 8.314 J/(K.mol) .

6.2.2. Electrochemistry

The energy conversion within a SOFC unit is based on electrochemical reactions at electrodes/electrolyte interfaces, called also the three phase boundaries (TPB). The ideal electromotive force or Open-circuit potential (OCP), assuming a unit cell supplied with pure hydrogen and oxygen, is given by the Nernst equation (Aguiar et al., 2004; Campanari and Iora, 2004)

$$U_{TPB}^{OCP} = U_{H_2}^0 - \frac{\mathfrak{R}T}{2F} \ln \left(\frac{p_{H2O,fuel}}{p_{H_2,fuel} \left(p_{O_2,air} \right)^{\frac{1}{2}}} \right) \tag{6.10}$$

Here $p_{H_2O,fuel}$, $p_{H_2,fuel}$ and $p_{O_2,air}$ are the partial pressures of water, hydrogen and oxygen, respectively, at the fuel and air channels. The partial pressures p_k are related to the species ($k = H_2,\ O_2,\ H_2O$) molar concentration C_k, by $p_k = C_k \mathfrak{R}T$ (Khaleel et al., 2004). $U_{H_2}^0$ is the standard cell potential that depends on the change of Gibb's free energy when all of the species are at a pressure of 1.0 atm (Khaleel et al., 2004). The dependence on the temperature of $U_{H_2}^0(T)$ is given by the following equation (Lu et al., 2006)

$$U_{H_2}^0(T) = \left(U_{H_2}^0 \right)_{ref} + \frac{(\Delta S)_{ref}}{4F} (T - 1023) \tag{6.11}$$

where $\left(U_{H_2}^0 \right)_{ref} = 0.9915V$ and $(\Delta S)_{ref} = 2S_{H_2O} - 2S_{H_2} - S_{O_2}$ are the standard cell potential and the change of entropy at a reference temperature $T = 1023K$.

In-service the output voltage of a SOFC unit is lower than the ideal electromotive force given by Eq. (6.10) due to mainly Ohmic (η_{Ohm}), concentration (η_{conc}) and activation (η_{act}) losses (Colpan et al., 2007; Lee et al., 2011). Thus the cell voltage is given by the following equation

$$U = U_{TPB}^{OCP} - (\eta_{Ohm} + \eta_{conc,anode} + \eta_{conc,cathode} + \eta_{act,anode} + \eta_{act,cathode}) \tag{6.12}$$

6.2.2.1. Ohmic Overpotentials

The Ohmic overpotential represents the resistance to the flow of ions through the electrolyte and flow of the electrons through the cell's anode and cathode. This voltage drop is important in SOFC and is dependent linearly on the current density according to Ohm's law:

$$\eta_{Ohm} = jR_{Ohm} \tag{6.13}$$

Here the overall resistance of the cell R_{Ohm}, which includes electronic and ionic resistances, is given function of the thicknesses of cell components (anode/electrolyte/cathode), and the ionic and electronic conductivities of cell components (Aguiar et al., 2004).

$$R_{Ohm} = \frac{\tau_{anode}}{\sigma_{anode}} + \frac{\tau_{electrolyte}}{\sigma_{electrolyte}} + \frac{\tau_{cathode}}{\sigma_{cathode}} \tag{6.14}$$

where τ_{anode}, $\tau_{electrolyte}$ and $\tau_{cathode}$ stand for the thickness of the anode, electrolyte and cathode layers, respectively. σ_{anode} and $\sigma_{cathode}$ are the electronic conductivity of the anode and cathode. And $\sigma_{electrolyte}$ is the ionic conductivity of the electrolyte.

6.2.2.2. Concentration Overpotentials

The concentration overpotential represents the resistance to mass transport through the cell porous electrodes that leads to species concentration gradient. Physical processes that contribute to the occurrence of concentration overpotentials include gas species molecular transport through the electrode pores to/from the reaction sites, as well as the consumption of reactants and production of water at the TPB (Aguiar et al., 2004). When the fuel cell is under no load (open-circuit), the reactant and product concentrations at the reaction sites are the same as those in the bulk channel flow. However, when the fuel cell is under normal operating conditions (closed-circuit), the fuel and oxidant consumption at the reaction site leads to a concentration gradient across the anode and cathode. Therefore, the species concentrations at TPB are different from those in the bulk and the channels. These losses can be evaluated by the following relation (Campanari

and Iora, 2004; Aguiar et al., 2004; Arpino et al., 2008)

$$\eta_{conc} = \frac{\Re T}{2F} \ln\left(\frac{p_{H_2O,TPB} p_{H_2,fuel}}{p_{H_2O,fuel} p_{H_2,TPB}}\right) + \frac{\Re T}{4F} \ln\left(\frac{p_{O_2,air}}{p_{O_2,TPB}}\right) \tag{6.15}$$

The first term on the right hand side of Eq. (6.15) represents the anodic overpotential, $\eta_{conc,anode}$:

$$\eta_{conc,anode} = \frac{\Re T}{2F} \ln\left(\frac{p_{H_2O,TPB} p_{H_2,fuel}}{p_{H_2O,fuel} p_{H_2,TPB}}\right) \tag{6.16}$$

The second term refers to the cathodic overpotential, $\eta_{conc,cathode}$:

$$\eta_{conc,cathode} = \frac{\Re T}{4F} \ln\left(\frac{p_{O_2,air}}{p_{O_2,TPB}}\right) \tag{6.17}$$

$p_{H_2O,fuel}$, $p_{H_2,fuel}$ and $p_{O_2,air}$ are the partial pressures of water, hydrogen and oxygen at the fuel and air channel, while $p_{H_2O,TPB}$, $p_{H_2,TPB}$ and $p_{O_2,TPB}$ are the partial pressures of H_2O, H_2 and O_2 at three-phase boundaries, respectively, as shown in Fig. 6.1.

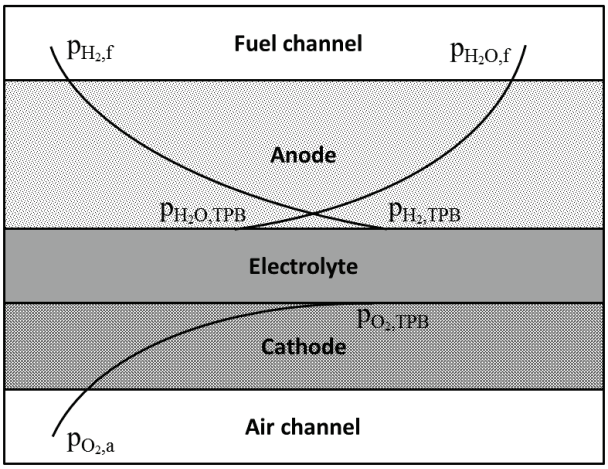

Figure 6.1.: Partial pressures at flow channels and TPB in SOFC

6.2.2.3. Activation Overpotentials

Activation overpotentials, which are related to the activation energy required by the chemical reactions, represent the kinetics of reaction at the cell active sites. Activation

overpotentials depend strongly on the operating temperature of SOFC. At a high operating temperature, the high kinetic activity at the reaction sites usually results in small activation overpotentials. However, with the decreasing of the operating temperature, activation potentials can become the most significant contribution to the drop of the cell voltage. Activation overpotentials are related to the current density by the non-linear Butler-Volmer equation

$$j = j_{0,electrode}\left[\exp\left(\frac{\alpha^A n_e F}{\Re T}\eta_{act,electrode}\right) - \exp\left(-\frac{\alpha^C n_e F}{\Re T}\eta_{act,electrode}\right)\right], \quad electrode \in \{anode,\ cathode\} \tag{6.18}$$

where α^A and α^C are the charge transfer coefficients for the anode and the cathode respectively. The exchange current density $j_{0,electrode}$, which depends on not only on the operating temperature and material properties, but also on the kinetic activity of the electrochemical reaction and the species concentrations (Celik et al., 2005), is expressed as

$$j_{0,anode} = \gamma_{anode}\left(\frac{p_{H_2,TPB}}{p_0}\right)\left(\frac{p_{H_2O,TPB}}{p_0}\right)\exp\left(-\frac{E_{anode}}{\Re T}\right) \tag{6.19}$$

$$j_{0,cathode} = \gamma_{cathode}\left(\frac{p_{O_2,TPB}}{p_0}\right)^{0.25}\exp\left(-\frac{E_{cathode}}{\Re T}\right) \tag{6.20}$$

Here p_0 is the reference pressure, γ_{anode} and $\gamma_{cathode}$ the anode and cathode pre-exponential coefficients, E_{anode} and $E_{cathode}$ the anode and cathode activation energy respectively.

The partial pressures at the TPB are calculated from the molar concentration along the anode/electrolyte and cathode/electrolyte interfaces, only on triangular elements in contact with these interfaces such as in Fig. 6.2. Further the partial pressures at the fuel and air channels are calculated on triangular elements in contact with the channels/electrodes interfaces (see Fig. 6.2). Finally the electrochemical equations are solved along the cell using the calculated partial pressures at TPB and channels on elements at the same position from the left of the cell (dashed line in Fig. 6.2).

To solve the above nonlinear system, we used an efficient nonlinear solver included in the

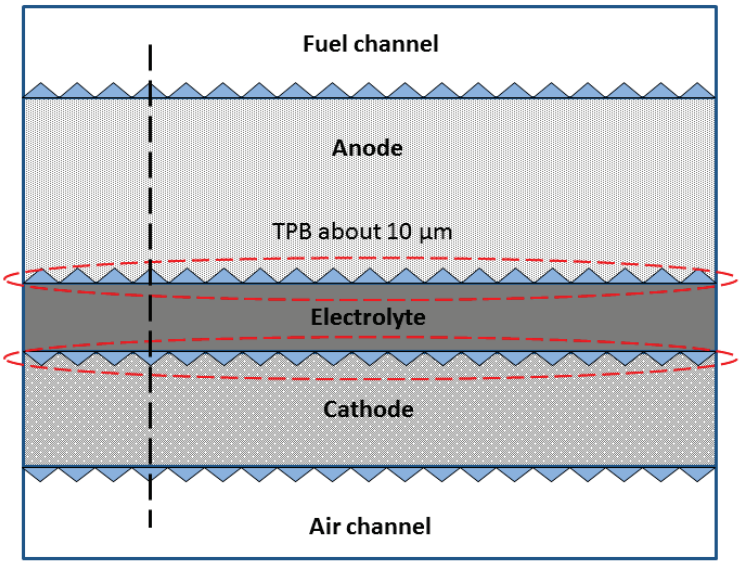

Figure 6.2.: Mesh elements at the cell interfaces

IMSL library (IMSL, 1994). The solver is based on the modified Powell hybrid algorithm which is alternative to the Newton's method.

6.2.3. Solving Procedure of the Multi-Physics Problem

Flow, heat and mass equations are solved sequentially which allows the use of different temporal discretization and therefore, allows achieving high accuracy for each equation. In this work, the fluid flow Eq. (6.2) is solved using an implicit time discretization whereas an explicit time discretization is preferred for the advective part of the heat transfer Eq. (6.3) and mass transfer Eq. (6.4). The unknowns are progressed from the time increment t_n to t_{n+1} as follows:

Step 1: With proposed flow velocities at the inlets of channels as boundary conditions, Darcy-Brinkman Eq. (6.2) is solved to obtain the fluid flow velocity $\mathbf{v}^{n+1}$ for the current time step.

Step 2: Update the heat and species fluxes at the anode/electrolyte and cathode/electrolyte interfaces where the electrochemical reactions take place. The updating equations are:

$$\dot{Q}_T^{n+1} = \frac{T^n \cdot j^n}{4F}\left(2S_{H_2O} - 2S_{H_2} - S_{O_2}\right) + j^n\left(\eta_{Ohm}^n + \eta_{act}^n\right) \tag{6.21}$$

$$\dot{Q}_{S,H_2}^{n+1} = -\frac{j^n}{2F},\ \dot{Q}_{S,H_2O}^{n+1} = \frac{j^n}{2F} \text{ and } \dot{Q}_{S,O_2}^{n+1} = -\frac{j^n}{4F} \tag{6.22}$$

Step 3: The heat and mass transfer Eq. (6.3) and Eq. (6.4) are solved using the flow velocity $\mathbf{v}^{n+1}$ and the fluxes $\dot{Q}_T^{n+1}$, $\dot{Q}_{S,H_2}^{n+1}$, $\dot{Q}_{S,H_2O}^{n+1}$ and $\dot{Q}_{S,O_2}^{n+1}$ on interfaces to get the temperature T^{n+1} as well as species concentration $C_{H_2}^{n+1}$, $C_{H_2O}^{n+1}$ and $C_{O_2}^{n+1}$ at t_{n+1}, respectively.

Step 4: The temperature and species concentrations are used to compute the local current density j^{n+1} in each element at the anode/electrolyte interface by solving Eq. (6.12) with a given operating potential. The Ohmic, activation and concentration overpotentials $\left(\eta_{Ohm}^{n+1},\ \eta_{act}^{n+1} \text{ and } \eta_{conc}^{n+1}\right)$ are obtained as well.

Step 5: Repeat step 1 to step 4 until the whole SOFC system gets steady state.

6.3. Validation

The validation of the mathematical model is conducted on existing SOFC current-voltage (I-V) curves from Rogers et al. (2003) as well experimental results from Fernández-González et al. (2014). Note that these experiments were conducted at constant temperature; therefore in the numerical simulation the heat transfer equation is omitted.

6.3.1. Validation on Rogers et al. (2003) Results

The experimental results of Rogers et al. (2003) were used by Hussain et al. (2006) and Tseronis et al. (2012) to validate their respective SOFC mathematical models. In these experiments the SOFC unit is supplied with 95% hydrogen and 5% water as fuel. While on the cathode side, the SOFC cell is supplied with air containing 21% oxygen and 79% nitrogen. The used model parameters and cell dimensions to predict the I-V curve is reported in Tab. 6.1.

Table 6.1.: Parameters used for SOFC model validation on Rogers et al. (2003) experiments

Operating temperature	$T = 1073.0$ K
Operating pressure	$p = 1.0$ atm
Fuel channel inlet velocity	$v_{fuel} = 0.4$ m/s
Air channel inlet velocity	$v_{air} = 1.0$ m/s
Fuel composition	$x_{H_2} : x_{H_2O} = 0.95 : 0.05$
Air composition	$x_{O_2} : x_{N_2} = 0.21 : 0.79$
Porosity of anode and cathode	$\varepsilon = 0.375$
Tortuosity of anode and cathode	$\tau_g = 1.0$
Average pore radius	$r_p = 2.6 \times 10^{-6}$ m
Fuel cell length	$L = 0.016$ m
Anode electrode layer thickness	$\tau_{anode} = 0.001$ m
Cathode electrode layer thickness	$\tau_{cathode} = 0.00005$ m
Electrolyte thickness	$\tau_{electrolyte} = 0.00001$ m
Anode electrode conductivity	$\sigma_{anode} = 71428.57$ Sm^{-1}
Cathode electrode conductivity	$\sigma_{cathode} = 5376.34$ Sm^{-1}
Electrolyte conductivity	$\sigma_{electrolyte} = 0.64$ Sm^{-1}
Anode pre-exponential coefficient	$\gamma_{anode} = 7.0 \times 10^9$ Am^{-2}
Cathode pre-exponential coefficient	$\gamma_{cathode} = 7.0 \times 10^9$ Am^{-2}
Anode activation energy	$E_{anode} = 1.1 \times 10^5$ J.mol^{-1}
Cathode activation energy	$E_{cathode} = 1.2 \times 10^5$ J.mol^{-1}

In Fig. 6.3, the predicted results are compared to the experimental ones and good agreement is found, except at low cell voltage where the I-V curve seems to drop toward zero voltage faster than the predictions of Hussain et al. (2006) and Tseronis et al. (2012). Indeed their I-V curves seem to stabilize approximately at the operating voltage of 0.4V, while experiments usually show a drop of the operating voltage to zero at low operating voltages (Fernández-González et al., 2014). However the drop of our predicted I-V curve

seems to be not enough to match the experiment for low operating voltage, such as will be seen on the validation of the model on the experiment of (Fernández-González et al., 2014) in Fig. 6.5.

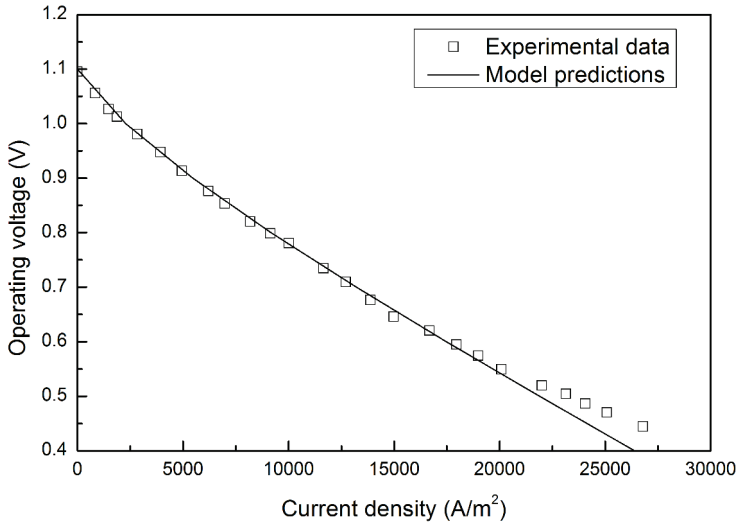

Figure 6.3.: Comparison between the model predictions and experimental results

The predicted gases consumption and water production (Fig. 6.4 (a): hydrogen, Fig. 6.4 (b): oxygen, Fig. 6.4 (c): water) are reported in Fig. 6.4 at steady state. In each subfigure ((a), (b) or (c)) in Fig. 6.4, the three horizontal layers separated by bold lines are: fuel channel (top), anode/electrolyte/cathode (middle) and air channel (bottom). Fig. 6.4 (a) and (c) show the accumulation of the fuel consumption and water production, respectively, along the cell's fuel channel and anode. Since the cathode is very thin, the oxygen consumption (Fig. 6.4 (b)) is only visible in the air channel.

6.3.2. Validation on Fernandez Gonzalez et al. (2014) Results

The SOFC cell tested for obtaining the current-voltage curves (I-V) at different temperatures (Fig. 6.5) is a planar SOFC, where the electrolyte is yttria (8 mol%) stabilized

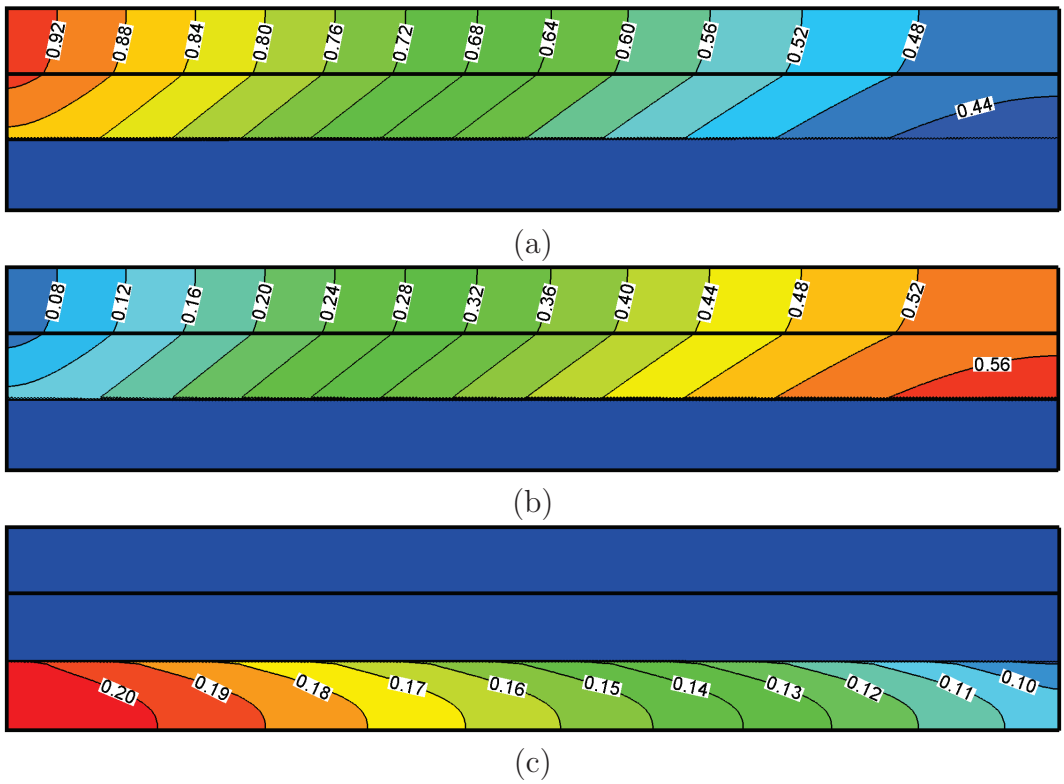

Figure 6.4.: Molar fraction of (a) hydrogen, (b) oxygen, (c) water with operating voltage 0.4V

zirconia (YSZ) provided by Pi-KEM Ltd. (Staffordshire, UK). The anode is a mix of NiO (99,99%; (Sigma-Aldrich, St.Louis, MO, USA) and YSZ in the ratio 60 wt% of NiO and 40% wt% YSZ (Ruiz-Morales et al., 2008; Zhu and Deevi, 2003). The cathode used is platinum paste (Metalor, Birmingham, UK). The electrolyte and the anode material are sintered at 1523K during 4 hours, under reducing conditions. A high temperature ceramic adhesive, Ceramabond™ 552 (Aremco Products, Inc. Valley Cottage, NY, USA), was used for fixing the SOFC cell to the electrochemical measurement setup. The detailed procedure used for preparing this cell is published in (Fernández-González et al., 2014).

The current-voltage curves (I-V) of the manufactured SOFC, were recorded on Zahner elektrick IM6 ex FRA (ZAHNER-Elektrik GmbH & Co.KG, Kronach, Germany) in pure, humidified hydrogen for the anode and pure dry oxygen for the cathode, in the 100 mHz to 300 kHz frequency range with an a.c signal of 50 mV. The I-V curves were obtained in the range of 1123K to 973K, controlling the temperature of the experiment with a

thermocouple close to the sample, keeping constant temperature during the tests.

The model parameters and the cell dimensions used to predict the cell energy efficiency are reported in Tab. 6.2. The predicted I-V curves are compared to the experimental results in Fernández-González et al. (2014) and reported in Fig. 6.5. At high cell voltage the predict I-V curves are in good agreement with the experiments. At low cell voltage the experimental I-V curves slop change leading to a decrease of the current density. This discrepancy becomes important at low cell operating temperatures. A comparison of the predicted power density to the experimental one is illustrated in Fig. 6.6 at temperature of 1123K. Since the power density is deduced from the I-V curve, the agreement of experimental and prediction I-V curves is reflected on the power density curves.

Table 6.2.: Parameters used for SOFC model validation on Fernández-González et al. (2014) experiments

Operating temperature	$T = 973.0 - 1073.0$ K
Operating pressure	$p = 1.0$ atm
Fuel composition	$x_{H_2} : x_{H_2O} = 0.95 : 0.05$
Oxidant composition	$x_{O_2} = 1.0$
Porosity of anode and cathode	$\varepsilon = 0.4$
Tortuosity of anode and cathode	$\tau_g = 4.5$
Average pore radius	$r_p = 2.6 \times 10^{-6}$ m
Fuel cell length	$L = 0.005$ m
Fuel and air channel width	$W = 0.0005$ m
Anode electrode layer thickness	$\tau_{anode} = 0.00001$ m
Cathode electrode layer thickness	$\tau_{cathode} = 0.00002$ m
Electrolyte thickness	$\tau_{electrolyte} = 0.000025$ m
Anode electrode conductivity	$\sigma_{anode} = \frac{9.5 \times 10^7}{T} \exp\left(-\frac{1150}{T}\right)\ \Omega^{-1}\mathrm{m}^{-1}$
Cathode electrode conductivity	$\sigma_{cathode} = \frac{4.2 \times 10^7}{T} \exp\left(-\frac{1200}{T}\right)\ \Omega^{-1}\mathrm{m}^{-1}$
Electrolyte conductivity	$\sigma_{electrolyte} = 3.34 \times 10^4 \exp\left(-\frac{10300}{T}\right)\ \Omega^{-1}\mathrm{m}^{-1}$
Anode pre-exponential coefficient	$\gamma_{anode} = 7.0 \times 10^9\ \mathrm{Am}^{-2}$
Cathode pre-exponential coefficient	$\gamma_{cathode} = 7.0 \times 10^9\ \mathrm{Am}^{-2}$
Anode activation energy	$E_{anode} = 1.2 \times 10^5\ \mathrm{J.mol}^{-1}$
Cathode activation energy	$E_{cathode} = 1.1 \times 10^5\ \mathrm{J.mol}^{-1}$

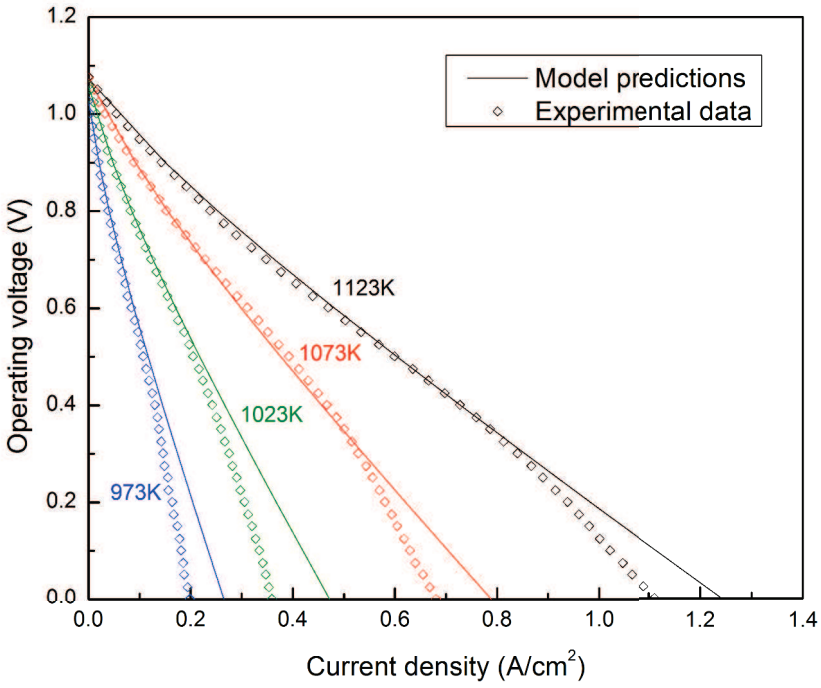

Figure 6.5.: Cell voltage versus current density over the temperature range 973K-1123K

6.4. In-service SOFC Simulation

In this section, simulations are conducted to investigate the effect of the heat generation due to the electrochemical reactions on the cell energy conversion. To this aim simulations are conducted at constant inlet fuel and air temperatures using the model parameters reported in Tab. 6.2, corresponding to the experiments in Fernández-González et al. (2014). The parameters regarding the heat transfer equation are listed in Tab. 6.3.

The heat source (Eq. (6.5)), due to the heat generation of the electrochemical reactions, is considered on electrolyte/anode interface. Fig. 6.7 shows the temperature distribution within the cell at inlet temperature of 1123K and operating voltage of 0.6V. Note that the two bold horizontal lines within Fig. 6.7 are used to separate the three zones of the cell:

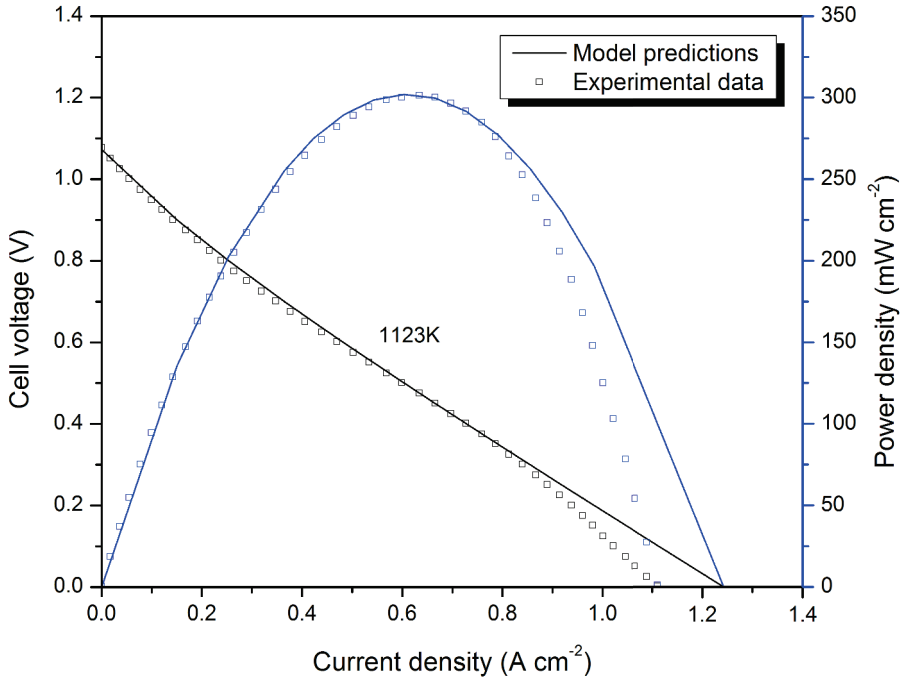

Figure 6.6.: Cell voltage and power density versus current density at 1123K

fuel channel (top), anode/electrolyte/cathode (middle) and the cathode (bottom). Within the cell, a part of the heat generated by the electrochemical reactions is transported out of the cell by conduction and convection through the porous electrodes then the fuel and air channels. Even the electrochemical heat generation is considered only on the electrolyte/anode interface, the difference between the temperatures of the two interfaces of the electrolyte with the porous electrode remains negligible (see Fig. 6.8).This difference is due to the inlet higher velocity of the air compared to the fuel one.

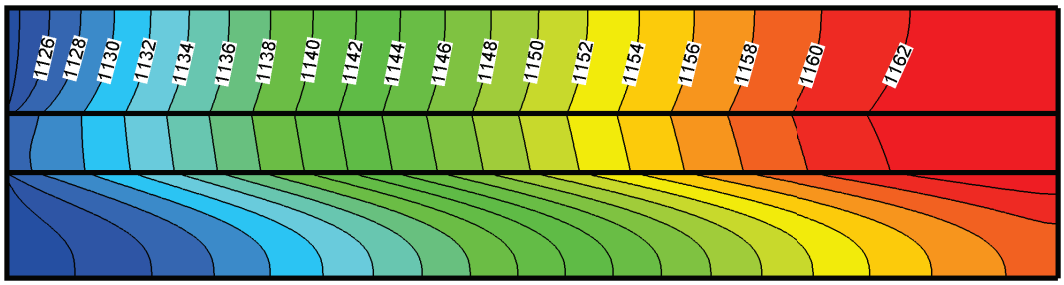

Figure 6.7.: Temperature distribution in SOFC at operating voltage 0.6V and flow inlet temperature 1123K

Table 6.3.: Heat transfer parameters used for in-service SOFC simulation

Volumetric heat capacity	$(\rho c)_{hydrogen} = 0.3395 \times 10^3$ J/(m^3 K)
	$(\rho c)_{oxygen} = 0.3741 \times 10^3$ J/(m^3 K)
	$(\rho c)_{anode} = 8.811 \times 10^5$ J/(m^3 K)
	$(\rho c)_{cathode} = 3.634 \times 10^6$ J/(m^3 K)
	$(\rho c)_{electrolyte} = 3.318 \times 10^6$ J/(m^3 K)
Thermal conductivity	$k_{hydrogen} = 0.450$ J/(s m K)
	$k_{oxygen} = 0.0692$ J/(s m K)
	$k_{anode} = 0.60$ J/(s m K)
	$k_{cathode} = 2.26$ J/(s m K)
	$k_{electrolyte} = 1.55$ J/(s m K)

Fig. 6.9 shows the cell energy efficiency in the isothermal and non-isothermal cases, where the inlet temperature is of 1123K. The low current density at high operating voltage results in weak source term (Eq. (6.5)) in the heat transfer equation, which in turn leads to low electrochemical heat generation and low variation of the cell temperature. Indeed the temperature along the cell at the electrolyte/anode interface is reported in Fig. 6.10, where the maximum variation of the temperature is 6K at 0.9V and 13.5K at 0.8V. Therefore the isothermal and non-isothermal I-V curves are comparable. However, below the operating voltage of 0.7V the high current density results in a high source term and high heat generation that shift the I-V curve towards higher operating voltages. This trend is observed in Fig. 6.10 where the decrease of the cell operating voltage leads to an increase of the heat generation by the electrochemical reactions.

6.5. Conclusions

The multi-physics phenomena taking place in SOFC during service are solved successfully using the DB-EC model. The coupled fluid flow, energy transfer and mass transport are solved at a transient regime using finite element based numerical schemes that deal with the transition between flow-channel/porous electrodes interfaces without any special treatment. The heat generation, as well as the species consumption and production due to the electrochemical reactions are considered on the electrodes/electrolyte interfaces in the energy and mass balance equations. The electrochemistry equations are solved at each

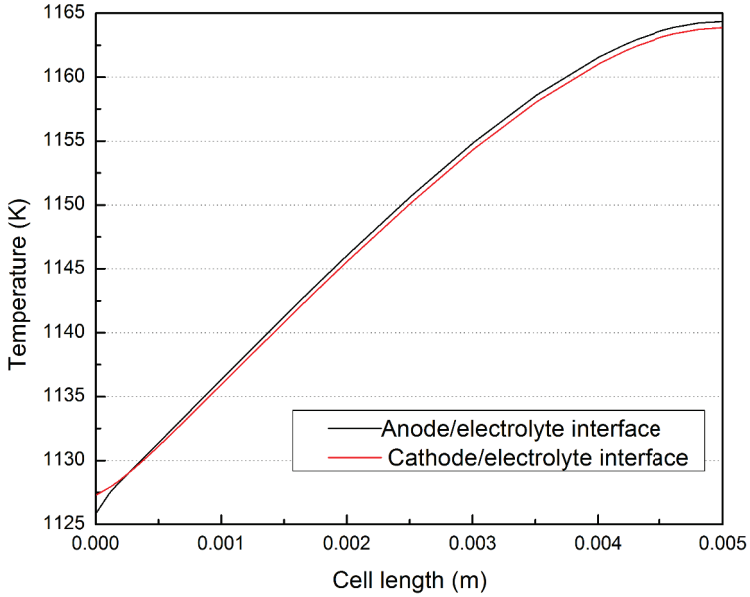

Figure 6.8.: Temperature variations at interfaces with operating voltage 0.6V and flow inlet temperature 1123K

time step to get the local current density at a given cell potential. The predicted I-V curves are validated by comparing with experiments at different constant temperatures (973K - 1123K). Further, simulations are conducted to investigate the effect of the electrochemical generated heat on the cell overall temperature and energy conversion, taking a constant inlet fuel and air temperatures of 1123K. After these validations and applications, several conclusions can be drawn:

1. The model better reproduces the experiment at high operating voltage and temperature. In general the model matches the experiments at operating voltages above 0.4V.

2. The resulted temperature distributions from the in-service SOFC simulation show that the electrochemical generated heat is weak at high operating voltage.

3. The decrease of the cell operating voltage results in an increase of the heat generated by the electrochemical reaction, which in turn leads to an increase of gases consumption and then current density.

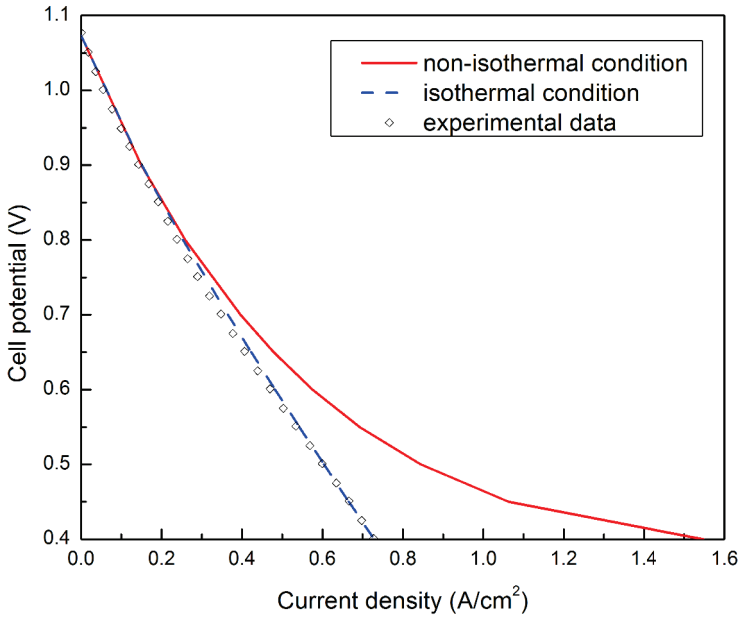

Figure 6.9.: Cell voltage versus current density with temperature 1123K at the flow inlet

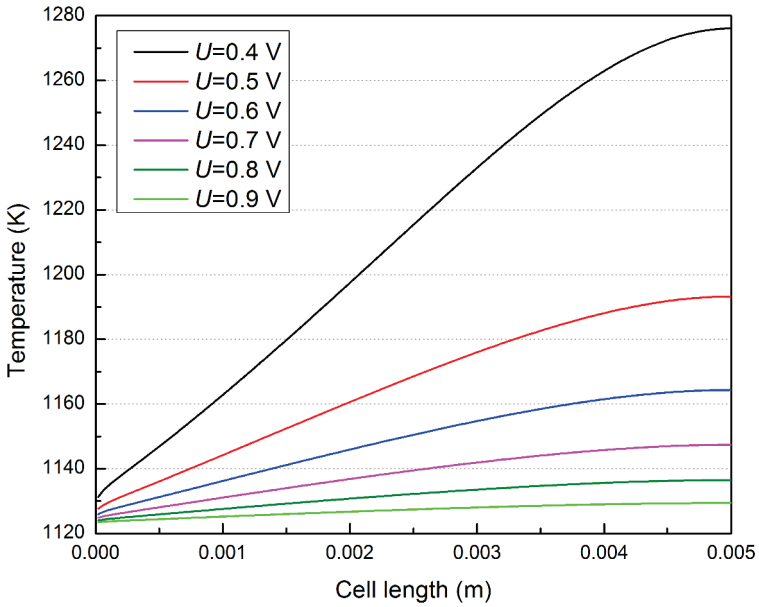

Figure 6.10.: Temperature values at anode/electrolyte interface along the cell length (flow inlet temperature 1123K)

7. Conclusion

Due to their complex temperature profile during service, ceramic based SOFC components undergo severe thermal and mechanical loading that lead to cracks nucleation and propagation. In this thesis, attempts are made to model the multi-physical phenomenon taking place in a SOFC unit in presence of a crack. To this aim, several numerical models are implemented and used to study the sensitivity of the processing and material parameters on crack propagation paths within a SOFC unit.

In Chapter 1, a short literature review on existing experiments and modeling related to energy efficiency and mechanical reliability of SOFCs is introduced, and the objectives of the thesis are addressed.

Chapter 2 is devoted to the model development and validation of coupled fluid flow, heat and mass transfer in porous media. A DB model including both heat and mass buoyancy effects on Darcy-Brinkman flow is implemented on the basis of the NS code developed by Younes et al. (2014). In the DB model, Darcy-Brinkman equation is solved with the nonconforming CR method. While the convection-diffusion heat and mass transport equations are discretized using a combination of DG and MPFA methods. Besides, to reduce the computational time of the coupled problem, a non-iterative time stepping scheme is used to adapt the time step length. For validation, the DB model is used to calculate the double-diffusive natural convection in a square porous cavity with different mesh sizes. In parallel, a steady state semi-analytical solution is developed for this problem using the FG method, to verify the performance of the numerical DB model. Comparison between the numerical and semi-analytical solutions shows that the numerical solutions are weakly dependent on the grid size and in good agreement with the FG solutions.

In the third chapter, we consider the existence of static cracks in the SOFC electrodes to study the effect of fluid flow and heat transport on the stress state at the vicinity of

cracks. To this aim, the Darcy-XFEM model is developed, where the FEM and XFEM are combined to solve the multi-physical problem in cracked porous media. It bears emphasizing that the heat transfer equation is solved using a time splitting procedure. The fluid convection-diffusion heat equation is solved using DG and MPFA methods. In the meantime, to better handle the presence of cracks, the solid heat conduction is discretized using the XFEM. Then the XFEM is also adopted to solve the thermo-mechanical problem by using the temperature resulted from the heat equations as body forces. The impact of the fluid flow and heat transfer on the stress state at the crack tip is evaluated using the SIF evolution. After validation, the model is used to study the effect of fluid flow and heat transfer on the thermo-mechanical behavior of the cracked porous media. It is found that on one side, the temperature distribution and stress concentration are significantly influenced by the variation of the crack angle. On the other side, the SIFs at the crack tips are affected directly by the temperature gradient in the vicinity of the crack.

The fourth chapter is devoted to the crack propagation in the SOFC-like multilayered structure, where a cracked porous material layer is located between a flow channel and a dense material layer. The DB-XFEM model is used to investigate the influence of heat transfer, fluid flow and material properties on the crack propagation. The porous electrodes are taken isotropic. The same governing equations and numerical methods as in Darcy-XFEM model are considered, except that in the DB-XFEM model, the fluid flow is governed by Navier-Stokes in the SOFC flow channels and Darcy-Brinkman in the porous media (anode and cathode), which avoids the interfacial conditions between the channel and porous media. The maximum principle stress criterion is used to determine the crack growth direction (crack orientation angle). After validation, the impact of the flow configurations and electrodes porosities on crack propagation within the SOFC unit are investigated. The effects of other material properties on crack propagation, including the permeability, thermal conductivity and Young's modulus of the porous electrode, are also studied. These parametric studies reveal that the crack propagation has a complex dependence on the material and process parameters within a SOFC unit. Firstly, the crack propagation is due to the built up of residual stresses resulting from the temperature gradient and the mismatch of the layer's physical properties. Secondly, the temperature gradient and the mismatch of the layer's physical properties influence directly the crack orientation amplitude and the deviation from the interface. Finally, the increase of the

permeability and thermal conductivity of the porous electrode results in a decrease of crack orientation amplitude.

In the fifth chapter, the DB-XFEM code is used to investigate the effect of the porous material anisotropy on crack propagation in multilayered SOFC unit. Hence, to take into account the anisotropy, the DB-XFEM model developed in the fourth chapter for the isotropic case is upgraded by using different enrichment functions. Porous material with anisotropic thermal and mechanical properties is constructed using an existing optimization tool based on the statistical continuum theory. Different anisotropies and porosities of the SOFC electrodes are used to investigate their effects on the crack propagation. Studies on the SIFs and crack propagation paths show that, on one hand, the onset of the crack propagation can be delayed either by increasing the anisotropy degree or by decreasing the pores volume fraction of the electrode. On the other hand, the increase of the porous electrodes anisotropy degrees and the pores volume fraction both result in a decrease of crack orientation amplitude and lead to larger deviation of the crack path from the porous media/dense media interface.

Finally, in the sixth chapter, the energy conversion performance of a SOFC unit is investigated by considering the electrochemical reactions taking place at anode/electrolyte and cathode/electrolyte interfaces. An EC model which takes into account the Ohmic, activation and concentration losses is implemented to calculate the current density and the cell potential. The temperature field and species concentrations in the cell are obtained by solving the gas flow, heat and mass transfer equations, with adoption of the DB model introduced in Chapter 2. The heat generation and species consumption/production due to the electrochemical reactions are taken into account as source terms in the heat and mass transfer equations. The governing equations in the DB-EC model are coupled and solved without any special treatment for transition between flow-channel/porous electrodes interfaces. The DB-EC model is validated by comparing the predicted SOFC I-V curves to experimental ones from the literature at different constant temperatures. Results show that the model matches the experiments at operating voltages above 0.4V. Further, simulations are conducted to investigate the effect of the electrochemical generated heat on the cell overall temperature and energy conversion efficiency, taking a constant inlet fuel and air temperatures of 1123K. Regarding the energy conversion performance of the SOFC unit, the decrease of the operating voltage leads to a higher heat generation by the

electrochemical reactions, which in turn results in a high current density.

Perspectives

In this work, we have developed an effective model to simulate fluid flow, heat and mass transfer, crack propagation and electrochemical reactions in a planar SOFC unit. Parametric studies have been done to investigate the effect of the process and material parameters on crack propagation as well as the energy conversion performance in SOFC unit.

Further study might be conducted to highlight the effect of microstructure anisotropy on the energy conversion performances of SOFCs. In fact, microstructure anisotropy enhances the thermal conductivity in preferential direction, which in turn avoids temperature gradient that results in cracks nucleation within the electrodes. Further, enhancing the thermal conductivity in preferential direction will also accelerate the SOFC heating during the heating process, and then reduces the SOFC start-up time.

A. Résumé en Français

Au cours des dernières décennies, les piles à combustible à oxyde solide (SOFC) sont devenues un dispositif prometteur de conversion d'énergie. Ceci est dû principalement à leur efficacité de conversion d'énergie, leur flexibilité du choix du carburant et leurs faibles émissions de polluants. Cependant, la température de fonctionnement élevée de cette variante de piles à combustible induit divers problèmes d'endommagement et de fissuration. Par conséquent, l'optimisation de leur durée de vie reste un problème à résoudre. Dans cette thèse, une approche numérique combinant la méthode des éléments finis (FEM) et la méthode des éléments finis étendus (XFEM) est développée. Le but est de modéliser le problème multiphysique comportant : l'écoulement du fluide, le transfert de la chaleur, le transfert de masse, les réactions électrochimiques et thermomécanique dans une unité de pile à combustible. Dans un premier temps, pour prédire la distribution de la température et des espèces dans le milieu poreux des électrodes, un modèle de Darcy-Brinkman (DB) couplant l'écoulement du gaz, le transfert de chaleur et le transport de masse est développé. Ensuite, la méthode XFEM est introduite pour modéliser la présence des fissures dans les électrodes. Le modèle DB-XFEM combiné est utilisé par la suite pour étudier l'effet de l'écoulement du fluide, le transfert de chaleur et des propriétés thermomécaniques du matériau sur la nucléation et la propagation des fissures. Enfin, un modèle électrochimique (EC) est développé et combiné avec le modèle DB pour étudier les performances de conversion d'énergie dans la cellule de la pile à combustible. Il s'est avéré à l'issue de cette thèse que le modèle proposé est robuste et précis pour résoudre les problèmes multi-physiques dans une unité de la pile à combustible à oxyde solide. Les méthodes numériques avancées utilisées permettent d'obtenir des calculs précis et un cout réduit. Enfin, les études paramétriques menées durant cette thèse révèlent la dépendance de la propagation des fissures et des performances électrochimiques, des propriétés thermomécaniques du matériau poreux de la pile.

A.1. Introduction

La particularité de pile à combustible à oxyde solide est sa haute température de fonctionnement qui présente de nombreux avantages. Par exemple, à haut température, l'activité cinétique est élevée et le nickel est suffisant comme catalyseur, ce qui élimine la nécessité d'utiliser des métaux coûteux (Yakabe et al., 2004; Recknagle et al., 2010). Cependant, la haute température peut conduire à des dégradations des matériaux de la pile. En effet, le gradient thermique et les différents coefficients de dilatation thermique des composants de la pile (Anode/électrolyte/cathode) peuvent conduire à la formation des contraintes résiduelles dans le voisinage des interfaces de la pile, ce qui contribuent à sa dégradation (Yakabe et al., 2004; Bouhala et al., 2010). En outre, les processus de refroidissement et de chauffage, impliquées pendant le fonctionnement de la pile, peuvent conduire à la formation des contraintes résiduelles et possible nucléation des fissures dans le voisinage des interfaces: anode/électrolyte et électrolyte/cathode (Qu et al., 2006). Les chargements thermomécanique pendant le fonctionnement de la pile conduisent au propagation de ces fissures qui peuvent être dévier par les interface de la pile (électrodes/électrolytes) ou pénétrer dans l'électrolyte (Joulaee et al., 2009). En conséquence, d'une part, la présence de fissures dans la pile génère de la chaleur en raison de la résistance ohmique à la pointe de la fissure, qui à son tour affecte considérablement les performances électrochimiques de la pile. D'autre part, les fissures qui pénètrent dans l'électrolyte permettent la fuite du carburant de l'anode à la cathode, ce qui détériore la pile. De plus, les chemins de propagation de fissures dépendent non seulement de la nature de la structure multicouche de la pile, mais également de la microstructure poreuses de ces électrodes. En effet, des défauts d'homogénéité de la microstructure introduits par la distribution spatiale des pores affectent les chemins de propagation des fissures.

A.2. Objectifs

Bien que des études antérieures aient montré un réel progrès sur la modélisation des piles à combustible à oxyde solide, un modèle numérique complet est encore à son stade précoce de développement. En effet, la plupart de ces outils informatiques sont basés sur des codes commerciaux d'éléments finis ou codes simplifiés maison, où les phénomènes multiphysique

dans la pile ne sont pas entièrement résolu, en ignorant la plupart du temps les zones poreuses (Recknagle et al., 2003; Aguiar et al., 2004). En outre, les outils numériques actuels ne prennent pas compte de la corrélation entre la microstructure des électrodes, la performance en conversion d'énergie et la dégradation. En fait, la concentration et la distribution des pores affecte la résistance à la fracture des matériaux poreux (Joulaee et al., 2007). En outre, l'orientation des pores conduit à une connectivité élevée et aussi a une conductivité thermique et électrique élevés dans la direction d'orientation des pores (Mikdam et al., 2013a;b), ce qui améliore le transfert des gaz aux sites actifs et réduit les gradients thermiques à l'intérieur de la pile.

L'objectif de cette thèse est de développer un outil numérique basé sur une combinaison de la méthode éléments finis (FEM) et la méthode élément finis étendu (XFEM), pour résoudre le problème multiphysique dans la pile et prédire l'amorcement et le chemin de propagation d'une fissure existante dans la pile. Des schémas de la méthode élément finis avancés vont être considérés pour résoudre le problème multiphysique. La méthode élément finis étendu va être utilisée pour décrire la discontinuité induite par la fissure et la singularité à la pointe de la fissure. Aussi l'effet de la microstructure des électrodes poreuses et l'anisotropie sur l'amorcement et le chemin de propagation sera étudiée. Enfin, la capacité du modèle numérique développé à prédire le rendement de la conversion énergétique de la pile sera démontré et validés.

A.3. Réponse thermomécanique d'un matériau poreux fissuré: effet de l'écoulement du fluide et transfert de la chaleur

La méthodologie suivie pour la résolution de l'écoulement du fluide, le transfert de chaleur et la réponse thermomécanique dans un milieu poreux isotrope fissuré, se résume comme suit:

- La loi de Darcy est utilisée pour décrire l'écoulement du fluide dans le milieu poreux fissuré. L'équation est résolue en utilisant la méthode des éléments finis non conforme.

- Un schéma combinant FEM/XFEM est utilisé pour résoudre l'équation de transfert de chaleur dans le milieu poreux fissuré.
- La température obtenue est utilisée pour résoudre le problème thermomécanique dans le milieu poreux fissuré en utilisant la méthode élément finis étendu. Ensuite, les facteurs d'intensité de contrainte (FIC) sont calculés en utilisant la technique J-intégral à chaque incrément de temps.

A.3.1. Ecoulement dans un milieu poreux: équation de Darcy

Les équations décrivant l'écoulement dans un milieu poreux sont données par l'équation du bilan de masse et la loi de Darcy:

$$\begin{cases} s\dfrac{\partial p}{\partial t} + \nabla.\mathbf{q} = Q_f \\ \mathbf{q} = -K\nabla p \end{cases} \tag{A.1}$$

Où s est l'emmagasinement spécifique de la matière poreuse, K est la conductivité hydraulique, Q_f est le terme source par unité de surface, p est la pression et $\mathbf{q}$ la vitesse de Darcy.

Combinant l'équation du bilan de masse avec l'équation de Darcy conduit à l'équation de diffusivité:

$$s\frac{\partial p}{\partial t} + \nabla.\left(-K\nabla p\right) = Q_f \tag{A.2}$$

La méthode élément finis non-conforme est utilisée pour résoudre l'équation de l'écoulement du fluide en raison de sa simplicité et ces propriétés de conservation de masse. L'équation de l'écoulement est discrétisée en utilisant des éléments triangulaire linéaire (Fig. A.1).

La pression est supposée varier de façon linéaire à l'intérieur de chaque élément triangulaire E:

$$p_E = p_i\varphi_i^E + p_j\varphi_j^E + p_k\varphi_k^E \tag{A.3}$$

Où les degrés de liberté de la pression sont situés au milieu des arrêtes de l'élément.

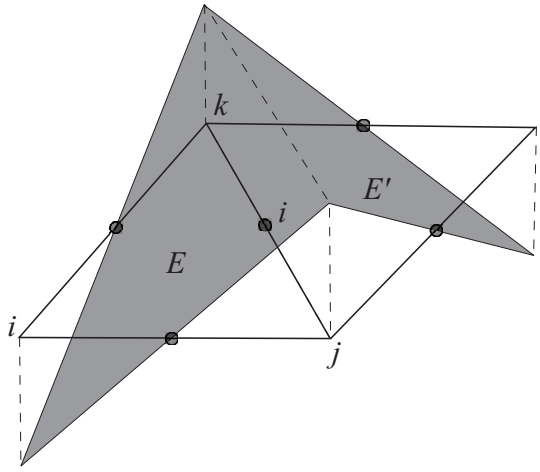

Figure A.1.: La fonction d'interpolation linéaire du champ de pression

La pression p_i est inconnue au milieu de l'arête i, qui est situé en face du nœud i. La fonction d'interpolation φ_i^E est différente de zéro uniquement à l'intérieur des deux éléments adjacents E et E' partageant l'arête i. La fonction est donné par:

$$\varphi_i^E = \frac{1}{|E|}\left[x\left(y_k - y_j\right) + y\left(x_j - x_k\right) + \frac{1}{2}\left(y_j x_k + y_j x_i - y_k x_i - y_k x_j - y_i x_j + y_i x_k\right)\right] \tag{A.4}$$

La formulation variationnelle de l'équation (A.2) en utilisant la fonction de test φ_i s'écrit:

$$\int_\Omega s\frac{\partial p}{\partial t}\varphi_i + \int_\Omega \nabla.\left(-K\nabla p\right)\varphi_i = \int_\Omega Q_f \varphi_i \tag{A.5}$$

Le premier terme pour un arête intérieur i conduit à:

$$\int_\Omega s\frac{\partial p}{\partial t}\varphi_i = \frac{1}{3}\frac{\partial p_i}{\partial t}\left(s_E\left|E\right| + s_{E'}\left|E'\right|\right) \tag{A.6}$$

De la même manière, le terme source conduit à:

$$\int_\Omega Q_f \varphi_i = \frac{Q_f^E\left|E\right|}{3} + \frac{Q_f^{E'}\left|E'\right|}{3} \tag{A.7}$$

En utilisant la formule de Green, le deuxième terme de l'équation (A.5) s'écrit,

$$\int_{\Omega} \nabla.\left(-K\nabla p\right)\varphi_i = \int_{\Omega} \left(K\nabla p\right)\nabla\varphi_i - \int_{\Gamma} \varphi_i \left(K\nabla p\right)\eta_{\Gamma} d\Gamma \tag{A.8}$$

Dans le cas d'une arête intérieur i, elle se simplifie à:

$$\begin{aligned}\int_{\Omega} \nabla.\left(-K\nabla p\right)\varphi_i = &\frac{1}{|E|}\sum_{j=1}^{3} p_{E,j}\left(\nabla\varphi_{E,j}^{T} K_E \nabla\varphi_{E,i}\right) \\ &+ \frac{1}{|E'|}\sum_{j=1}^{3} p_{E',j}\left(\nabla\varphi_{E',j}^{T} K_{E'} \nabla\varphi_{E',i}\right)\end{aligned} \tag{A.9}$$

Utilisation une discrétisation implicite en temps, la forme finale est donnée par:

$$\begin{aligned}&\left(\frac{s_E\,|E| + s_{E'}\,|E'|}{3}\right)\frac{p_i^{n+1} - p_i^n}{\triangle t} - \frac{1}{|E|}\sum_{j=1}^{3} p_{E,j}^{n+1}\left(\nabla\varphi_{E,j}^{T} K_E \nabla\varphi_{E,i}\right) \\ &\quad - \frac{1}{|E'|}\sum_{j=1}^{3} p_{E,j}^{n+1}\left(\nabla\varphi_{E',j}^{T} K_{E'} \nabla\varphi_{E',i}\right) = \frac{Q_f^E\,|E|}{3} + \frac{Q_f^{E'}\,|E'|}{3}\end{aligned} \tag{A.10}$$

Cela conduit à un système final à résoudre avec une matrice symétrique définie positive.

Une fois que ce système est résolu, la vitesse de $\mathbf{q}^E$ du Darcy dans l'élément E et le flux Q_i^E sur chaque arête de l'élément E peut être calculée en utilisant les valeurs locales de la pression $p_{E,j}^{n+1}$.

A.3.2. Transfert de chaleur

Le transfert de chaleur en milieu poreux est régi par conduction de chaleur dans la phase solide et du transport de chaleur dans la phase liquide. Sous l'hypothèse de l'équilibre thermique entre le fluide et les phases solides et négligeant toutes les variations de densité, la température T du milieu poreux est régie par l'équation suivante de conservation de l'énergie totale:

$$\left(\rho c\right)_{PM}\frac{\partial T}{\partial t} + \nabla.\left(\rho_f c_f \mathbf{q} T\right) - \nabla.\left(\mathbf{k}_{PM}\nabla T\right) = Q_T \tag{A.11}$$

Où Q_T représente une terme source dans le milieu poreux. En présence de fissures, le tenseur $\mathbf{k}_{PM}$, qui comprend la dispersion thermique dans la phase liquide et la conduction thermique dans les deux phases liquides et solides, est défini comme suit:

$$\mathbf{k}_{PM} = \begin{cases} \mathbf{k}^f & \text{inside the crack} \\ \mathbf{k}^f + \mathbf{k}^s & \text{other parts} \end{cases} \tag{A.12}$$

Où $\mathbf{k}^f$ comprend la dispersion thermique et la conduction thermique dans la phase liquide, et $\mathbf{k}^s$ est la conduction thermique dans la phase solide. $\mathbf{k}^f$ et $\mathbf{k}^s$ sont donné par:

$$k_{ij}^f = \underbrace{\rho_f c_f \left[\alpha_T \left|\mathbf{q}\right| \delta_{ij} + \left(\alpha_L - \alpha_T\right) \frac{q_i q_j}{\left|\mathbf{q}\right|} \right]}_{dispersive} + \underbrace{\varepsilon k_f \delta_{ij}}_{conductive} \tag{A.13}$$

$$k_{ij}^s = \left(1 - \varepsilon\right) k_s \delta_{ij} \tag{A.14}$$

où α_L et α_T sont respectivement les dispersivities thermique longitudinale et transversale, δ_{ij} est la fonction delta de Kronecker. k_f et k_s sont les conductibilités thermique de la phase liquide et la phase solide, respectivement.

Pour tenir compte de l'existence d'une fissure, nous supposons que la fissure est fines qui n'influencent pas l'écoulement du fluide. Par conséquent, la pression et la distribution de la température dans la phase liquide reste continue même en présence de cracks. Par contre, la conduction de chaleur dans la phase solide est affectée par la fissure ce qui conduit à une discontinuité et singularité du champ de température et du flux respectivement.

Le fractionnement du temps est utilisé pour permettre différents traitements du transfert de chaleur dans les phases solide et fluide. A chaque pas de temps Δt, l'équation de transport de chaleur est d'abord résolu pour calculer $T^{n+1,*}$, la température causé par le transfert thermique dans la phase fluide:

$$\left(\rho c\right)_{PM} \frac{T^{n+1,*} - T^n}{\Delta t} + \nabla.\left(\rho_f c_f \mathbf{q} T\right) - \nabla.\left(\mathbf{k}^f \nabla T\right) = Q_T^f \tag{A.15}$$

Ensuite, la température finale de est obtenue en prenant en compte le transfert de chaleur

dans la phase solide en utilisant comme température initiale:

$$(\rho c)_{PM}\frac{T^{n+1}-T^{n+1,*}}{\Delta t}-\nabla.\left(\mathbf{k}^{s}\nabla T\right)=Q_{T}^{s} \tag{A.16}$$

Discrétisation de l'équation de la chaleur dans la phase fluide Une combinaison de méthodes DG et MPFA sont utilisée pour résoudre le terme d'advection-dispersion dans la phase fluide (Bear, 1972). La méthode DG est utilisée pour la discrétisation de la partie advection. La partie de diffusion est résolue en utilisant la méthode MPFA (Younes and Fontaine, 2008a; Aavatsmark et al., 1996). La méthode MPFA utilise plus de deux éléments pour calculer les flux à travers les arêtes d'élément. La méthode est localement conservatrice et peut gérer des maillages irréguliers sur des domaines hétérogènes anisotropes. L'équation de la chaleur peut être écrite sous la forme mixte suivante:

$$\begin{cases}(\rho c)_{PM}\dfrac{\partial T}{\partial t}+\nabla.\left(\rho_{f}c_{f}\mathbf{q}T\right)+\nabla.\mathbf{q}^{cd}= & Q_{T}^{f}\\ \\ \mathbf{q}^{cd}=-\mathbf{k}^{f}\nabla T\end{cases} \tag{A.17}$$

Où $\mathbf{q}^{cd}$ est le flux de conduction diffusion, qui est supposé de varier linéairement à l'intérieur de l'élément E, donc:

$$\nabla.\mathbf{q}^{cd}=\frac{1}{|E|}\sum_{i}Q_{\partial Ei}^{cd} \tag{A.18}$$

Où $Q_{\partial Ei}^{cd}$ est le flux de chaleur par conduction diffusion à travers le l'arête i de l'élément E. Nous utilisons la méthode DG où la solution approchée $T\left(\boldsymbol{x},t\right)$ est exprimée avec des fonctions de base linéaire ψ_{i}^{E} sur chaque élément:

$$T_{h}\left(\boldsymbol{x},t\right)\mid_{E}=\sum_{i=1}^{3}T_{i}^{E}\left(t\right)\psi_{i}^{E}\left(\boldsymbol{x}\right) \tag{A.19}$$

ou $T_i^E(t)$ $(i = 1,\ 2,\ 3)$ sont les trois inconnues coefficients correspondant aux degrés de liberté qui sont la valeur moyenne de la température définie au centre de gravité de triangle $(\bar{x}_E, \bar{y}_E)$ et ses écarts dans chaque directions d'espace (Cockburn et al., 1989). Ainsi dérivant la formulation variationnelle de l'équation de transport de chaleur et en utilisant la formule de Green, résulte en:

$$\int_E (\rho c)_{PM} \frac{\partial T}{\partial t} \psi_i^E + \int_{\partial E} \rho_f c_f T \psi_i^E \mathbf{q} \cdot \boldsymbol{\eta}_{\partial E} - \int_E \rho_f c_f T \mathbf{q} \cdot \nabla \psi_i^E + \sum_j \frac{Q_{\partial Ej}^{cd}}{|E|} \int_E \psi_i^E = \int_E Q_T \psi_i^E \tag{A.20}$$

Discrétisation de l'équation de la chaleur dans la phase solide La méthode élément finis étendu est utilisée pour discrétiser l'équation de la chaleur dans la phase solide en prenant en compte l'effet de la fissure sur la distribution température:

$$T^h(\boldsymbol{x}) = \sum_{i \in N_\Omega} \Upsilon_i(\boldsymbol{x}) T_i + \sum_{i \in N_\Gamma} \Upsilon_i(\boldsymbol{x}) H^T(\boldsymbol{x}) a_i + \sum_{i \in N_\Lambda} \Upsilon_i(\boldsymbol{x}) br^T(\boldsymbol{x}) b_i \tag{A.21}$$

Υ_i est la fonction de forme sur le nœud i, N_Ω l'ensemble des nœuds de domaine, N_Γ le nombre des nœuds des éléments traversés par la surface de la fissure, N_Λ le nombre des nœuds dans la zone de pointe de la fissure, T_i température au nœud i, a_i, b_i des degrés de liberté correspondant au nœud enrichis, $H^T(\boldsymbol{x})$ et $br^T(\boldsymbol{x})$ les fonctions d'enrichissement de la discontinuité et la singularité.

Substituant la température approchée dans la forme variationnelle de équation de transport de la chaleur, multipliant l'équation par la fonction de la forme et en utilisant la

formule de Green le système suivant est obtenu:

$$(\rho c)_{PM}\begin{bmatrix} R_{ij}^{TT} & R_{ij}^{Ta} & R_{ij}^{Tb} \\ R_{ij}^{aT} & R_{ij}^{aa} & R_{ij}^{ab} \\ R_{ij}^{bT} & R_{ij}^{ba} & R_{ij}^{bb} \end{bmatrix}\begin{bmatrix} \dfrac{\partial T_j}{\partial t} \\ \dfrac{\partial a_j}{\partial t} \\ \dfrac{\partial b_j}{\partial t} \end{bmatrix} + k_{ij}^{s}\begin{bmatrix} G_{ij}^{TT} & G_{ij}^{Ta} & G_{ij}^{Tb} \\ G_{ij}^{aT} & G_{ij}^{aa} & G_{ij}^{ab} \\ G_{ij}^{bT} & G_{ij}^{ba} & G_{ij}^{bb} \end{bmatrix}\begin{bmatrix} T_j \\ a_j \\ b_j \end{bmatrix}$$
$$= Q_T^s \cdot |E| + k_{ij}^{s}\left(\nabla T \cdot \mathbf{n}_{\partial\Omega}\right)\frac{|\partial El|}{2} \tag{A.22}$$

Les éléments $[R]$ et $[G]$ dans les matrices de l'équation (A.22) sont donnés par:

$$\begin{cases} R_{ij}^{TT} = \int_E \Upsilon_j \Upsilon_i \\ R_{ij}^{Ta} = \int_E H^T(\boldsymbol{x})\,\Upsilon_j \Upsilon_i \\ R_{ij}^{Tb} = \int_E br^T(\boldsymbol{x})\,\Upsilon_j \Upsilon_i \end{cases} \tag{A.23}$$

$$\begin{cases} R_{ij}^{aT} = \int_E \Upsilon_j H^T(\boldsymbol{x})\,\Upsilon_i \\ R_{ij}^{aa} = \int_E H^T(\boldsymbol{x})\,\Upsilon_j H^T(\boldsymbol{x})\,\Upsilon_i \\ R_{ij}^{ab} = \int_E br^T(\boldsymbol{x})\,\Upsilon_j H^T(\boldsymbol{x})\,\Upsilon_i \end{cases} \tag{A.24}$$

$$\begin{cases} R_{ij}^{bT} = \int_E \Upsilon_j br^T(\boldsymbol{x})\,\Upsilon_i \\ R_{ij}^{ba} = \int_E H^T(\boldsymbol{x})\,\Upsilon_j br^T(\boldsymbol{x})\,\Upsilon_i \\ R_{ij}^{bb} = \int_E br^T(\boldsymbol{x})\,\Upsilon_j br^T(\boldsymbol{x})\,\Upsilon_i \end{cases} \tag{A.25}$$

$$\begin{cases} G_{ij}^{TT} = \int_E \left(\dfrac{\partial \Upsilon_j}{\partial x}\dfrac{\partial \Upsilon_i}{\partial x} + \dfrac{\partial \Upsilon_j}{\partial y}\dfrac{\partial \Upsilon_i}{\partial y} \right) \\ G_{ij}^{Ta} = \int_E \left(\dfrac{\partial \left(H^T(\boldsymbol{x})\,\Upsilon_j \right)}{\partial x}\dfrac{\partial \Upsilon_i}{\partial x} + \dfrac{\partial \left(H^T(\boldsymbol{x})\,\Upsilon_j \right)}{\partial y}\dfrac{\partial \Upsilon_i}{\partial y} \right) \\ G_{ij}^{Tb} = \int_E \left(\dfrac{\partial \left(br^T(\boldsymbol{x})\,\Upsilon_j \right)}{\partial x}\dfrac{\partial \Upsilon_i}{\partial x} + \dfrac{\partial \left(br^T(\boldsymbol{x})\,\Upsilon_j \right)}{\partial y}\dfrac{\partial \Upsilon_i}{\partial y} \right) \end{cases} \tag{A.26}$$

$$\begin{cases} G_{ij}^{aT} = \int_E \left(\dfrac{\partial \Upsilon_j}{\partial x}\dfrac{\partial \left(H^T(\boldsymbol{x})\,\Upsilon_i \right)}{\partial x} + \dfrac{\partial \Upsilon_j}{\partial y}\dfrac{\left(H^T(\boldsymbol{x})\,\Upsilon_i \right)}{\partial y} \right) \\ G_{ij}^{aa} = \int_E \left(\dfrac{\partial \left(H^T(\boldsymbol{x})\,\Upsilon_j \right)}{\partial x}\dfrac{\left(H^T(\boldsymbol{x})\,\Upsilon_i \right)}{\partial x} + \dfrac{\partial \left(H^T(\boldsymbol{x})\,\Upsilon_j \right)}{\partial y}\dfrac{\left(H^T(\boldsymbol{x})\,\Upsilon_i \right)}{\partial y} \right) \\ G_{ij}^{ab} = \int_E \left(\dfrac{\partial \left(br^T(\boldsymbol{x})\,\Upsilon_j \right)}{\partial x}\dfrac{\left(H^T(\boldsymbol{x})\,\Upsilon_i \right)}{\partial x} + \dfrac{\partial \left(br^T(\boldsymbol{x})\,\Upsilon_j \right)}{\partial y}\dfrac{\left(H^T(\boldsymbol{x})\,\Upsilon_i \right)}{\partial y} \right) \end{cases} \tag{A.27}$$

$$\begin{cases} G_{ij}^{bT} = \int_E \left(\dfrac{\partial \Upsilon_j}{\partial x} \dfrac{\partial \left(br^T(\boldsymbol{x}) \Upsilon_i \right)}{\partial x} + \dfrac{\partial \Upsilon_j}{\partial y} \dfrac{\left(br^T(\boldsymbol{x}) \Upsilon_i \right)}{\partial y} \right) \\ G_{ij}^{ba} = \int_E \left(\dfrac{\partial \left(H^T(\boldsymbol{x}) \Upsilon_j \right)}{\partial x} \dfrac{\left(br^T(\boldsymbol{x}) \Upsilon_i \right)}{\partial x} + \dfrac{\partial \left(H^T(\boldsymbol{x}) \Upsilon_j \right)}{\partial y} \dfrac{\left(br^T(\boldsymbol{x}) \Upsilon_i \right)}{\partial y} \right) \\ G_{ij}^{bb} = \int_E \left(\dfrac{\partial \left(br^T(\boldsymbol{x}) \Upsilon_j \right)}{\partial x} \dfrac{\left(br^T(\boldsymbol{x}) \Upsilon_i \right)}{\partial x} + \dfrac{\partial \left(br^T(\boldsymbol{x}) \Upsilon_j \right)}{\partial y} \dfrac{\left(br^T(\boldsymbol{x}) \Upsilon_i \right)}{\partial y} \right) \end{cases} \tag{A.28}$$

A.3.3. Modèle thermomécanique

L'équation d'équilibre et les conditions aux limites d'un domaine 2D délimité par Γ sont données par:

$$\begin{array}{ll} \nabla_s \boldsymbol{\sigma} + \mathbf{b} = 0 & \text{in } \Omega \\ \mathbf{u} = \bar{\mathbf{u}} & \text{on } \Gamma_u \\ \boldsymbol{\sigma} \cdot \mathbf{n} = \bar{\mathbf{t}} & \text{on } \Gamma_t \end{array} \tag{A.29}$$

où, $\boldsymbol{\sigma}$ est le tenseur de Cauchy, ∇_s est la partie symétrique de l'opérateur divergence, $\mathbf{b}$ est la force de volumique par unité de volume, $\mathbf{u}$ est le vecteur de déplacement, $\mathbf{n}$ est la normale unitaire extérieure, $\bar{\mathbf{u}}$ et $\bar{\mathbf{t}}$ sont respectivement les déplacements et tractions prescrites au limites Γ_u et Γ_t.

La loi de comportement pour un problème thermoélastique est donnée par la loi de Hooke généralisée:

$$\boldsymbol{\sigma} = \mathbf{C} : \mathbf{D} - (\beta^* \Delta T)\, \mathbf{I} \tag{A.30}$$

Où $\mathbf{C}$ est le tenseur de rigidité, $\mathbf{D} = \nabla_s \mathbf{u}$ est le tenseur de déformation, $\Delta T = T - T_0$ est la variation de température entre les étapes actuelle et initiale, $\beta^* = \beta_T E_m / (1 - 2\nu)$ est une constante dépendant des propriétés thermomécanique du matériau.

La forme faible de l'équation d'équilibre peut être écrite comme:

$$\int_{\Omega} \delta\mathbf{D} : \boldsymbol{\sigma} d\Omega = \int_{\Omega} \delta\mathbf{u} \cdot \mathbf{b} d\Omega + \int_{\Gamma_t} \delta\mathbf{u} \cdot \bar{\mathbf{t}} d\Gamma_t \tag{A.31}$$

En substituant Eq. (A.30) dans Eq. (A.31), la forme faible, écrit:

$$\int_{\Omega} \mathbf{D}\left(\delta\mathbf{u}\right) : \left(\mathbf{C} : \mathbf{D}\left(\mathbf{u}\right) - \left(\beta^* \Delta T\right)\mathbf{I}\right) d\Omega = \int_{\Omega} \delta\mathbf{u} \cdot \mathbf{b} d\Omega + \int_{\Gamma_t} \delta\mathbf{u} \cdot \bar{\mathbf{t}} d\Gamma_t \tag{A.32}$$

Utilisation de la méthode d'élément finis étendu le déplacement peut être approximée comme suivant:

$$\mathbf{u}^h\left(\boldsymbol{x}\right) = \sum_{i \in N} \Upsilon_i \mathbf{u}_i + \sum_{i \in N_\Gamma} \Upsilon_i H\left(\boldsymbol{x}\right) \mathbf{c}_i + \sum_{i \in N_\Lambda} \Upsilon_i \sum_k br_k\left(\boldsymbol{x}\right) \mathbf{d}_i^k \tag{A.33}$$

Où $\mathbf{c}_i$ et $\mathbf{d}_i^k$ sont degrés de la liberté sur la surface et la pointe de la fissure. Les fonctions $br_k\left(\boldsymbol{x}\right)$ décrivant la singularité a la pointe de la fissure sont donées par:

$$br_{1-4}\left(r, \vartheta\right) = \left\{ \sqrt{r} \sin\frac{\vartheta}{2}, \sqrt{r} \cos\frac{\vartheta}{2}, \sqrt{r} \sin\frac{\vartheta}{2} \sin\vartheta, \sqrt{r} \cos\frac{\vartheta}{2} \sin\vartheta \right\} \tag{A.34}$$

En substutuant Eq. (A.33) dans Eq. (A.31), conduit au le système d'équation suivant:

$$\mathbf{KU} = \mathbf{F} \tag{A.35}$$

$$\mathbf{K}_{ij} = \int_{\Omega} \mathbf{B}_i^T \mathbf{C} \mathbf{B}_j d\Omega \tag{A.36}$$

$$\mathbf{f}_i = \int_{\Omega} \mathbf{B}_i^T \left(\beta^* \triangle T\right) \mathbf{I} d\Omega + \int_{\Omega} \Upsilon_i^T \mathbf{b} d\Omega + \int_{\Gamma_t} \Upsilon_i^T \bar{\mathbf{t}} d\Gamma_t \tag{A.37}$$

$\mathbf{B}_i$ est la matrice des dérivés des fonctions de forme sur le nœud i. Quand le nœud n'est

pas enrichi la matrice $\mathbf{B}_i$ est donnée par:

$$\mathbf{B}_i = \begin{bmatrix} \Upsilon_{i,x} & 0 \\ 0 & \Upsilon_{i,y} \\ \Upsilon_{i,y} & \Upsilon_{i,x} \end{bmatrix} \tag{A.38}$$

Où $\Upsilon_{i,x}$ et $\Upsilon_{i,y}$ sont les dérivés de des fonctions de forme:

$$\Upsilon_{i,x} = \frac{\partial \Upsilon_i}{\partial x},\ \Upsilon_{i,y} = \frac{\partial \Upsilon_i}{\partial y} \tag{A.39}$$

Quand le nœud est enrichi et sur la surface de la fissure, la matrice $\mathbf{B}_i$ est donnée par:

$$\mathbf{B}_i = \begin{bmatrix} \Upsilon_{i,x} & 0 & \Upsilon_{i,x} H(\boldsymbol{x}) & 0 \\ 0 & \Upsilon_{i,y} & 0 & \Upsilon_{i,y} H(\boldsymbol{x}) \\ \Upsilon_{i,y} & \Upsilon_{i,x} & \Upsilon_{i,y} H(\boldsymbol{x}) & \Upsilon_{i,x} H(\boldsymbol{x}) \end{bmatrix} \tag{A.40}$$

Quand le nœud est enrichi et sur la surface la pointe de la fissure, la matrice $\mathbf{B}_i$ est donnée par:

$$\mathbf{B}_i = \begin{bmatrix} \Upsilon_{i,x} & 0 & \mathcal{X}^i_{1,x} & 0 & \mathcal{X}^i_{2,x} & 0 & \mathcal{X}^i_{3,x} & 0 & \mathcal{X}^i_{4,x} & 0 \\ 0 & \Upsilon_{i,y} & 0 & \mathcal{X}^i_{1,y} & 0 & \mathcal{X}^i_{2,y} & 0 & \mathcal{X}^i_{3,y} & 0 & \mathcal{X}^i_{4,y} \\ \Upsilon_{i,y} & \Upsilon_{i,x} & \mathcal{X}^i_{1,y} & \mathcal{X}^i_{1,x} & \mathcal{X}^i_{2,y} & \mathcal{X}^i_{2,x} & \mathcal{X}^i_{3,y} & \mathcal{X}^i_{3,x} & \mathcal{X}^i_{4,y} & \mathcal{X}^i_{4,x} \end{bmatrix} \tag{A.41}$$

Où $\mathcal{X}^i_{k,x} = \Upsilon_{i,x} br_k(\boldsymbol{x}) + \Upsilon_i br_{k,x}(\boldsymbol{x})$ et $\mathcal{X}^i_{k,y} = \Upsilon_{i,y} br_k(\boldsymbol{x}) + \Upsilon_i br_{k,y}(\boldsymbol{x})$, avec $k = 1...4$.

A.3.4. Facteurs d'intensité de contrainte

Les facteurs d'intensité de contrainte (FIC) sont calculés en utilisant l'interaction intégrale qui est dérivé de la technique J-intégral. Cette technique suppose l'existence d'un mode

auxiliaire $\left(\sigma_{ij}^{(2)}, D_{ij}^{(2)}, u_i^{(2)}\right)$ associé au mode réel $\left(\sigma_{ij}^{(1)}, D_{ij}^{(1)}, u_i^{(1)}\right)$. En utilisant le principe de superposition et la théorie de Green, l'intégrale d'interaction entre l'État (1) et l'État (2) est définit par (Bouhala et al., 2010; 2012; Duflot, 2008)

$$I^{(1,2)} = \int_A \left[\sigma_{ij}^{(1)} \frac{\partial u_i^{(2)}}{\partial x_1} + \sigma_{ij}^{(2)} \frac{\partial u_i^{(1)}}{\partial x_1} - \mathcal{W}^{(1,2)} \delta_{1j}\right] \frac{\partial q_A}{\partial x_j} dA + \int_A \left[\beta^* trace\left(D^{(2)}\right) \frac{\partial T}{\partial x_1}\right] q_A dA \tag{A.42}$$

où A est un domaine intégration entourant la pointe de la fissure, comme le montre la Fig. A.2. q_A est la fonction de pondération définie sur le domaine intégration A qui prend une valeur de l'unité à la pointe de la fissure et de zéro sur le contour Γ (Fig. A.2).

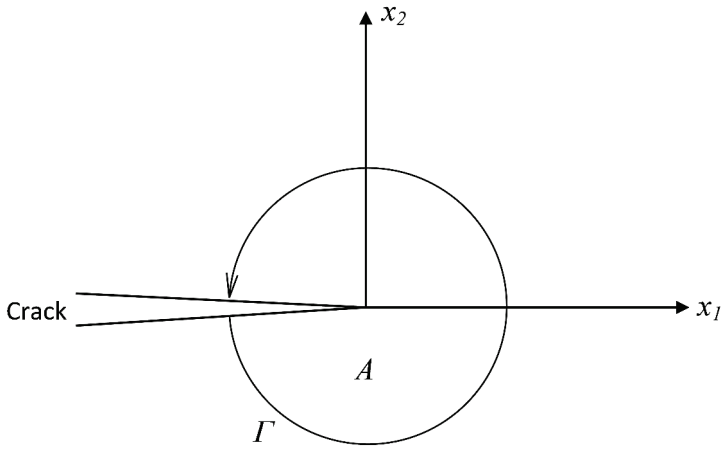

Figure A.2.: Le domaine intégration A et le contour Γ entourant la pointe de la fissure

L'énergie de déformation d'interaction $\mathcal{W}^{(1,2)}$ est calculée dans le cas d'un problème thermomécaniques par:

$$\mathcal{W}^{(1,2)} = \frac{1}{2}\left(\sigma_{ij}^{(1)} D_{ij}^{(2)} + \sigma_{ij}^{(2)} D_{ij}^{(1)} - \beta^* D_{ij}^{(2)} \Delta T\right) \tag{A.43}$$

Notez que l'intégral d'interaction est une fonction du FIC des deux états (1) et (2):

$$I^{(1,2)} = \frac{2}{E_m^*}\left(K_I^{(1)} K_I^{(2)} + K_{II}^{(1)} K_{II}^{(2)}\right) \tag{A.44}$$

K_I et K_{II} sont les FIC pour mode I et II respectivement, avec $E_m^* = E_m/\left(1-\nu^2\right)$ dans le cas d'un problème à déformation plane et $E_m^* = E_m$ dans le cas d'un problème à contrainte plane. Combinant Eq. (A.42) et Eq. (A.44), les FIC peuvent être calculées en choisissant le mode auxiliaire adéquate. Par exemple, pour calculer K_I, nous choisissons le mode I pur comme un mode auxiliaire avec un FIC unitaire. Ce choix conduit à $K_I^{(2)} = 1$, $K_{II}^{(2)} = 0$, donc Eq. (A.44) est réduite à $I^{(1,2)} = 2K_I^{(1)}/E_m^*$. Pour cette pur mode I, les champs de contrainte et de déplacement sont donnés en termes de coordonnées polaires locales autour de la pointe de la fissure par:

$$\sigma_{xx} = \frac{K_I}{\sqrt{2\pi r}} \cos\frac{\vartheta}{2}\left(1 - \sin\frac{\vartheta}{2}\sin\frac{3\vartheta}{2}\right) \tag{A.45}$$

$$\sigma_{yy} = \frac{K_I}{\sqrt{2\pi r}} \cos\frac{\vartheta}{2}\left(1 + \sin\frac{\vartheta}{2}\sin\frac{3\vartheta}{2}\right) \tag{A.46}$$

$$\sigma_{xy} = \frac{K_I}{\sqrt{2\pi r}} \sin\frac{\vartheta}{2}\cos\frac{\vartheta}{2}\cos\frac{3\vartheta}{2} \tag{A.47}$$

$$u_x = \frac{K_I}{2\mu}\sqrt{\frac{r}{2\pi}} \cos\frac{\vartheta}{2}\left(\kappa - 1 + 2\sin^2\frac{\vartheta}{2}\right) \tag{A.48}$$

$$u_y = \frac{K_I}{2\mu}\sqrt{\frac{r}{2\pi}} \sin\frac{\vartheta}{2}\left(\kappa + 1 - 2\cos^2\frac{\vartheta}{2}\right) \tag{A.49}$$

De même, K_{II} peut être obtenue en choisissant un mode II pur comme mode auxiliaire avec SIC unitaire ($K_I^{(2)} = 0$, $K_{II}^{(2)} = 1$). Les solutions exactes de contraintes et de déplacements pour le mode de cisaillement sont données par:

$$\sigma_{xx} = -\frac{K_{II}}{\sqrt{2\pi r}} \sin\frac{\vartheta}{2}\left(2 + \cos\frac{\vartheta}{2}\cos\frac{3\vartheta}{2}\right) \tag{A.50}$$

$$\sigma_{yy} = \frac{K_{II}}{\sqrt{2\pi r}} \sin\frac{\vartheta}{2} \cos\frac{\vartheta}{2} \cos\frac{3\vartheta}{2} \tag{A.51}$$

$$\sigma_{xy} = \frac{K_{II}}{\sqrt{2\pi r}} \cos\frac{\vartheta}{2} \left(1 - \sin\frac{\vartheta}{2} \sin\frac{3\vartheta}{2}\right) \tag{A.52}$$

$$u_x = \frac{K_{II}}{2\mu}\sqrt{\frac{r}{2\pi}} \sin\frac{\vartheta}{2} \left(\kappa + 1 + 2\cos^2\frac{\vartheta}{2}\right) \tag{A.53}$$

$$u_y = -\frac{K_{II}}{2\mu}\sqrt{\frac{r}{2\pi}} \cos\frac{\vartheta}{2} \left(\kappa - 1 - 2\sin^2\frac{\vartheta}{2}\right) \tag{A.54}$$

Le module de cisaillement μ_m et la constante de Kolosov κ sont définis en termes du module de Young et le coefficient de Poisson par:

$$\mu_m = \frac{E_m}{2\,(1+\nu)},\ \kappa = 3 - 4\nu \tag{A.55}$$

A.3.5. Application et validation

Une plaque rectangulaire avec des dimensions ($W = 1$ m, $L = 0,5$ m) et des conditions aux limites (voir la Fig. A.3) Que ceux utilisés dans la littérature(Duflot, 2008; Murakami et al., 1987; Prasad et al., 1994a), est considéré dans ce travail. Une fissure inclinée est positionnée dans le centre de la plaque. Comme conditions aux limites, le fond de la plaque est maintenue à une température $T = -T_0$, et la partie supérieure de la plaque présente une température de $T = T_0$ ($T_0 = 100$°C dans cet exemple). Les limites gauche et droite ainsi que la fissure sont considérées adiabatique. Les propriétés du matériau de la plaque sont rapportées dans la Tab. A.1. La simulation est effectuée en utilisant une longueur de fissure $2a$ qui varient de 0,4 m à 1,2 m avec un pas de 0,2 m, tandis que

l'angle de la fissure varie de 0° à 90° avec un pas de 15°.

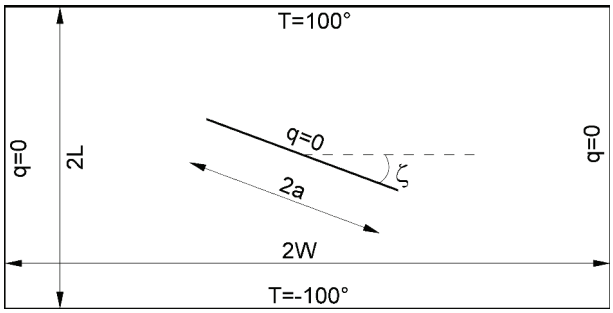

Figure A.3.: Plaque rectangulaire avec une fissure inclinée adiabatique

Table A.1.: Propriétés du matériau de la plaque rectangulaire

Module de Young	$E_m = 7,4 \times 10^4$ MPa
Coefficient de Poisson	$\nu = 0,3$
Coefficient de dilatation thermique	$\beta_T = 1,67 \times 10^{-5}/°\text{C}$
Capacité thermique volumique	$\rho C = 2,3 \times 10^5$ J/(m^3°C)
Conductivité thermique	$k = 4,0 \times 10^2$ J/(sm°C)

Fig. A.4 montre le contour de température obtenues et les contraintes calculées après 5s, 30s et 400s dans le cas ou $a/W = 0,3$ et $\zeta = 45°$. Cette figure montre bien les discontinuités de température à la surface de la fissure et les concentrations de contraintes aux extrémités de la fissure.

Pour étudier l'état de contrainte à la pointe de la fissure, les FIC sont calculés à partir des solutions de déplacements et des contraintes à chaque pas de temps. Les FIC obtenus à l'état transitoire sont normalisées par:

$$F_{I,II} = \frac{K_{I,II}}{\beta_T T_0 \, (W/L) \, E_m \sqrt{2W}} \tag{A.56}$$

Où T_0 est la température prescrite à la limite de la plaque, $F_{I,II}$ les FIC normalisés pour mode I et II. Les courbes de la Fig. A.5 illustre l'évolution des FIC normalisées en fonction du temps pour différentes longueurs de fissure tandis que les courbes de la Fig. A.6 montrent leur évolution pour différents angles de la fissure. Ces figures montrent que dans des cas, les FIC peuvent avoir un maximum avant d'éteindre le régime permanent. Par

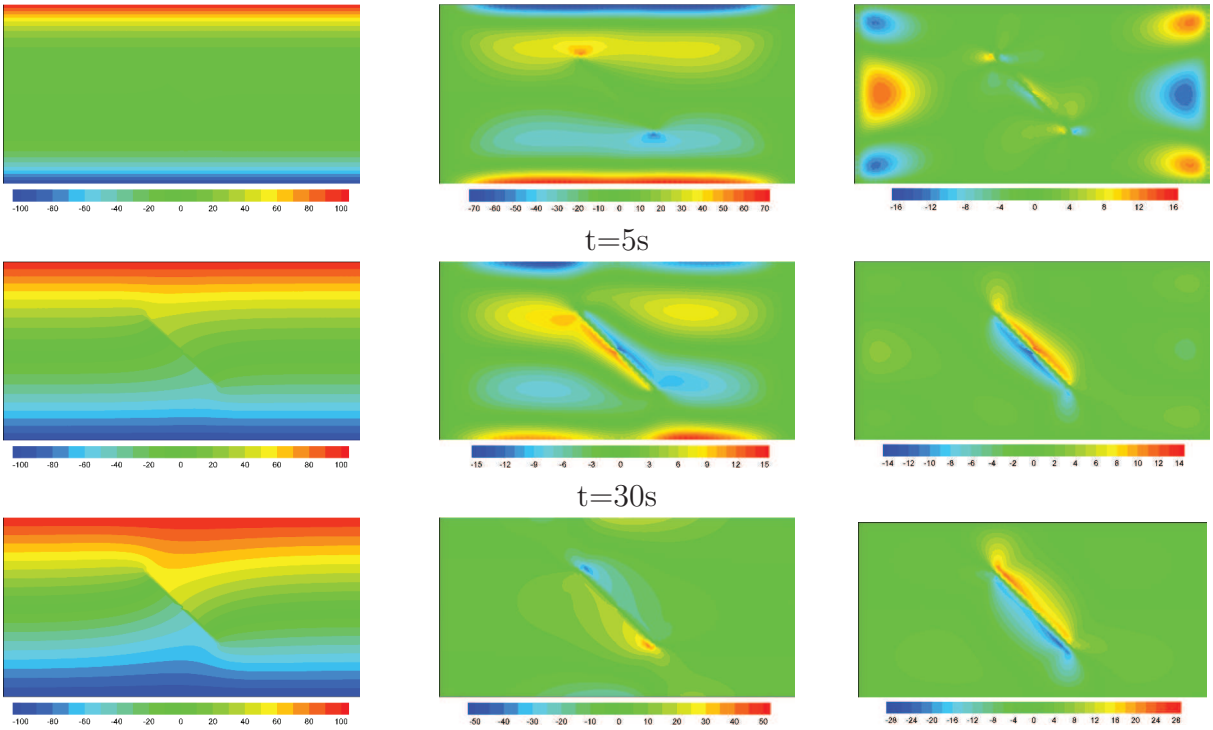

Figure A.4.: Le contour de température et les contraintes aux différents temps de simulation ($a/W = 0,3$, $\zeta = 45°$)

exemple, dans le cas du $a/W = 0,3$ et $\zeta = 90°$, la valeur de F_I est élevée au début de la simulation (temps $<$ 30s) et devient nulle au régime permanent (temps $>$ 100s), voir Fig. A.6 (a). Une autre remarque importante peut être soulevée concernant la valeur négative du F_{II} au début des simulations, voir Fig. A.5 (b) et Fig. A.6 (b). Notez que, à la fois F_I et F_{II} subissent un changement important avant de converger à leurs valeurs au régime permanent. Par conséquent, les critères du nucléation et propagation de la fissure doivent prendre en compte cette évolution de la FIC.

Pour vérifier la précision du modèle thermo-mécanique proposée, les FIC normalisées obtenues au régime permanent sont comparés avec ceux publiés dans Duflot (2008), Murakami et al. (1987) et Prasad et al. (1994a). Tab. A.2 résume les valeurs de F_I et F_{II} obtenu au régime permanent pour diverses longueurs de fissure et un angle de fissure est égal à 30 °. Tab. A.3 résume les valeurs de F_I et F_{II} obtenu au régime permanent

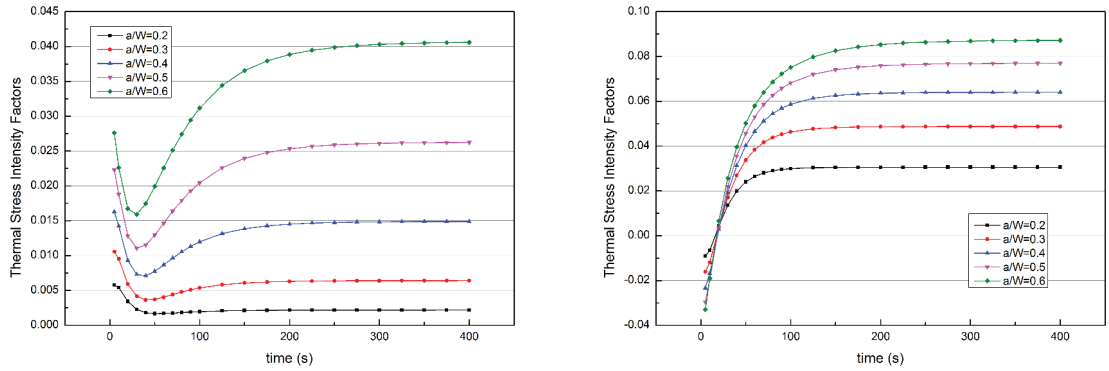

(a) F_I (b) F_{II}

Figure A.5.: L'évolution des FIC normalisées en fonction du temps pour $\zeta = 30°$ et a/W varié

de la présente étude, et ceux de la littérature pour différents angles de crack et d'une longueur de la fissure de $a/W = 0,3$. Les résultats obtenus sont en accord avec ceux de la littérature.

Table A.2.: FIC normalisées pour la fissure inclinée adiabatique, $\zeta = 30°$ et a/W varié

	F_I				F_{II}			
a/W	Cette étude	Duflot (2008)	Prasad (1994)	Murakami (1987)	Cette étude	Duflot (2008)	Prasad (1994)	Murakami (1987)
0,2	0,0022	0,0020	0,002	0,002	0,0306	0,0302	0,030	0,030
0,3	0,0064	0,0068	0,006	0,008	0,0488	0,0489	0,048	0,048
0,4	0,0149	0,0149	0,014	0,015	0,0641	0,0650	0,064	0,064
0,5	0,0262	0,0265	0,026	0,027	0,0769	0,0774	0,076	0,076
0,6	0,0406	0,0407	0,040	0,041	0,0872	0,0878	0,087	0,086

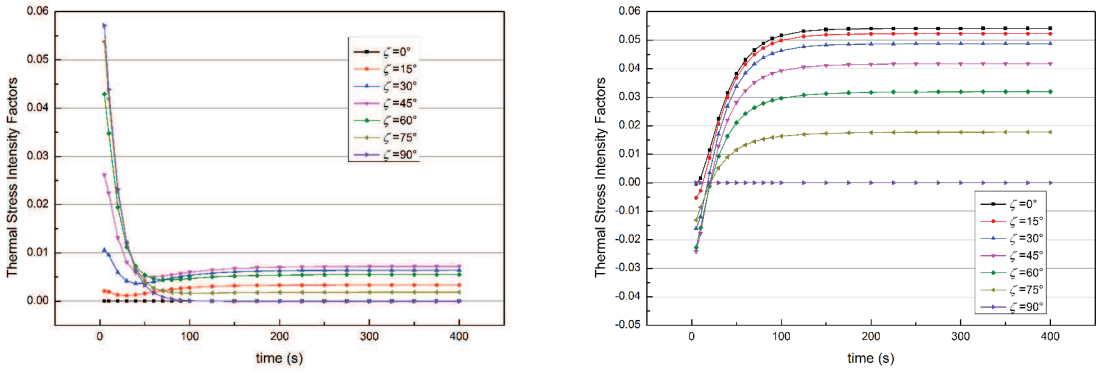

(a) F_I (b) F_{II}

Figure A.6.: L'évolution des FIC normalisées en fonction du temps pour $a/W = 0,3$ et angle de la fissure ζ varié

Table A.3.: FIC normalisées pour la fissure inclinée adiabatique, $a/W = 0,3$ et ζ varié

	F_I				F_{II}			
ζ	Cette étude	Duflot (2008)	Prasad (1994)	Murakami (1987)	Cette étude	Duflot (2008)	Prasad (1994)	Murakami (1987)
0°	0,0000	0,0000	0,0000	0,0000	0,0541	0,0546	0,054	0,054
15°	0,0034	0,0038	0,0036	0,0038	0,0523	0,0533	0,054	0,054
30°	0,0064	0,0068	0,0064	0,0071	0,0488	0,0489	0,048	0,048
45°	0,0072	0,0076	0,0071	0,0077	0,0418	0,0420	0,041	0,042
60°	0,0055	0,0054	0,0049	0,0053	0,0319	0,0322	0,032	0,032
75°	0,0018	0,0017	0,0010	0,0023	0,0178	0,0180	0,018	0,018
90°	0,0000	0,0000	0,0003	0,0000	0,0000	0,0000	0,000	0,000

A.4. Propagation de fissure dans un bi-matériau dense/poreux: application au pile à combustible a oxyde solide

A.4.1. Formulation du problème

Dans le paragraphe précédent, nous avons modélisé la réponse d'un milieu poreux fissuré sous un chargement multiphysics en utilisant FEM/XFEM. L'étude a été limitée à un milieu poreux avec des fissures statiques, où l'écoulement du fluide a été décrit

par l'équation de Darcy. Le présent paragraphe est consacré à la propagation d'une fissure situé dans une couche de matériau poreux entre un canal d'écoulement et d'une couche de matériaux denses (voir Fig. A.7). Cette structure (canal d'écoulement/couche poreuse/couche dense) est typique au pile à combustible oxyde solide, où le fluide pénètre dans la structure multicouche, avec un débit et une température constante, à travers le canal d'écoulement puis se diffuse ensuite dans la couche poreuse.

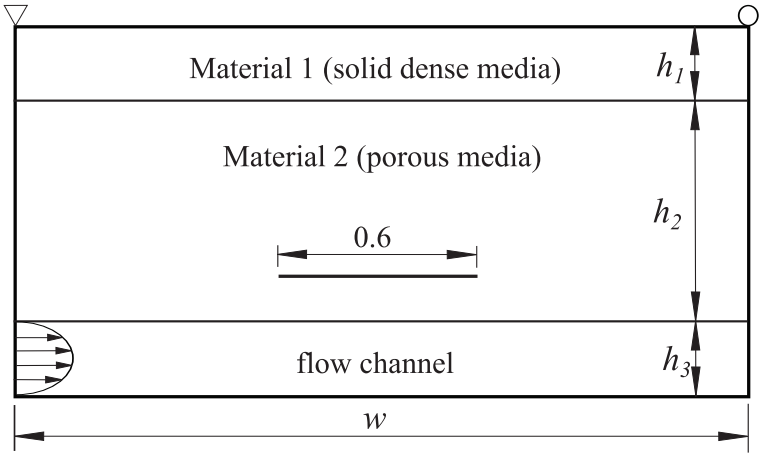

Figure A.7.: Demi-structure avec trois couches et une fissure interne

Le modèle DB-XFEM décrit dans le paragraphe précédent, est utilisé ici pour résoudre l'écoulement du fluide, le transfert de chaleur, la réponse thermomécanique et la propagation des fissures dans la structure multicouche. La méthodologie suivie se résume comme suit:

- Navier-Stokes et Darcy-Brinkman équations sont résolues respectivement dans le canal d'écoulement et le matériau poreux en utilisant la méthode Crouzeix-Raviart non conforme.
- Le transfert de chaleur est divisé en deux équations et ensuite résolu avec des méthodes numérique différent: une équation est résolution par une combinaison des méthodes DG et MPFA, l'autre équation est résolu avec XFEM pour tenir compte de la fissure.

- Le champ de la température résultant de l'équation de transport de chaleur est utilisé comme une force interne, et le problème thermomécanique dans la structure multicouche est résolu avec XFEM.
- Les facteurs d'intensité de contrainte sont calculés pour chaque incrément de temps durant la simulation pour décider si la fissure se propage ou non.
- Le critère de maximum de contrainte principale est utilisé pour déterminer l'orientation de la propagation des fissures.

A.4.2. Application et validation

Unité d'une pile à combustible d'oxyde solide est constituée par un électrolyte solide dense situé entre une anode et une cathode poreuse, et deux canaux d'écoulement adjacents aux couches poreuses. Au cours du fonctionnement, l'écoulement pénètre dans la structure multicouche à travers le canal d'écoulement, avec une température et un dedit d'entrée constante, puis diffuse dans la couche poreuse adjacent (voir Fig. A.8). Une fissure horizontale d'une épaisseur de 0,25 mm et longueur de 6 mm est supposée localiser dans la cathode poreuse. La fissure commence à se propager lorsque la FIC équivalent surmonte la ténacité des matériaux. Au cours de la propagation, la fissure est supposée garder une épaisseur constante.

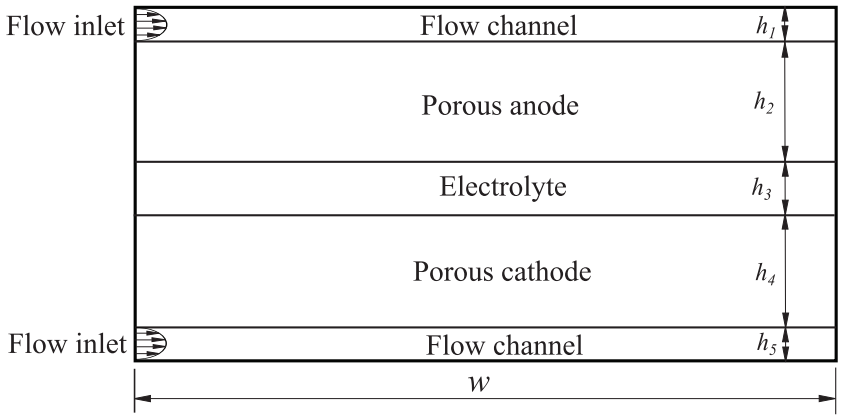

Figure A.8.: Une unité de SOFC

Fig. A.9 montre le trajet de propagation de la fissure pour différentes porosités du matériau de l'anode et la cathode. Pour tous les porosités considéré, la propagation de la fissure commence pointe gauche de la fissure, puis suivie par la pointe de la fissure droite. En outre, le temps de début de propagation de la fissure augmente avec la diminution de la porosité. En raison de la charge complexe induit par la variation de la répartition spatiale de la température, la pointe gauche de la fissure se propage vers l'interface électrolyte/cathode tandis que la pointe droite de la fissure se propage vers l'interface canal/cathode. Une fois à proximité de l'interface électrolyte/cathode, la fissure se dévie due au rapport des propriétés mécaniques entre la cathode et l'électrolyte.

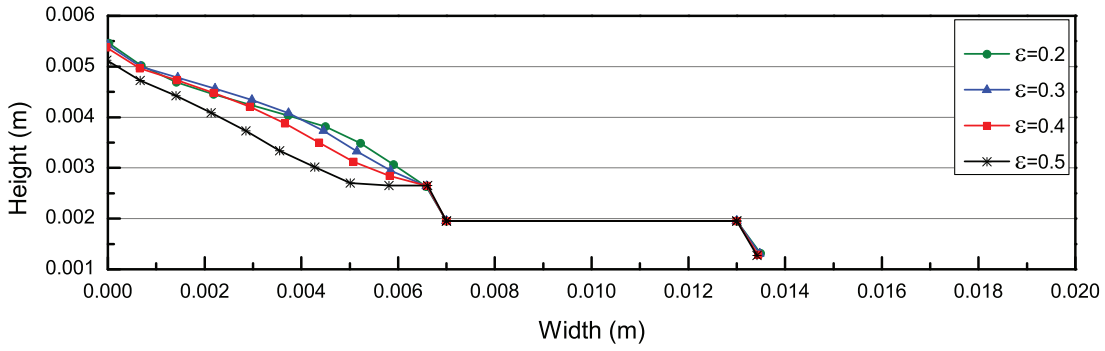

Figure A.9.: Positions de pointes de la fissure pour différentes porosités du matériau

Fig. A.10 illustre les déplacements, la température et les contours des composants de contraintes à la fin de la simulation dans le cas où la porosité des électrodes est de 0,2. Les contraintes résiduelles au voisinage des interfaces électrodes/d'électrolyte sont plus élevés sur le côté gauche de la cellule en raison de la faible épaisseur de l'anode qui permet une diffusion de la température. Les contraintes résiduelles varient avec la porosité des électrodes puis affecte les chemins de propagation de la fissure.

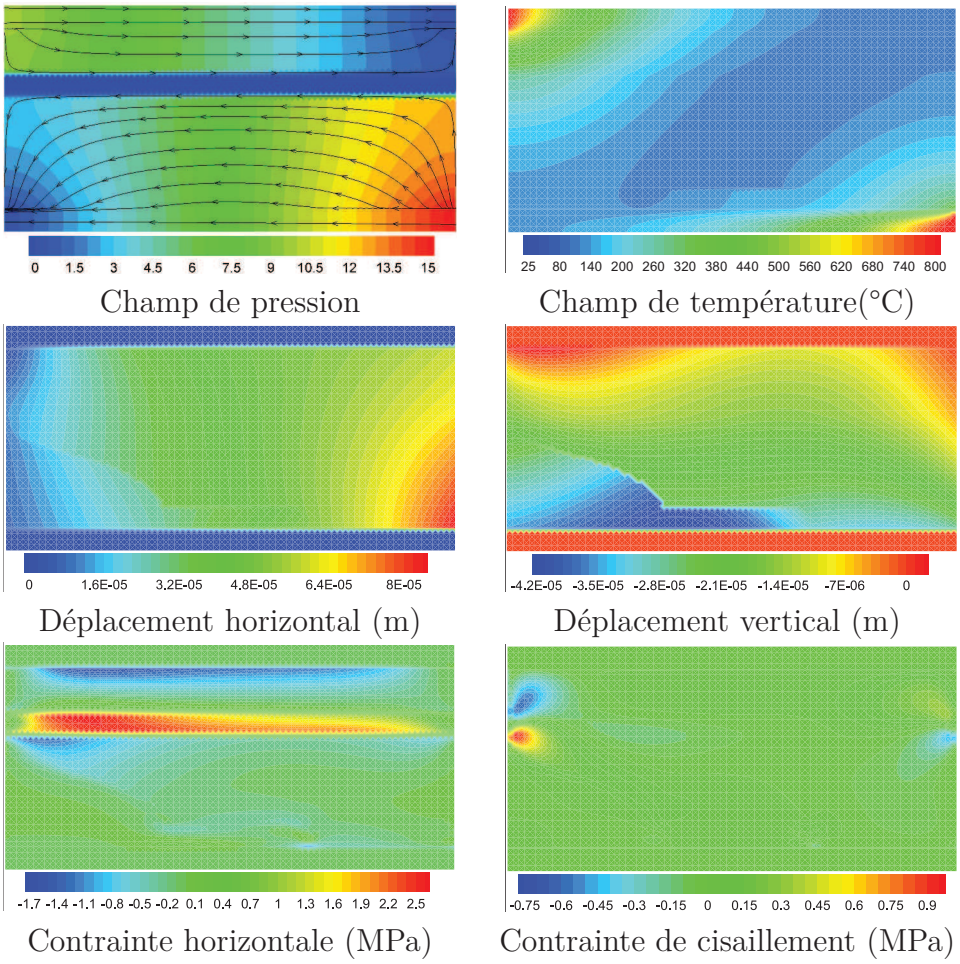

Figure A.10.: Contours obtenu à la fin de la simulation pour la porosité 0,2

A.5. Couplage des réactions chimiques au transfert de l'énergie et de masse dans les piles à combustible à oxyde solide: Effet de la température sur la performance électrochimique

Les discretizations des équations du transfert de l'énergie et de masse sont décrites en détails dans le paragraphe 2. Dans ce paragraphe Les équations d'électrochimie utilisées pour calculer l'efficacité énergétique de la cellule sont introduites et résolus.

La conversion de l'énergie dans une unité de pile à combustible a oxyde solide est basées sur les réactions électrochimiques au interfaces électrodes/d'électrolyte. La force électromotrice ou potentiel en circuit ouvert, en supposant une cellule alimentée en hydrogène et en l'oxygène pur, est donnée par l'équation de Nernst (Aguiar et al., 2004; Campanari and Iora, 2004)

$$U_{TPB}^{OCP} = U_{H_2}^0 - \frac{\Re T}{2F} \ln \left(\frac{p_{H2O,fuel}}{p_{H_2,fuel} \left(p_{O_2,air} \right)^{\frac{1}{2}}} \right) \tag{A.57}$$

Ou $p_{H_2O,fuel}$, $p_{H_2,fuel}$, et $p_{O_2,air}$ sont les pressions partielles de l'eau, de l'hydrogène et de l'oxygènedans canaux de combustible et de l'air, respectivement. Les pressions partielles p_k sont liées aux concentration molaire des espèces $C_k (k = H_2,\ O_2,\ H_2O)$, par $p_k = C_k \Re T$ (Khaleel et al., 2004). $U_{H_2}^0$ est le potentiel standard de la cellule qui dépend de la variation de l'énergie libre de Gibbs lorsque toutes les espèces sont à une pression de 1,0 atm (Khaleel et al., 2004). La dépendance de la température de $U_{H_2}^0 (T)$ est donné par l'équation suivante (Lu et al., 2006)

$$U_{H_2}^0 (T) = \left(U_{H_2}^0 \right)_{ref} + \frac{(\Delta S)_{ref}}{4F} (T - 1023) \tag{A.58}$$

Ou $\left(U_{H_2}^0 \right)_{ref} = 0.9915V$ et $(\Delta S)_{ref} = 2S_{H_2O} - 2S_{H_2} - S_{O_2}$ sont le potentiel standard de la cellule et le changement d'entropie à une température de référence $T = 1023K$.

En service la tension de sortie d'une unité de pile à combustible à oxyde solide est inférieure à la force électromotrice idéale donnée par Eq. (A.57), en raison principalement aux pertes ohmique (η_{Ohm}), du concentration (η_{conc}) et de l'activation (η_{act}) (Colpan et al., 2007; Lee et al., 2011). Ainsi, la tension de cellule est donnée par l'équation suivante:

$$U = U_{TPB}^{OCP} - (\eta_{Ohm} + \eta_{conc,anode} + \eta_{conc,cathode} + \eta_{act,anode} + \eta_{act,cathode}) \tag{A.59}$$

A.5.1. Résistance Ohmic

La résistance ohmique représente la résistance au transport d'ions à travers l'électrolyte et le flux des électrons à travers l'anode et la cathode de la cellule. Cette perte de tension

dépend linéairement de la densité de courant selon la loi d'Ohm:

$$\eta_{Ohm} = jR_{Ohm} \tag{A.60}$$

la résistance globale de la cellule R_{Ohm}, qui comprend des résistances électroniques et ioniques, est donnée en fonction de l'épaisseur des composants de la cellule (anode/électrolyte /cathode), et les conductivités ioniques et électroniques des composants cellulaires (Aguiar et al., 2004).

$$R_{Ohm} = \frac{\tau_{anode}}{\sigma_{anode}} + \frac{\tau_{electrolyte}}{\sigma_{electrolyte}} + \frac{\tau_{cathode}}{\sigma_{cathode}} \tag{A.61}$$

Où τ_{anode}, $\tau_{electrolyte}$, et $\tau_{cathode}$ représentent l'épaisseur des couches d'anode, d'électrolyte et de cathode, respectivement. σ_{anode} et $\sigma_{cathode}$ sont la conductivité électronique de l'anode et de la cathode. $\sigma_{electrolyte}$ est la conductivité ionique de l'électrolyte.

A.5.2. Perte de concentration

La perte de concentration représente la résistance de transport de masse à travers les électrodes poreuses de la cellule qui conduit à un gradient de concentration. Lorsque la pile à combustible n'est soumise à aucune charge (circuit ouvert), les concentrations de réactif et de produit sur les sites de réaction sont les mêmes que ceux dans le canal. Toutefois, lorsque la pile à combustible est dans des conditions normales de fonctionnement (circuit-fermé), la consommation de carburant et de l'oxydant au niveau du site de réaction conduit à un gradient de concentration à travers l'anode et la cathode. Par conséquent, les concentrations des espèces au site de réactions sont différentes de ceux dans les électrodes poreuses et les canaux. Ces pertes peuvent être évaluées par la relation suivante (Campanari and Iora, 2004; Aguiar et al., 2004; Arpino et al., 2008):

$$\eta_{conc} = \frac{\Re T}{2F} \ln\left(\frac{p_{H_2O,TPB} p_{H_2,fuel}}{p_{H_2O,fuel} p_{H_2,TPB}}\right) + \frac{\Re T}{4F} \ln\left(\frac{p_{O_2,air}}{p_{O_2,TPB}}\right) \tag{A.62}$$

Le premier terme du côté droit de Eq. (A.62) représente la perte anodique, $\eta_{conc,anode}$:

$$\eta_{conc,anode} = \frac{\Re T}{2F} \ln\left(\frac{p_{H_2O,TPB} p_{H_2,fuel}}{p_{H_2O,fuel} p_{H_2,TPB}}\right) \tag{A.63}$$

Le second terme se réfère à la perte cathodique, $\eta_{conc,cathode}$:

$$\eta_{conc,cathode} = \frac{\Re T}{4F} \ln\left(\frac{p_{O_2,air}}{p_{O_2,TPB}}\right) \tag{A.64}$$

$p_{H_2O,fuel}$, $p_{H_2,fuel}$ et $p_{O_2,air}$ sont les pressions partielles de l'eau, de l'hydrogène et de l'oxygène au niveau du canal de carburant et d'air, tandis que $p_{H_2O,TPB}$, $p_{H_2,TPB}$ et $p_{O_2,TPB}$ sont les pressions partielles de H_2O, H_2 et O_2 aux site de réactions électrochimiques, respectivement.

A.5.3. Perte d'activation

Perte d'activation, qui sont liés à l'énergie d'activation requise par les réactions chimiques, représentent la cinétique de la réaction au niveau des sites actifs de la cellule. Perte d'activation dépendent fortement de la température de fonctionnement de pile. A une température de fonctionnement élevée, l'activité cinétique élevée au niveau des sites de réaction se traduit généralement par de faible perte d'activation. Cependant, avec la diminution de la température de fonctionnement, le potentiel d'activation peuvent devenir la contribution la plus significative à la baisse de la tension de cellule. La perte d'activation est reliés à la densité de courant par l'équation non-linéaire de Butler-Volmer:

$$j = j_{0,electrode}\left[\exp\left(\frac{\alpha^A n_e F}{\Re T}\eta_{act,electrode}\right) - \exp\left(-\frac{\alpha^C n_e F}{\Re T}\eta_{act,electrode}\right)\right],$$
$$electrode \in \{anode,\ cathode\} \tag{A.65}$$

où α^A et α^C sont les coefficients de transfert de charge pour l'anode et la cathode respectivement. La densité de courant d'échange $j_{0,electrode}$, qui dépend non seulement de température de fonctionnement et les propriétés du matériaux, mais également de l'activité cinétique de la réaction électrochimique et les concentrations d'espèces (Celik et al., 2005), est exprimée par:

$$j_{0,anode} = \gamma_{anode}\left(\frac{p_{H_2,TPB}}{p_0}\right)\left(\frac{p_{H_2O,TPB}}{p_0}\right)\exp\left(-\frac{E_{anode}}{\Re T}\right) \tag{A.66}$$

$$j_{0,cathode} = \gamma_{cathode} \left(\frac{p_{O_2,TPB}}{p_0} \right)^{0.25} \exp\left(-\frac{E_{cathode}}{\Re T} \right) \tag{A.67}$$

A.5.4. Validation

Pour la validation les équations électrochimiques sont combinés avec les celles de l'écoulement du fluide, transfert de chaleur et transport de masse. La validation du modèle mathématique est effectuée en comparant les courbes courant-tension (I-V) expérimental (Rogers et al., 2003) à celles prédit par le modèle.

Dans la Fig. A.11, les résultats prédits sont comparés aux valeurs expérimentales. Les prédictions sont proches de l'expérience sauf à basse tension où la courbe I-V semble se rapprocher de la tension zéro plus rapidement que les prévisions de Hussain et al. (2006) et Tseronis et al. (2012). En effet leurs courbes I-V semblent stabiliser à peu près à la tension de fonctionnement de 0,4 V, tandis que les expériences montrent habituellement une chute de la tension de fonctionnement à zéro des basses tensions de fonctionnement.

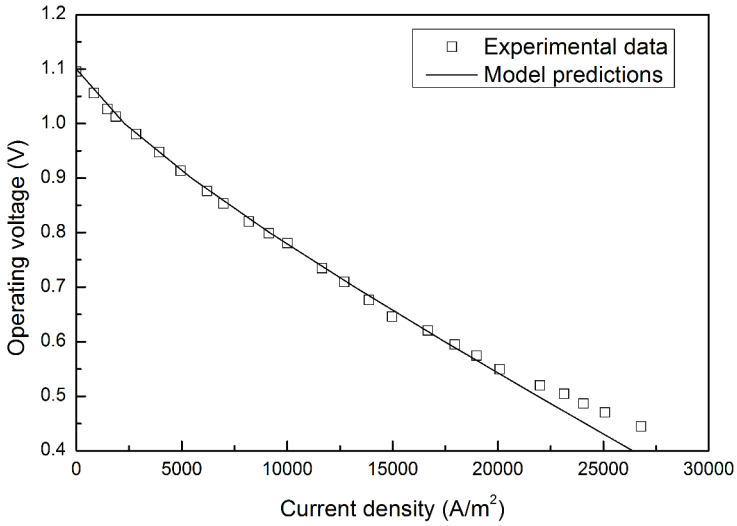

Figure A.11.: Comparison entre les prédictions du modèle et les résultats expérimentaux

Bibliography

Aavatsmark, I., T. Barkve, Ø. Bøe, and T. Mannseth: 1996, 'Discretization on non-orthogonal, quadrilateral grids for inhomogeneous, anisotropic media'. *Journal of computational physics* **127**(1), 2–14.

Achenbach, E.: 1994, 'Three-dimensional and time-dependent simulation of a planar solid oxide fuel cell stack'. *Journal of Power Sources* **49**(1), 333–348.

Aguiar, P., C. Adjiman, and N. P. Brandon: 2004, 'Anode-supported intermediate temperature direct internal reforming solid oxide fuel cell. I: model-based steady-state performance'. *Journal of Power Sources* **138**(1), 120–136.

Alavyoon, F.: 1993, 'On natural convection in vertical porous enclosures due to prescribed fluxes of heat and mass at the vertical boundaries'. *International Journal of Heat and Mass Transfer* **36**(10), 2479–2498.

Alavyoon, F., M. Yoshio, and K. Shigeo: 1994, 'On natural convection in vertical porous enclosures due to opposing fluxes of heat and mass prescribed at the vertical walls'. *International journal of heat and mass transfer* **37**(2), 195–206.

Alazmi, B. and K. Vafai: 2001, 'Analysis of fluid flow and heat transfer interfacial conditions between a porous medium and a fluid layer'. *International Journal of Heat and Mass Transfer* **44**(9), 1735–1749.

Aliabadi, M. and P. Sollero: 1998, 'Crack growth analysis in homogeneous orthotropic laminates'. *Composites science and technology* **58**(10), 1697–1703.

Amhalhel, G. and P. Furmański: 1997, 'Problems of modeling flow and heat transfer in porous media'. *Journal of Power Technologies* **85**, 55–88.

Amiri, A. and K. Vafai: 1994, 'Analysis of dispersion effects and non-thermal equilibrium, non-Darcian, variable porosity incompressible flow through porous media'. *International Journal of Heat and Mass Transfer* **37**(6), 939–954.

Angirasa, D., G. Peterson, and I. Pop: 1997, 'Combined heat and mass transfer by natural convection with opposing buoyancy effects in a fluid saturated porous medium'. *International journal of heat and mass transfer* **40**(12), 2755–2773.

Arnold, D. N.: 1993, 'On nonconforming linear-constant elements for some variants of the Stokes equations'. *Istit. Lombardo Accad. Sci. Lett. Rend. A* **127**, 83–93.

Arnold, D. N., F. Brezzi, B. Cockburn, and L. D. Marini: 2002, 'Unified analysis of discontinuous Galerkin methods for elliptic problems'. *SIAM journal on numerical analysis* **39**(5), 1749–1779.

Arpino, F., A. Carotenuto, N. Massarotti, and P. Nithiarasu: 2008, 'A robust model and numerical approach for solving solid oxide fuel cell (SOFC) problems'. *International Journal of Numerical Methods for Heat & Fluid Flow* **18**(7/8), 811–834.

Asadpoure, A. and S. Mohammadi: 2007, 'Developing new enrichment functions for crack simulation in orthotropic media by the extended finite element method'. *International Journal for Numerical Methods in Engineering* **69**(10), 2150–2172.

Asadpoure, A., S. Mohammadi, and A. Vafai: 2006a, 'Crack analysis in orthotropic media using the extended finite element method'. *Thin-Walled Structures* **44**(9), 1031–1038.

Asadpoure, A., S. Mohammadi, and A. Vafai: 2006b, 'Modeling crack in orthotropic media using a coupled finite element and partition of unity methods'. *Finite Elements in analysis and Design* **42**(13), 1165–1175.

Autissier, N., D. Larrain, D. Favrat, et al.: 2004, 'CFD simulation tool for solid oxide fuel cells'. *Journal of Power Sources* **131**(1), 313–319.

Azoti, W., A. Tchalla, Y. Koutsawa, A. Makradi, G. Rauchs, S. Belouettar, and H. Zahrouni: 2013, 'Mean-field constitutive modeling of elasto-plastic composites using two (2) incremental formulations'. *Composite Structures* **105**, 256–262.

Bae, J.-S. and S. Krishnaswamy: 2001, 'Subinterfacial cracks in bimaterial systems subjected to mechanical and thermal loading'. *Engineering Fracture Mechanics* **68**(9), 1081–1094.

Barnett, D. and R. Asaro: 1972, 'The fracture mechanics of slit-like cracks in anisotropic elastic media'. *Journal of the Mechanics and Physics of Solids* **20**(6), 353–366.

Bear, J.: 1972, 'Dynamics of fluids in porous media'. *American Elseuier*.

Beavers, G. S. and D. D. Joseph: 1967, 'Boundary conditions at a naturally permeable wall'. *Journal of fluid mechanics* **30**(01), 197–207.

Belytschko, T. and T. Black: 1999, 'Elastic crack growth in finite elements with minimal remeshing'. *International journal for numerical methods in engineering* **45**(5), 601–620.

Belytschko, T., N. Moës, S. Usui, and C. Parimi: 2001, 'Arbitrary discontinuities in finite elements'. *International Journal for Numerical Methods in Engineering* **50**(4), 993–1013.

Bennacer, R., A. Tobbal, H. Beji, and P. Vasseur: 2001, 'Double diffusive convection in a vertical enclosure filled with anisotropic porous media'. *International journal of thermal sciences* **40**(1), 30–41.

Berning, T., D. M. Lu, and N. Djilali: 2002, 'Three-dimensional computational analysis of transport phenomena in a PEM fuel cell'. *Journal of power sources* **106**(1), 284–294.

Bhatnagar, H., S. Ghosh, and M. E. Walter: 2010, 'A parametric study of damage initiation and propagation in EB-PVD thermal barrier coatings'. *Mechanics of Materials* **42**(1), 96–107.

Boaro, M., J. M. Vohs, and R. J. Gorte: 2003, 'Synthesis of Highly Porous Yttria-Stabilized Zirconia by Tape-Casting Methods'. *Journal of the American Ceramic Society* **86**(3), 395–400.

Boey, F. and A. Tok: 2003, 'Porous AlN ceramic substrates by reaction sintering'. *Journal of Materials Processing Technology* **140**(1), 413–419.

Bogy, D.: 1972, 'The plane solution for anisotropic elastic wedges under normal and shear loading'. *Journal of Applied Mechanics* **39**(4), 1103–1109.

Bordas, S., S. Natarajan, P. Kerfriden, C. E. Augarde, D. R. Mahapatra, T. Rabczuk, and S. D. Pont: 2011, 'On the performance of strain smoothing for quadratic and enriched finite element approximations (XFEM/GFEM/PUFEM)'. *International Journal for Numerical Methods in Engineering* **86**(4-5), 637–666.

Bouhala, L., S. Belouettar, A. Makradi, and Y. Remond: 2010, 'Study of interface influence on crack growth: Application to Solid Oxide Fuel Cell like materials design'. *Materials & Design* **31**(3), 1033–1041.

Bouhala, L., A. Makradi, and S. Belouettar: 2012, 'Thermal and thermo-mechanical influence on crack propagation using an extended mesh free method'. *Engineering Fracture Mechanics* **88**, 35–48.

Bouhala, L., Q. Shao, Y. Koutsawa, A. Younes, P. Núñez, A. Makradi, and S. Belouettar: 2013, 'An XFEM crack-tip enrichment for a crack terminating at a bi-material interface'. *Engineering Fracture Mechanics* **102**, 51–64.

Bowie, O. and C. Freese: 1972, 'Central crack in plane orthotropic rectangular sheet'. *International Journal of Fracture Mechanics* **8**(1), 49–57.

Burman, E. and P. Hansbo: 2005, 'Stabilized Crouzeix-Raviart element for the Darcy-Stokes problem'. *Numerical Methods for Partial Differential Equations* **21**(5), 986–997.

Campanari, S. and P. Iora: 2004, 'Definition and sensitivity analysis of a finite volume SOFC model for a tubular cell geometry'. *Journal of Power Sources* **132**(1), 113–126.

Canuto, C., M. Y. Hussaini, A. Quarteroni, and T. A. Zang: 2006, 'Spectral methods. Scientific Computation'.

Carbonell, R. G. and S. Whitaker: 1984, 'Heat and mass transfer in porous media'. In: *Fundamentals of transport phenomena in porous media*. Springer, pp. 121–198.

Celik, I., S. R. Pakalapati, and M. D. Salazar-Villalpando: 2005, 'Theoretical calculation of the electrical potential at the electrode/electrolyte interfaces of solid oxide fuel cells'. *Journal of Fuel Cell Science and Technology* **2**(4), 238–245.

Chang, M.-H., F. Chen, and B. Straughan: 2006, 'Instability of Poiseuille flow in a fluid overlying a porous layer'. *Journal of Fluid Mechanics* **564**, 287–303.

Cheddie, D. F. and N. D. Munroe: 2007, 'A dynamic 1D model of a solid oxide fuel cell for real time simulation'. *Journal of Power Sources* **171**(2), 634–643.

Chen, X., Q. Liu, K. Khor, and S. Chan: 2007, 'High-performance (La, Sr)(Cr, Mn) O_3/(Gd, Ce) $O_{2-\delta}$ composite anode for direct oxidation of methane'. *Journal of power sources* **165**(1), 34–40.

Christou, M. and C. Christov: 2005, 'Interacting localized waves for the regularized long wave equation via a Galerkin spectral method'. *Mathematics and Computers in Simulation* **69**(3), 257–268.

Cieszko, M. and J. Kubik: 1999, 'Derivation of matching conditions at the contact surface between fluid-saturated porous solid and bulk fluid'. In: *Porous Media: Theory and Experiments*. Springer, pp. 319–336.

Cockburn, B., S.-Y. Lin, and C.-W. Shu: 1989, 'TVB Runge-Kutta local projection discontinuous Galerkin finite element method for conservation laws III: one-dimensional systems'. *Journal of Computational Physics* **84**(1), 90–113.

Colpan, C. O., I. Dincer, and F. Hamdullahpur: 2007, 'Thermodynamic modeling of direct internal reforming solid oxide fuel cells operating with syngas'. *International Journal of Hydrogen Energy* **32**(7), 787–795.

Costa, B.: 2004, 'Spectral methods for partial differential equations'. *CUBO, A Mathematical Journal* **6**, 1–32.

Costamagna, P., A. Selimovic, M. Del Borghi, and G. Agnew: 2004, 'Electrochemical model of the integrated planar solid oxide fuel cell (IP-SOFC)'. *Chemical Engineering Journal* **102**(1), 61–69.

Crouzeix, M. and P.-A. Raviart: 1973, 'Conforming and nonconforming finite element methods for solving the stationary Stokes equations I'. *ESAIM: Mathematical Modelling and Numerical Analysis - Modélisation Mathématique et Analyse Numérique* **7**(R3), 33–75.

Dagan, G. et al.: 1989, *Flow and transport in porous formations*. Springer-Verlag GmbH & Co. KG.

De Borst, R., J. Réthoré, and M.-A. Abellan: 2006, 'A numerical approach for arbitrary cracks in a fluid-saturated medium'. *Archive of Applied Mechanics* **75**(10-12), 595–606.

Diersch, H.-J. and O. Kolditz: 1998, 'Coupled groundwater flow and transport: 2. Thermohaline and 3D convection systems'. *Advances in Water Resources* **21**(5), 401–425.

Discacciati, M., E. Miglio, and A. Quarteroni: 2002, 'Mathematical and numerical models for coupling surface and groundwater flows'. *Applied Numerical Mathematics* **43**(1), 57–74.

Djadel, K. and S. Nicaise: 2008, 'A non-conforming finite volume element method of

weighted upstream type for the two-dimensional stationary Navier–Stokes system'. *Applied Numerical Mathematics* **58**(5), 615–634.

Duflot, M.: 2008, 'The extended finite element method in thermoelastic fracture mechanics'. *International journal for numerical methods in engineering* **74**(5), 827–847.

Durran, D. R.: 1999, *Numerical methods for wave equations in geophysical fluid dynamics*, No. 32. Springer.

Edwards, M. G. and C. F. Rogers: 1998, 'Finite volume discretization with imposed flux continuity for the general tensor pressure equation'. *Computational Geosciences* **2**(4), 259–290.

Ehrhardt, M.: 2000, 'An Introduction to Fluid-Porous Interface, Coupling'. *Weierstrass Institute for Applied Analysis and Stochastics, Berlin, Germany.*

Ehrhardt, M.: 2010, 'An Introduction to Fluid-Porous Interface Coupling'.

Ene, H. I. and E. Sanchez-Palencia: 1975, 'Equations et phénomenes de surface pour l'écoulement dans un modele de milieu poreux'. *Journal de mécanique* **14**(1), 73–108.

Fahs, M. and A. Younes: 2014, 'A High-Accurate Fourier-Galerkin Solution for Buoyancy-Driven Flow in a Square Cavity'. *Numerical Heat Transfer, Part B: Fundamentals* **65**(6), 495–517.

Ferguson, J., J. Fiard, and R. Herbin: 1996, 'Three-dimensional numerical simulation for various geometries of solid oxide fuel cells'. *Journal of Power Sources* **58**(2), 109–122.

Fernández-González, R., E. Hernández, S. Savvin, P. Núñez, A. Makradi, N. Sabaté, J. Esquivel, and J. Ruiz-Morales: 2014, 'A novel microstructured metal-supported solid oxide fuel cell'. *Journal of Power Sources* **272**, 233–238.

Fortin, M. and F. Brezzi: 1991, *Mixed and hybrid finite element methods.* Springer.

Fries, T.-P. and T. Belytschko: 2010, 'The extended/generalized finite element method: an overview of the method and its applications'. *International Journal for Numerical Methods in Engineering* **84**(3), 253–304.

García, F., A. Sáez, and J. Domínguez: 2004, 'Traction boundary elements for cracks in anisotropic solids'. *Engineering analysis with boundary elements* **28**(6), 667–676.

Girault, V. and P.-A. Raviart: 1979, 'Finite element approximation of the Navier-Stokes equations'. *Lecture Notes in Mathematics, Berlin Springer Verlag* **749**.

Glatzmaier, G. C. and W. F. Ramirez: 1988, 'Use of volume averaging for the modeling of thermal properties of porous materials'. *Chemical engineering science* **43**(12), 3157–3169.

Gobbe, C. and M. Quintard: 1994, 'Macroscopic description of unsteady heat transfer in heterogeneous media'. *High Temperatures. High Pressures* **26**(1), 1–14.

Goharzadeh, A., A. Khalili, and B. B. Jørgensen: 2005, 'Transition layer thickness at a fluid-porous interface'. *Physics of Fluids (1994-present)* **17**(5), 057102.

Gowda, V., J. Jaffré, et al.: 1993, 'A discontinuous finite element method for scalar nonlinear conservation laws'.

Goyeau, B., D. Lhuillier, D. Gobin, and M. Velarde: 2003, 'Momentum transport at a fluid–porous interface'. *International Journal of Heat and Mass Transfer* **46**(21), 4071–4081.

Goyeau, B., J.-P. Songbe, and D. Gobin: 1996, 'Numerical study of double-diffusive natural convection in a porous cavity using the Darcy-Brinkman formulation'. *International Journal of Heat and Mass Transfer* **39**(7), 1363–1378.

Gresho, P. M., R. L. Sani, and M. S. Engelman: 1998, *Incompressible flow and the finite element method: advection-diffusion and isothermal laminar flow*. Wiley New York.

Hansbo, P. and M. G. Larson: 2003, 'Discontinuous Galerkin and the Crouzeix–Raviart element: application to elasticity'. *ESAIM: Mathematical Modelling and Numerical Analysis* **37**(01), 63–72.

Hettich, T., A. Hund, and E. Ramm: 2008, 'Modeling of failure in composites by X-FEM and level sets within a multiscale framework'. *Computer Methods in Applied Mechanics and Engineering* **197**(5), 414–424.

Hettich, T. and E. Ramm: 2006, 'Interface material failure modeled by the extended finite-element method and level sets'. *Computer Methods in Applied Mechanics and Engineering* **195**(37), 4753–4767.

Huang, Z., Z. Suo, G. Xu, J. He, J. Prevost, and N. Sukumar: 2005, 'Initiation and arrest

of an interfacial crack in a four-point bend test'. *Engineering fracture mechanics* **72**(17), 2584–2601.

Hussain, M., X. Li, and I. Dincer: 2006, 'Mathematical modeling of planar solid oxide fuel cells'. *Journal of Power Sources* **161**(2), 1012–1022.

IMSL, I.: 1994, *IMSL MATH/LIBRARY.: Fortran subroutines for mathematical applications*, Vol. 2. Visual Numerics, Incorporated.

Jäger, W. and A. Mikelić: 2001, 'On the roughness-induced effective boundary conditions for an incompressible viscous flow'. *Journal of Differential Equations* **170**(1), 96–122.

Jäger, W., A. Mikelic, et al.: 1996, 'On the boundary conditions at the contact interface between a porous medium and a free fluid'. In: *Pisa, Classe Fisiche e Matematiche-Serie IV*.

Jiang, S. P., X. Chen, S. Chan, J. Kwok, and K. Khor: 2006, '(La 0.75 Sr 0.25)(Cr 0.5 Mn 0.5) O 3/YSZ composite anodes for methane oxidation reaction in solid oxide fuel cells'. *Solid State Ionics* **177**(1), 149–157.

Jones, I.: 1973, 'Low Reynolds number flow past a porous spherical shell'. In: *Mathematical Proceedings of the Cambridge Philosophical Society*, Vol. 73. pp. 231–238.

Joulaee, N., A. Makradi, S. Ahzi, and M. A. Khaleel: 2007, 'Fracture toughness and crack deflection in porous multilayered ceramics: application to NiO-YSZ'. In: *Materials science forum*, Vol. 553. pp. 69–74.

Joulaee, N., A. Makradi, S. Ahzi, M. A. Khaleel, and B. Koeppel: 2009, 'Prediction of crack propagation paths in the unit cell of SOFC stacks'. *International Journal of Mechanics and Materials in Design* **5**(3), 217–230.

Kang, Y.-W., J. Li, G.-Y. Cao, H.-Y. Tu, J. Li, and J. Yang: 2009, 'A reduced 1D dynamic model of a planar direct internal reforming solid oxide fuel cell for system research'. *Journal of Power Sources* **188**(1), 170–176.

Kavetski, D., P. Binning, and S. Sloan: 2001, 'Adaptive time stepping and error control in a mass conservative numerical solution of the mixed form of Richards equation'. *Advances in water resources* **24**(6), 595–605.

Kaviany, M.: 1995, 'Principles of Heat Transfer in Porous Media'. *Springer, New York.*

Khadiri, A., R. Bennacer, M. Hasnaoui, and A. Amahmid: 2011, 'Two-and three-dimensional multiple steady states in a porous cavity heated and salted from below'. *International Journal of Thermal Sciences* **50**(6), 918–929.

Khaleel, M. A., Z. Lin, P. Singh, W. Surdoval, and D. Collin: 2004, 'A finite element analysis modeling tool for solid oxide fuel cell development: coupled electrochemistry, thermal and flow analysis in MARC®'. *Journal of Power Sources* **130**(1), 136–148.

Khoei, A. and E. Haghighat: 2011, 'Extended finite element modeling of deformable porous media with arbitrary interfaces'. *Applied Mathematical Modelling* **35**(11), 5426–5441.

Khoei, A., S. Moallemi, and E. Haghighat: 2012, 'Thermo-hydro-mechanical modeling of impermeable discontinuity in saturated porous media with X-FEM technique'. *Engineering Fracture Mechanics* **96**, 701–723.

Kim, S. J. and C. Y. Choi: 1996, 'Convective heat transfer in porous and overlying fluid layers heated from below'. *International journal of heat and mass transfer* **39**(2), 319–329.

Kirby, R.: 2000, 'A posteriori error estimates and local time-stepping for flow and transport problems in porous media'. Ph.D. thesis, Ph. D. thesis, University of Texas at Austin, Austin, TX.

Klausen, R. A. and T. Russell: 2004, 'Relationships among some locally conservative discretization methods which handle discontinuous coefficients'. *Computational Geosciences* **8**(4), 341–377.

Konz, M., P. Ackerer, A. Younes, P. Huggenberger, and E. Zechner: 2009, 'Two-dimensional stable-layered laboratory-scale experiments for testing density-coupled flow models'. *Water resources research* **45**(2).

Kopriva, D. A.: 2009, *Implementing spectral methods for partial differential equations: Algorithms for scientists and engineers*. springer.

Koutsawa, Y., S. Belouettar, A. Makradi, and S. Tiem: 2011, 'Automatic differentiation of micromechanics incremental schemes for coupled fields composite materials: Effective properties and their sensitivities'. *Composites Science and Technology* **71**(2), 113–121.

Kramer, J., R. Jecl, and L. Škerget: 2007, 'Boundary domain integral method for the study of double diffusive natural convection in porous media'. *Engineering analysis with boundary elements* **31**(11), 897–905.

Kuo, M. and D. Bogy: 1974, 'Plane solutions for the displacement and traction-displacement problems for anisotropic elastic wedges'. *Journal of Applied Mechanics* **41**(1), 197–202.

Kuznetsov, A.: 1996, 'Analytical investigation of the fluid flow in the interface region between a porous medium and a clear fluid in channels partially filled with a porous medium'. *Applied Scientific Research* **56**(1), 53–67.

Kuznetsov, A.: 1997, 'Influence of the stress jump condition at the porous-medium/clear-fluid interface on a flow at a porous wall'. *International Communications in Heat and Mass Transfer* **24**(3), 401–410.

Kuznetsov, A.: 1998a, 'Analytical investigation of Couette flow in a composite channel partially filled with a porous medium and partially with a clear fluid'. *International journal of heat and mass transfer* **41**(16), 2556–2560.

Kuznetsov, A.: 1998b, 'Analytical study of fluid flow and heat transfer during forced convection in a composite channel partly filled with a Brinkman–Forchheimer porous medium'. *Flow, Turbulence and Combustion* **60**(2), 173–192.

Kuznetsov, A.: 1999, 'Fluid mechanics and heat transfer in the interface region between a porous medium and a fluid layer: a boundary layer solution'. *Journal of Porous Media* **2**(3), 309–321.

Lampe, V.: 2013, 'Modelling Fluid Flow and Heat Transport in Fractured Porous Media'.

Larrain, D., F. Maréchal, D. Favrat, et al.: 2004, 'Generalized model of planar SOFC repeat element for design optimization'. *Journal of Power Sources* **131**(1), 304–312.

Lashtabeg, A., J. Drennan, R. Knibbe, J. L. Bradley, and G. Q. Lu: 2009, 'Synthesis and characterisation of macroporous Yttria Stabilised Zirconia (YSZ) using polystyrene spheres as templates'. *Microporous and Mesoporous Materials* **117**(1), 395–401.

Laurencin, J., G. Delette, M. Dupeux, and F. Lefebvre-Joud: 2007, 'A numerical approach to predict the SOFC fracture: The case of an anode supported cell'. *ECS Transactions* **7**(1), 677–686.

Laurencin, J., G. Delette, F. Lefebvre-Joud, and M. Dupeux: 2008, 'A numerical tool to estimate SOFC mechanical degradation: case of the planar cell configuration'. *Journal of the European Ceramic Society* **28**(9), 1857–1869.

Laurencin, J., G. Delette, B. Morel, F. Lefebvre-Joud, and M. Dupeux: 2009, 'Solid oxide fuel cells damage mechanisms due to Ni-YSZ re-oxidation: case of the anode supported cell'. *Journal of Power Sources* **192**(2), 344–352.

Layton, W. J., F. Schieweck, and I. Yotov: 2002, 'Coupling fluid flow with porous media flow'. *SIAM Journal on Numerical Analysis* **40**(6), 2195–2218.

Le Bars, M. and M. Worster: 2006, 'Interfacial conditions between a pure fluid and a porous medium: implications for binary alloy solidification'. *Journal of Fluid Mechanics* **550**, 149–173.

Lecampion, B.: 2009, 'An extended finite element method for hydraulic fracture problems'. *Communications in Numerical Methods in Engineering* **25**(2), 121–133.

Lee, T. S., J. Chung, and Y.-C. Chen: 2011, 'Design and optimization of a combined fuel reforming and solid oxide fuel cell system with anode off-gas recycling'. *Energy Conversion and Management* **52**(10), 3214–3226.

Lekhnitskii, S.: 1965, 'Theory of elasticity of an anisotropic elastic body, 1963'. *Hoden-Day, San Francisco*.

Levec, J. and R. Carbonell: 1985a, 'Longitudinal and lateral thermal dispersion in packed beds. Part I: Theory'. *AICHE journal* **31**(4), 581–590.

Levec, J. and R. Carbonell: 1985b, 'Longitudinal and lateral thermal dispersion in packed beds. Part II: Comparison between theory and experiment'. *AIChE journal* **31**(4), 591–602.

Li, J. and Z. Chen: 2008, 'A new local stabilized nonconforming finite element method for the Stokes equations'. *Computing* **82**(2-3), 157–170.

Lin, D.: 1993, 'Unsteady natural convection heat and mass transfer in a saturated porous enclosure'. *Wärme-und Stoffübertragung* **28**(1-2), 49–56.

Lin, T., C. Huang, and T. Chang: 1990, 'Transient binary mixture natural convection in square enclosures'. *International Journal of Heat and Mass Transfer* **33**(2), 287–299.

Lin, Y. and S. Beale: 2006, 'Performance predictions in solid oxide fuel cells'. *Applied mathematical modelling* **30**(11), 1485–1496.

Lu, N., Q. Li, X. Sun, and M. Khaleel: 2006, 'The modeling of a standalone solid-oxide fuel cell auxiliary power unit'. *Journal of Power Sources* **161**(2), 938–948.

Malashetty, M.: 1993, 'Anisotropic thermoconvective effects on the onset of double diffusive convection in a porous medium'. *International journal of heat and mass transfer* **36**(9), 2397–2401.

Mchirgui, A., N. Hidouri, M. Magherbi, and A. B. Brahim: 2012, 'Entropy generation in double-diffusive convection in a square porous cavity using Darcy–Brinkman formulation'. *Transport in porous media* **93**(1), 223–240.

Miglio, E., A. Quarteroni, and F. Saleri: 2003, 'Coupling of free surface and groundwater flows'. *Computers & fluids* **32**(1), 73–83.

Mikdam, A., R. Belouettar, D. Fiorelli, H. Hu, and A. Makradi: 2013a, 'A tool for design of heterogeneous materials with desired physical properties using statistical continuum theory'. *Materials Science and Engineering: A* **564**, 493–500.

Mikdam, A., A. Makradi, S. Ahzi, H. Garmestani, D. Li, and Y. Remond: 2009, 'Effective conductivity in isotropic heterogeneous media using a strong-contrast statistical continuum theory'. *Journal of the Mechanics and Physics of Solids* **57**(1), 76–86.

Mikdam, A., A. Makradi, Y. Koutsawa, and S. Belouettar: 2013b, 'Microstructure effect on the mechanical properties of heterogeneous composite materials'. *Composites Part B: Engineering* **44**(1), 714–721.

Moës, N. and T. Belytschko: 2002, 'Extended finite element method for cohesive crack growth'. *Engineering fracture mechanics* **69**(7), 813–833.

Moës, N., M. Cloirec, P. Cartraud, and J.-F. Remacle: 2003, 'A computational approach to handle complex microstructure geometries'. *Computer methods in applied mechanics and engineering* **192**(28), 3163–3177.

Moës, N., J. Dolbow, and T. Belytschko: 1999, 'A finite element method for crack growth without remeshing'. *International journal for numerical methods in engineering* **46**, 131–150.

Mohammadnejad, T. and A. Khoei: 2012, 'Hydro-mechanical modeling of cohesive crack propagation in multiphase porous media using the extended finite element method'. *International Journal for Numerical and Analytical Methods in Geomechanics*.

Mohammadnejad, T. and A. Khoei: 2013, 'An extended finite element method for fluid flow in partially saturated porous media with weak discontinuities; the convergence analysis of local enrichment strategies'. *Computational Mechanics* **51**(3), 327–345.

Motamedi, D. and S. Mohammadi: 2010a, 'Dynamic analysis of fixed cracks in composites by the extended finite element method'. *Engineering Fracture Mechanics* **77**(17), 3373–3393.

Motamedi, D. and S. Mohammadi: 2010b, 'Dynamic crack propagation analysis of orthotropic media by the extended finite element method'. *International journal of fracture* **161**(1), 21–39.

Motamedi, D. and S. Mohammadi: 2012, 'Fracture analysis of composites by time independent moving-crack orthotropic XFEM'. *International Journal of Mechanical Sciences* **54**(1), 20–37.

Murakami, Y. et al.: 1987, *Stress intensity factors handbook*. Pergamon press.

Natarajan, S., P. Kerfriden, D. R. Mahapatra, and S. P. A. Bordas: 2014, 'Numerical analysis of the inclusion-crack interaction by the extended finite element method'. *International Journal for Computational Methods in Engineering Science and Mechanics* **15**(1), 26–32.

Neale, G. and W. Nader: 1974, 'Practical significance of Brinkman's extension of Darcy's law: coupled parallel flows within a channel and a bounding porous medium'. *The Canadian Journal of Chemical Engineering* **52**(4), 475–478.

Nield, D. A.: 1983, 'The boundary correction for the Rayleigh-Darcy problem: limitations of the Brinkman equation'. *Journal of Fluid Mechanics* **128**, 37–46.

Nield, D. A. and A. Bejan: 2006, *Convection in porous media*. springer.

Nithiarasu, P., K. Seetharamu, and T. Sundararajan: 1996, 'Double-diffusive natural convection in an enclosure filled with fluid-saturated porous medium: a generalized non-Darcy approach'. *Numerical Heat Transfer, Part A Applications* **30**(4), 413–426.

Noorishad, J., C. Tsang, and P. Witherspoon: 1984, 'Coupled thermal-hydraulic-mechanical phenomena in saturated fractured porous rocks: Numerical approach'. *Journal of Geophysical Research: Solid Earth (1978–2012)* **89**(B12), 10365–10373.

Ochoa-Tapia, J. A. and S. Whitaker: 1995a, 'Momentum transfer at the boundary between a porous medium and a homogeneous fluid–I. Theoretical development'. *International Journal of Heat and Mass Transfer* **38**(14), 2635–2646.

Ochoa-Tapia, J. A. and S. Whitaker: 1995b, 'Momentum transfer at the boundary between a porous medium and a homogeneous fluid–II. Comparison with experiment'. *International Journal of Heat and Mass Transfer* **38**(14), 2647–2655.

Ochoa-Tapia, J. A. and S. Whitaker: 1997, 'Heat transfer at the boundary between a porous medium and a homogeneous fluid'. *International Journal of Heat and Mass Transfer* **40**(11), 2691–2707.

Ochoa-Tapia, J. A. and S. Whitaker: 1998, 'Heat transfer at the boundary between a porous medium and a homogeneous fluid: the one-equation model'. *Journal of Porous Media* **1**(1).

Pasternak, I.: 2012, 'Boundary integral equations and the boundary element method for fracture mechanics analysis in 2D anisotropic thermoelasticity'. *Engineering Analysis with Boundary Elements* **36**(12), 1931–1941.

Payne, L. and B. Straughan: 1998, 'Analysis of the boundary condition at the interface between a viscous fluid and a porous medium and related modelling questions'. *Journal de mathématiques pures et appliquées* **77**(4), 317–354.

Peng, Z., K. Mahone, and M. Liu: 2000, 'Preparation of mesoporous La0. 85Sr0. 15MnO3 using a surfactant-templated sol-gel process'. *Journal of materials science letters* **19**(16), 1473–1476.

Perry Murray, E. and S. Barnett: 2001, '(La, Sr) MnO_3–(Ce, Gd) O_{2-x} composite cathodes for solid oxide fuel cells'. *Solid State Ionics* **143**(3), 265–273.

Poulikakos, D. and M. Kazmierczak: 1987, 'Forced convection in a duct partially filled with a porous material'. *ASME J. Heat Transfer* **109**(3), 653–662.

Powell, M.: 1968, 'On the calculation of orthogonal vectors'. *The Computer Journal* **11**(3), 302–304.

Powell, M. J.: 1964, 'An efficient method for finding the minimum of a function of several variables without calculating derivatives'. *The computer journal* **7**(2), 155–162.

Prasad, N., M. Aliabadi, and D. Rooke: 1994a, 'The dual boundary element method for thermoelastic crack problems'. *International Journal of Fracture* **66**(3), 255–272.

Prasad, N., M. Aliabadi, and D. Rooke: 1994b, 'Incremental crack growth in thermoelastic problems'. *International journal of fracture* **66**(3), R45–R50.

Press, W. H.: 2007, *Numerical recipes 3rd edition: The art of scientific computing*. Cambridge university press.

Qu, J., A. Fedorov, S. Graham, and C. Haynes: 2006, 'FY 2006 annual report'. *Office of Fossil Energy Fuel Cell Program* p. 215.

Quintard, M., M. Kaviany, and S. Whitaker: 1997, 'Two-medium treatment of heat transfer in porous media: numerical results for effective properties'. *Advances in Water resources* **20**(2), 77–94.

Quintard, M. and S. Whitaker: 1993, 'One-and two-equation models for transient diffusion processes in two-phase systems'. *Advances in heat transfer* **23**, 369–464.

Quintard, M. and S. Whitaker: 1995, 'Local thermal equilibrium for transient heat conduction: theory and comparison with numerical experiments'. *International Journal of Heat and Mass Transfer* **38**(15), 2779–2796.

Quintard, M. and S. Whitaker: 1996a, 'Transport in chemically and mechanically heterogeneous porous media. I: Theoretical development of region-averaged equations for slightly compressible single-phase flow'. *Advances in water resources* **19**(1), 29–47.

Quintard, M. and S. Whitaker: 1996b, 'Transport in chemically and mechanically heterogeneous porous media. II: Comparison with numerical experiments for slightly compressible single-phase flow'. *Advances in water resources* **19**(1), 49–60.

Recknagle, K. P., E. M. Ryan, B. J. Koeppel, L. A. Mahoney, and M. A. Khaleel: 2010, 'Modeling of electrochemistry and steam-methane reforming performance for simulating pressurized solid oxide fuel cell stacks'. *Journal of Power Sources* **195**, 6637–6644.

Recknagle, K. P., R. E. Williford, L. A. Chick, D. R. Rector, and M. A. Khaleel: 2003, 'Three-dimensional thermo-fluid electrochemical modeling of planar SOFC stacks'. *Journal of Power Sources* **113**(1), 109–114.

Ren, Q., Y. Dong, and T. Yu: 2009, 'Numerical modeling of concrete hydraulic fracturing with extended finite element method'. *Science in China Series E: Technological Sciences* **52**(3), 559–565.

Rethore, J., R. d. Borst, and M.-A. Abellan: 2007, 'A two-scale approach for fluid flow in fractured porous media'. *International Journal for Numerical Methods in Engineering* **71**(7), 780–800.

Richardson, S.: 1971, 'A model for the boundary condition of a porous material. Part 2'. *Journal of Fluid Mechanics* **49**(02), 327–336.

Riviére, B.: 2005, 'Analysis of a discontinuous finite element method for the coupled Stokes and Darcy problems'. *Journal of Scientific Computing* **22**(1), 479–500.

Rogers, W. A., R. S. Gemmen, C. Johnson, M. Prinkey, and M. Shahnam: 2003, 'Validation and application of a CFD-based model for solid oxide fuel cells and stacks'. In: *ASME 2003 1st International Conference on Fuel Cell Science, Engineering and Technology*. pp. 517–520.

Rosenberg, N. and F. Spera: 1992, 'Thermohalin convection in a porous medium heated from below'. *International Journal of Heat and Mass Transfer* **35**(5), 1261–1273.

Ruiz-Morales, J., J. Canales-Vázquez, D. Marrero-López, J. Peña-Martínez, D. Pérez-Coll, P. Núñez, J. Rodríguez-Placeres, B. Ballesteros-Pérez, V. Dorta-Martín, and C. Savaniu: 2008, *Pilas de Combustible de óxidos sólidos (SOFC)*. Centro de la Cultura Popular Canaria.

Ruiz-Morales, J. C., J. Canales-Vázquez, J. Peña-Martínez, D. Marrero-López, J. T. Irvine, and P. Núñez: 2006, 'Microstructural optimisation of materials for SOFC applications using PMMA microspheres'. *Journal of Materials Chemistry* **16**(6), 540–542.

Saaltink, M. W., J. Carrera, and S. Olivella: 2004, 'Mass balance errors when solving the convective form of the transport equation in transient flow problems'. *Water Resources Research* **40**(5).

Saffman, P. G.: 1971, 'Boundary condition at surface of a porous medium'. *Studies in Applied Mathematics* **50**(2), 93.

Sahraoui, M. and M. Kaviany: 1992, 'Slip and no-slip velocity boundary conditions at interface of porous, plain media'. *International Journal of Heat and Mass Transfer* **35**(4), 927–943.

Schieweck, F. and L. Tobiska: 1989, 'A nonconforming finite element method of upstream type applied to the stationary Navier-Stokes equation'. *ESAIM: Mathematical Modelling and Numerical Analysis-Modélisation Mathématique et Analyse Numérique* **23**(4), 627–647.

Schlünder, E.: 1975, 'Equivalence of one-and two-phase models for heat transfer processes in packed beds: one dimensional theory [1]'. *Chemical Engineering Science* **30**(4), 450–452.

Schrefler, B. A., S. Secchi, and L. Simoni: 2006, 'On adaptive refinement techniques in multi-field problems including cohesive fracture'. *Computer methods in applied mechanics and engineering* **195**(4), 444–461.

Secchi, S., L. Simoni, and B. A Schrefler: 2007, 'Mesh adaptation and transfer schemes for discrete fracture propagation in porous materials'. *International journal for numerical and analytical methods in geomechanics* **31**(2), 331–345.

Selcuk, A. and A. Atkinson: 1997, 'Elastic properties of ceramic oxides used in solid oxide fuel cells (SOFC)'. *Journal of the European Ceramic Society* **17**(12), 1523–1532.

Shi, Z. and X. Wang: 2007, 'Comparison of Darcy's Law, the Brinkman Equation, the Modified NS Equation and the Pure Diffusion Equation in PEM Fuel Cell Modeling'. In: *Excerpt from the Proceeding of the COMSOL Conference*.

Shiah, Y. and C. Tan: 2000, 'Fracture mechanics analysis in 2-D anisotropic thermoelasticity using BEM'. *Computer Modeling in Engineering & Sciences* **1**(3), 91–99.

Sih, G. C., P. Paris, and G. Irwin: 1965, 'On cracks in rectilinearly anisotropic bodies'. *International Journal of Fracture Mechanics* **1**(3), 189–203.

Sloan, S. W. and A. J. Abbo: 1999, 'Biot consolidation analysis with automatic time stepping and error control Part 1: theory and implementation'. *International Journal for Numerical and Analytical Methods in Geomechanics* **23**(6), 467–492.

Sollero, P. and M. Aliabadi: 1993, 'Fracture mechanics analysis of anisotropic plates by the boundary element method'. *International Journal of Fracture* **64**(4), 269–284.

Sollero, P. and M. Aliabadi: 1995, 'Anisotropic analysis of cracks in composite laminates using the dual boundary element method'. *Composite structures* **31**(3), 229–233.

Sollero, P., M. Aliabadi, and D. Rooke: 1994, 'Anisotropic analysis of cracks emanating from circular holes in composite laminates using the boundary element method'. *Engineering Fracture Mechanics* **49**(2), 213–224.

Sukumar, N., Z. Huang, J.-H. Prévost, and Z. Suo: 2004, 'Partition of unity enrichment for bimaterial interface cracks'. *International Journal for Numerical Methods in Engineering* **59**(8), 1075–1102.

Sukumar, N. and J.-H. Prévost: 2003, 'Modeling quasi-static crack growth with the extended finite element method Part I: Computer implementation'. *International Journal of Solids and Structures* **40**(26), 7513–7537.

Taylor, G.: 1971, 'A model for the boundary condition of a porous material. Part 1'. *Journal of Fluid Mechanics* **49**(02), 319–326.

Torquato, S.: 2002, *Random heterogeneous materials: microstructure and macroscopic properties*, Vol. 16. Springer.

Trevisan, O. V. and A. Bejan: 1985, 'Natural convection with combined heat and mass transfer buoyancy effects in a porous medium'. *International Journal of Heat and Mass Transfer* **28**(8), 1597–1611.

Truong, H. and G. E. Zinsmeister: 1978, 'Experimental study of heat transfer in layered composites'. *International Journal of Heat and Mass Transfer* **21**(7), 905–909.

Tsai, T. and S. A. Barnett: 1997, 'Increased solid-oxide fuel cell power density using interfacial ceria layers'. *Solid State Ionics* **98**(3), 191–196.

Tseronis, K., I. Bonis, I. Kookos, and C. Theodoropoulos: 2012, 'Parametric and transient analysis of non-isothermal, planar solid oxide fuel cells'. *International Journal of Hydrogen Energy* **37**(1), 530–547.

Tummala, R. and A. Friedberg: 1970a, 'Thermal expansion of composites as affected by the matrix'. *Journal of the American Ceramic Society* **53**(7), 376–380.

Tummala, R. R. and A. Friedberg: 1970b, 'Thermal expansion of composite materials'. *Journal of Applied Physics* **41**(13), 5104–5107.

Tupholme, G.: 1974, 'A study of cracks in orthotropic crystals using dislocation layers'. *Journal of Engineering Mathematics* **8**(1), 57–69.

Turek, S.: 1996, 'A comparative study of some time-stepping techniques for the incompressible Navier-Stokes equations: From fully implicit nonlinear schemes to semi-implicit projection methods'. *International Journal for Numerical Methods in Fluids* **22**(10), 987–1011.

Urquiza, J., D. N'dri, A. Garon, and M. Delfour: 2008, 'Coupling stokes and darcy equations'. *Applied Numerical Mathematics* **58**(5), 525–538.

Vafai, K.: 2000, *Handbook of Porous Media*. Marcel Dekker, New York.

Vafai, K. and S. Kim: 1990, 'Fluid mechanics of the interface region between a porous medium and a fluid layer – an exact solution'. *International Journal of Heat and Fluid Flow* **11**(3), 254–256.

Vafai, K. and R. Thiyagaraja: 1987, 'Analysis of flow and heat transfer at the interface region of a porous medium'. *International Journal of Heat and Mass Transfer* **30**(7), 1391–1405.

Viola, E., A. Piva, and E. Radi: 1989, 'Crack propagation in an orthotropic medium under general loading'. *Engineering Fracture Mechanics* **34**(5), 1155–1174.

Vortmeyer, D.: 1975, 'Axial heat dispersion in packed beds'. *Chemical Engineering Science* **30**(8), 999–1001.

Vortmeyer, D. and R. Schaefer: 1974, 'Equivalence of one-and two-phase models for heat transfer processes in packed beds: one dimensional theory'. *Chemical Engineering Science* **29**(2), 485–491.

Wakao, N., S. Kaguei, and T. Funazkri: 1979, 'Effect of fluid dispersion coefficients on particle-to-fluid heat transfer coefficients in packed beds: correlation of Nusselt numbers'. *Chemical engineering science* **34**(3), 325–336.

Wang, G., Y. Yang, H. Zhang, and W. Xia: 2007, '3-D model of thermo-fluid and electrochemical for planar SOFC'. *Journal of power sources* **167**(2), 398–405.

Whitaker, S.: 1986, 'Local thermal equilibrium: an application to packed bed catalytic reactor design'. *Chemical Engineering Science* **41**(8), 2029–2039.

Whitaker, S.: 1991, 'Improved constraints for the principle of local thermal equilibrium'. *Industrial & Engineering Chemistry Research* **30**(5), 983–997.

Williams, G. A. and C. T. Miller: 1999, 'An evaluation of temporally adaptive transformation approaches for solving Richards' equation'. *Advances in Water Resources* **22**(8), 831–840.

Wong, K. F. and A. Dybbs: 1976, 'An experimental study of thermal equilibrium in liquid saturated porous media'. *International Journal of Heat and Mass Transfer* **19**(2), 234–235.

Xia, W., Y. Yang, and Q. Wang: 2009, 'Effects of operations and structural parameters on the one-cell stack performance of planar solid oxide fuel cell'. *Journal of Power Sources* **194**(2), 886–898.

Xue, X., J. Tang, N. Sammes, and Y. Du: 2005, 'Dynamic modeling of single tubular SOFC combining heat/mass transfer and electrochemical reaction effects'. *Journal of Power Sources* **142**(1), 211–222.

Yakabe, H., Y. Baba, T. Sakurai, and Y. Yoshitaka: 2004, 'Evaluation of the residual stress for anode-supported SOFCs'. *Journal of Power Sources* **135**(1), 9–16.

Younes, A. and P. Ackerer: 2008, 'Solving the advection–dispersion equation with discontinuous Galerkin and multipoint flux approximation methods on unstructured meshes'. *International Journal for Numerical Methods in Fluids* **58**(6), 687–708.

Younes, A. and P. Ackerer: 2010, 'Empirical versus time stepping with embedded error control for density-driven flow in porous media'. *Water Resources Research* **46**(8).

Younes, A. and V. Fontaine: 2008a, 'Efficiency of mixed hybrid finite element and multipoint flux approximation methods on quadrangular grids and highly anisotropic media'. *International Journal for Numerical Methods in Engineering* **76**(3), 314–336.

Younes, A. and V. Fontaine: 2008b, 'Hybrid and multi-point formulations of the lowest-order mixed methods for Darcy's flow on triangles'. *International journal for numerical methods in fluids* **58**(9), 1041–1062.

Younes, A., A. Makradi, A. Zidane, Q. Shao, and L. Bouhala: 2014, 'A combination of Crouzeix-Raviart, Discontinuous Galerkin and MPFA methods for buoyancy-driven flows'. *International Journal of Numerical Methods for Heat & Fluid Flow* **24**(3), 735–759.

Zamani, A. and M. R. Eslami: 2010, 'Implementation of the extended finite element method for dynamic thermoelastic fracture initiation'. *International Journal of Solids and Structures* **47**(10), 1392–1404.

Zanotti, F. and R. Carbonell: 1984a, 'Development of transport equations for multiphase system–I: General Development for two phase system'. *Chemical Engineering Science* **39**(2), 263–278.

Zanotti, F. and R. Carbonell: 1984b, 'Development of transport equations for multiphase systems–II: Application to one-dimensional axi-symmetric flows of two phases'. *Chemical engineering science* **39**(2), 279–297.

Zanotti, F. and R. Carbonell: 1984c, 'Development of transport equations for multiphase systems–III: Application to heat transfer in packed beds'. *Chemical engineering science* **39**(2), 299–311.

Zhu, W. and S. Deevi: 2003, 'A review on the status of anode materials for solid oxide fuel cells'. *Materials Science and Engineering: A* **362**(1), 228–239.

Zi, G. and T. Belytschko: 2003, 'New crack-tip elements for XFEM and applications to cohesive cracks'. *International Journal for Numerical Methods in Engineering* **57**(15), 2221–2240.

Nomenclature

Roman Symbols

$\mathbf{C}$	Material stiffness tensor (MPa)
C	Species concentration (mol m^{-3})
c	specific heat capacity (J kg^{-1} K^{-1})
$\mathbf{D}$	Strain tensor
$\mathfrak{d}$	Specific heat capacities ratio ($(\rho c)_{PM}/\rho_f c_f$)
D	Species molecular diffusivity (m^2 s^{-1})
D_A	Darcy number
$E_{electrode}$	Electrode activation energy (J mol^{-1})
E_m	Young's modulus (MPa)
F	Faraday constant (C mol^{-1})
F_I, F_{II}	Normalized stress intensity factors for mode I and mode II (MPa $m^{0.5}$)
g	Gravitational acceleration (m s^{-2})
Gr	Grashof number
$I^{(1,2)}$	Interaction integral between state (1) and state (2) (MPa m)
j	Current density (A m^{-2})
$j_{0,electrode}$	Exchange current density (A m^{-2})
$\mathbf{k}$	Thermal conductivity tensor in anisotropic material (W m^{-1} K^{-1})
K	Permeability of the porous medium (m^2)

k	Thermal conductivity (W m^{-1} K^{-1})
K_I, K_{II}	Stress intensity factors for mode I and mode II (MPa m$^{0.5}$)
K_{Ieq}	Equivalent stress intensity factor (MPa m$^{0.5}$)
K_{Ic}	Material toughness (MPa m$^{0.5}$)
Le	Lewis number
N	Buoyancy ratio
Nu	Nusselt number
P	Dimensionless pressure
p	Pressure (Pa)
Pr	Prandtl number
$\mathbf{q}$	Darcy's velocity (m s^{-1})
Q_f	Fluid source term (s^{-1})
Q_S	Species source term (mol m^{-3} s^{-1})
Q_T	Heat source term (J m^{-3} s^{-1})
$\mathfrak{R}$	Universal gas constant (J K^{-1} mol^{-1})
Ra^*	Thermal porous Rayleigh number
R_k	Thermal conductivity ratio (k_{PM}/k_f)
R_{Ohm}	Total cell resistance (Ω m^2)
r_p	Average pore size of the porous medium (m)
ΔS	Entropy change of the reaction (J K^{-1} mol^{-1})
$\mathbf{S}$	Material compliance tensor (MPa^{-1})
s	Specific storativity (m^{-1})
Sh	Sherwood number
T	Temperature (K)

$\mathbf{u}$	Displacement vector (m)
$U^0_{H_2}$	Standard cell potential (V)
$\mathbf{v}\,(v_x, v_y)$	Velocity components (m s^{-1})
V_X, V_Y	Dimensionless velocity components (m s^{-1})
$\mathcal{W}$	Interaction strain energy (MPa)

Greek Symbols

α	Thermal diffusivity (m^2 s^{-1})
α_L, α_T	Longitudinal and transverse thermal dispersivities (J m^{-3} s^{-1})
β_C	Solutal volumetric expansion coefficient (m^3 mol^{-1})
β_T	Thermal volumetric expansion coefficient (K^{-1})
ε	Porosity of the medium
η_{act}	Activation overpotential (V)
η_{conc}	Concentration overpotential (V)
η_{Ohm}	Ohmic overpotential (V)
γ	kinematic viscocity (m^2 s^{-1})
γ_e	Temporal truncation error tolerance
$\gamma_{electrode}$	Electrode pre-exponential coefficient (A m^{-2})
κ	Kolosov constant
Λ	Viscosity ratio (μ_e/μ)
λ	Species diffusivity ratio (D_e/D)
μ	Fluid dynamic viscosity (kg m^{-1} s^{-1})
μ_e	Effective viscosity (kg m^{-1} s^{-1})
μ_m	Shear mudulus (MPa)
ν	Poisson's ratio

ϕ	Dimensionless concentration
ρ	Density (kg m^{-3})
$\boldsymbol{\sigma}$	Cauchy stress tensor (MPa)
$\sigma_{electrode}$	Electronic conductivity (Ω^{-1} m^{-1})
$\tau_{electrode}$	Electrode thickness (m)
τ_g	Tortuosity of the porous medium
θ	Dimensionless temperature
ϑ_p	Crack growth direction

Subscripts

0	Reference
air	Air channel
C	Solutal
e	Effective
f	Fluid phase
$fuel$	Fuel channel
H_2	Hydrogen
H_2O	Water
O_2	Oxygen
PM	Porous medium
s	Solid phase
T	Thermal

Abbreviations

CR	Crouzeix-Raviart
DB	Darcy-Brinkman

DG	Discontinuous Galerkin
FEM	Finite Element Method
FG	Fourier Galerkin
MPFA	Multi-Point Flux Approximation
NS	Navier-Stokes
OCP	Open-Circuit Potential
SIF	Stress Intensity Factor
SOFC	Solid Oxide Fuel Cell
TPB	Three Phase Boundary
XFEM	eXtended Finite Element Method